EXPERIMENTAL INVESTIGATION OF STEEL FIBER REINFORCED CONCRETE AS SUPPLEMENTAL REINFORCEMENT IN BRIDGE DECKS

A Thesis

by

JOSHUA A MCMAHON

Submitted to the Office of Graduate and Professional Studies of
Texas A&M University
in partial fulfillment of the requirements for the degree of

MASTER OF SCIENCE

Chair of Committee,	Anna Birely
Committee Members,	Philip Park
	Anastasia Muliana
Head of Department,	Robin Autenrieth

December 2016

Major Subject: Civil Engineering

ABSTRACT

Research on fiber reinforced concrete has been ongoing since the 1960's. The current state of knowledge of SFRC demonstrates the benefits of the fibers in regards to the ductility, energy dissipation, and strength improvements of the reinforced concrete matrix. However, further validation of SFRC as supplemental or alternative reinforcement needs to be conducted before bridge deck designs using SFRC may be utilized. The interaction between FRC and steel reinforcement needs to be identified as current practice in the United States and Canada require positive reinforcement as an anti-progressive collapse mechanism regardless of the reinforcement or concrete matrix detailing. Low dosages of fibers could also be used to satisfy service requirement while steel reinforcement satisfies the strength requirements. As a result, the behavior of a SFRC deck under service conditions must also be investigated. The lack of practical, large scale experiments and a simple and reliable method for accurately determining the tensile residual stress for SFRC has prevented the adoption of building codes regarding SFRC in the United States.

This research identified the possible use of steel fiber reinforced concrete (SFRC) in bridge decks as supplemental reinforcement. A case study analysis was conducted to identify how the performance of SFRC was influenced by the bridge deck geometry, steel reinforcement ratio, and SFRC residual strength. The analysis shows that the addition of fibers permits a reduction of traditional steel reinforcement while achieving design requirements. Findings of the theoretical study was verified in an experimental parameter study of individual SFRC slab-strips subjected to four point bending tests. The slab-strips investigated the depth of the bridge deck, the ratio of steel reinforcement, and its location in the cross-section. The load-deformation and crack patterning of the slab-strips describe the strength and failure behavior of SFRC. A full-scale bridge deck was designed and tested using AASHTO LRFD design procedures and the results of the slab-strip tests. A yield line analysis was conducted on the bridge deck results to show the benefits of SFRC with respect to theoretical predictions. Based on the results of each phase of testing, design recommendations are provided to predict the capacity of SFRC slabs.

CONTRIBUTORS AND FUNDING SOURCES

Contributors

The theoretical and experimental work presented in this thesis was supported by a thesis committee consisting of Dr. Anna Birely [advisor], Dr. Philip Park of the Department of Civil Engineering and Dr. Anastasia Muliana of the Department of Mechanical Engineering.

All other work presented in this thesis was completed by the graduate student, Joshua McMahon.

Funding Sources

This thesis was funded in part through grants from the Federal Highway Administration, U.S. Department of Transportation, Arizona DOT SPR-705. The contents do not necessarily reflect the official views or policies of the Arizona Department of Transportation or the Federal Highway Administration, U.S. Department of Transportation.

TABLE OF CONTENTS

Page

LIST OF FIGURES

Page

LIST OF TABLES

Page

1. INTRODUCTION

Fiber reinforced concrete (FRC) is a composite material created by mixing small, discrete fibers in a concrete mix. The fibers are uniformly dispersed and randomly oriented. When small cracks begin to form in the concrete, the fibers act as reinforcement to restrain the opening of the cracks. Consequently, the post-cracking response of the concrete is enhanced compared to the same concrete without fiber. The characteristics of the post-crack response are dependent on the fiber volume and characteristic. Fibers can be made out of a wide variety of material, including steel. Steel fiber reinforced concrete (SFRC) provides the dual benefit of adding both stiffness and strength to traditional concrete mixes. This thesis is focused on the use of SFRC for bridge decks.

Research on FRC has been ongoing since the 1960's. The current state of knowledge of SFRC demonstrates the benefits of the fibers in regards to the ductility, energy dissipation, and strength improvements of the reinforced concrete matrix. However, the implementation of SFRC in transportation structures necessitates investigation to ensure that the material benefits are efficiently harnessed and that appropriate design procedures are adopted to ensure safe, efficient designs are developed. Gaps from previous research that must be addressed include the interaction of SFRC and traditional reinforcement in bridge decks, the impact of SFRC on the service level behavior of bridge decks, and the two-way behavior of decks with orthotropic reinforcement and SFRC.

1.1 Objective

To advance the knowledge of SFRC as supplemental reinforcement in bridge decks, the following objectives were established:

1. Investigate the effect of SFRC on strength and serviceability of individual slab-strip specimens representative of a bridge deck.
2. Investigate the effect of SFRC on strength and serviceability of a large-scale bridge deck.
3. Investigate the effect of SFRC on the relationship between steel reinforcement ratio and residual strength of SFRC.
4. Provide design recommendations for the use of SFRC in bridge decks.

1.2 Outline of Document

Section 2 presents a literature review establishing the necessary background for the research in this thesis, including design methods for SFRC, use of SFRC in structural applications, and other methods explored to reduce the amount of steel used in bridge decks.

Section 3 presents the results of a preliminary investigation into the use of SFRC in bridge deck. The impact of adding SFRC with varying levels of post-cracking tensile strength were evaluated to establish the estimated impact of SFRC on the service stress and ultimate strength in bridges designed in accordance with typical practice of the Arizona Department of Transportation.

The results of the Section 3 case studies were used to develop an experimental test program investigating the one-way behavior of slab strips. Section 4 presents the results of these tests, which investigated the amount and location of traditional reinforcement to improve understanding. Section 5 presents analysis of the slab strip tests in Section 4, with an emphasis on inverse analysis to establish material properties for use in moment-curvature analysis.

Based on the results of the slab strip tests and subsequent analysis, an experimental test of a full-scale bridge deck was conducted. The results of this test are presented in Section 6. Section 7 presents an analysis of this data, with an emphasis on calculation of the ultimate strength using yield line analysis.

Section 8 presents recommendations for use of SFRC in design and lays out potential design procedures that for evaluation of service stresses. Section 9 provides a summary of the thesis.

2. LITERATURE REVIEW

The purpose of the literature review is to identify the advantages and disadvantages of using FRC. Sections 2.1 and 2.2 provide the characteristics and general behavior of FRC. Section 2.3 discusses currently approved and proposed design methods will be discussed to demonstrate the incorporation of FRC design into structural elements. Section 2.4 explores the experimental and real-world applications of FRC in structural components to demonstrate the benefits and feasibility of FRC in practice.

2.1 Behavior of FRC

The addition of fibers to the concrete matrix enhances both the compressive and tensile response of concrete; however, the effect is more profound in the tension response. Prior to the formation of the first crack, both the compression and tension response of FRC do not deviate from the traditional constitutive models used for plain concrete (PC). Therefore, neither the tensile cracking stress nor the maximum compressive strength are affected by the fibers. The fibers are then "engaged" after cracking occurs. The fibers behave similar to confining reinforcement in the compressive response of FRC, reducing the rate of degradation of the compressive strength and increasing the maximum compressive strain as shown by Figure 1.

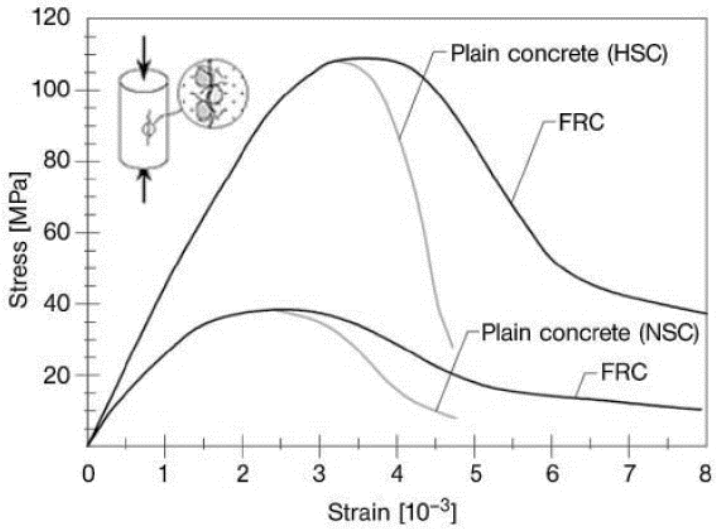

Figure 1. Comparison of Compression Response of FRC and PC (fib 2013)

The tension response of FRC after cracking occurs is significantly different than the response of PC. The fibers allow the concrete to have a residual tensile strength whose magnitude is dependent on the volume and type of fibers added. Naaman and Reinhardt (2006) proposed a classification system to identify the tensile response of FRC as a result of the varying post-crack residual strength. With sufficient volume of fibers, the tensile stress can continue to increase beyond the cracking stress. This behavior is classified as strain-hardening. If the fibers provide a residual tensile strength that gradually declines as the strain increases the behavior is classified as strain-softening.

Kim et al (2008) applied the same classification system to the flexural response of FRC as shown in Figure 2. Deflection hardening occurs when the modulus of rupture is larger than limit of proportionality; otherwise, the FRC is classified as deflection softening.

Despite the similar classification system, the "critical" dosage required for the hardening effect to manifest is different for the tensile strain and deflection responses. A residual stress of 35% of the cracking stress is sufficient for deflection hardening to occur according to Soranakom and Mobasher (2007). This level of residual stress is classified as strain-softening as the residual stress is less than the cracking stress of FRC. Willie et al (2014) illustrates the different performance combinations for FRC based on strain and deflection softening or hardening as shown in Figure 3. The varying levels of performance for FRC demonstrate the need for accurate methods for obtaining the constitutive relationships for the composite material.

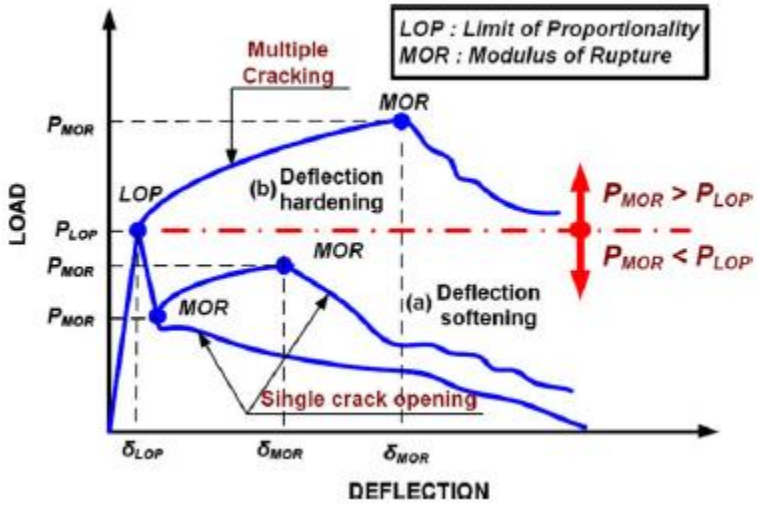

Figure 2. Generalized Load-Deflection Response of FRC (Kim et al 2008)

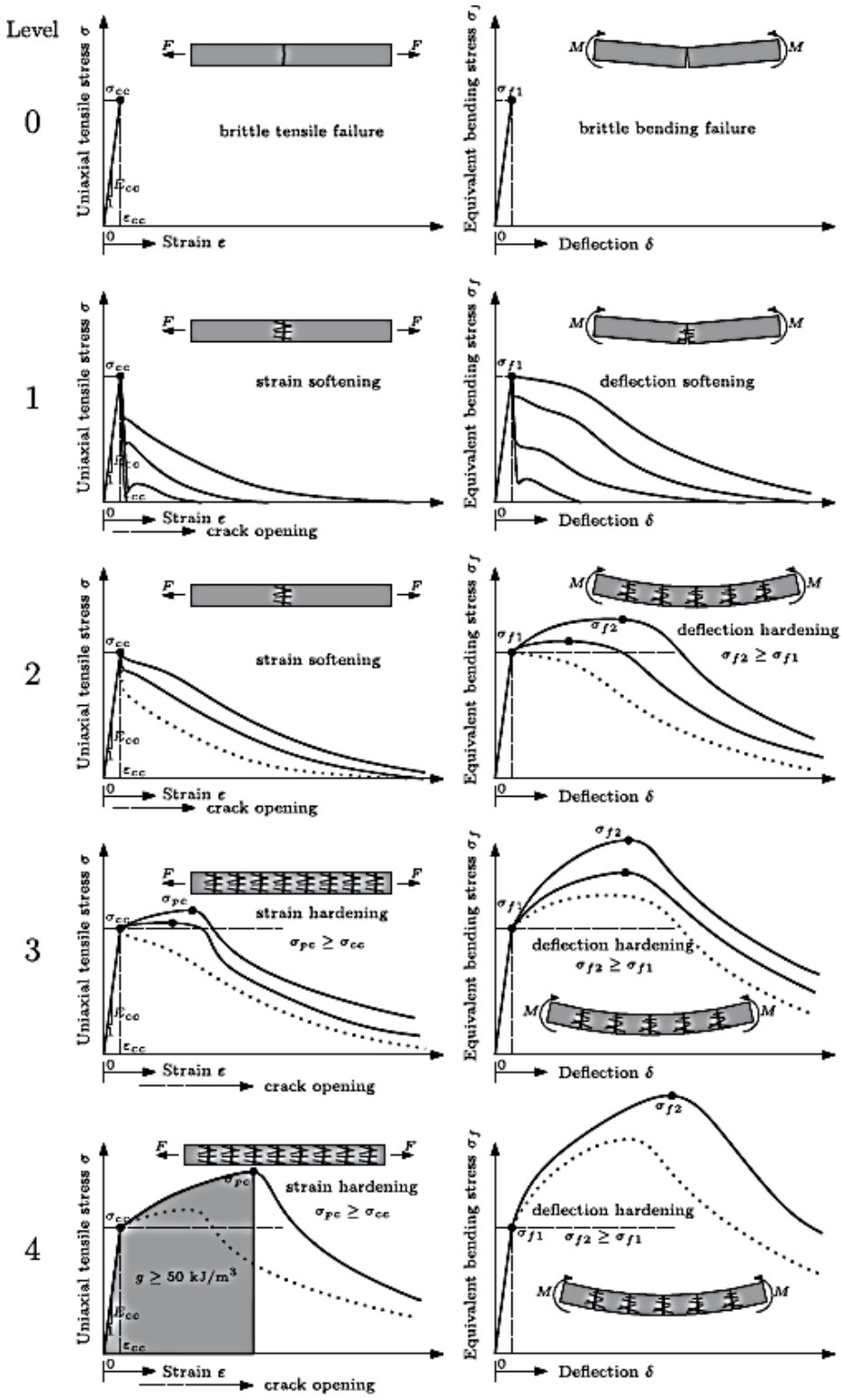

Figure 3. Performance Levels of FRC (Willie et al 2014)

2.2 Standard Material Tests

2.2.1 Compression

Section 2.1 discussed the compression response of SFRC and its similarity to the compression response of PC. Therefore, the standard tests used for PC are suitable for determining the compression response for FRC. The American Society of Testing and Materials (ASTM) specify two tests to determine the compressive strength and modulus of elasticity of concrete: ASTM C39 – "Standard Test Method for Compressive Strength of Cylindrical Concrete Specimens" and ASTM C469 – "Standard Test Method for Static Modulus of Elasticity and Poisson's Ratio of Concrete in Compression." The tests are conducted by subjecting a cylindrical specimen to an axial compressive load until failure as shown in Figure 4.

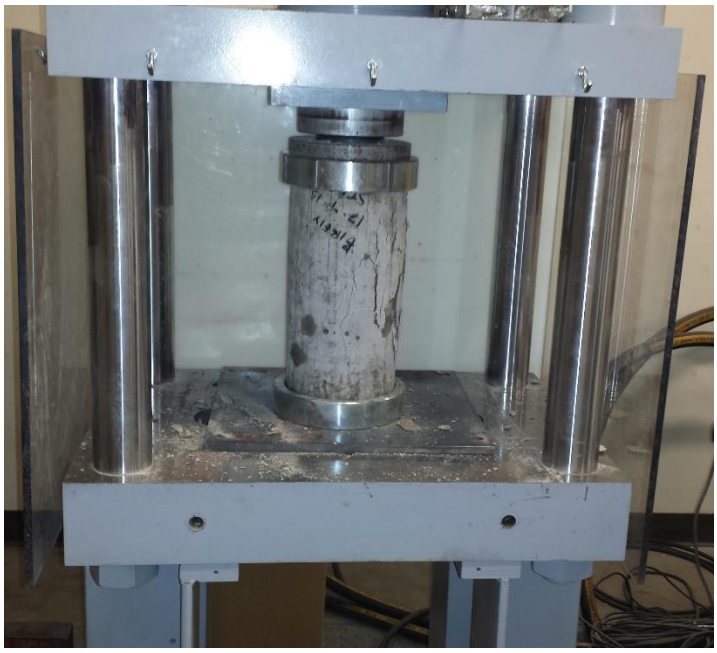

Figure 4. ASTM C39 - Compression of 6 in x 12 in Cylinder

2.2.2 Tension

The brittle nature and non-uniformity of the concrete matrix prevents a specimen from obtaining a uniform stress when subjected to uniaxial tension. The difficulty of conducting a uniaxial test

has hindered the adoption of a standard for uniaxial tension of FRC or PC (Willie et al 2014). Methods have been proposed for obtaining the tension response that include various gripping conditions and specimen shapes such as dogbone, unnotched, and notched prisms. Unnotched prisms and dogbone tests have been shown to obtain the the post-crack response of FRC (Willie et al 2014). However, the location of the tensile cracks from these methods are inconsistent (Woods 2012). Furthermore, the response recorded during the uniaxial tests are localized failures of the FRC and do not adequately capture the overall performance of FRC. Direct uniaxial tension tests are typically not utilized as a result of these complications.

2.2.3 Bending

Various methods have been developed to determine the flexural response of FRC. These tests are used to infer information regarding the tensile constitutive relationship of FRC due to the inability to conduct direct uniaxial tension tests. ASTM has developed two methods for determine the flexural response of FRC: ASTM C1609 – "Standard Test Method for Flexural Performance of Fiber-Reinforced Concrete (Using Beam with Third-Point Load)" and ASTM C1399 – "Standard Test Method for Obtaining Average residual-Strength of Fiber-Reinforced Concrete." ASTM C1609 utilizes an unnothced prism (6 x 6 x 20 inches) that is subjected to four point bending as shown in Figure 5.

Figure 5. ASTM C1609 – Four Point Bending Test of Concrete Prism (6 in x 6 in x 20 in)

Despite the adoption of these procedures by ASTM, a direct conversion of the flexural response to a tension response does not exist (ACI 544 2016). One method for obtaining the tension response from standard flexural tests is to utilize a parametric stress-strain curve and back-calculate the required parameters to obtain the force-deflection response measured during the flexural test (Soranakom and Mobasher 2007, Soranakom et al 2008, and Mobasher et al 2015).

Figure 6 shows the notched-prism flexural tests used in design procedures proposed by RILEM TC162-TDF (2003) and fib (2013). Empirical relationships have been developed relating the tensile response with the crack mouth opening displacement (CMOD) of the notched prism as discussed in Section 2.3.

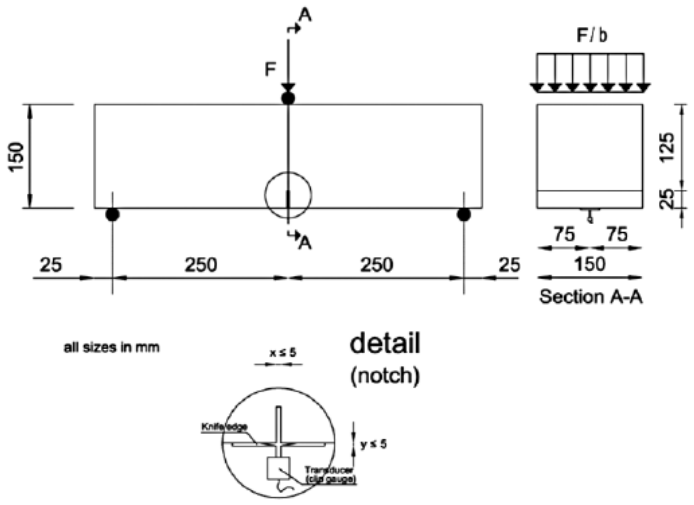

Figure 6. Test Setup Required for Flexural Test EN-14651 (fib 2013)

2.3 Design Methods

A design procedure for FRC has not been adopted by building codes in the United States. However, other countries and organizations have adopted methods for designing with FRC. Additionally, various researchers have proposed simplified and closed-form solutions for the flexural design of FRC.

2.3.1 RILEM TC 162-TDF Method

RILEM is an international organization created for the study of construction materials, systems, and structures. The European pre-standard, ENV 1992-1-1 was used as the framework for the design standard.

The method is based on the fictitious crack model (FCM) originally proposed by Hillerborg et al (1976) (RILEM TC 162-TDF 2002). The FCM divides the crack region into three zones: the process zone, the aggregate interlock zone, and the traction free zone as shown in Figure 7. Stress can be transferred through the process and aggregate interlock zones, but cannot be transferred through the traction free zone. The stress capacity of each zone is defined by a stress-crack opening relationship determined through standard bending tests with notched prismatic members.

The RILEM technical committee adopted this FCM concept and modified it to include the contribution of steel fibers (RILEM TC 162-TDF 2002).The steel fibers bridge each zone, including the traction free zone, effectively increasing the stress capacity of the crack as demonstrated in Figure 7.

Flexural testing is conducted to determine the relationship between the stress and the crack mouth opening displacement. Testing in accordance with the RILEM bending test is achieved by subjecting a 150 x 150 x 550 mm (6 x 6 x 22 inches) concrete specimen to a three point bending test (RILEM TC 162-TDF 2002). The prismatic specimen is notched at its midpoint on the tension face to a depth of 25 mm (1 inch) to simulate a crack in the specimen. As the bending test is conducted, the CMOD is measured until the beam fails. An example of the applied load and CMOD relationship is shown in Figure 8.

The stress-crack opening relationship is paired with empirical equations to relate the flexural and compressive strengths to the mean and characteristic flexural tensile strength (RILEM TC 162-TDF 2003). Figure 9 shows the general stress-crack opening relationship and compression curve for SFRC materials. The design of an SFRC member can be achieved with the constitutive models, strain compatibility, and cross section equilibrium as shown in Figure 10.

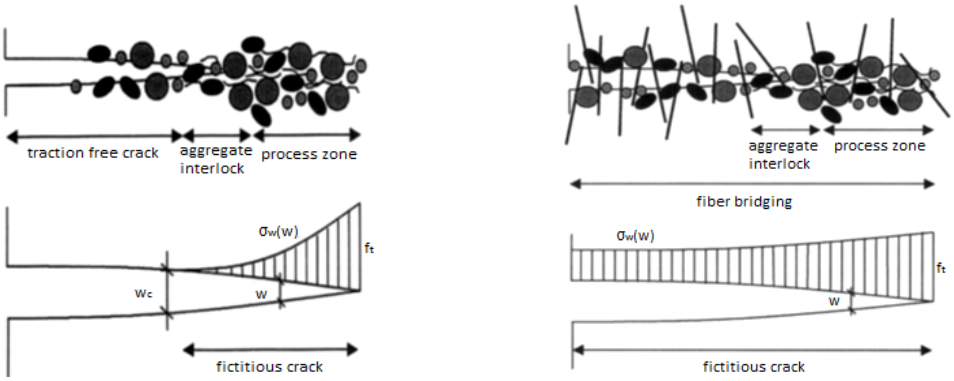

(a) Without Steel Fibers (b) With Steel Fibers

Figure 7. Fictitious Crack Model of FRC (RILEM TC 162-TDF 2002)

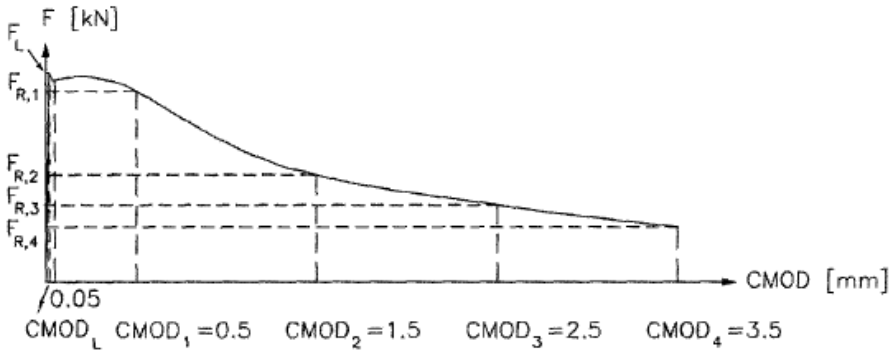

Figure 8. Typical Load - CMOD Relationship (RILEM TC 162-TDF 2003)

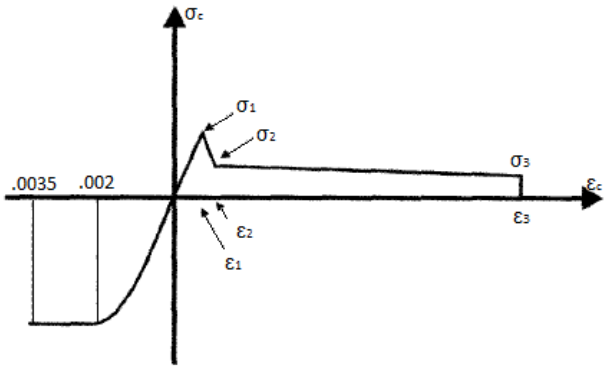

Figure 9. Stress - Strain Constitutive Relationship (RILEM TC 162-TDF 2003)

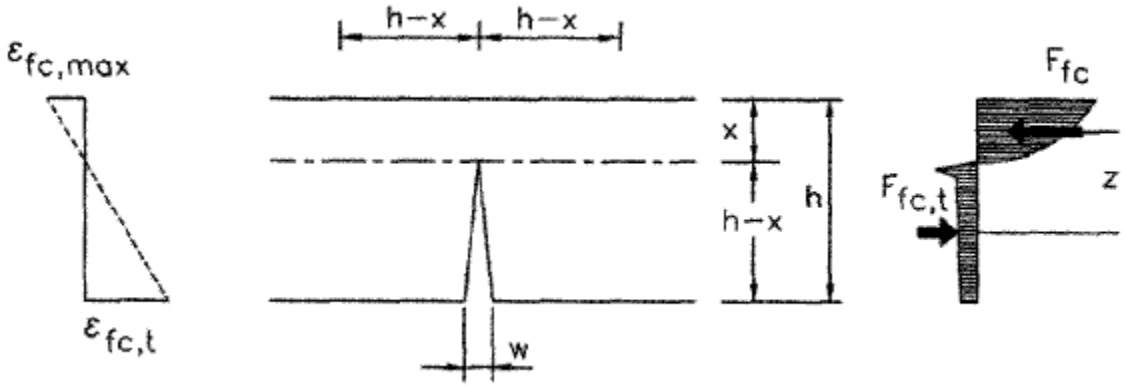

Figure 10. Strain Compatibility and Cross Section Equilibrium for SFRC (RILEM TC 162-TDF 2003)

$$\sigma_1 = 0.7 f_{fctm,fl}(1.6 - d) \quad (1)$$

$$\sigma_2 = 0.45 f_{R,1} k_h \quad (2)$$

$$\sigma_2 = 0.37 f_{R,4} k_h \quad (3)$$

Where $f_{fctm,fl}$ is the mean flexural tensile strength, d is the depth to steel reinforcement, $f_{R,1}$ and $f_{R,4}$ are the residual flexural stresses at $CMOD_1$ and $CMOD_4$ respectively, and k_h is the size correction factor.

The design standard limits the maximum compressive strain to 0.0035 and the maximum tensile strain in typical steel reinforcement to 0.025. Additionally, the committee discovered that the accuracy of the design method varied with member depth and introduced a size correction factor (RILEM TC 162-TDF 2003).

The RILEM design standard addresses cracking through an equation to calculate the minimum area of traditional steel reinforcement. If the calculated minimum area is less than zero, the steel fibers are sufficient to limit cracking. Additionally, the moment-curvature relationship and moment-area theorems can be used to calculate the deflection of the member.

2.3.2 Fib Model Code For Concrete Structures (fib)

The "Model Code for Concrete Structures" utilizes a stress-crack width relationship similar to the RILEM method. The constitutive relationship is determined through a notched flexural test, EN14651. Two simplified post-cracking constitutive laws are provided by the code: rigid-plastic and linear model as shown in Figure 11. From the stress-crack width relationship, the strain is determined based on the characteristic length (l_{cs}). The characteristic length for FRC is the equal to the spacing of cracks, and may be equal to the depth of the beam when plane section analysis is performed.

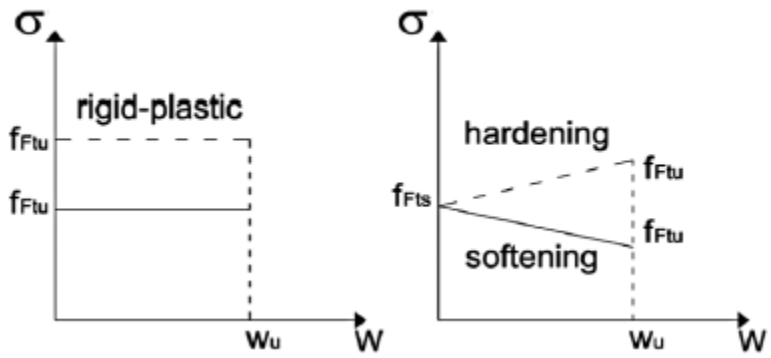

Figure 11. Simplified Constitutive Models
"Model Code for Concrete Structures" (fib 2013)

Rigid-Plastic Model

$$f_{Ftu} = \frac{f_{R3}}{3} \quad (4)$$

Linear Model

$$f_{Fts} = 0.45 f_{R1} \quad (5)$$

$$f_{Ftu} = f_{Fts} - \frac{w_u}{CMOD_3}(f_{Fts} - 0.5 f_{R3} + f_{R1}) \quad (6)$$

Convert crack width to strain

$$\varepsilon = \frac{w}{l_{cs}} \quad (7)$$

Where f_{Ftu} is the residual strength for the ultimate limit state, $f_{R3}$is the residual stress determined from EN14651 at $CMOD_3$, $f_{Fts}$is the serviceability residual strength, f_{R1} is the residual stress determined from EN14651 at $CMOD_1$, w_u is the crack opening corresponding to the ultimate limit state, $CMOD_3$ is the crack mouth opening displacement of 2.5 mm, ε is the strain at w, and l_{cs} is the characteristic length or crack spacing for FRC.

Once the constitutive relationship is determined, the ultimate limit state is designed as normal with the addition of the FRC contributions. Figure 12 demonstrates the state of stresses at the ultimate limit state.

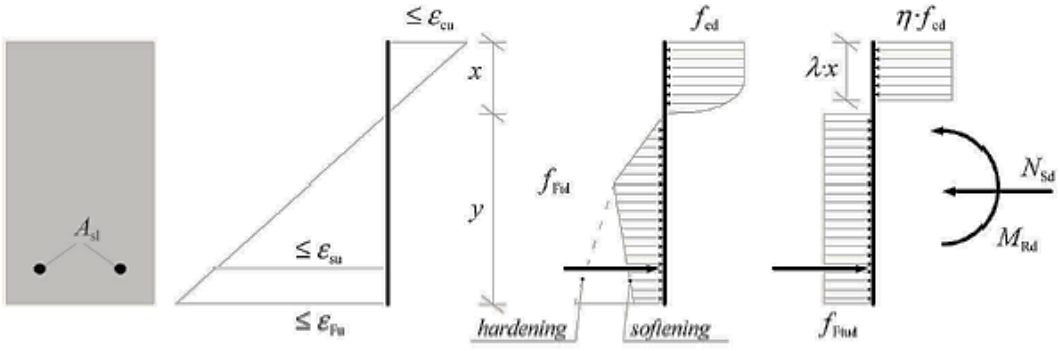

Figure 12. Ultimate Limit State of FRC Member (fib 2013)

2.3.3 Soranakom and Mobasher 2009 and Mobasher 2012

Soranakom and Mobasher proposed a design procedure that utilizes the basis of the RILEM TC-162-TDF design procedure in conjunction with definitions of the ACI 318 for a simplified strain-softening SFRC as shown in Figure 13. Mobasher (2012) extends the RILEM constitutive models to strain hardening FRC as shown in Figure 14. Both procedures assume that the fibers do not affect the stress or strain prior to the initial cracking of the specimen. Therefore, the cracking stress, strain, and modulus of elasticity are defined by ACI 318 and Hooke's Law. The stress-strain relationship and subsequent calculations are simplified by normalizing the constitutive relationships by the cracking stress and strain as demonstrated in Figure 14.

The simplification used in Figure 13 is based on the stress-strain relationship proposed by Lim et al (1987). The post cracking stress, σ_p, corresponds to the residual stress σ_2 of the RILEM TC-162-TDF design method, which is found by the RILEM deflection-controlled bending test. The yield compressive strain, σ_{cy}, is defined by the authors as 85 percent of the compressive strength.

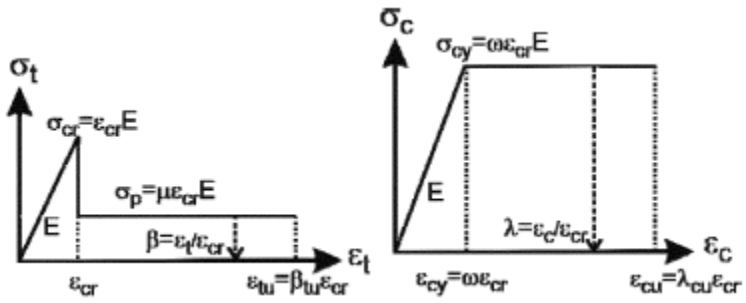

Figure 13. Idealized Constitutive SFRC Model (Soranakom and Mobasher 2007)

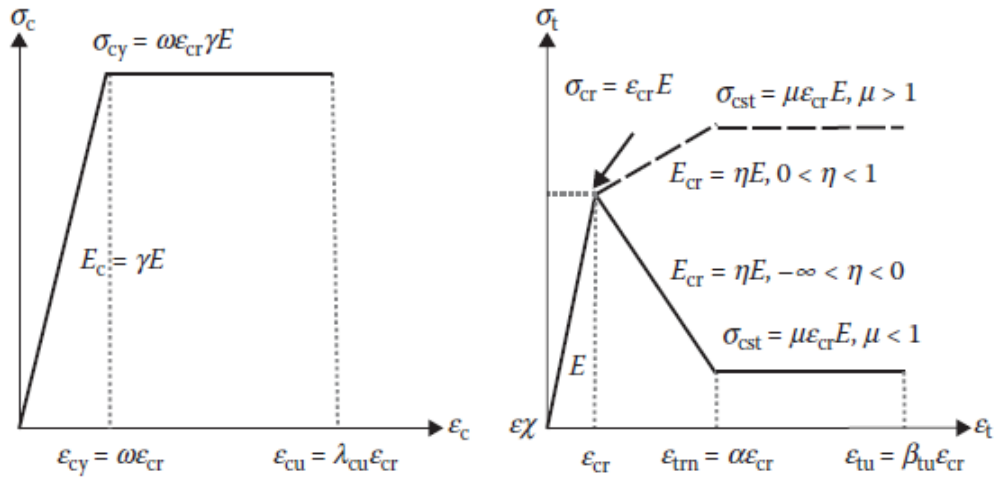

Figure 14. Compression (Left) and Tension (Right) Stress - Strain Relationship (Mobasher 2012)

The stress-strain relationships in Figure 13 and Figure 14 can be described by the cracking tensile stress, strain, and modulus of elasticity defined by ACI 318 in addition to seven parameters normalized by the cracking stress.

$$\sigma_{cr} = 7.5\sqrt{f'c} \quad (8)$$

$$E_c = 57000\sqrt{f'c} \quad (9)$$

$$\varepsilon_{cr} = \frac{\sigma_{cr}}{E_c} \quad (10)$$

Where σ_{cr} is the cracking stress as defined by ACI 318, E_c is the modulus of elasticity of concrete as defined by ACI 318, ω is ratio of the yield compressive stress to the cracking stress, γ is the ratio of the compressive modulus of elastic of concrete to the tensile modulus of elasticity, λ is the ratio of the ultimate compressive strain to the cracking strain, μ is the ratio of the post-crack tensile stress to the cracking stress, α is the ratio of the post-crack tensile strain to the cracking strain, β is the ratio of the ultimate tensile strain, ε_{tu} , to the cracking tensile strain, and η is the ratio of the modulus of elasticity of cracked concrete, E_{cr}, to the tensile modulus of elasticity.

The constitutive model, strain compatibility, and cross section equilibrium was used to determine closed form equations for the moment – curvature relationship. The authors found that by

allowing the normalized ultimate compressive strain, $\lambda_{cu,}$ to approach infinity, the nominal moment capacity for strain-softening SFRC could be closely approximated by:

$$\Phi_p M_n = \Phi_p m_\infty M_{cr} \quad (11)$$

$$m_\infty = \frac{3\omega\mu}{\omega + \mu} \quad (12)$$

$$M_{cr} = \frac{\sigma_{cr} b h^2}{6} \quad (13)$$

Where m_∞ is the ultimate normalized moment capacity and M_{cr} is the moment corresponding to the cracking stress.

The method was verified against experimental tests conducted by previous researchers (Soranakom and Mobasher 2007). The comparison demonstrated that the design procedure yielded near experimental values. The authors proposed a reduction factor, ϕ_p, of 0.7 to ensure a safe design.

2.3.4 Round Slabs and Yield Line Theory

Researchers investigating the use of SFRC in elevated flat slabs supported on columns have utilized yield line theory in conjunction with data determined from the testing of round slabs (Destrée and Mandl 2008). The test includes subjecting a simply supported, circular slab to an increasing point load at its center while the deflection is measured as shown in Figure 15.

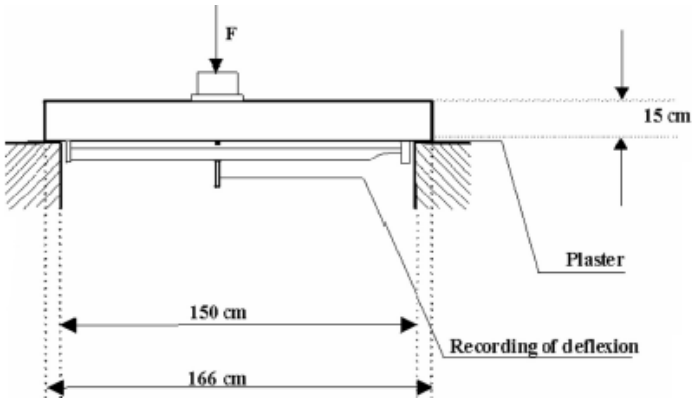

Figure 15. Test Setup for Round SFRC Slabs (Destrée and Mandl 2008)

The load is increased until the typical “fan” rupture pattern is achieved. The method was compared to several full scale tests of elevated flat slabs (Destrée and Mandl 2008). The design method resulted in capacities that were significantly less than experimental values leading to safety factors in excess of five. However, when compared to typical prismatic beam procedures, the round slab and yield line theory design method resulted in larger capacities.

2.3.5 American Concrete Institute (ACI)

Currently, the generally accepted design for structural concrete, Building Code Requirements for Structural Concrete (ACI 318), does not provide provisions for determining the moment capacity of fiber reinforced concrete. The specification does allow for the use of steel fibers as shear reinforcement if three conditions are met:

1. The weight of added fibers exceeds 100 pounds per cubic foot.
2. The residual strength corresponding to a midspan deflection of 1/300 of the span length, obtained from flexural testing, is at least 90 percent of the first-peak strength.
3. The residual strength corresponding to a midspan deflection of 1/150 of the span length, obtained from flexural testing, is at least 75 percent of the first-peak strength.

ACI Committee 544 has published several documents concerning fiber reinforced concrete. Design Considerations for Steel Fiber Reinforced Concrete (ACI 544.4R 1988) was published in 1988 and was reapproved in 2009. The document does not specify a design procedure. Rather, ACI 544.4R demonstrates methods utilized in research conducted prior to its original publication date. For example, the flexural design procedure proposed by Henager and Doherty in 1976 is included in ACI 544.4R for FRC beams containing both fibers and reinforcing steel bars.

Other documents published by ACI Committee 544, such as Measurement of Properties of Fiber Reinforced Concrete (ACI 544.2R 1999), and Guide for Specifying, Proportioning, and Production of Fiber-Reinforced Concrete (ACI 544.3R), provide insight on the effects of adding fibers to the concrete matrix, applications of FRC, and considerations for the mix design. However, at the present, ACI does not offer design specifications for FRC.

2.4 Structural Applications

Researchers have been utilizing the improved strength and performance of FRC in numerous applications. Some of the largest gains have been realized in seismic design, slabs-on-ground and flat elevated slabs, prestressed girders, and bridge decks.

2.4.1 Seismic Design

Several researchers have shown that the addition of up to 2 percent by volume of steel hook end are beneficial in seismic design and result in increased ductility, damage tolerance, energy

dissipation, and confinement (Lequesne et al 2013, Niwa et al 2012, Campione 2002, Aviram et al 2014).

Lequesne et al (2013) investigated the use of a strain hardening SFRC in coupling beams and plastic hinge regions of shear walls and found that, with the addition of 1.5 percent by volume of steel hook end fibers, the coupling beams failed in flexure, rather than shear, at large drift ratios (Lequesne et al 2013). The confining properties of the SFRC enabled the researchers to reduce the area of diagonal reinforcement by as much as 70 percent in addition to eliminating transverse reinforcement after a distance equal to half of the height of the coupling beam away from the wall to beam interface. The study has led to the implementation of SFRC coupling beams in a 440 ft tall residential building in Seattle, Washington with shear wall cores (Lequesne et al 2011).

Researchers at the Tokyo Institute of Technology found that SFRC aided in the prevention of anchorage failures of beam-column joints (Niwa et al 2012). Niwa et al (2012) determined that the addition of hook end fibers at 1.5 percent by volume allowed them to reduce the amount of longitudinal reinforcement and transverse reinforcement by as much as 29 percent in beam-column joints while still maintaining the ductility and energy dissipation of code compliant beam-column joints.

Campione (2002) suggested that SFRC used in conjunction with traditional steel reinforcement in columns could lead to a reduction in the amount of transverse reinforcement required to adequately confine a column. Aviram et al (2014) utilized the improved ductility and confinement of SFRC to reduce the amount of transverse steel in bridge columns imposed to bidirectional loading (Aviram et al 2014). They demonstrated that the SFRC columns did not exhibit significant spalling and could effectively decrease the amount of required transverse reinforcement by half.

Ultimately, the use of SFRC has improved the reinforcement congestion in many seismic applications without negatively affecting the ductility and energy dissipation of these systems. These studies have demonstrated the confining nature and energy dissipation attributed to SFRC; however, these seismic applications do not address the supplemental strength provided by the added fibers.

2.4.2 Beams

Kwak et al (2002) investigated the influence of concrete strength and the volume of fibers on the flexural response of beams. A total of twelve beams with a cross section of 125 mm (5 inch) x 250 mm (10 inch) were subjected to two point loads 400 mm (16 inches) apart centered at the beam's midpoint. The length of the beams varied from 1548 mm (5 ft) to 2396 mm (8 ft). The specimens included traditional steel reinforcement in the longitudinal direction, but not the transverse as shown in Figure 16.

As the beam increased in length and fiber content, the mode of failure transformed from shear to flexural (Kwak et al 2002). The addition of steel fibers increased the shear strength of the concrete beams by as much as 180 percent. The largest increases were observed in beams with the lowest shear-span ratios, or shortest length; however, the longer beams failed in flexure and could not achieve its maximum shear strength. Ultimately, the researchers evaluated existing methods for determining the shear strength of SFRC members and proposed a new equation to determine the shear strength utilizing their data and data from several other tests.

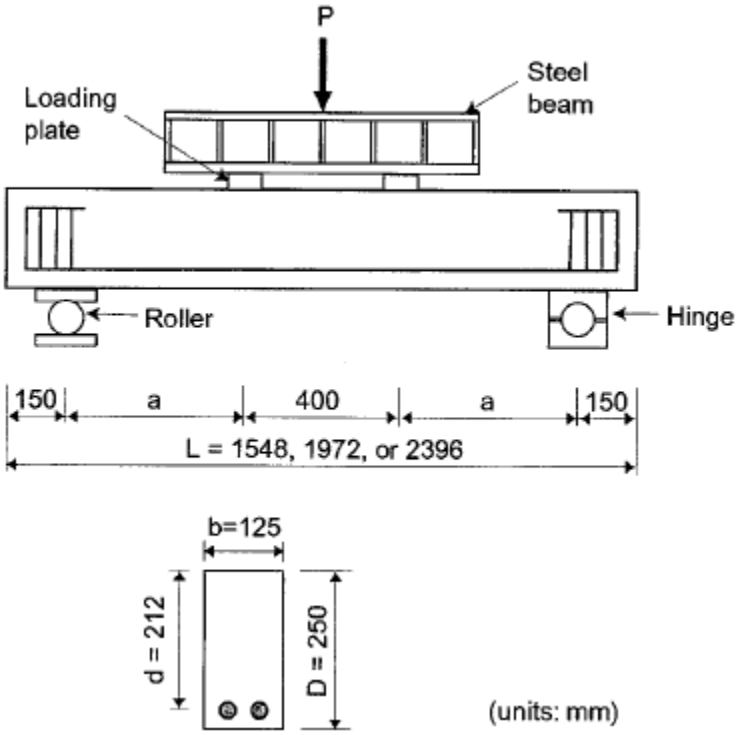

Figure 16: Experimental Beam Setup (Kwak et al 2002)

Dinh et al (2011) investigated 27 large-scale beams with varying amounts of steel fibers and longitudinal reinforcement. Traditional longitudinal reinforcement was included to ensure that the beams failed in shear rather than flexure. The depth of the SFRC specimens varied from 455 mm (18 inches) to 685 mm (27 inches) to account for size effects. The researchers analyzed the resulting data using a crack width versus stress relationship determined from standard four-point bending tests and equilibrium. Figure 17 demonstrates the expected stress profile at a diagonal crack in an SFRC specimen (Dinh et al 2011). This method has resulted in predicted strengths of approximately 80 percent of the actual shear strengths measured during the experiment. The

benefit of the stress profile approach is that it does not require direct knowledge of the post-crack strength of SFRC, rather, the information from four-point bending tests is sufficient.

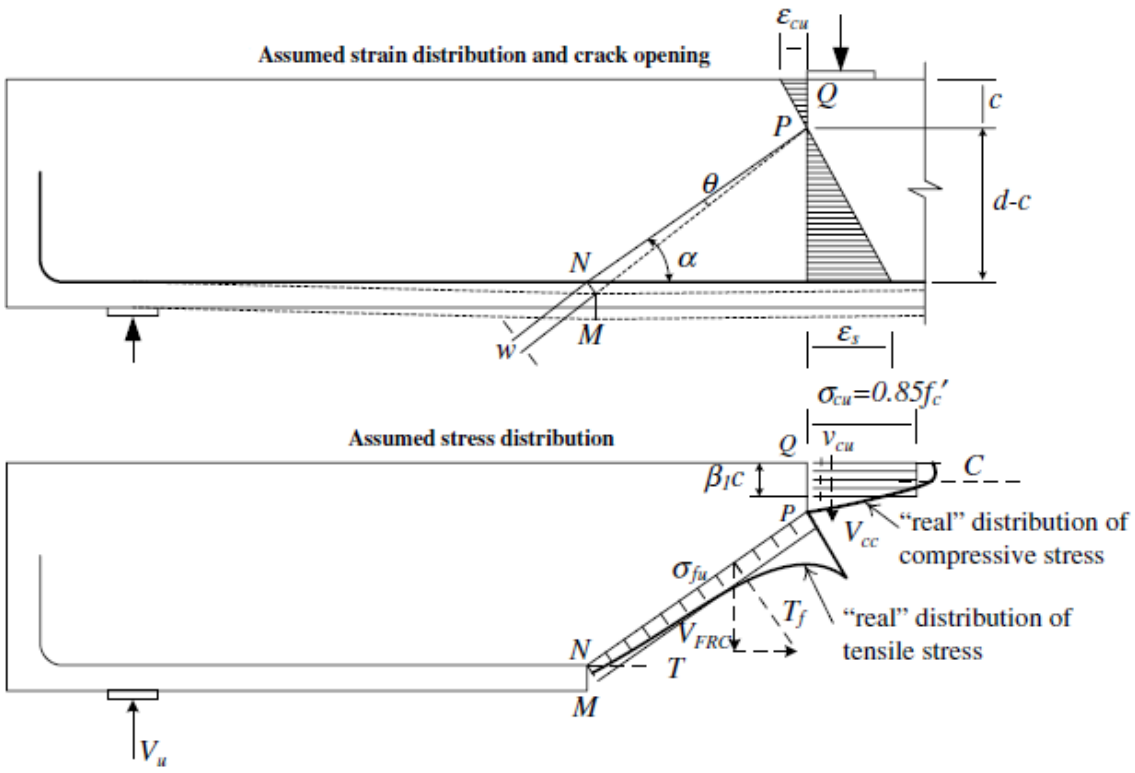

Figure 17: Assumed Stress and Strain Profile for Diagonal Shear Cracks (Dinh et al 2011)

The use of SFRC in prestressed beams has also been investigated. Dhonde et al (2005) used SFRC in the end regions of prestressed beams in an effort to reduce the amount of cracking and transverse reinforcement (Dhonde et al 2005). They tested seven prestressed beams with varying volumes of steel fibers and transverse reinforcement. The use of steel fibers successfully reduced or eliminated visible cracking in the end regions of the I-girder. Additionally, the fibers changed the failure from a brittle one to a ductile one. The best performing prestressed girder used 1.5 percent fibers by volume and no transverse steel in the end regions underscoring the effectiveness of SFRC as a crack retarder and shear reinforcement alternative.

2.4.3 Slabs

SFRC has been used in several slab-on-ground and elevated slab applications. As of recent, over 65 multi-story buildings utilize SFRC flat slabs without traditional reinforcement (Destrée 2009).

The span to thickness ratio of the slabs range from 25 to 30 and commonly have a depth of approximately 0.2 m (7.9 inches) spanning between 5 m (16 ft) and 8 m (26 ft) in each direction.

Many researchers agree that typical flexural tests and beam analysis severely underestimate the capacity of SFRC two way slabs (Roesler et al 2004, Destrée and Mandl 2008, Destrée 2009, Mobasher and Destrée 2010, Michels et al 2011). Roesler et al (2004) experimented with SFRC slabs under monotonic loading and found that the slabs' flexural strengths were as much as 30 percent larger than equivalent beam tests (Roesler et al 2004). Destrée and Mandl investigated the collapse load for four full scale slabs supported on columns and found that their capacity was five times larger than predicted by round slab tests and yield line theory and 15 times larger than predicted by typical beam flexural tests (Destrée and Mandl 2008). The disparity between the beam flexural test and round slab tests is due to the inability of beam flexural tests to adequately model multiple macro-cracking and load redistribution. SFRC flat slabs benefit from having multiple yield lines, and therefore multiple macro-crack formations that aid in redistributing the load (Mobasher and Destrée 2010). In addition to large factors of safety found in flexural design, numerous studies also show that SFRC elevated slabs can withstand point loads over 600 kN (67 ton) without sustaining punching shear failures. SFRC slabs are competitive and safe alternatives to traditionally reinforced concrete slabs when their design strengths are determined adequately (Destrée and Mandl 2008).

Fall et al (2014) tested simply supported two-way slabs with SFRC made with approximately 0.35 percent by volume of double-hooked fibers. Slabs were approximately 80 mm (3.1 inches) thick with a) conventional reinforcement with plain concrete, b) conventional reinforcement with SFRC, or c) SFRC without conventional reinforcement. Slabs with conventional reinforcement and SFRC had larger strengths and more, but narrower, cracks than conventional reinforcement alone. The SFRC-only slab had a limited crack pattern and did not exhibit bending hardening.

2.4.4 Steel Free and Steel Reduced Bridge Deck

Some estimate that over 120,000 bridges in the US are in need of repair due to steel reinforcement corrosion resulting in damaging concrete spalling (Chandrangsu 2003). The steel free bridge deck has long been a goal of many designers and researchers. The cost of construction materials may potentially be larger due to the addition of steel fibers; however, the reduction of labor and maintenance in addition to a longer serviceable life could offset this increase.

Mufti et al (1993) explored the effectiveness of arching, or compressive membrane, action in the flexural design of bridge decks (Mufti et al 1993). Their goal was to alter the failure mode from flexural failure to a punching shear failure. The experiment involved subjecting quarter scaled bridge decks, supported on two steel girders, to concentrated loads at various locations as shown in Figure 18.

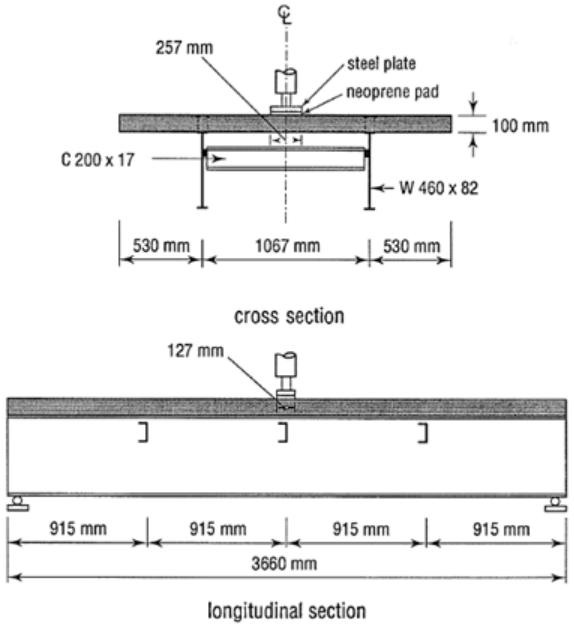

Figure 18. 1/4 Scale Bridge Deck Test (Mufti et al 1993)

The researchers eliminated all steel reinforcement from the bridge deck and utilized polypropylene fibers to control temperature and shrinkage cracks. They found that the eliminated steel reinforcement contributed significantly to the lateral restraint of the bridge deck that promotes arching action. Their first test resulted in typical flexural failure with a longitudinal crack through the deck due to the lack of lateral restraint. In subsequent tests, Mufti et al (1993) added an increasing amount of steel straps welded to the top flange of the steel girders supporting the deck and successfully transitioned the mode of failure from flexural to punching shear as desired on the third specimen. Officials in Tama County, Iowa utilized this design procedure and successfully built a full scale bridge that performed adequately under their load testing (Dunn et al 2005). The bridge consisted of polypropylene fibers and fiber reinforced polymer (FRP) bars, both intended as temperature and shrinkage reinforcement, in addition to exterior steel straps attached to the top flange of the supporting girders to provide lateral restraint. The addition of steel straps are less than idea for the bridge superstructure and this experiment did not take advantage of fibers that improve the strength and performance of concrete.

Naaman and Chandrangsu utilized the basis of the Mufti et al (1993) experimentation and structurally capable fibers to eliminate only the top layers of reinforcement while keeping the bottom layers to promote arching action and prevent accidental loading and failure (Naaman and

Chandrangsu 2004). In 2004, they experimented with bridge decks using a reduced amount of traditional steel reinforcement and three different types of structural fibers, Torex, Spectra, and PVA. Fibers were introduced into the concrete mixes at 2 percent, Torex and PVA, and 1.75 percent, Spectra, by volume based on prior experimental results to best optimize the response of 4 by 7 inch FRC beams. Figure 19 demonstrates the results of the Torex (TOR-1), Spectra (SP-1), and PVA (PVA-1) beams in comparison to the traditionally reinforced control specimen (CONT-1). As demonstrated by Figure 19, the Torex and Spectra FRC beams exhibited increased strength, ductility, and stiffness with respect to the control specimen while the PVA FRC beam exhibited an increased ductility, but comparable strength and stiffness in comparison to the control specimen.

Naaman et al (2007) expanded this experiment to investigate the punching shear response of FRC bridge decks with reduced steel. They subjected simply supported slabs 810 x 810 x 180 mm (32 x 32 x 7 inches) in dimension to a point load at its center. The experiment consisted of Torex, Spectra, and PVA fiber specimens with varying amounts of top and bottom steel. Figure 20 demonstrates the results of the experiment on the Torex, Spectra, and PVA FRC slabs without any traditional reinforcement, TOR-0T-0L, SPE-0T-0L, and PVA-0T-0L respectively, in comparison to the control specimen with code compliant reinforcing, CON-2T-2L. The Torex and Spectra FRC slabs performed as well or better than the control slab. Additionally, the authors suggested that the punching shear capacity of the FRC slabs can be safely taken as twice the strength recommended by ACI code.

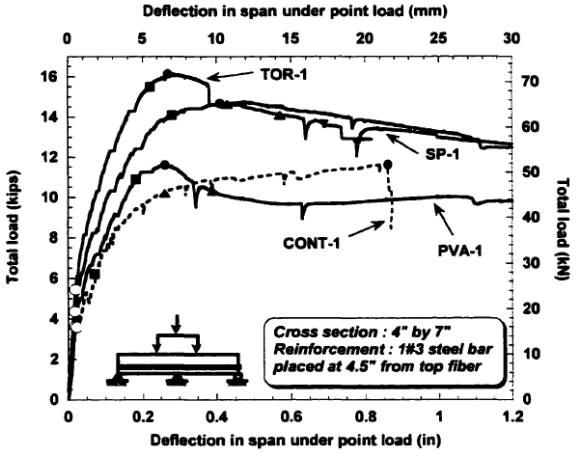

Figure 19. Series 1 Results of 3 FRC Beams with Reduced Steel Reinforcement, Torex (TOR-1), Spectra (SP-1), and PVA (PVA-1), and 1 Traditionally Reinforced Beam (CONT-1) (Chandrangsu 2003)

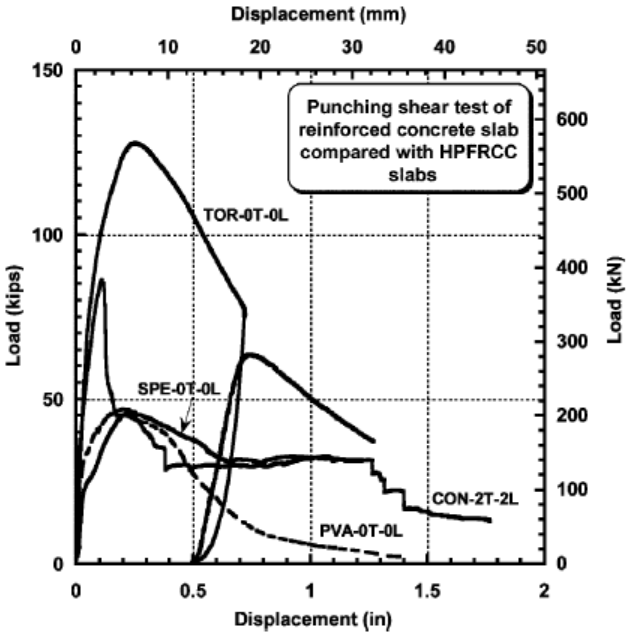

Figure 20. Punching Shear Evaluation of 3 FRC Slabs without Traditional Steel Reinforcement, Torex (TOR-0T-0L), Spectra (SP-0T-0L), and PVA (PVA-0T-0L), and 1 Traditionally Reinforced Slab (CON-2T-2L) (Naaman et al 2007)

Ostertag and Blunt performed four point bending tests on Hybrid FRC beams measuring 6 x 6 x 24 inches utilizing different mixes to determine their feasibility for use in approach slabs. They chose a hybrid FRC mix to minimize the volume of fibers needed as the difficulty of placing concrete increases with the volume of fibers has been well documented. The idea of the hybrid mix is to include micro-fibers, PVA fibers, to delay the onset of micro-cracks and macro-fibers, steel hooked end fibers, to delay the onset of macro-cracks (Ostertag and Blunt 2008). As shown in Figure 21, the addition of fibers into the concrete matrix increased the flexural capacity of the beams. Additionally, the gain observed from adding fibers diminishes as the amount of traditional reinforcement increases underscoring the larger influence of steel reinforcement over the tension capacity of the FRC.

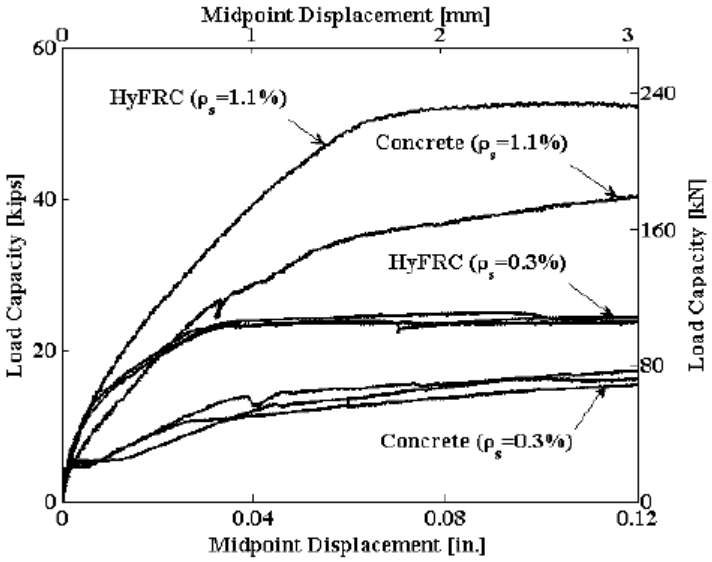

Figure 21. Four Point Bending Test of Hybrid FRC with Varying Ratios of Traditional Steel Reinforcement (Ostertag and Blunt 2008)

As can be seen throughout all the aforementioned experiments, the addition of fibers into the concrete matrix yields better performance and strength in comparison to their traditionally reinforced counterpart. As suggested by Ostertag and Blunt, the geometry, ratio of steel reinforcement and fiber volume are means for optimizing the performance and cost of fiber reinforced concretes (Ostertag and Blunt 2008). However, FRC is not the only method being investigated to reduce or eliminate traditional steel reinforcement.

Researchers in Wisconsin have investigated steel free bridge decks on wide flange concrete girders. Bae et al (2010) propose using steel rods to connect the webs of adjacent wide flange girders in order to promote arching action in addition to using polypropylene fibers in the concrete mix to prevent temperature and shrinkage cracking (Bae et al 2010). Experimental tests have demonstrated that the slab fails in punching shear beneath the wheel load similar to experiments conducted by Mufti et al (1993). Additionally, Bae et al found that the reduced clear span of the bridge deck, due to the wide flanges of the girders, and the added lateral restraint cause the bridge deck to behave similar to a D region in short beams (Bae. et al 2011). Through the use of the strut and tie method, they were able to accurately determine capacity of the steel free concrete deck. However, this procedure is limited to decks with a thickness of greater than 7.5 in and a clear span of less than 5 ft.

2.5 Experimental Investigation Of Bridge Decks

Two other bridge decks that have geometries and testing procedures similar to the large scale bridge deck investigated in this thesis have been tested at Texas A&M. Mander et al (2009) investigated full-depth precast, prestressed concrete overhang bridge deck panels and Gar et al (2013) investigated full-depth precast, prestressed panels with AFRP strands.

Mander et al (2009) investigated the feasibility and failure capacity of precast overhang panels. Current bridge deck overhangs are cast-in place sections that require formwork and falsework be installed on the edge of a bridge deck supported by the exterior girder. This process is time consuming, expensive, and potentially dangerous. The goal of the precast overhang panels is to provide a method for increasing the speed of construction for the overhangs while also reducing the cost.

The experimental tests were achieved by constructing two 18 ft wide bridge decks supported by three girders, Figure 22. The overall thickness of the decks were approximately 8 inches consisting of the precast, prestressed panel and a conventional cast-in-place deck over the interior spans. The precast panels were connected to the bridge deck via the cast-in-place interior deck and shear pockets located along the exterior support beams. The supporting beams sat directly on the strong-floor of the laboratory to decouple the longitudinal and transverse bending. Numerous load patterns consistent with AASHTO LRFD Bridge Design Specifications were tested to accurately detail the performance of the overhang panels. One of the bridge deck specimens was constructed with a traditional cast-in-place over hang so that the performance of the precast panels could be compared directly with current practices.

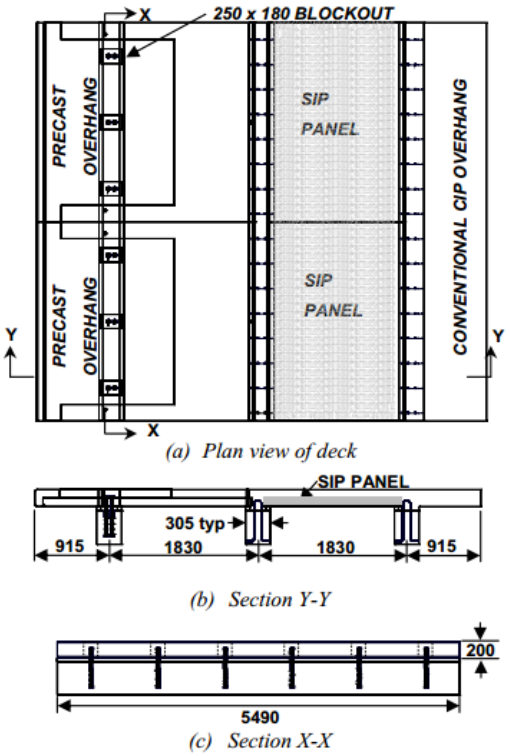

Figure 22. Bridge Deck Geometry for Mander et al (2009)

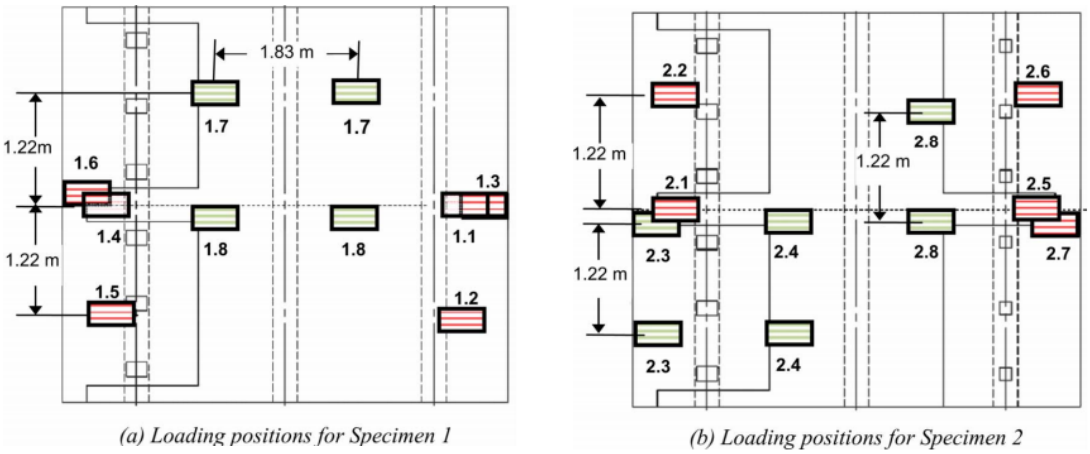

Figure 23. Loading Patterns for Mander et al (2009)

The researchers utilized a modified yield line theory to accurately predict the collapse load of each of their tests. The yield line theory had to be altered to account for a shear-flexural failure

due to the seam in the two stage construction. The overhang panels demonstrated a 13 percent reduction in capacity in comparison to the traditional cast-in-place overhangs; however, all load patterns investigated satisfied the AASHTO factored load due to the substantial strength of the current design procedures.

Gar et al (2014) investigated substituting traditional prestressed steel with aramid fiber reinforced polymer (AFRP) strands. AFRP was investigated because of its tensile capacity and its ability to withstand harsh environments without corroding. The experiment was performed by constructing a bridge deck with an identical geometry to the decks tested by Mander et al (2009) as shown in Figure 24. The bridge deck consisted of full-depth precast panels reinforced with AFRP and were attached to the supporting girders through shear pockets.

The researchers' experimental results concluded that the AFRP bridge deck performed satisfactorily and exceeded the minimum design loads by a minimum of 40 percent. Additionally, the measured deflections at the maximum load were 1 mm (0.04 inches), well below the maximum allowable deflection.

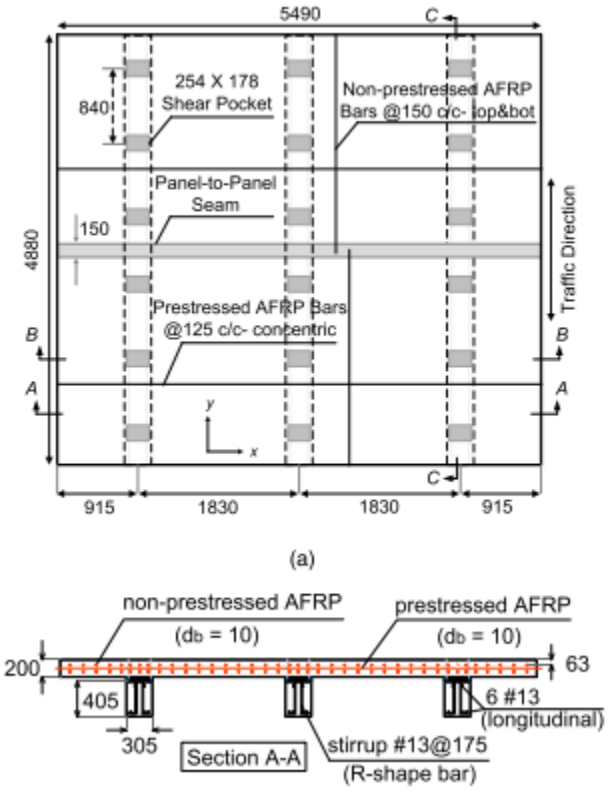

Figure 24. Bridge Deck Geometry for Gar et al (2014)

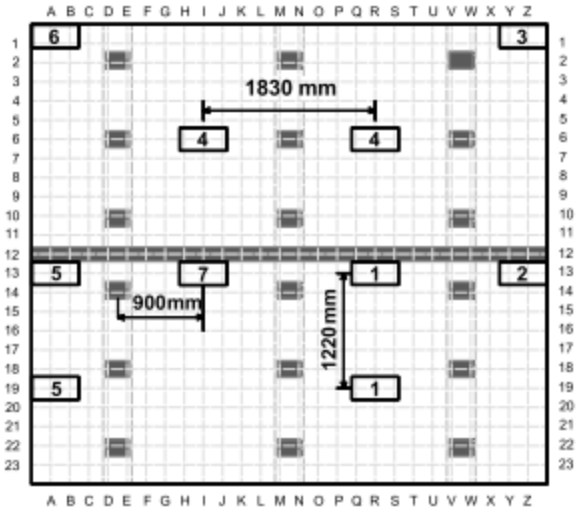

Figure 25. Loading Patterns for Gar et al (2014)

These experimental programs conducted by Mander et al (2009) and Gar et al (2014) will provide a comparison for the bridge deck investigated as part of this thesis. The "control" specimens will allow for the researcher to identify the effects of SFRC as it pertains to crack distribution, failure pattern, deflections, and load capacities.

2.6 Affect Of FRC On Concrete Mix Design

The addition of fibers to the concrete matrix adversely affects the workability of fresh concrete. The volume percentage and aspect ratio of fibers, coarse aggregate size, and methods of introducing the fibers into the concrete mix are the most influential factors governing the mix workability (ACI 544 1998). As a result, various concrete mixes utilizing admixtures, supplemental cementitious materials, and small coarse aggregate have been found in current literature.

Significant effort has been made to create new mix designs suited for the addition of fibers and to verify the ability of already established mix designs to accept fibers. Liao et al (2006) investigated self-consolidating high performance SFRC mix designs. A total of 6 designs were tested using direct compression and tension tests. Their goal was to develop a workable mix that could be easily implemented and delivered by ready mix concrete companies. Successful designs were achieved by adjusting the amount of coarse and fine aggregates and the method for creating the concrete mix. Dhonde et al (2005) also developed a self-consolidating concrete mix in addition to utilizing mix designs already approved by Texas Department of Transportation (TxDOT). They observed with mechanical vibration that the workability of the TxDOT mixes with steel fibers was adequate and that the rate of placing concrete affected the self-consolidating

concrete mix. Aviram et al (2014) utilized two mix designs, one similar to the Liao et al (2006) recommendations and one generic ready mix design. The ready mix design could not be placed without the addition of water resulting in a significant loss of compressive strength.

The method of introducing the steel fibers to the concrete mix also influences the workability of the concrete mix and tendency of balling for the fibers. There are two general methods for adding fibers to the concrete mix: introducing the fibers after the concrete has already been mixed or introducing them with the coarse aggregates (ACI 544 1998). Liao et al (2006) added the fibers, at a slow steady rate, after the concrete mix had been formed. Using this method, the concrete mix should have a slump 1 to 3 inches greater than the desired final slump before the addition of fibers. Overall, 52 different concrete mixture proportions were recorded from the literature review. Table 1 demonstrates the average water, fine aggregate, and coarse aggregates to cement ratios. Additionally, the average 28 day compressive strength and coarse aggregate size are reported. For comparison, the TxDOT and Arizona Department of Transportation (ADOT) requirements for structural concrete have also been included (TxDOT 2014 and ADOT 2006).

Table 1: Mix Design Averages and DOT Requirements

	Literature Average	**TxDOT Requirements**	**ADOT Requirements**
Compressive Strength, f'c (psi)	6270	4000	4500
Maximum Water:Cement	0.45	0.45	0.5
Fine Aggregate:Cement	1.72	N.A.	N.A.
Coase Aggregate:Cement	1.98	N.A.	N.A.
Coarse Aggregate Size (in)	0.57	0.75-1.75	N.A.
Most Common Cement Type	Other	N.A.	II, III, V

As demonstrated, the compressive strength of the SFRC used in previous studies significantly exceed the minimum requirements of both TxDOT and ADOT. Furthermore, ADOT requires approval for non-prestressed concrete with a compressive strength above 6000 psi (ADOT 2011).

Nine of the 52 mix designs meet the requirements of ADOT, most failing due to the type of cement used, internationally graded cement.

3. CASE STUDIES

3.1 Introduction

A parameter study was conducted on two bridge deck structural systems and one structural component to characterize the effect of adding steel fibers to bridge structures. The case studies consisted of a slab-girder bridge deck, a slab bridge, and a structural railing. The goal of each study is to examine the effects of steel fiber reinforced concrete (SFRC) on the behavior of each system by varying their material and geometric properties, such as the compressive strength of concrete, the post-crack strength of the SFRC and the location and area of traditional steel reinforcement.

Each study utilized a consistent derivation for the SFRC stress-strain response. The compression response of the SFRC was derived utilizing the same philosophy presented by Lequesne (2011). Specifically, the stress-strain behavior was determined utilizing the Modified Kent Park model with a post-peak descending slope, Z, of 50 as shown in Figure 26. The tension response was determined using the method proposed by Soranakom and Mobasher (2007) as shown in Figure 27 and discussed in Section 2.

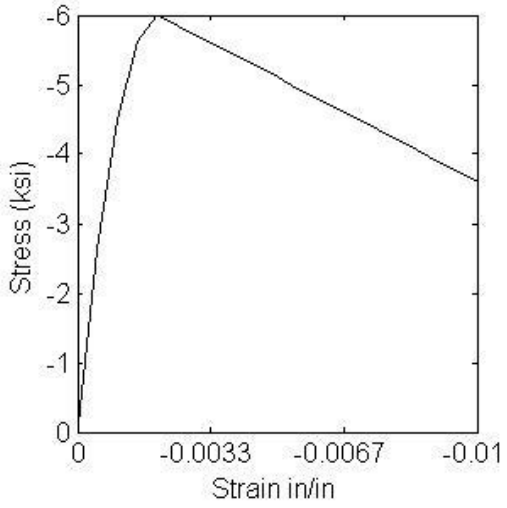

Figure 26. Modified Kent Park - Compression Stress-Strain

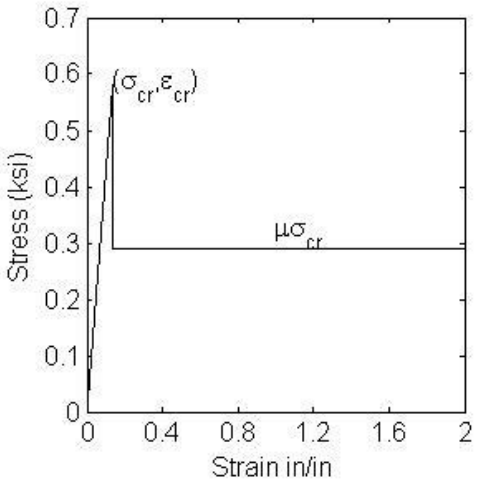

Figure 27. Soranakom and Mobasher (2007) Tensile Stress-Strain

3.2 Slab-Girder Bridge Design

3.2.1 Modeling and Analysis

The slab-girder deck is one of the most common systems utilized for bridge design. A three span rectangular girder system, as demonstrated by Figure 28, was utilized for this study. The capacity requirements of the system were determined using the effective width procedure (AASHTO 2014). The applied wheel load is distributed longitudinally, or parallel to the girders, over an effective width that is determined based on the girder spacing (Equation 1 and Equation 2). This procedure results in a moment demand per linear foot.

$$EW_{m^+} = 26.6 + 6.6S \quad \textbf{(14)}$$

$$EW_{m^-} = 48 + 3S \quad \textbf{(15)}$$

Where EW_{m^+} and EW_{m^-} is the effective width for the positive and negative moment regions respectively and S is the girder spacing.

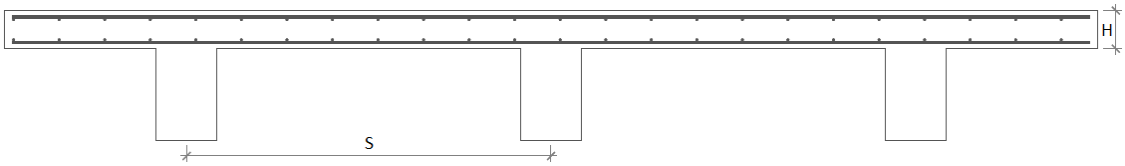

Figure 28. Traditional Slab-Girder Bridge

The parameters investigated in this case study were the girder spacing, thickness of the concrete deck, the concrete compressive strength, the post-crack tensile strength, and the traditional steel reinforcing layout. Table 2 details the organization and values used for each parameter. The median deck thickness value for each girder spacing was chosen to be the minimum required depth based on *ADOT Bridge Design Guidelines* (2011).

The post-crack tensile strength is characterized by the ratio, denoted μ, of the residual strength to the cracking strength of SFRC. Varying the post-crack strength ratio accounts for a varying percentage of fiber.

Table 3 details the steel reinforcement layouts utilized and how the area of reinforcement was determined. The AAHSTO empirical design procedure was utilized for the area of steel reinforcement used for steel profiles 2-4.

A naming pattern using the parameters of each model was created to easily identify the results of each analysis: concrete matrix – girder spacing – compressive strength – deck thickness – post-crack tensile strength ratio – steel profile. For example, FRC-S6-F4500-H75-mu2-steel1 signifies a fiber reinforced concrete deck with a girder spacing of six ft., compressive strength of 4500 psi, thickness of 7.5 inches, post-crack tensile strength ratio of 0.2, and traditional reinforcement layout determined using ultimate strength design.

Table 2. Model Parameters

Girder Spacing - S (ft.)	Deck Thickness - H (in)	f'c (ksi)	μ	Steel Profile
6	5.5	4.5 6 7.5	0.2 .8 1.4	Steel Profiles 1-6
	7.5			
	9.5			
8	6			
	8			
	10			
12	7.5			
	9.5			
	11.5			

Table 3. Steel Profiles

Steel Profile	Steel Location and Design Procedure			Illustration
	Negative Moment Region	Positive Moment Region	Mid-Depth	
1	Strength	Strength	-	Figure 29
2	0.18	0.27	-	
3	-	-	Strength	Figure 30
4	-	-	0.27	
5	-	-	0.18	
6	-	-	-	Figure 31

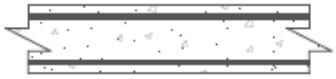

Figure 29. Traditional Reinforcement

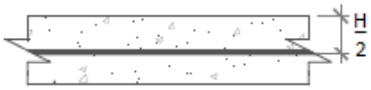

Figure 30. Reinforcement at Center Only

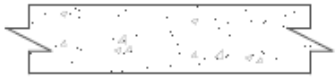

Figure 31. SFRC Only

A moment-curvature analysis was conducted for the 486 SFRC bridge deck configurations shown in the test matrix. The analyses used the general material models presented in Section 3.1 for the compressive and tensile response of SFRC. A computer program developed by the University of California at Berkley, OpenSEES, was used to perform the analyses. The material response was modeled as a multilinear-elastic curve and the cross-section was sub-divided into multiple slices or fibers to achieve the analyses. The results were compiled and normalized to evaluate the effect of SFRC on the strength and service performance on slab-girder bridges.

3.2.2 Strength Results

Sample SFRC moment-curvature results are displayed in Figure 32 and Figure 33. Figure 34 demonstrates the effect of adding a varying amount of steel fibers to a plain concrete section with conventional steel reinforcement designed in accordance with AASHTO procedures. As demonstrated, the addition of steel fibers increases the moment capacity of the cross section; however, it also decreases the curvature at the nominal moment. The additional tension capacity of the steel fiber reinforced concrete delays the initial traditional steel reinforcement yielding and reduces its strain at the nominal moment.

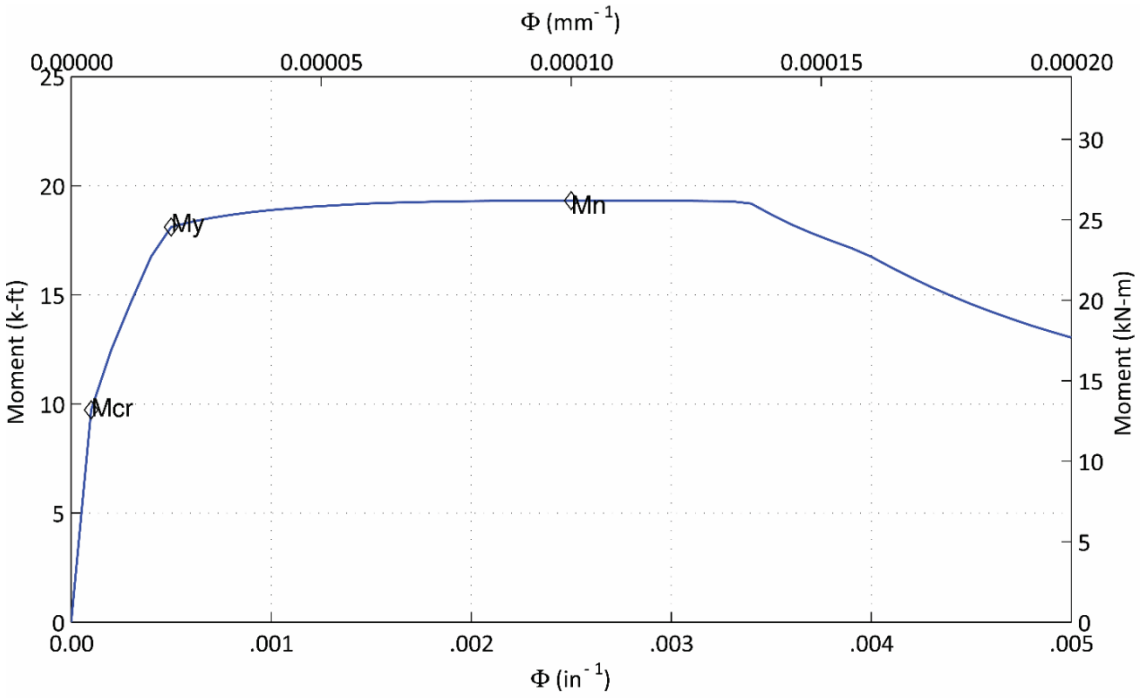

Figure 32. Moment vs Curvature for FRC-S8-F4500-H80-Mu8-Steel2

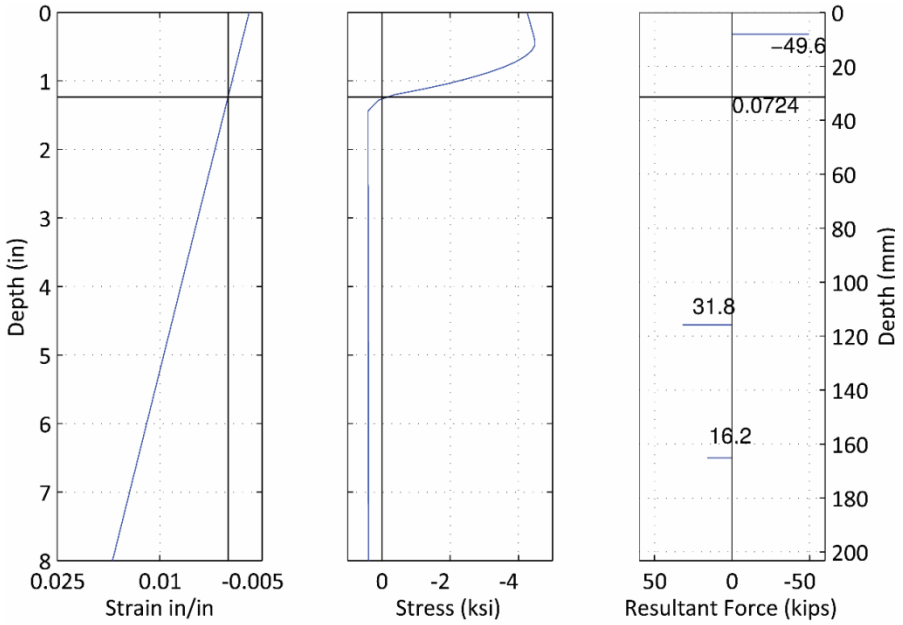

Figure 33. Stress and Strain Profiles for FRC-S8-F4500-H80-mu8-Steel2

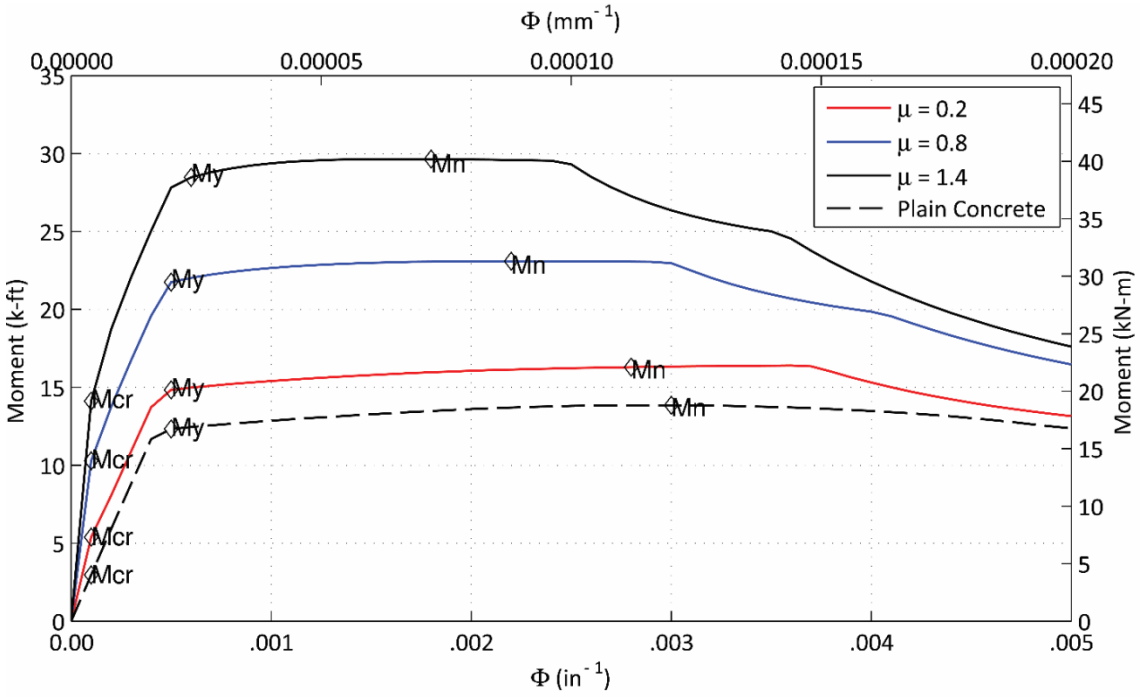

Figure 34. Moment vs Curvature Response for SFRC and Plain Concrete Sections with Conventional Steel Designed in Accordance with AASHTO

The moment and curvature corresponding to the nominal compressive strain of $\varepsilon_c = 0.003$ for each SFRC model was extracted from the data set to simplify the analysis and presentation of the case study. Each moment and curvature pair were normalized by the results of a reference section corresponding to plain concrete cross-section with conventional steel reinforcement designed in accordance with AASHTO. Figure 35 demonstrates this procedure for the results shown in Figure 34. The strength reduction factors (ϕ factor) were accounted for in the secondary axes of each plot. The use of steel fibers for concrete strength design adds uncertainty to the overall concrete design process. Successfully achieving the post-crack tensile strength depends on numerous factors such as the fiber volume, fiber orientation, aggregate size, etc. Accordingly, the strength reduction factor proposed by Soranakom and Mobasher (2007) is 0.70 in comparison to 0.90 specified by AASHTO. Therefore, unity in the design strength of SFRC and plain concretes occurs at 1.29 as demonstrated by Figure 35.

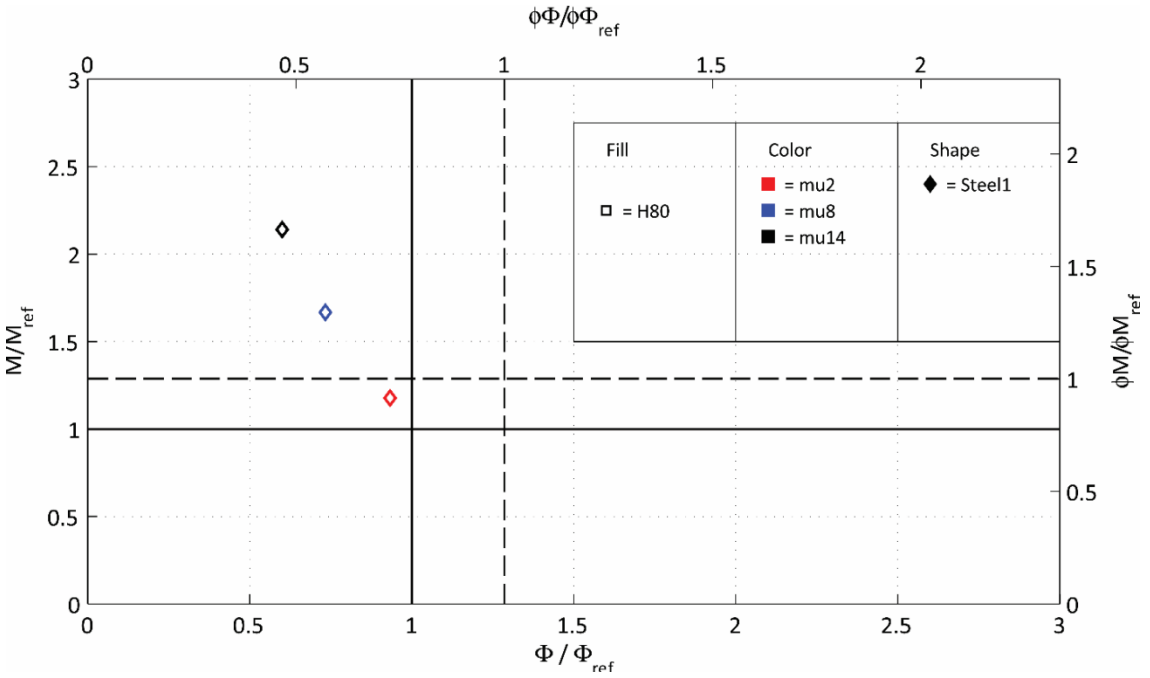

Figure 35. Normalized Moment vs. Curvature for S8-F4500-H80-muALL-Steel1

3.2.2.1 Reference Concrete Deck with Steel Fibers

Figure 35 demonstrate the normalized moment capacity as a result of the addition of the steel fibers in a bridge deck with supporting girders spaced at 8 ft. Adding steel fibers to the reference deck results in an increase in the moment capacity, but a decrease in the curvature at the nominal moment. The magnitude of the change in the strength and curvature correlates with the amount of fibers added to the concrete matrix, or the achieved post-crack tensile strength. The addition of a small amount of fibers changed the moment capacity and curvature by less than 10%. The addition of a large amount of fibers resulting in tensile strain hardening, mu14, increased the capacity by more than 100% and reduced the curvature by 50%.

3.2.2.2 Varied Depth

Figure 36 shows the relationship between the depth of the member and the reference concrete deck with SFRC. Decreasing the depth of the concrete deck counteracts the decrease in curvature due to the addition of SFRC, but it also decreases the amount of moment capacity gained due to the fibers. The magnitude of this effect correlates to the amount of fibers added. Conversely, increasing the depth of the reference section further increases it moment capacity and reduces

its corresponding curvature. To efficiently utilize the benefits of SFRC the depth should be decreased to increase curvature and reduce the design strength back towards unity.

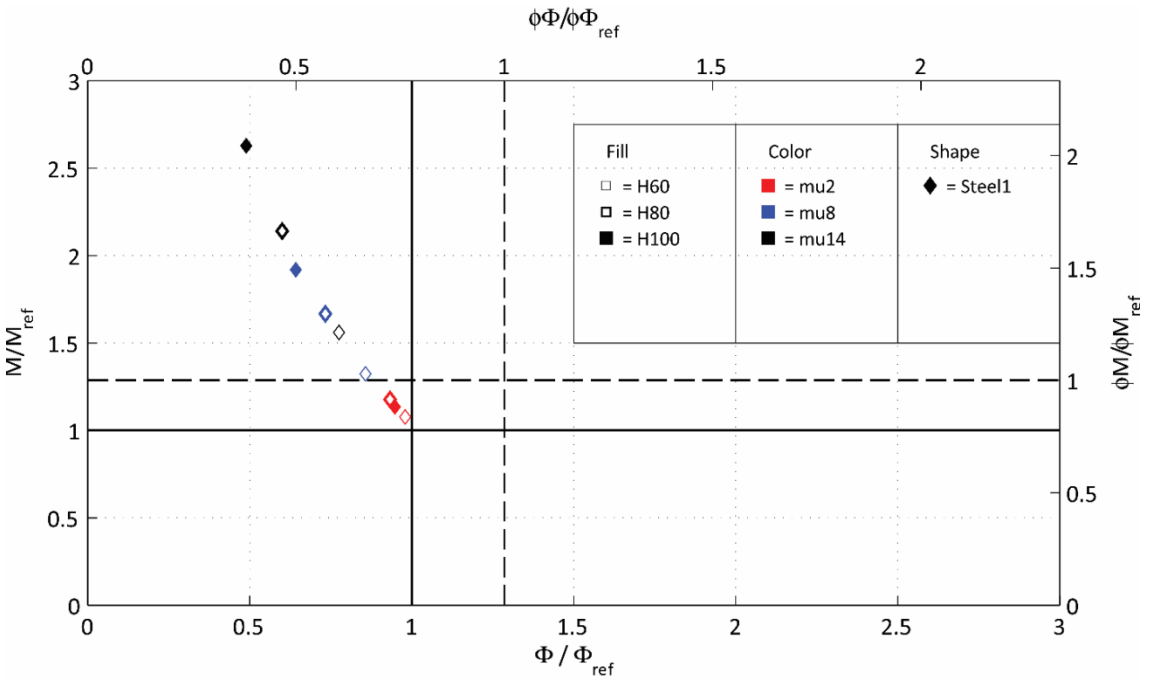

Figure 36. Normalized Moment vs. Curvature for S8-F4500-HALL-muALL-Steel1

3.2.2.3 Varied Steel Profiles

In addition to modifying the depth to efficiently capture the benefits of SFRC, the amount of steel and/or its location can be changed. Figure 37 shows the effect of reducing the amount of conventional steel to the AASHTO empirical design. Reducing the steel area yields a similar result to reducing the depth of the section; the moment capacity is decreased and the curvature at nominal is increased. The reduced area of steel achieves the required design strength with a moderate addition of steel fibers, mu8.

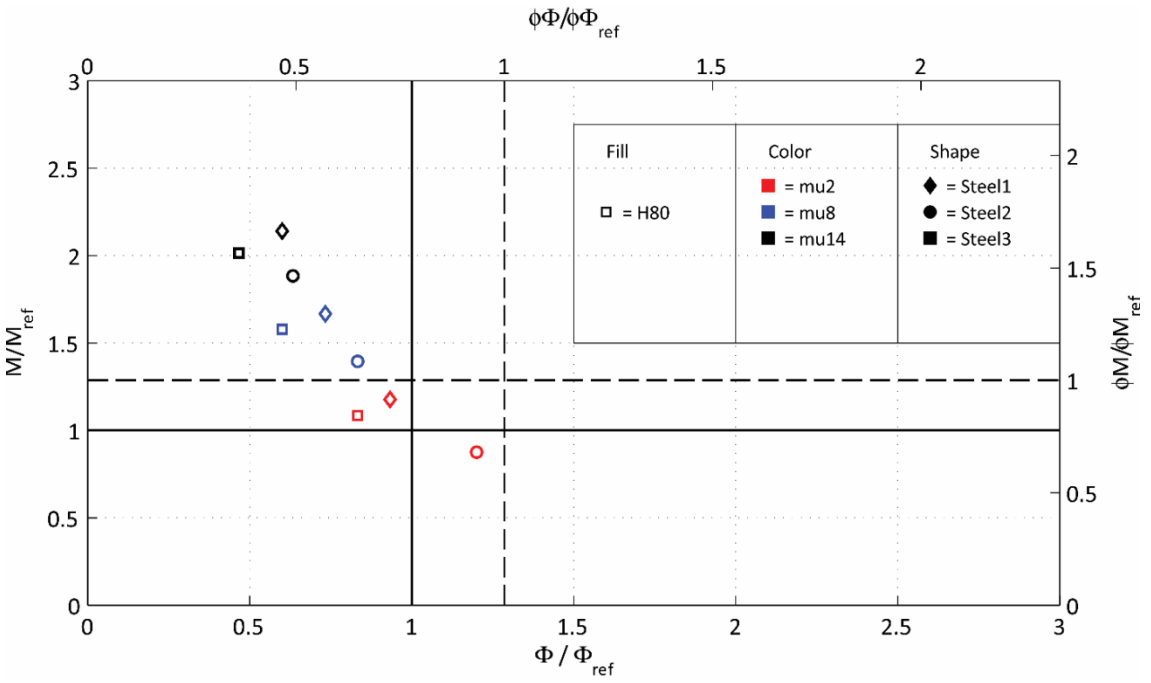

Figure 37. Normalized Moment vs. Curvature for S8-F4500-H80-muALL-Steel1-3

Relocating all conventional steel to the center of the cross-section was also investigated. This configuration is advantageous as it allows the steel reinforcement to provide both negative and positive moment capacity. Designing this section in accordance with AASHTO (Steel3) results in an over-reinforced section with the addition of SFRC. Therefore, a reduction in the area of steel located at mid depth was investigated as shown in Figure 38. Again, reducing the area of conventional steel reinforcement allows the moment and curvature to trend towards unity. Incorporating a moderate amount of steel fibers (mu8) and a reduced steel area at mid depth (Steel4) resulted in an increase in expected strength with a minor decrease in curvature. However, to achieve an appropriate design strength either more steel fibers or more steel reinforcement must be added.

Ultimately, with a significant amount of steel fibers (mu14), all conventional steel may be removed from the section (Steel6) while still being able to achieve the design strength. The case study demonstrates that the use of SFRC allows the designer to both relocate steel reinforcement to advantageous locations and reduce the area of steel reinforcement and section depth.

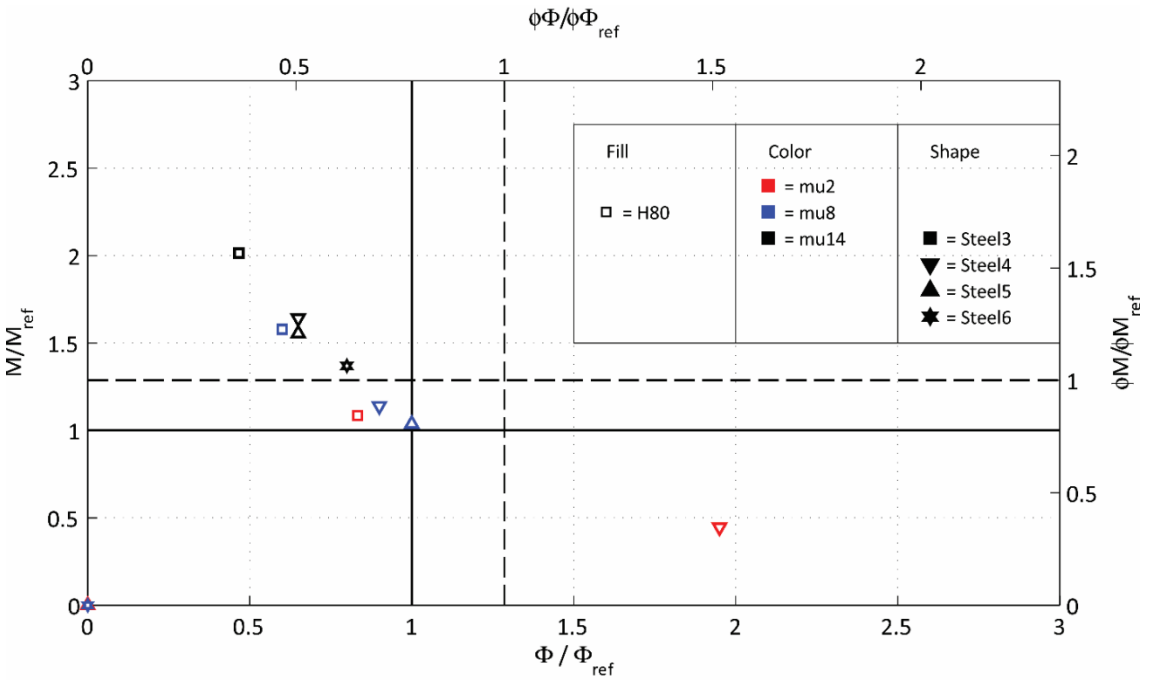

Figure 38. Normalized Moment vs. Curvature for S8-F4500-H80-muALL-Steel3-6

Caution must be exercised, without a sufficient post-crack tensile strength, the compression region of the cross section can fail to achieve the nominal strain. A total of 94 of the SFRC configurations failed to achieve the nominal compressive strain due to insufficient tensile capacity and a shallow neutral axis.

3.2.3 Service Results

The service performance of the SFRC models was also investigated. The service moment was computed for each span length and used with the moment-curvature analysis to determine the resulting steel stress. The steel stress must be less than 24 ksi to satisify the ADOT (2009) service limit state. Section 3.2.3.1 discusses the relationship between the dosage of steel fibers and the percentage of steel reinforcement and Section 3.2.3.2 discusses the effect of the depth and steel fibers on the service performance of SFRC.

3.2.3.1 Varied Steel Reinforcement Ratio

Figure 39 shows service performance of SFRC models supported by girders spaced 8 ft apart. The models are all 8 inches deep and have steel reinforcement ratio for either the service, strength, or AASHTO empirical designs. The horizontal line in the figure signifies the maximum allowable

service stress. The figure shows the effect of reducing the amount of conventional steel from the traditional service design to the strength and AASHTO empirical design. The service performance of the SFRC models behaves in a similar manner to the strength performance. The addition of fibers enhances the service performance by reducing the stress in the steel reinforcement. The addition of a low amount of steel fibers, mu2, enhances the traditional strength design to sufficient service performance. However, this dosage of fiber is not sufficient to improve the AASHTO empirical design to an acceptable service stress. Increasing the dosage of fibers, mu8, improves the performance enough so that the AASHTO empirical design also satisfies the service design. As was observed with the strength results, steel fibers will allow for the reduction of the steel reinforcement while still maintaining satisfactory service performance.

The stress of the SFRC models mu8 and mu14 are nearly identical suggesting that the post-cracking stiffness of the SFRC specimens increases as the dosage of fiber increases. The increased stiffness aids the models in achieving the service moment sooner after cracking occurs.

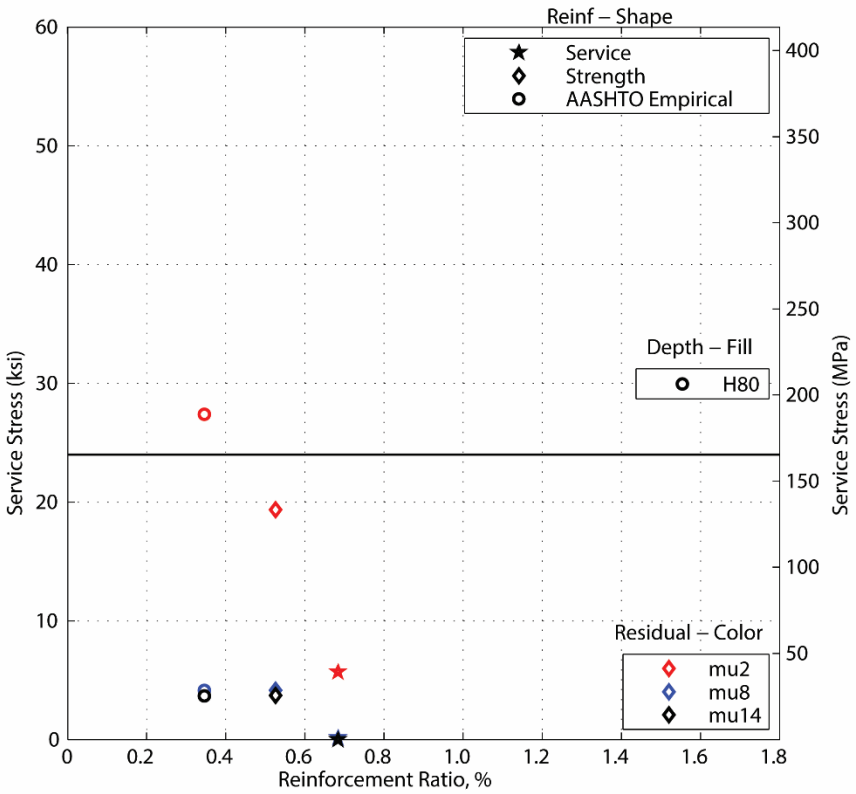

Figure 39. Service Performance S8-F4500-H80-muALL-Steel1-2-Service

3.2.3.2 Varied Depth

The comparisons made from Figure 39 were expanded to include the effect of different percentages of steel reinforcement, dosage rate of fibers, and depths of concrete as shown in Figure 40. Increasing the depth by 2 inches to 10 inches increases the cracking moment of the models such that they achieve the service moment prior to cracking as shown by the solid points in the figure. Decreasing the depth of the cross-section to 6 inches has a similar effect as decreasing the steel reinforcement. The decreased depth with the strength reinforcement ratio and residual strength of mu2 nearly satisfies the service limit state. Both the steel reinforcement ratio and depth of the section can be decreased with the addition of a moderate amount of steel fibers, mu8. The three models that fail to satisfy the service limit state had either significantly reduced steel, AASHTO empirical, or had a thin cross-section.

As was observed with the strength results, a combination of reduced steel and reduced depth can be utilized with the addition of fibers. Both the strength and AASHTO empirical designs of a 6 inch deck can satisfy the service limit state with the correct dosage of steel reinforcement.

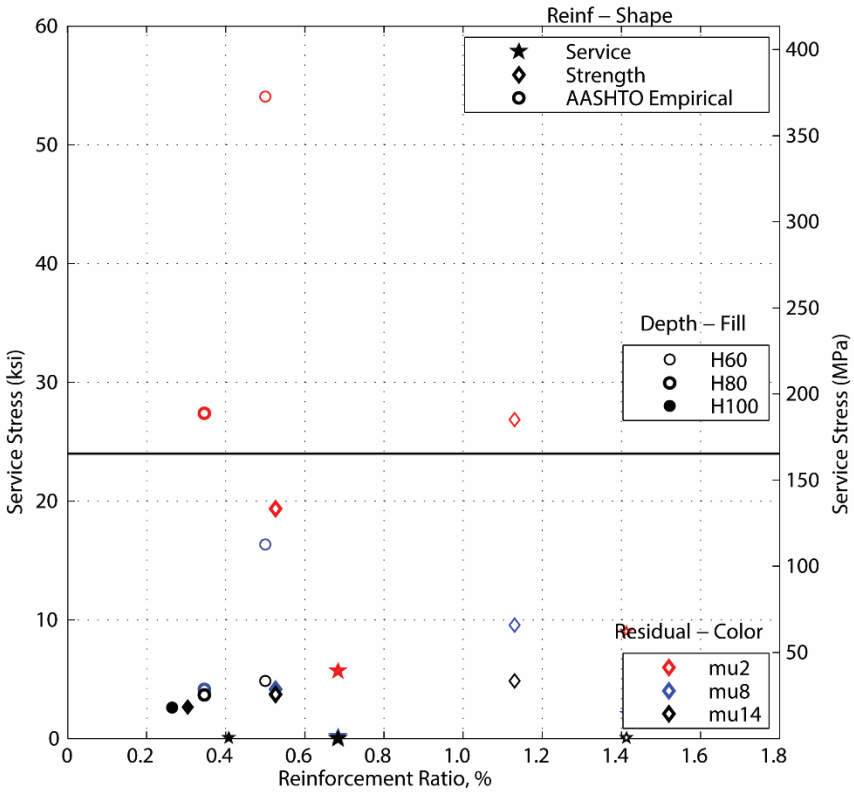

Figure 40. Service Performance S8-F4500-HALL-muALL-Steel1-2-Service

3.2.4 Additional Observations

Several of the analyses yielded a significantly reduced curvature for acceptable levels of strength. The strain at the extreme steel fiber in each section was calculated to determine the significance in the curvature reduction. As exhibited by Table 8, the largest decrease in curvature was observed in the reference sections (Steel1) and sections with all steel relocated to mid depth (Steel3). Figure 41 shows the strain at the extreme steel fiber for each of these configurations. The majority of analyzed sections maintain a steel strain above the ACI 318 requirements for tension-controlled members. Only the sections with "lumped" steel resulted in smaller strain and "transition" members with strength reduction (ϕ) factors less than 0.90.

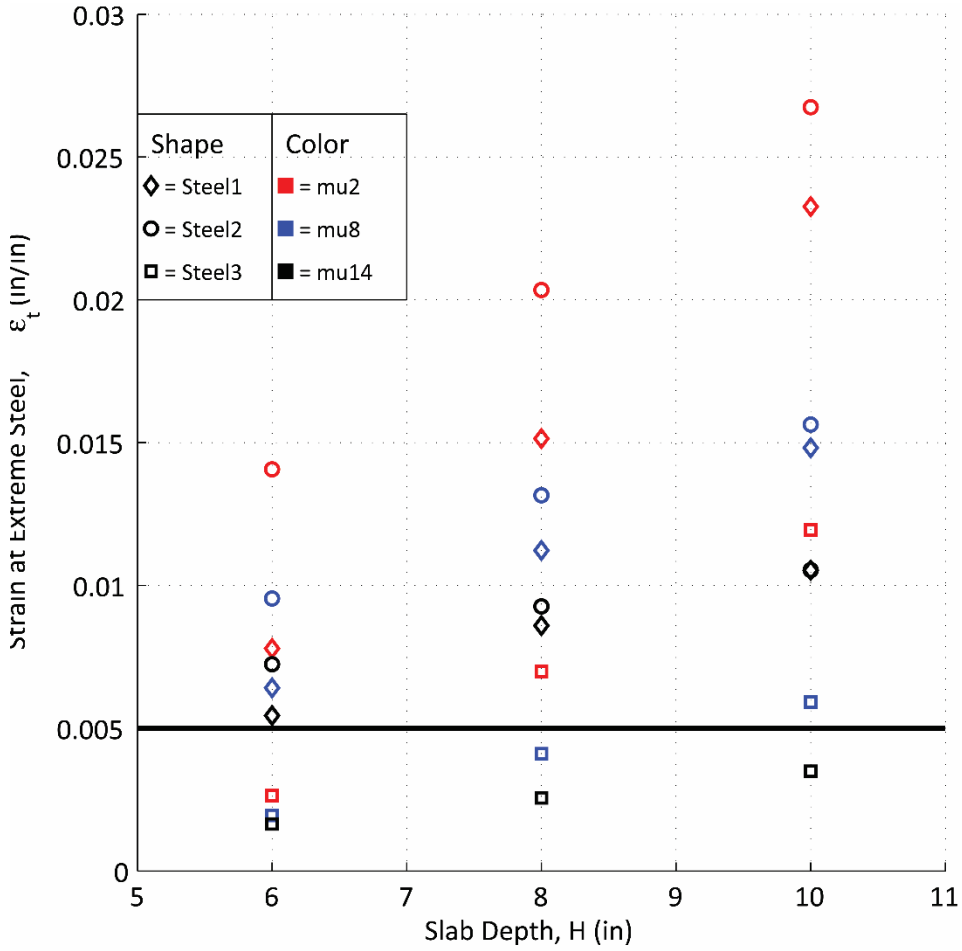

Figure 41. Strain at Extreme Steel Fiber vs. Depth for S8-F4500

Figure 42 demonstrates the influence of steel fibers in regard to varying the concrete compressive strength. The data exhibits a "clumping" corresponding to the compressive strength and steel profile. A slight increase in the moment capacity for larger compressive strengths is observed; however, the compressive strength is overall insignificant in determining the response of SFRC bridge deck. The primary contributors to the strength of the SFRC deck are the slab depth, post-crack tensile strength, and area of traditional steel reinforcement.

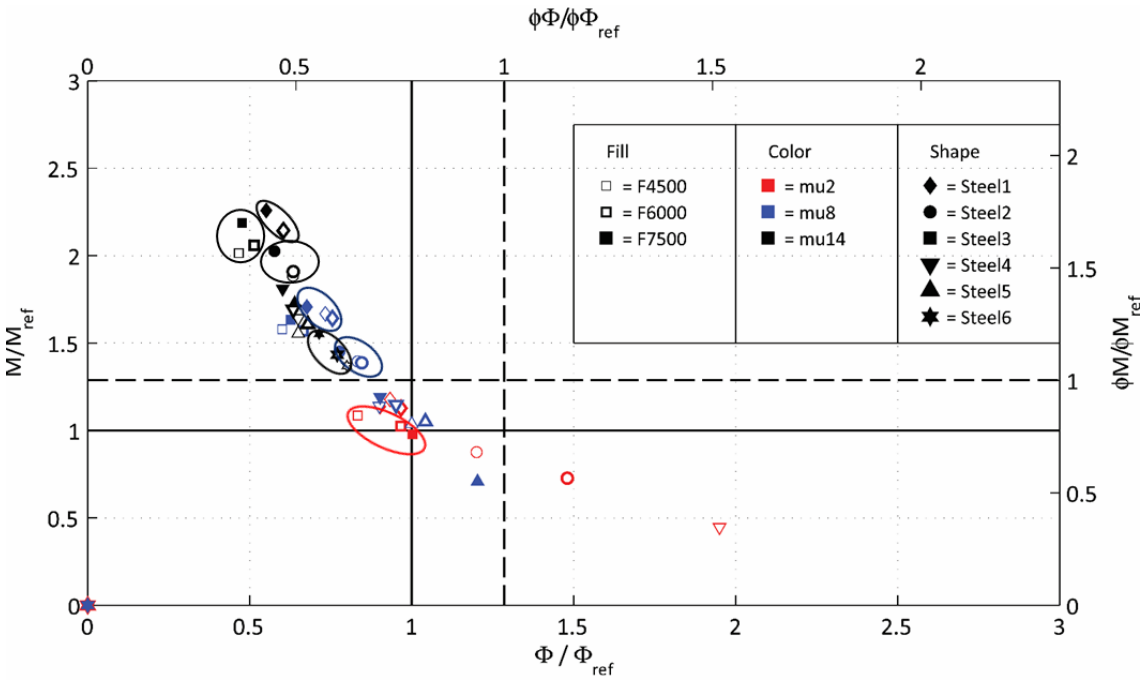

Figure 42. Normalized Moment vs. Curvature for S8-H80 with Varied f'c, Mu, and Steel Profiles

Table 4 - Table 9 summarize the results of the case study for each girder span investigated. The results reflect the appropriate strength reduction factors and highlight the configurations that satisfy the design strength requirements. The tables demonstrate that the trends associated with the SFRC on the capacity and curvature of each deck are maintained for each girder spacing. In most cases; however, the effectiveness of the SFRC decreases with increased girder spacing and moment demand.

Table 4. Normalized Moment for S6-F4500

		Steel1	Steel2	Steel3	Steel4	Steel5	Steel6
H55	mu2	1.08	0.67	1.00	0.41	NA	NA
	mu8	1.33	0.96	1.23	0.76	0.68	NA
	mu14	1.57	1.22	1.36	1.05	0.98	0.82
H75	mu2	1.13	0.94	1.05	0.49	NA	NA
	mu8	1.63	1.47	1.57	1.19	1.08	NA
	mu14	2.12	1.96	2.02	1.71	1.61	1.41
H95	mu2	1.12	1.15	1.05	0.58	NA	NA
	mu8	2.04	2.06	1.98	1.71	1.57	NA
	mu14	2.83	2.85	2.74	2.50	2.39	2.14

Table 5. Normalized Moment for S8-F4500

		Steel1	Steel2	Steel3	Steel4	Steel5	Steel6
H60	mu2	1.08	0.62	1.00	0.36	NA	NA
	mu8	1.32	0.90	1.20	0.72	0.64	NA
	mu14	1.56	1.16	1.33	1.00	0.94	0.80
H80	mu2	1.18	0.88	1.09	0.45	NA	NA
	mu8	1.67	1.39	1.58	1.14	1.04	NA
	mu14	2.14	1.88	2.01	1.64	1.55	1.37
H100	mu2	1.13	0.97	1.06	0.49	NA	NA
	mu8	1.92	1.82	1.84	1.51	1.40	NA
	mu14	2.63	2.54	2.51	2.23	2.13	1.92

Table 6. Normalized Moment Capacity for S12-F4500

		Steel1	Steel2	Steel3	Steel4	Steel5	Steel6
H75	mu2	1.07	0.56	1.06	0.29	NA	NA
	mu8	1.36	0.88	1.27	0.71	0.65	NA
	mu14	1.63	1.17	1.41	1.02	0.96	0.84
H95	mu2	1.11	0.68	1.09	0.34	NA	NA
	mu8	1.58	1.23	1.54	1.01	0.93	NA
	mu14	2.04	1.70	1.93	1.49	1.42	1.27
H115	mu2	1.11	0.77	1.13	0.39	0.00	0.00
	mu8	1.85	1.61	1.81	1.35	1.26	0.00
	mu14	2.51	2.28	2.41	2.02	1.94	1.77

Table 7. Normalized Curvature for S6-F4500 with Varied Depth, Mu, and Steel Profiles

		Steel1	Steel2	Steel3	Steel4	Steel5	Steel6
H60	mu2	0.98	1.48	0.83	2.22	NA	NA
	mu8	0.87	1.10	0.72	1.25	1.48	NA
	mu14	0.76	0.91	0.64	0.97	1.02	1.25
H75	mu2	0.96	1.11	0.90	1.81	NA	NA
	mu8	0.74	0.77	0.62	0.83	0.97	NA
	mu14	0.59	0.62	0.49	0.60	0.65	0.79
H95	mu2	0.87	0.87	0.87	1.45	NA	NA
	mu8	0.57	0.57	0.50	0.60	0.63	NA
	mu14	0.42	0.42	0.37	0.41	0.45	0.48

Table 8.Normalized Curvature for S8-F4500 with Varied Depth, Mu, and Steel Profiles

		Steel1	Steel2	Steel3	Steel4	Steel5	Steel6
H60	mu2	0.98	1.55	0.78	2.39	NA	NA
	mu8	0.86	1.14	0.69	1.29	1.47	NA
	mu14	0.78	0.94	0.65	0.98	1.04	1.29
H80	mu2	0.93	1.20	0.83	1.95	0.00	0.00
	mu8	0.73	0.83	0.60	0.90	1.00	0.00
	mu14	0.60	0.63	0.47	0.65	0.65	0.80
H100	mu2	0.95	1.07	0.92	1.79	0.00	0.00
	mu8	0.64	0.67	0.55	0.69	0.73	0.00
	mu14	0.49	0.49	0.40	0.50	0.50	0.60

Table 9. Normalized Curvature for S12-F4500 with Varied Depth, Mu, and Steel Profiles

		Steel1	Steel2	Steel3	Steel4	Steel5	Steel6
H75	mu2	0.99	1.55	0.65	2.52	NA	NA
	mu8	0.86	1.08	0.60	1.16	1.36	NA
	mu14	0.73	0.86	0.56	0.84	0.91	1.10
H95	mu2	0.95	1.34	0.76	2.23	NA	NA
	mu8	0.76	0.88	0.53	0.92	0.97	NA
	mu14	0.61	0.65	0.46	0.63	0.69	0.74
H115	mu2	0.94	1.22	0.80	2.03	NA	NA
	mu8	0.66	0.69	0.52	0.73	0.78	NA
	mu14	0.49	0.49	0.38	0.47	0.52	0.57

3.3 Slab Bridge Design

3.3.1 Modeling and Analysis

A simply-supported slab bridge deck was analyzed in a manner similar to the parameter study conducted for the slab-girder bridge deck. Slab bridge decks utilize girders that are orientated perpendicular to vehicle traffic and are characterized by short spans and a large thickness in comparison to slab-girder bridge decks. The capacity requirements of the system were determined utilizing the effective width procedure (AASHTO 2014). For a slab bridge spanning less than 30 ft, the effective width is determined the same was as slab-girder decks utilizing equations 14 and 15 presented in Section 3.2.1.

Table 10 presents values for each parameter investigated. The median thickness for each girder spacing was chosen as the minimum required depth based on AAHSTO requirements. Table 11 details the area of steel reinforcement used near the tension face of the deck. The minimum area of steel required for temperature and shrinkage was used near the compression face of the deck. The same name convention utilized for the slab-girder deck was used for the slab bridge deck.

Table 10. Slab Bridge Parameters

Span Length (ft.)	Deck Thickness (in)	f'c (ksi)	μ	Steel Profile
15	9.5	4.5 6 7.5	0.2 .8 1.4	Steel Profiles 1-4
	12			
	14.5			
30	15.5			
	19.5			
	23.5			

Table 11. Steel Profiles for Slab Bridge

Steel Profile	Steel Area and Design Procedure	Illustration
1	Strength	Figure 29
2	80% of Strength	
3	50% of Strength	
4	-	

3.3.2 Results

A total of 216 SFRC bridge decks were analyzed as part of this case study. Approximately 20% of the decks, 44 total, failed to reach the nominal compressive strain. Each deck was compared to the typical reinforced concrete bridge deck with appropriately designed steel reinforcement to demonstrate the effect of adding steel fibers on the concrete's strength and serviceability. Figure 43 demonstrates the effects of steel fibers on a bridge deck spanning 30 ft with a varying deck depth.

3.3.2.1 Reference Concrete Deck with Steel Fibers

In a similar manner to the slab-girder bridge case study, the addition of steel fibers to the reference deck, a deck with minimum depth, compressive strength, and ultimate strength design steel, increases the moment capacity while decreasing the curvature at the nominal moment. Adding a small amount of fibers, mu2, results in a small increase in the moment capacity. Alternatively, adding a large amount of fibers, mu14, increases the moment capacity by 75%, but decreases the curvature at nominal moment by 55%.

3.3.2.2 Varied Depth and Steel Profile

The depth of the cross-section and area of traditional steel reinforcement can be reduced to increase the ductility back to the ductility observed in the reference deck with steel fibers. Utilizing the ultimate strength design steel with a minimum amount of fibers, mu2, the depth of the cross section can be reduced by 20%. Alternatively, adding an excessive amount of fibers to the minimum cross section depth allows for the complete exclusion of traditional steel reinforcement. The depth may be reduced by 20% and the area of traditional steel reinforcement may be reduced 66% with the addition of a moderate amount of steel fibers, mu8.

Ultimately, the addition of steel fibers allows the designer to both reduce the depth of the concrete slab and area of steel reinforcement while maintaining the required strength. As a

result, the curvature at nominal will also decrease, but can be increased with smaller depths and steel area.

Table 12 and Table 13 summarize the results of the case study with respect to the girder spacing and slab depth. Strength reduction factors are considered when evaluating slab bridge configurations. The values in these tables demonstrate that the girder spacing is not a significant factor in the response of the SFRC decks with respect to the ADOT designed decks. Additionally, the concrete compressive strength is insignificant in the response of the SFRC decks as shown in Figure 44. Both of the aforementioned trends were also observed in the slab-girder bridge deck.

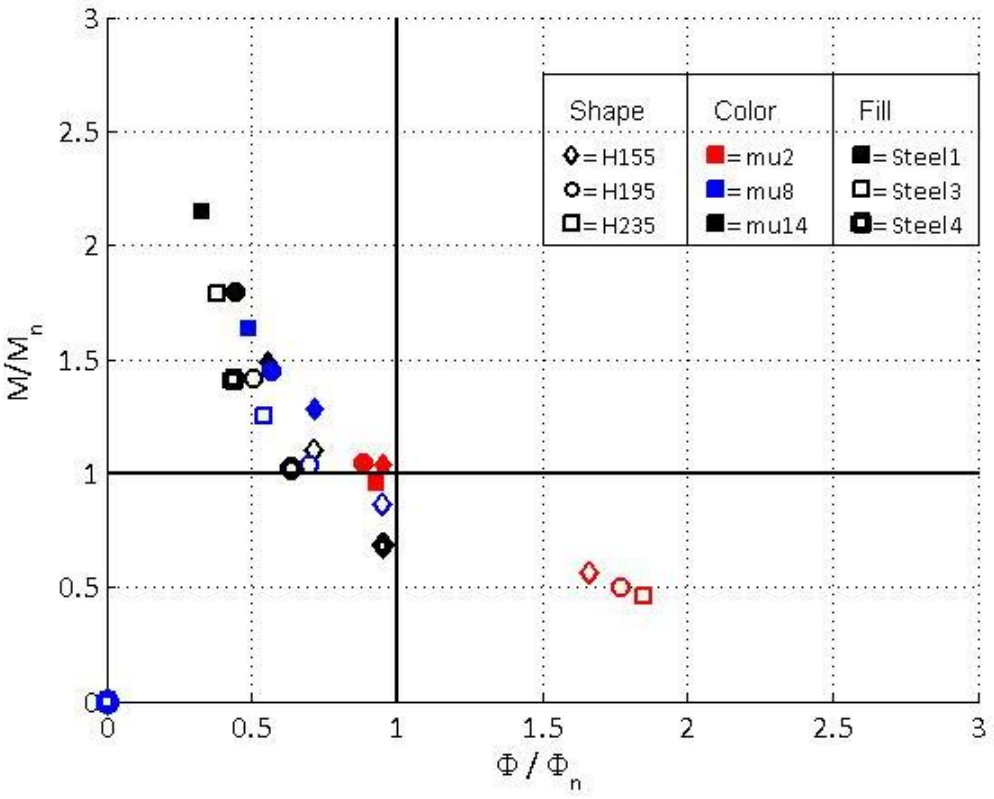

Figure 43. Normalized Moment vs. Curvature for S30-F4500 with Varied Depth, Mu, and Steel Profiles

Table 12. Normalized Moment Capacity for S15-F4500

		Steel1	Steel2	Steel3	Steel4
H95	mu2	1.05	0.87	0.60	NA
	mu8	1.27	1.11	0.85	NA
	mu14	1.46	1.31	1.08	0.65
H120	mu2	1.06	0.87	0.52	NA
	mu8	1.44	1.28	1.03	NA
	mu14	1.77	1.63	1.39	0.99
H145	mu2	1.00	0.78	NA	NA
	mu8	1.63	1.48	1.24	NA
	mu14	2.12	1.98	1.76	1.38

Table 13. Normalized Moment Capacity for S30-F4500

		Steel1	Steel2	Steel3	Steel4
H155	mu2	1.04	0.86	0.57	NA
	mu8	1.28	1.12	0.86	NA
	mu14	1.49	1.34	1.10	0.68
H195	mu2	1.05	0.83	0.50	NA
	mu8	1.45	1.29	1.04	NA
	mu14	1.80	1.65	1.42	1.02
H235	mu2	0.96	0.75	0.46	NA
	mu8	1.64	1.48	1.25	NA
	mu14	2.15	2.00	1.78	1.41

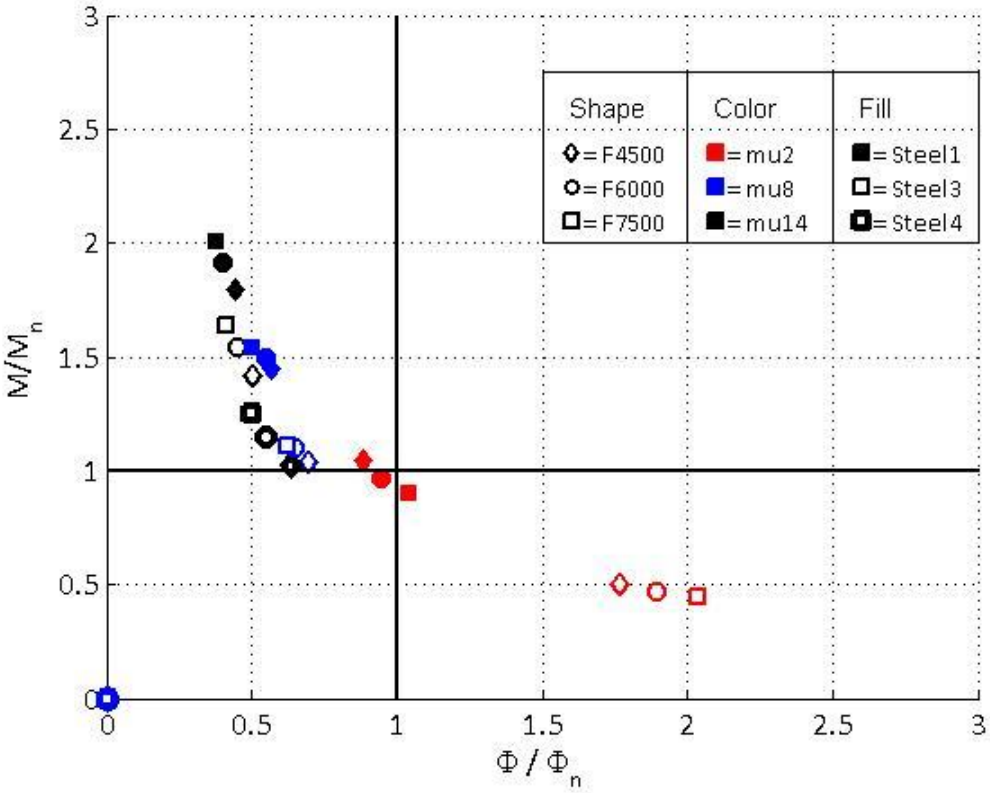

Figure 44. Normalized Moment vs. Curvature for S30-H195 with Varied f'c, Mu, and Steel Profiles

3.4 Railing

3.4.1 Modeling and Analysis

The design of bridge railings is based on a yield line theory analysis. A set of equations to determine lateral load capacity for a concrete barrier is presented in AASHTO LRFD Bridge Design Specifications (2014). There are six categories for longitudinal bridge railings that correspond to the expected impact loading and barrier strength. The reference barrier dimensions and steel reinforcement is exhibited in Figure 45 and will be evaluated based on railing category TL-4. Table 14 demonstrates the organization and values used for each parameter investigated and Table 15 details the area of steel reinforcement used.

$$R_w = \frac{2}{2L_c - L_t}\left(8M_B + 8M_W + \frac{M_C L_C^2}{H}\right) \quad (16)$$

$$L_C = \frac{L_t}{2} + \sqrt{\left(\frac{L_t}{2}\right)^2 + \frac{8H(M_b + M_w)}{M_c}} \quad (17)$$

Where R_w is the transverse railing resistance, L_c is the critical length of yield line, L_t is the length of distributed impact load, M_b is the flexural capacity of beam at top of wall, M_w is the flexural capacity of wall about its vertical axis, and M_c is the flexural capacity of wall about an axis parallel to the wall.

Table 14. Railing Parameters

Wall Thickness (in)	f'c (ksi)	μ	Steel Profile
8	4.5	0.2	Steel Profiles 1-4
10	6	.8	
12	7.5	1.4	

Table 15. Steel Profiles for Railing

Steel Profile	Steel Area and Design Procedure	Illustration
1	Reference	Figure 45
2	66% Reference	
3	33% Reference	
4	-	

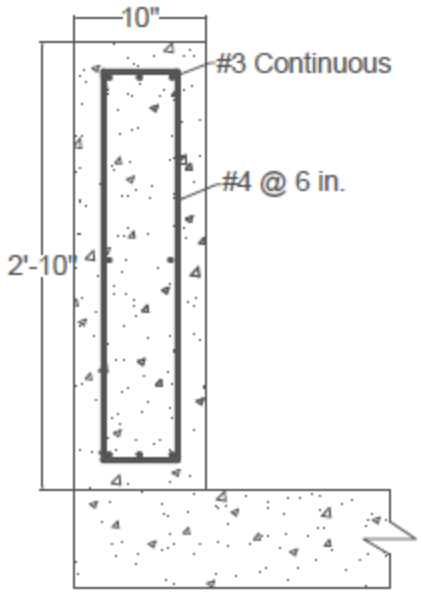

Figure 45. Reference Barrier Design

3.4.2 Results

Figure 46 and demonstrate the effect of adding fibers to a concrete railing with regards to the reference concrete railing shown above. Without changing the thickness of the wall, the addition a small amount of fibers, mu2, allows the steel reinforcement to be reduced by 33%. Increasing the amount of added fibers to a moderate amount, mu8, allows for the complete exclusion of the steel reinforcement while maintaining the minimum required strength.

Alternatively, both the wall thickness and steel reinforcement may be reduced by 20% and 66% respectively while maintaining the required strength. Both the wall thickness and steel reinforcement can be significantly altered with the use of steel fibers.

As shown in Figure 47, the concrete compressive strength is not as significant as the wall thickness and area of steel reinforcement. This is consistent with the conclusions of both bridge systems case study.

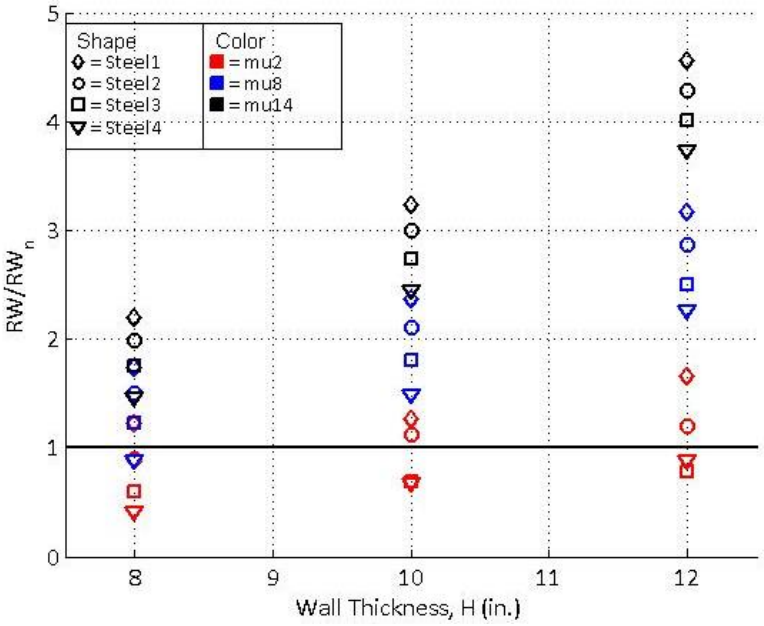

Figure 46. Normalized Collision Load vs Wall Thickness for F4500 with Varied Mu and Steel Profiles

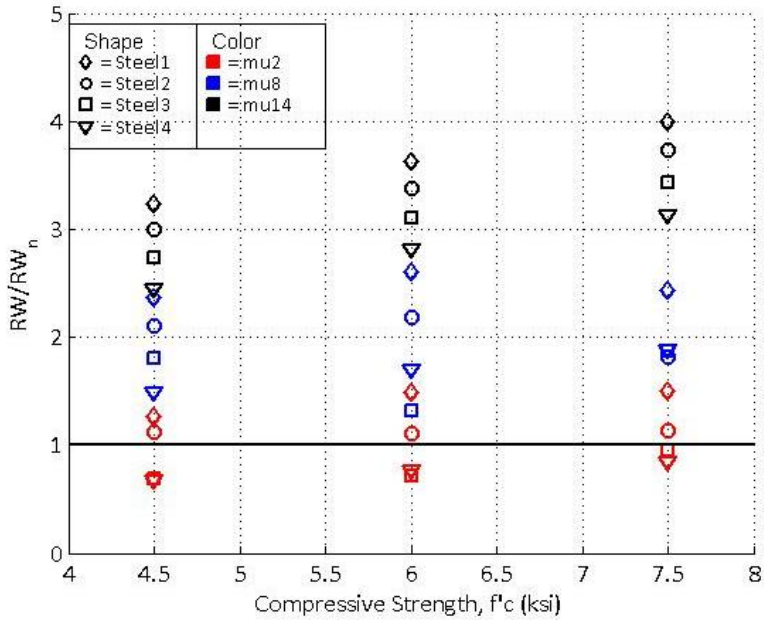

Figure 47. Normalized Collision Load vs Concrete Compressive Strength for H100 with Varied Mu and Steel Profiles

3.5 Conclusion

The three case studies demonstrated the effects of SFRC on the capacity of different bridge decks and elements. The results of each study yielded similar trends corresponding to the addition of strength due to the steel fibers in relation to conventional steel reinforcement, concrete compressive strength, and section geometry.

- The addition of steel fibers results in an increase in moment capacity and decrease in curvature at the nominal moment.
- Decreasing the depth of the section reduces the moment capacity, but also increases the curvature at nominal.
- With a moderate amount of steel fibers, the amount of conventional steel reinforcement may be reduced or lumped into advantageous locations, such as at mid-depth
- With an excessive amount of steel fibers, the conventional steel reinforcement may be excluded completely.
- The benefits of SFRC decrease as the moment demand increases for slab-girder bridge decks while the moment demand does not affect the benefits from SFRC.
- The design of concrete railings is based on yield line theory.
- The addition of steel fibers results in an increase in collision failure load.
- Decreasing the thickness of the cross-section reduces the moment capacity, but also increases the curvature at nominal.
- With an excessive amount of steel fibers, the traditional steel may be excluded completely.
- With a moderate amount of steel fibers, both the wall thickness and area of traditional steel may be reduced by 20% and 66% respectively.
- The concrete compressive strength slightly increases the capacity of the railing.

Ultimately, the use of SFRC adds to the reinforcement of a section and must be balanced by a reduction in conventional steel or depth. Otherwise, the section will begin to become over-reinforced resulting in a lower curvature at nominal and potentially a brittle failure. Further caution must be taken when utilizing the procedure of the case study. Each case study simply selected levels of residual tensile strength without regards to how to achieve the stated levels. Furthermore, each analysis used a strip-method treating each deck as a beam with unit width. While this may be appropriate for decks behaving in a one-way manner, this procedure will result in an underestimation of strength when considering two-way slabs (Destrée and Mandl 2008).

4. EXPERIMENTAL TEST PROGRAM OF SLAB STRIPS

4.1 Introduction

The design of a concrete bridge deck commonly utilizes the moment capacity of a strip of the deck. Both the AASHTO effective width approach and nonlinear yield line analysis use this information to determine deck strength. The case studies presented in 3 used this same approach. To better understand and predict the response of a SFRC slab-beam bridge deck, an experimental study was conducted on simply supported slab strip specimens.

This section will detail the experimental test program used to investigate the moment capacity, deflection, cracking pattern, and failure mode of slab strips. The goal of the study is to validate the findings of case studies presented in 3 and determine appropriate relations between the slab depth, fiber volume percentage, and conventional steel reinforcement. The information obtained from this study will be utilized to design a large scale slab-girder deck specimen.

First, the test matrix developed for this experimental program is explained in Section 4.2. Casting of the SFRC and its material properties are discussed in sections 4.3 and 4.4. Section 4.5 describes the setup and instrumentation used to conduct the experimental tests and the results of the tests are presented in section4.6. Finally, the results are evaluated in section 4.7 and conclusions made in section 4.8.

4.2 Design Of Test Matrix

The geometry and conventional steel reinforcement of the slab strip specimens were chosen to capture the typical reinforced concrete bridge deck design currently used by ADOT. Different depths and percentages of steel reinforcement were investigated to determine the most efficient use of steel fiber reinforced concrete with conventional steel reinforcement. Section 4.2.1 details the geometry of the test specimens. Section 4.2.2 details design of the strips and Section 4.2.3 discusses the volume of fiber utilized in the strips. Section 4.2.4 presents each of the specimens considered in the experimental program.

4.2.1 Dimensions

A benchmark slab strip was created based on the design requirements of ADOT and for the bridge deck test. Based on these guidelines, the large-scale test is expected to be 18 ft (5486 mm) wide and supported by three girders. This results in a girder spacing of 6 ft (1829 mm) with a 3 ft (914mm) overhang on each side of the deck.

The minimum deck depth required by ADOT for 6 ft (1829 mm) girder spacing is 8 inches (203 mm). This depth includes a 0.5 inches (12.7 mm) thick wearing surface that is excluded in strength

and service analysis. The benchmark slab strip has dimensions 7.5 inches x 18 inches x 8 ft long (190.5 mm x 457 mm x 2438 mm) as shown in Figure 48. An additional depth, 9 inches (229 mm), is also investigated to demonstrate the effect of SFRC and conventional steel reinforcement ratios in relation to the deck thickness. The deeper section corresponds to the minimum thickness for bridges with girder spacing of 11.5 ft (3505 mm).

The benchmark slab-strip width is 18 inches to accommodate multiple spacings of steel reinforcement.

Figure 48. Dimensions of Reference Slab-Strip Specimen

4.2.2 Design of Conventional Bridge Decks

The design of conventionally reinforced concrete bridge decks is typically controlled by the service limit state. The service limit state utilizes the allowable stress design and a maximum allowable tensile stress of 24 ksi (165 Mpa) in the conventional steel. This design is achieved using Hooke's law in an elastic analysis of the cross-section. The steel area is transformed into an equivalent concrete area to permit the analysis. The service condition is assumed to occur after the cross-section has cracked and the concrete does not provide any tension capacity. The service state demand is given by:

$$M_{Service} = 1.0(M_{DC} + M_{DW}) + 1.0(M_{LL+IM}) \quad \textbf{(18)}$$

Where $M_{Service}$ is the design moment at the service limit state, M_{DC} is the moment demand due to both structural and nonstructural components, M_{DW} is the moment demand due to the wearing surface, and M_{LL+IM} is the moment demand due to vehicular loads including impact.

Stress in the steel at this demand are shown in Figure 49 and calculated as:

$$f_s = \frac{M_{service}}{A_s jd} \quad \textbf{(19)}$$

$$\rho = \frac{A_s}{bd} \quad (20)$$

$$n = \frac{E_s}{E_c} \quad (21)$$

$$k = \sqrt{(n\rho)^2 + 2n\rho} - n\rho \quad (22)$$

$$j = 1 - \frac{k}{3} \quad (23)$$

Where ρ is the ratio of steel reinforcement area to concrete area; A_s is the area of steel reinforcement; b is the width of concrete beam; d is the depth of bottom layer of steel reinforcement; n is the ratio of steel and concrete modulus of elasticity; k is the ratio of neutral axis depth to depth; j is the ratio of moment arm between resultant forces to depth; f_s is the stress in steel reinforcement at service conditions; and $M_{service}$ is the design moment at the service limit state.

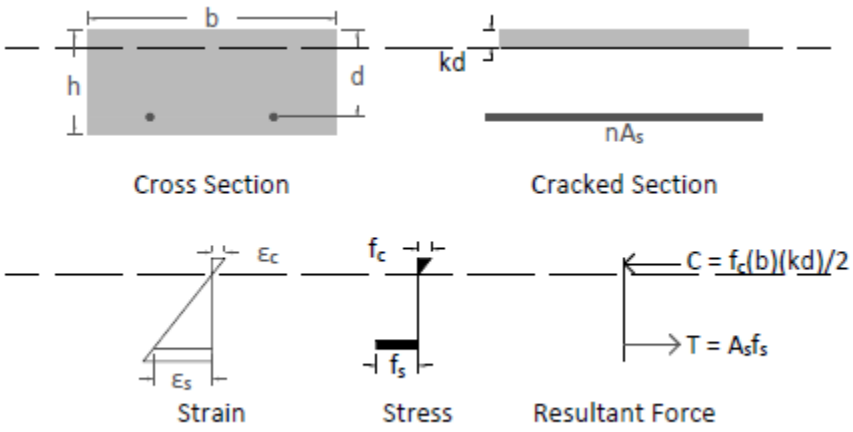

Figure 49. Service State Analysis – Elastic Sections

After the bridge deck has been designed for the service limit state, the ultimate limit state must be check. The resultant forces and moment capacity of the section are shown in Figure 50 and calculated as:

$$M_{Strength} = 1.25(M_{DC}) + 1.50(M_{DW}) + 1.75(M_{LL+IM}) \quad (24)$$

$$a = \frac{A_s f_y}{0.85 f_c' b} \quad (25)$$

$$M_n = A_s f_y \left(d - \frac{a}{2}\right) \quad (26)$$

Where a is the depth of compression stress block used for design; and M_n is the nominal moment capacity of the cross-section.

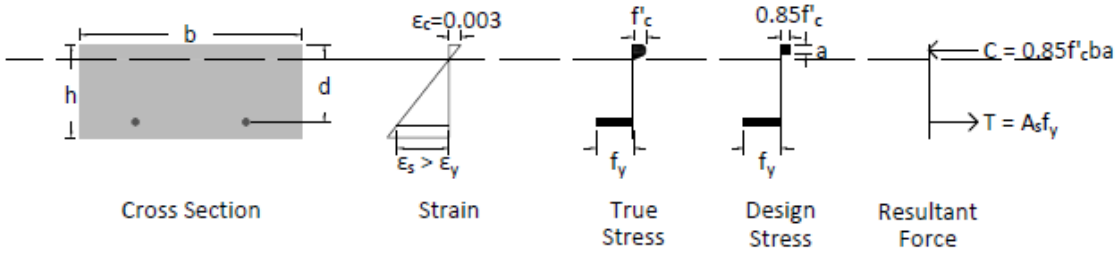

Figure 50. Ultimate State Analysis

The moment demands are determined in accordance with the ADOT Bridge Design Guidelines (2011) and Table A4-1 of AASHTO LRFD Bridge Design Specifications (2014). The large-scale SFRC bridge deck investigated in this thesis has un-factored moment demand of 4.83 k-ft in the positive bending region and 4.88 k-ft in the negative moment region. These demands were used to select the reinforcement provided in Table 16. These designs serve as benchmarks for the development of the test matrix.

Table 16. Steel Area Required to Meet ADOT Limit States

Limit State	Positive		Negative	
	Steel Layout	Steel Ratio, ρ (%)	Steel Layout	Steel Ratio, ρ (%)
Service	#5 @ 8 in	0.6	#5 @ 6.5 in	0.76
Strength	#5 @ 11 in	0.41	#5 @ 10 in	0.49

4.2.3 Steel Fiber Dosage

Two design philosophies were utilized for the determination of the volume of fibers used in the experimental program. The first philosophy is to achieve the largest gain in strength and ductility due to the fibers. This refers to the "maximum" fiber percentage. The second philosophy is to achieve a design that satisfies both the service and strength limit states while utilizing the amount of traditional steel reinforcement required for the strength design. This volume refers to the "minimum" fiber percentage.

The design philosophies are based on an experimental study conducted by Park et al (2015) that investigated the effect of different fiber volumes and types on standard tests for compression, tension, and flexure. The investigated hooked end and straight steel fibers introduced at volumes varying from 0% to 3%. Park et al found that the hook end fibers yielded larger improvements in the SFRC material tests than the straight fibers. The performance of the SFRC increased with an increased volume of fibers until 3%. Based on these findings, the "maximum" fiber percentage utilized for this experimental program is 2% by volume.

A theoretical analysis was conducted using the material properties calculated from the SFRC with 0.5% volume of fibers. The analysis demonstrated that the addition of fibers at this percentage was sufficient to elevate the traditional strength design such that it also satisfied the service limit state. Therefore, the "minimum" fiber percentage utilized for this experimental program is 0.5% by volume.

4.2.4 Test Matrix

The experimental test was conducted on 14 SFRC slab strips with a varying percentage of steel reinforcement, steel location, and slab depth as shown in Table 17 and Table 18. A naming scheme, shown in Figure 51, was developed to easily identify the characteristics of each slab strip. The name consists of the depth, fiber volume, and location, number, and size of steel reinforcement.

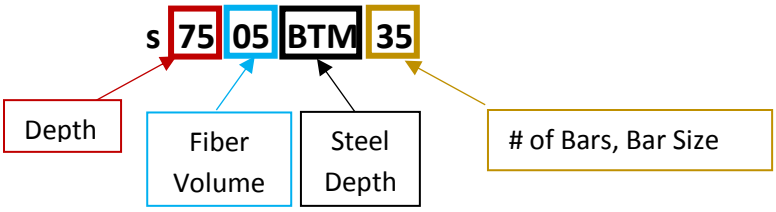

Figure 51. Naming Scheme

The amount of conventional steel reinforcement for two of the slab strips was chosen to represent the service (s7505BTM35) and strength (s7505BTM25) limit states. The remaining 12 slab strips varied to investigate the benefits of SFRC. Based on the results of the case study analysis, adding steel fibers increased the moment capacity of the reinforced concrete section, but also reduced the nominal curvature. Decreasing the area of steel reinforcement with SFRC increased the curvature to the nominal curvature and capacity of plain concrete. Therefore, the location and percentages of steel reinforcement is varied, as shown in Figure 52, to investigate the effectiveness of the SFRC on the strength, ductility, and crack management of the slab-strip.

Table 17. Test Matrix for 7.5 in Deep Slab Strip Specimens

		Steel Reinforcement				
Specimen	**Fiber Volume (%)**	**Size**	**# of Rebar**	**Spacing (in)**		**ρ (%)**
				Bottom	**Center**	
s7505BTM35	0.5	#5	3	6	-	0.86
s7505BTM25	0.5	#5	2	9	-	0.57
s7505BTM24	0.5	#4	2	9	-	0.37
s7505BTM23	0.5	#3	2	9	-	0.21
s7505CTR35	0.5	#5	3	-	6	0.86
s7505CTR25	0.5	#5	2	-	9	0.57
s7505NOS00	0.5	-	-	-	-	-
s7520NOS00	2.0	-	-	-	-	-

Table 18. Test Matrix for 9 in Deep Slab Strip Specimens

Beam	Fiber Volume (%)	Steel Reinforcement				
		Size	# of Rebar	Spacing (in)		ρ (%)
				Bottom	Center	
s9005BTM35	0.5	#5	3	6	-	0.69
s9005BTM25	0.5	#5	2	9	-	0.46
s9005BTM24	0.5	#4	2	9	-	0.30
s9005BTM23	0.5	#3	2	9	-	0.16
s9005NOS00	0.5	-	-	-	-	-
s9020NOS00	2.0	-	-	-	-	-

(a) Singly Reinforced at Bottom (b) Singly Reinforced at Center (c) No Reinforcement

Figure 52. Slab Strip Cross Sections

4.3 Specimen Casting

The method of adding the steel fiber to the concrete matrix can significantly affect the workability of the fresh mix. According to the manufacturer of the fibers utilized in this study, Bekaert, the fibers may either be introduced with the sand and aggregates or into the fresh mixed concrete. Additionally, Bekaert recommends adding the fibers at a continuous rate not to exceed 40 kg/min. Due to restrictions at the ready-mix concrete plant, the steel fibers were added to the fresh mix in accordance with the manufacturer's recommendations.

Despite efforts in the concrete mix proportions and procedures, issues with the SFRC workability were encountered. As a result, the 14 slab strip specimens were cast over two different days with two different fiber volumes

4.3.1 First Cast

Specimens utilizing the "maximum" fiber percentage, 2.0% by volume, were the first to be cast. At this volume of steel fibers, the workability of the fresh concrete mix was severely reduced. The fresh concrete mix without steel fibers had a slump of approximately 7.5 inches and was measured immediately after the concrete was batched into the truck. After measuring the slump,

the fibers were added directly into the concrete truck at the batching plant. The fibers were allowed to mix into the concrete matrix during the transport time to the laboratory, approximately 20 minutes away. Additional water was added to the concrete truck after it arrived to the laboratory elevating the water to cement ratio to 0.48. The concrete was allowed to mix at charging speed for an additional 5 minutes prior to measuring the slump again. Once the fibers were added, the slump was reduced to 0 inches as shown in Figure 53. There was significant clumping of the steel fibers and coarse aggregate as shown in Figure 54.

Figure 53. 2.0% SFRC Lack of Slump

Figure 54. Significant Clumping in SFRC

A concrete hopper was used to place SFRC for a 7.5 inch deep strip without conventional steel reinforcement (s7520NOS00) as shown in Figure 55. The SFRC did not flow from the hopper without significant vibration. Therefore, the following specimen, a 9 inch deep strip without conventional reinforcement (s9020NOS00), was cast directly from the concrete truck as shown in Figure 56. Both methods of placing the concrete required significant amount of internal and external vibration to consolidate the mix and an exceedingly large effort to finish the surface at this volume percentage.

Figure 55. Casting from Hopper

Figure 56. Casting From Truck - S9020NOS00

Overall, the concrete with 2.0 percent fibers was deemed impractical for use and the remaining concrete was discarded. The first cast yielded the two slab strips without steel and accompanying cylinders and prisms required for material testing (ASTM C1609, ASTM C39, and ASTM C469).

4.3.2 Second Cast

The fiber dosage rate was reduced to 0.5 percent by volume for the second cast. The percentage was chosen to ensure adequate workability of the SFRC while still providing an improved structural response. Based on the case study analysis presented in Section 2, a fiber dosage rate of 0.5 percent displayed an improved steel reinforcement stress at the service limit state. However, steel configurations presented in test matrix were still expected to not satisfy the service stress requirements. The range of expected service stress in the steel reinforcement provides a good distribution of results and effects of SFRC on the service behavior of the test specimens.

The steel fibers were added by a graduate student on-site of the experiment as shown in Figure 57. This procedure was chosen to ensure a slow and consistent addition of steel fibers to the fresh concrete mix and reduce the amount of time between addition of steel fibers and concrete placement:

1. Revolution rate was increased to charging speed
2. Steel fibers were added at a rate of approximately 24 kg/min
3. Addition of steel fibers required a total of 5 minutes for four cubic yards of concrete
4. Revolution rate of truck was decreased to mixing speed for 5 minutes

Figure 57. Adding Steel Fibers to Concrete Truck

Figure 58. Significant Slump of Fresh Mix Without Steel Fibers

Figure 59. Placing Concrete Directly into Forms

The steel fibers were evenly and randomly distributed using the specified method. The slump of the fresh concrete mix without steel fibers was 9 inches. The addition of steel fibers reduced the slump to 7 inches. SFRC was placed directly from the concrete truck into the slab strip forms to avoid any flow issues related to the concrete hopper used in first casting attempt, Figure 59. The

second cast yielded the remaining 12 slab strips and accompanying cylinders and prisms required for material testing (ASTM C1609, ASTM C39, and ASTM C469), Figure 60 and Figure 61.

Figure 60. Five of Twelve Completed SFRC Slab strips

Figure 61. Casts for ASTM Materials Tests on Way to Curing Room

4.4 Material Properties

Texas Department of Transportation (TxDOT) "Class S" concrete, conventional steel reinforcement with a yield strength of 60 ksi, and Dramix® 3D hooked end fibers were used to design the slab strip specimens. The specified concrete has a minimum compressive strength of 4000 psi. Section 4.4.1 and Section 4.4.2 discuss the material properties of the steel fibers and concrete, respectively, used for the experimental test program.

4.4.1 Steel Fiber Material Properties

The steel fibers utilized in the full-scale bridge deck experiment are consistent with the steel fibers used in the slab strip experimental program discussed in Section 3. The fiber has a length of 35 mm and a diameter of 0.55 mm. The aspect ratio, ratio of length to the diameter, is 65. The fiber has a tensile strength of 1.345 N/mm^2 and modulus of elasticity of 210 N/mm^2.

4.4.2 Concrete Material Properties

Concrete utilized in the experimental program was provided by a local ready mix concrete plant. The concrete was designed by the supplier to satisfy the requirements for a "Class S" TxDOT concrete mixture. TxDOT requires "Class S" concrete to be used in concrete bridge slabs. Table 19 demonstrates the TxDOT and ADOT requirements for concrete used in bridge decks. The lack

of workability is a primary concern for SFRC. Accordingly, a high range water reducer, or superplasticizer, was incorporated into the mix design.

Table 19. TxDOT and ADOT Mix Requirements for Concrete Bridge Decks

	TxDOT	ADOT
Compressive Strength, f'c (psi)	4000	4500
Maximum Water:Cement	0.45	0.5
Fine Aggregate:Cement	N.A.	N.A.
Coase Aggregate:Cement	N.A.	N.A.
Coarse Aggregate Size (in)	0.75-1.75	N.A.[1]
Allowable Cement Types	N.A.	II, III, V
Max Cementious Material (lbs/yd^3)	700	564-752
Slump (in.)	5.5	-[2]

[1] "Shall be chosen by the contractor and approved by the Engineer and shall conform to the size designation and grading requirements of AASHTO M 43. In choosing the size designation, the maximum size of coarse aggregate shall not be larger than 1/5 of the narrowest dimension between sides of adjacent forms, or 2/3 of the minimum clear spacing between reinforcing bars, or 1/3 the depth of the slab, whichever is least."

[2] "The proposed slump shall be chosen by the contractor. Concrete at the proposed slump shall be sufficiently able to allow proper placement without harmful segregation, bleeding, or incomplete consolidation." (ADOT 2009)

Standard tests for compressive (ASTM C39), tensile, and flexural (ASTM C1609) strengths, referenced in Section 3A, were conducted 28 days after the initial casting of the specimens. Additional compressive tests were conducted at 1, 7, and 14 days after the initial casting of the

specimens. A total of three specimens were cast for each test. The results of these tests are discussed in Sections 4.4.2.1, 4.4.2.2, and 4.4.2.3.

4.4.2.1 Compressive Strength

Concrete cylinders 6 by 12 inches were prepared in accordance with ASTM C192, "Standard Practice for Making and Curing Concrete Test Specimens in the Laboratory." The cylinders were cast in three equal lifts. After each lift, the SFRC was consolidated by rodding, 25 strokes per layer. After 24 hours of curing, the cylinders were removed from their molds and immediately transported to a moist curing room with an ambient temperature of 23°C and humidity of 100 percent. Each test was conducted in accordance with ASTM C39.

In addition to the cylinders cast for compression tests, three 4 by 8 inch cylinders were cast on each casting date to determine the modulus of elasticity for the SFRC in accordance with ASTM C469M, "Standard Test Method for Static Modulus of Elasticity and Poisson's Ratio of Concrete in Compression." The cylinders were also prepared in accordance with ASTM C192. The compressive test results for the concrete mix with fiber volume of 0.5% are shown in Figure 62 and Table 20. The test results for the concrete mix with a fiber volume of 2.0% are shown in Figure 63 and Table 21.

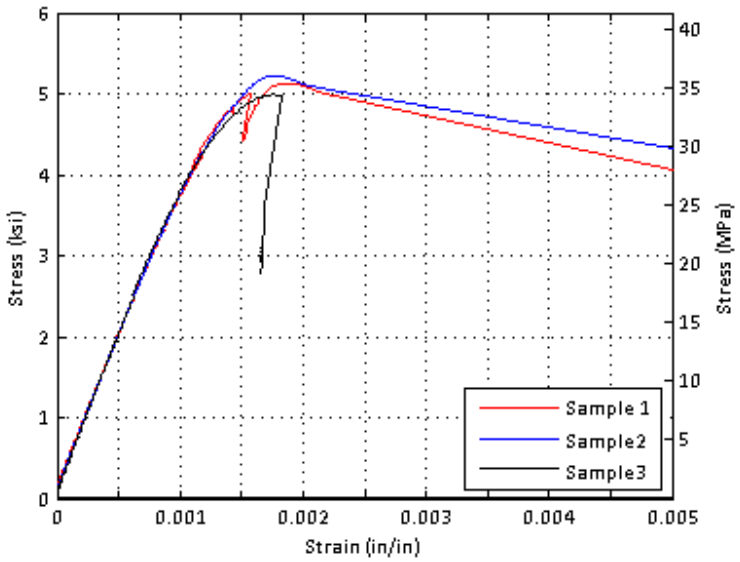

Figure 62. Stress-Strain Curve from ASTM C469 "Minimum" Fiber Percentage V_f = 0.5%

Table 20. ASTM C469 Results for "Minimum" Fiber Percentage, V_f = 0.5%

	Modulus of Elasticity (ksi)	Compressive Strength, f'c (ksi)
Sample 1	3730	5.12
Sample 2	3821	5.22
Sample 3	4530	4.99
Average	4027	5.11

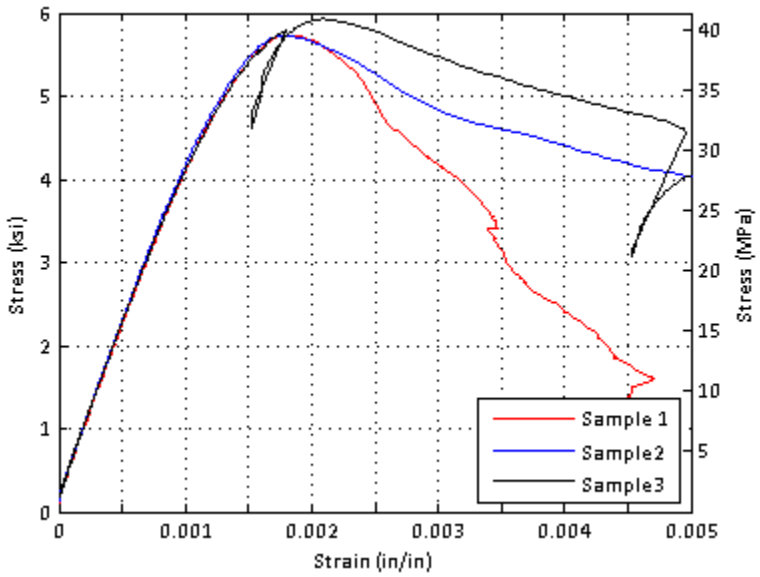

Figure 63. Stress-Strain Curve from ASTM C469 "Maximum" Fiber Percentage V_f = 2.0%

Table 21. ASTM C469 Results for "Maximum" Fiber Percentage, V_f = 2.0%

	Modulus of Elasticity (ksi)	Compressive Strength, f'c (ksi)
Sample 1	4122	5.73
Sample 2	4223	5.73
Sample 3	4165	5.93
Average	4170	5.80

4.4.2.2 Tensile Strength

Currently, there is not an ASTM standard for conducting a uniaxial test of SFRC. Therefore, the same uniaxial tensile test utilized in the experimental parameter study conducted by Park et al (2015) was used to measure the tensile properties of the SFRC specimens.

The test is conducted using 4 by 8 inch cylinders like the specimens used in the modulus of elasticity tests, ASTM C469M. Unbonded steel caps traditionally used for compression tests were modified by welding a threaded 1 inch steel rod to the ends of the caps. The threaded rod allows the caps to be attached to an MTS machine so that a tensile force may be applied. The concrete cylinders are attached to the unbonded caps with a high strength epoxy. The epoxy used was "Loctite High Strength Builders Formula" with a setting time of 5 minutes and capacity of 3500 psi. A linear variable differential transformer (LVDT) is attached to the cylinder with a 4 inch gauge length to measure the elongation of the specimen in the elastic region. Figure 64 shows the test setup. Figure 65 presents the results of the test procedure for both fiber dosages.

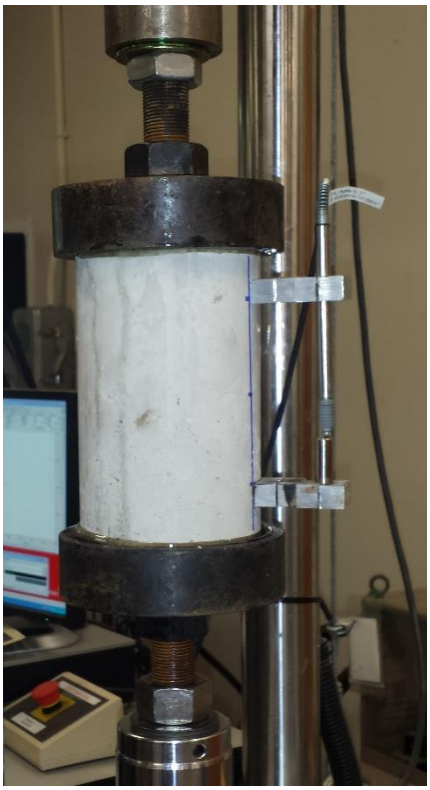

Figure 64. Uniaxial Tensile Test

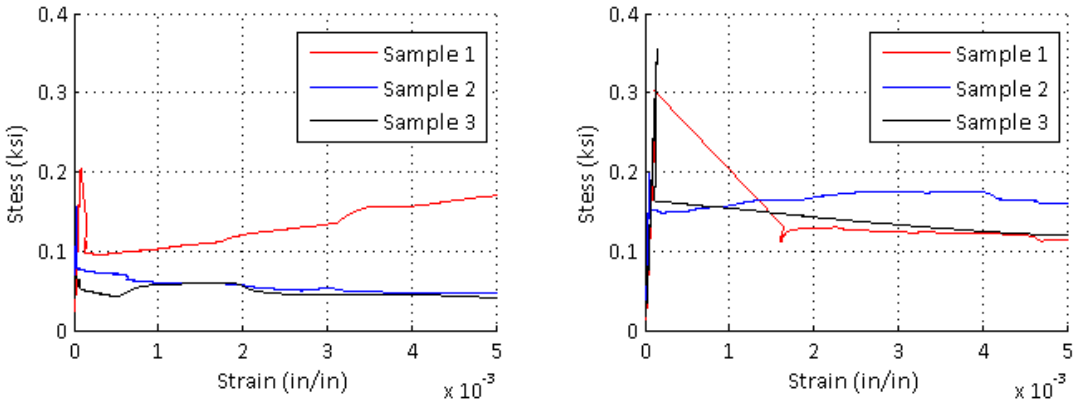

(a) (b)

Figure 65. Tensile Test Results for (a) V_f = 0.5% and (b) V_f = 2.0%

A total of six tests were conducted, three for each fiber dosage rate. Significant difficulties were encountered utilizing this procedure. Ultimately, the unpredictable failure location of the concrete specimen is less than ideal. A number of the test failed at the interface between the concrete specimen and epoxy. The crack migrated into the epoxy, as shown in Figure 66, allowing the adhesive to contribute to the post-crack response of the specimen. Sample 1 of the concrete with a fiber volume of 2.0% was the only test that failed inside the gauge length of the LVDT.

Figure 66. Failure of SFRC Cylinder in Epoxy-Concrete Interface (V_f = 0.5%, Sample 1)

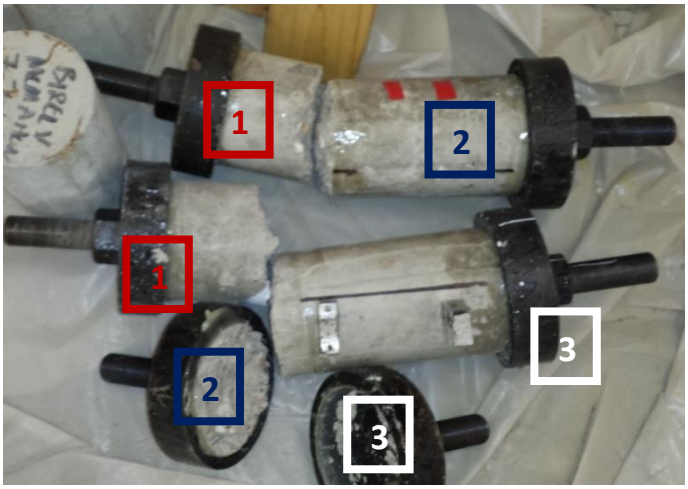

Figure 67. Failure Location of Each SFRC Uniaxial Tension Test (V_f = 2.0%,)

4.4.2.3 Flexural Strength

SFRC beams were prepared and tested in accordance with ASTM C1609, "Standard Test Method for Flexural Performance of Fiber-Reinforced Concrete (Using Beam with Third-Point Load)." Each beam is 150 mm by 150 mm by 500 mm (6 by 6 by 20 inches) in dimension and was consolidated by external vibration. Similar to the cylinders cast for the compression tests, the beam specimens were demolded after 24 hours and transported to a moist curing room.

Each flexural specimen was subjected to a third-point bending until failure. The tests were conducted using a displacement-control procedure at a rate of 0.025 in/min. Figure 68 and Table 22 show the results of ASTM C1609. Based on ASTM C1609, there are four values of interest in the force vs. deflection plots of the flexural tests:

1. First Peak Load, P_1: Load at first crack. Corresponds to a slope change in the deflection response.
2. Overall Peak Load, P_p: Maximum achieved load. Also referred to as the modulus of rupture.
3. Residual Load L/600, P_{600}: Residual capacity at a deflection of L/600.
4. Residual Load L/150, P_{150}: Residual capacity at a deflection of L/150.

The test results for each dosage volume satisfies the strength requirements of ACI 318 to allow for the use of steel fibers as shear reinforcement. However, the dosage volume of 0.5 percent by volume (65 lb/cy) is below the minimum specified rate by ACI. The three requirements to use steel fiber reinforcement in lieu of shear reinforcement is as follows:

4. The weight of added fibers exceeds 100 lb/cy.
5. The residual strength corresponding to a midspan deflection of 1/300 of the span length, obtained from flexural testing, is at least 90 percent of the first-peak strength.
6. The residual strength corresponding to a midspan deflection of 1/150 of the span length, obtained from flexural testing, is at least 75 percent of the first-peak strength.

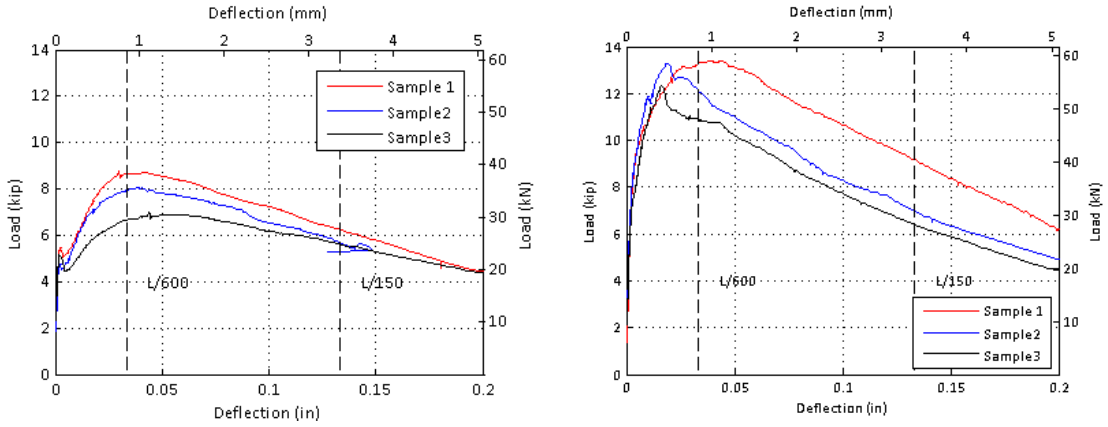

(a) (b)

Figure 68. ASTM C1609 Test Results for (a) V_f = 0.5% and (b) V_f = 2.0%

Table 22. Summary of Flexural Test Results

Dosage Rate	P_1 (kips)	f_{cr} (ksi)	P_P (kips)	f_{MOR} (ksi)	P_{600} (kips)	$f_{r,600}$ (ksi)	P_{150} (kips)	$f_{r,150}$ (ksi)
0.5%	5.1	0.48	7.9	0.73	7.7	0.72	5.9	0.54
2.0%	7.4	0.68	13.0	1.20	12.2	1.13	7.5	0.70

4.4.3 Steel Reinforcement Material Properties

A total of four samples were tested for each steel reinforcement size. The tests were conducted in accordance with ASTM A370, "Standard Test Methods and Definitions for Mechanical Testing of Steel Products." Elongation data was collected by three LVDT's with a gage length of 8 inches. Figure 69 through Figure 71 show the stress-strain relationship measured for each size of steel reinforcement.

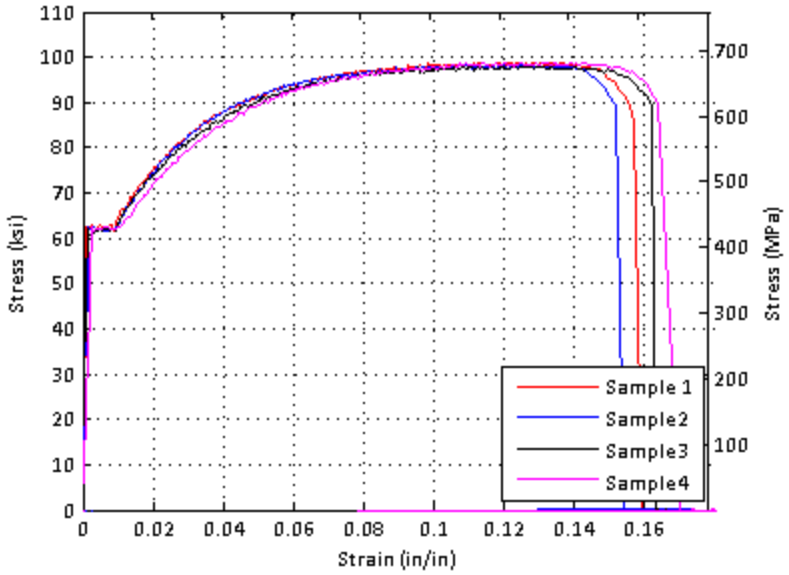

Figure 69. ASTM A370 Test For #3 Steel Reinforcement Bars

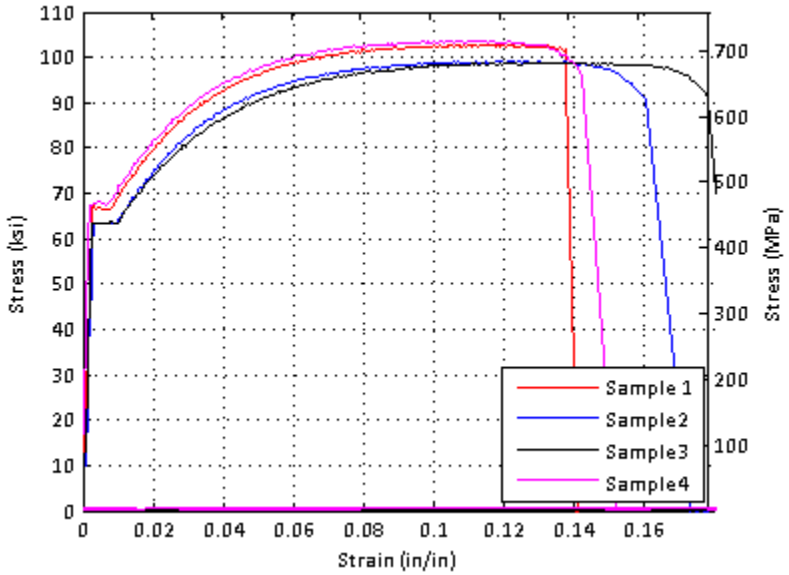

Figure 70. ASTM A370 Test For #4 Steel Reinforcement Bars

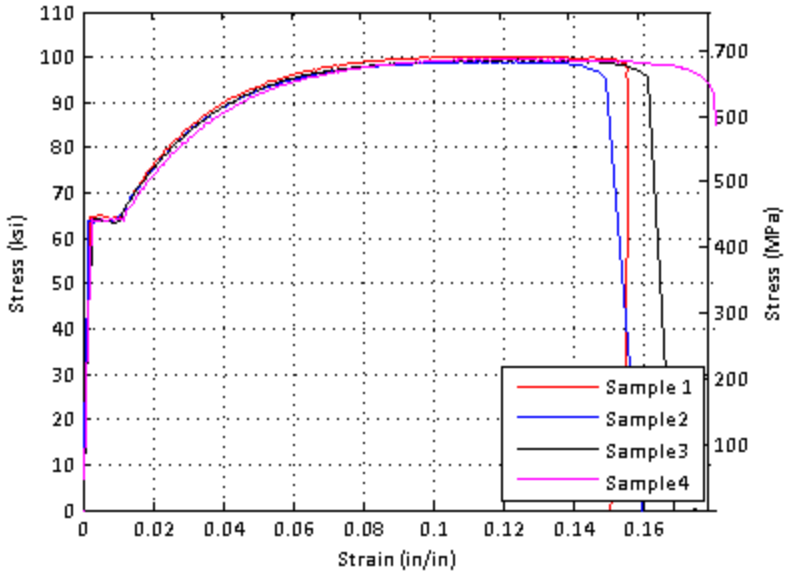

Figure 71. ASTM A370 Test For #5 Steel Reinforcement Bars

Table 23. Summary of Steel Reinforcement Properties for All Steel Bars

	#3		#4		#5	
	Yield Stress, f_y (ksi)	**Ultimate Stress, f_u (ksi)**	**Yield Stress, f_y (ksi)**	**Ultimate Stress, f_u (ksi)**	**Yield Stress, f_y (ksi)**	**Ultimate Stress, f_u (ksi)**
Sample 1	63	99	67	103	65	100
Sample 2	62	99	63	99	64	99
Sample 3	62	98	63	99	64	100
Sample 4	62	99	67	104	64	100
Average	62.3	98.8	65.0	101.3	64.3	99.8

4.5 Test Setup And Instrumentation

The slab strip specimens were subjected to a four-point bending flexural test as shown in Figure 72. The experimental tests were conducted using a 100 kip (444 kN) actuator. The test was conducted using a deflection-controlled philosophy. The deflection of the beam was increased at a rate of 0.05 inches per minute. The test was stopped at regular intervals to document the damage incurred by the beam. Crack locations, width, and height were recorded to document the damage progression of each specimen.

A load cell connected to the actuator recorded the applied load while string potentiometers located at 6 inch intervals recorded the deflection profile of the specimen. A LVDT was installed on the top and bottom of the slab strip specimen to determine the maximum strains and curvature experienced by each specimen. The gauge length of each LVDT was 2 ft to insure the primary failure plane fell within the readings of the LVDTs. Finally, strain gages were installed on the two outer conventional steel reinforcing bars in each specimen with traditional reinforcing steel.

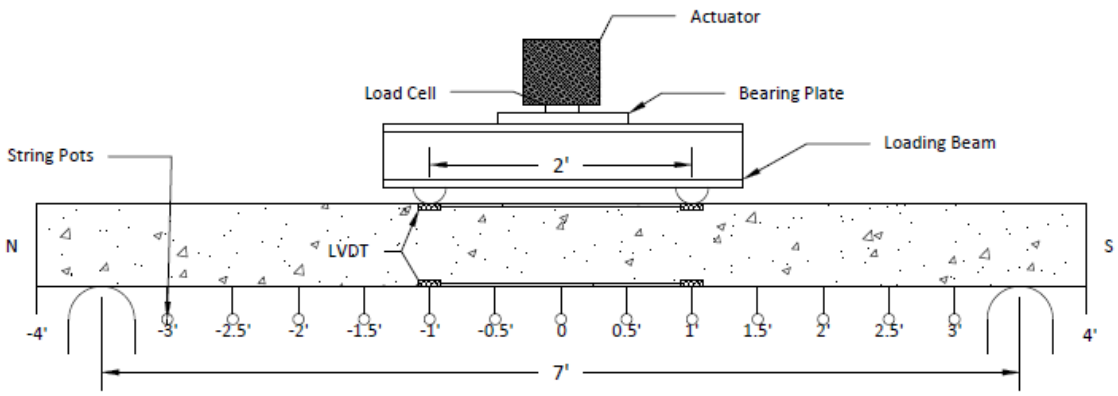

Figure 72. Experimental Test and Instrumentation Setup

In addition to the traditional instrumentation, the Optotrak Certus system from Northern Digital Inc. (NDI) was used to track the movement of several points on the west face of the beam. The Optotrak system utilizes LED markers glued to the specimen, a camera, and software that records the LED position over time. A grid of markers was placed on the west face of the specimen as shown in Figure 73 and Figure 74.

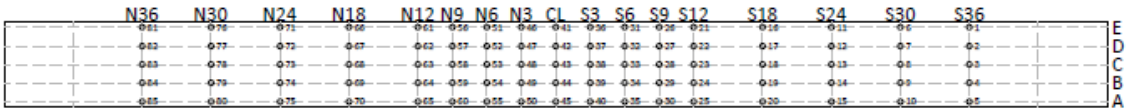

Figure 73. Opotrak Certus Grid Utilized for Test Program

Figure 74. Optotrak Certus Grid Utilized for Test Program

4.6 Test Results

The results from each test include the damage profile, deflected shape, and service and ultimate capacities. The damage profile in Section 4.6.1 summarizes the progression of cracks and crushing of concrete. The goal of the damage profile is to accurately determine the degree of damage to each strip specimen and compare each crack's size, width, and location to failure criteria specified by RILEM (2002) and fib (2010). The deflected shape of each specimen will demonstrate the deflection of the specimen in accordance to the string potentiometers and the Optotrak Certus system at the specimen's maximum capacity. The deflection data will be utilized to determine the curvature profile of each specimen. Finally, the capacity of each specimen is discussed in Section 4.6.2 detailing both the ultimate load as well as the stresses determined at service loads.

4.6.1 Damage Profile

The damage incurred by each specimen was observed and compared in three groups based on their steel reinforcement location: bottom, center, or none. The damage recorded consisted of the number of cracks, when they formed, their location, width, and height. The data was analyzed to identify trends amongst the groups. Appendix A provides an in-depth description of each individual test.

Throughout each experiment, the beams were examined for two failure criteria, the critical crack width and concrete crushing in the compression region. The critical crack width is defined by RILEM (2003) as 2.5 mm (0.1 inches). The failure progression for each SFRC slab-strip behaved in a similar manner. Several cracks would form over the length of the beam. The width of each crack

grew as the load was increased on the specimen. Eventually, the progression of damage in the beam localized in an individual crack referred to as the critical crack. Once localization of the failure began, the crack widths of all non-critical cracks remain constant while the critical crack width increased to beyond 10 mm (0.4 inches). The location and amount of steel reinforcement affected the number of cracks that formed and their growth rate.

4.6.1.1 Steel Reinforcement Located at Bottom

Overall, the behavior of the slab strips with steel located at the bottom of the specimen was consistent. Trends were observed in the number of cracks both inside and outside the constant moment region and the deflection step of the first crack in each region. The crack width of all non-critical cracks varied significantly between specimens. Table 24 summarizes the number of cracks, the deflection of the first crack, and the average crack width of the non-critical cracks at the time of failure.

Table 24. Properties of Non-Critical Cracks for Specimens with Steel Reinforcement Located at the Bottom

	Inside Constant Moment Region			Outside Constant Moment Region		
Specimen	**# of Cracks**	**$\delta_{first\ crack}$ (in)**	**Width, mm (in)**	**# of Cracks**	**$\delta_{first\ crack}$ (in)**	**Width, mm (in)**
s7505BTM35	8.5	0.1	0.41 (0.016)	7	0.2	0.13 (0.005)
s7505BTM25	6.5	0.10	0.40 (0.016)	6	0.15	0.31 (0.012)
s7505BTM23	6.5	0.10	0.60 (0.024)	4.5	0.15	0.17 (0.007)
s9005BTM35	8.5	0.10	0.54 (0.021)	7	0.15	0.15 (0.006)
s9005BTM25	5	0.05	0.98 (0.039)	5.5	0.2	0.31 (0.012)
s9005BTM24	6	0.08	0.19 (0.007)	5	0.15	0.22 (0.009)
s9005BTM23	4.5	0.10	0.41 (0.016)	4	0.15	0.68 (0.027)

Approximately the same number of cracks formed both inside and outside the constant moment region. As would be expected, the total number of cracks for each specimen decreased as the area of steel reinforcement decreased. This is a result of a hinge forming earlier in the lightly reinforced specimens, thus preventing the formation of additional cracks along the strip.

The first crack inside and outside of the constant moment region formed by the second (0.10 inches) and third (0.20 inches) deflection steps respectively. Generally, the critical crack was not one of the first cracks formed. As the area of steel reinforcement decreased, the formation of the critical crack occurred at an earlier deflection step.

Once the critical crack became obvious, the growth of the majority of the non-critical cracks slowed or stopped completely. No trend was observed in the width of non-critical cracks as shown by the variation in the crack widths reported in Table 24. The majority of the crack width growth for specimen S9005BTM24 occurred in the critical crack as demonstrated by an average constant moment region crack width of 0.19 mm. When the area of steel was smaller, the crack width growth was better distributed among the average number of cracks inside the constant moment region with an average width of 0.41 mm.

The majority of cracks extended vertically with slight horizontal progressions at locations of steel fibers and coarse aggregates. Branching of cracks was also observed near these locations. “Accessory” cracks commonly formed adjacent to primary cracks. These cracks formed within a fiber’s length horizontally from the primary crack, and rarely extended to the bottom of the specimen. Figure 75 shows the horizontal behavior of cracks with respect to the steel fibers and coarse aggregates. Figure 76 demonstrates the crack mapping at the conclusion of each test.

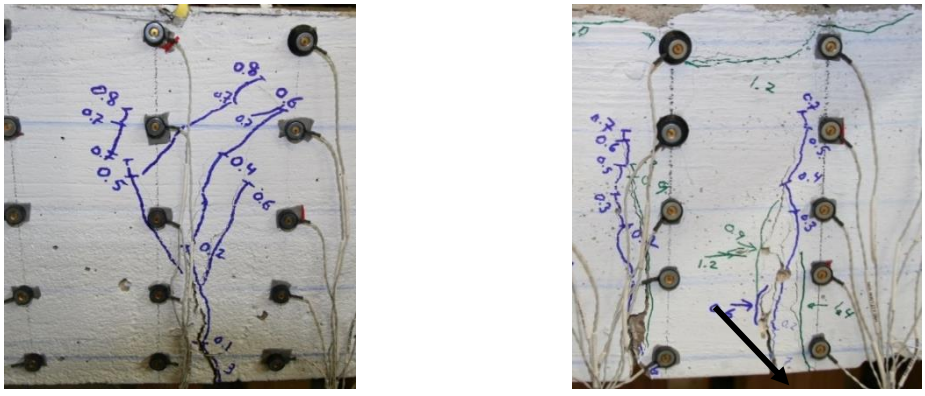

(a) (b)

Figure 75. SFRC Crack Behavior (a) Crack Branching - W3 S9005BTM25 and (b) "Accessory" Cracks - W7 S7505BTM35

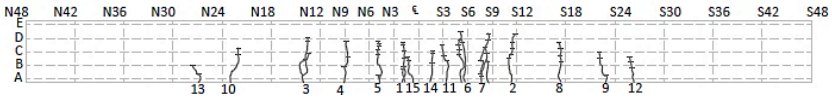

(a) West Face S7505BTM35

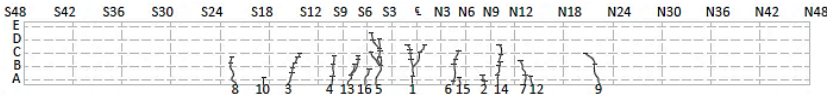

(b) East Face S7505BTM35

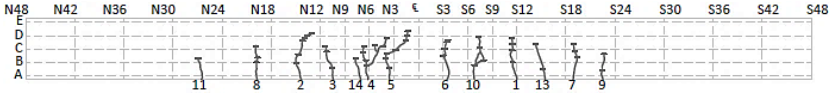

(c) West Face S7505BTM25

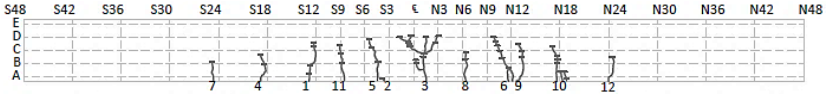

(d) East Face S7505BTM25

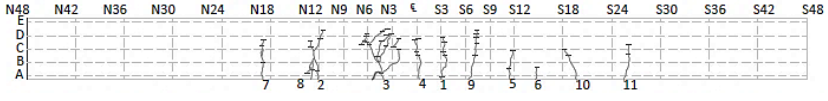

(e) West Face S7505BTM24

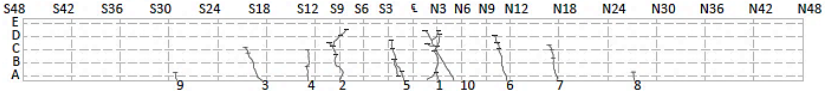

(f) East Face S7505BTM24

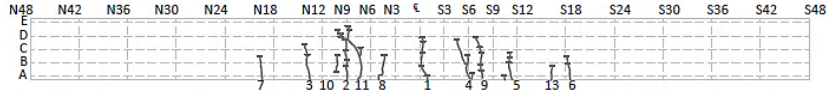

(g) West Face S7505BTM23

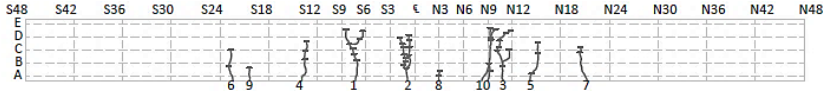

(h) East Face S7505BTM23

Figure 76. Crack Maps for Slab Strips 7.5 in Deep with Steel at Bottom

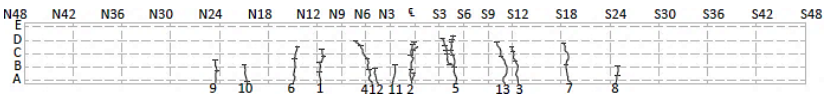

(a) West Face S9005BTM35

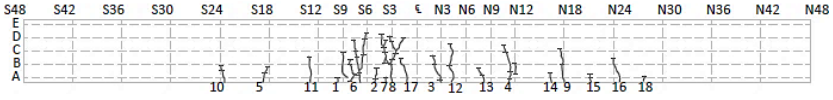

(b) East Face S9005BTM35

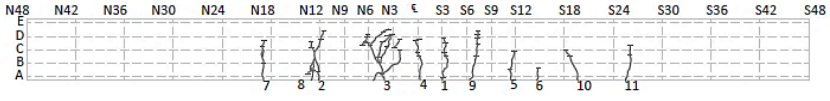

(c) West Face S9005BTM25

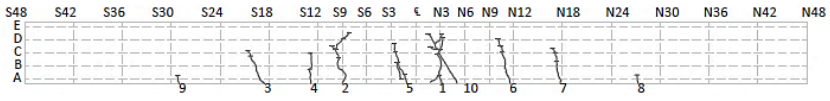

(d) East Face S9005BTM25

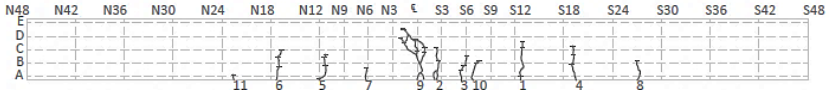

(e) West Face S9005BTM24

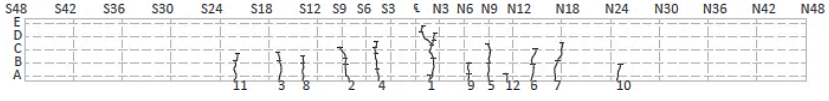

(f) East Face S9005BTM24

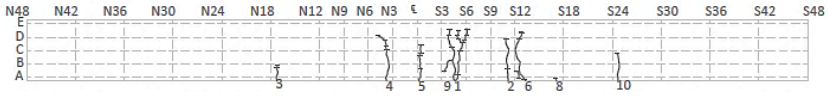

(g) West Face S9005BTM23

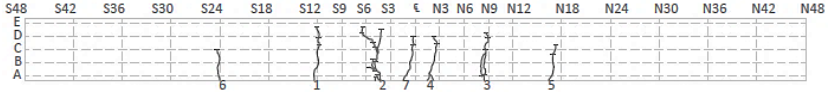

(h) East Face S9005BTM23

Figure 77. Crack Maps for Slab Strips 9.0 in Deep with Steel at Bottom

As each test progressed and the damage became more severe, steel fibers were visible bridging widening cracks. Steel fibers located near the surface of the specimen often resulted in spalling of the concrete. Fibers with sufficient coverage resulted in anchorage failure and the straightening of the hooked ends of the fiber. Figure 78 shows the failure of steel fibers. The fibers delayed or prevented the spalling of sizable pieces of concrete.

(a) (b)

Figure 78. Steel Fiber Failure (a) Spalling at Surface of Concrete - E2 S9005BTM23 (b) Steel Fiber Anchorage Failure

RILEM (2002) and fib (2013) classify failure as a maximum crack width of 2.5 mm. This criteria, along with crushing, was used in identifying failure of the tests. Failure is also commonly defined as crushing observed in the top section of the specimen. Table 25 demonstrates the crack characteristics associated with these two failure definitions.

The failure plane for every specimen with steel reinforcement at the bottom formed within 6 inches of the centerline of the specimen, except S7505BTM23 where the failure plane formed near the north loading point. The displacement step reported in Table 25 for the first observation of the critical crack is an average of the east and west faces. The deflection step when the critical crack first formed is inconsistent amongst the slab specimens. However, the

first observation of the maximum crack width occurred at earlier deflection steps for specimens with less steel reinforcement.

The thinner slab specimens, s7505-, exhibited crushing at a consistent displacement of 1.0 inch. Concrete crushing for the thicker specimens was not consistent, ranging from displacements of 0.6 to 0.9 inches. For each specimen the compression region above the critical crack was the first area to exhibit crushing. However, the crushed region extended horizontally as much as 18 inches. The specimens with a smaller area of steel reinforcement also had a smaller region of crushed concrete. Figure 80 and Figure 81 shows the condition of each slab-strip specimen with steel located at the bottom at a deflection of 1.2 inches. Crushing had already begun at this deflection step.

Table 25. Properties of Failure Criteria for Specimens with Steel Reinforcement Located at Bottom

	Critical Crack				Concrete Crushing		
Specimen	**Location**	**Crack #**	**$\delta_{first\ obs}$ (in)**	**$\delta_{2.50}$ (in)**	**Location**	**$\delta_{first\ obs}$ (in)**	**Width (in)**
s7505BTM35	S3-S6	E5/W6	0.2	1.2	S3-S6	1.0	12
s7505BTM25	N3-℄	E3/W5	0.15	0.9	N3-℄	1.0	9
s7505BTM24	S3	E1/W7	0.35	1.2	S3	1.0	6
s7505BTM23	N9	E10/W11	0.38	0.8	N12-N9	0.8	4.5
s9005BTM35	S3-S6	E6/W5	0.20	0.9	N6-S12	0.7	18
s9005BTM25	N6-N3	E1/W3	0.08	0.7	N6-℄	0.9	6
s9005BTM24	N3-℄	E1/W9	0.13	0.8	N3-S3	0.6	6
s9005BTM23	S3-S6	E2/W1	0.10	0.7	S3-S9	0.8	6

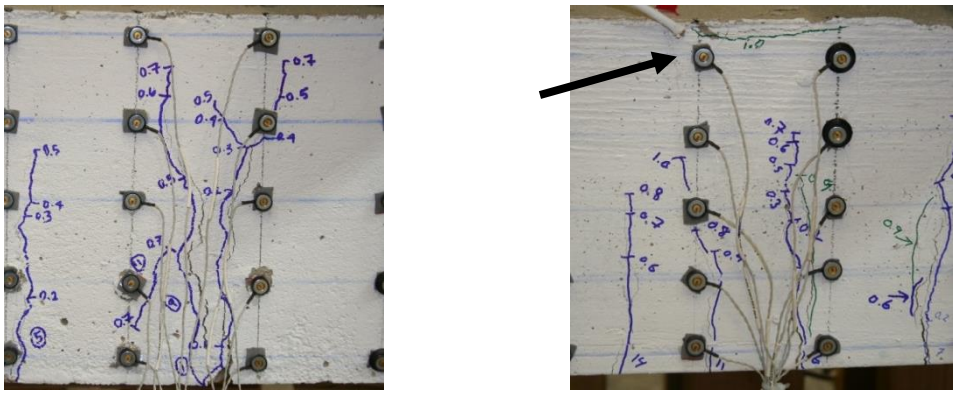

(a) S9005BTM23 (b) S7505BTM35

Figure 79. General Condition at Failure Criteria (a) Crack Width Greater than 2.5 mm S9005BTM23 and (b) Onset of Crushing S7505BTM35

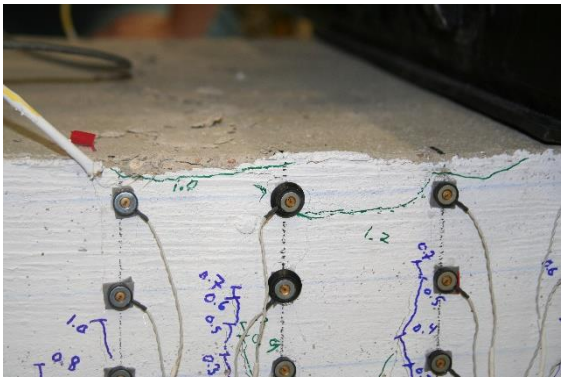

(a) s7505BTM35

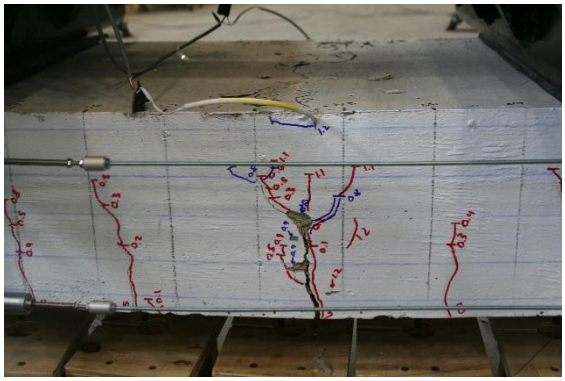

(b) s7505BTM25

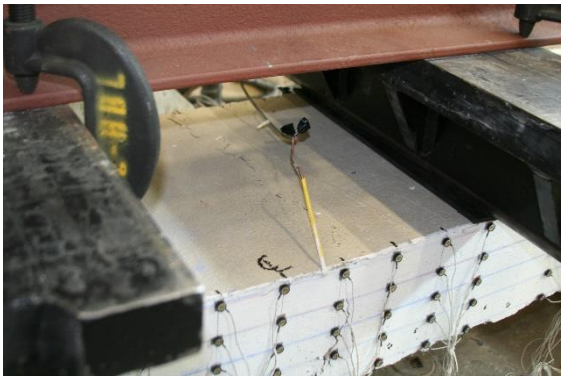

(c) s7505BTM24

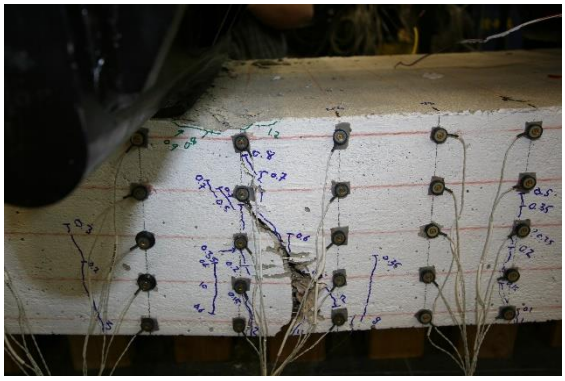

(d) s7505BTM23

Figure 80. Damage for Slab-Strip Specimens 7.5 in Deep with Steel at the Bottom at 1.2 in of Deflection

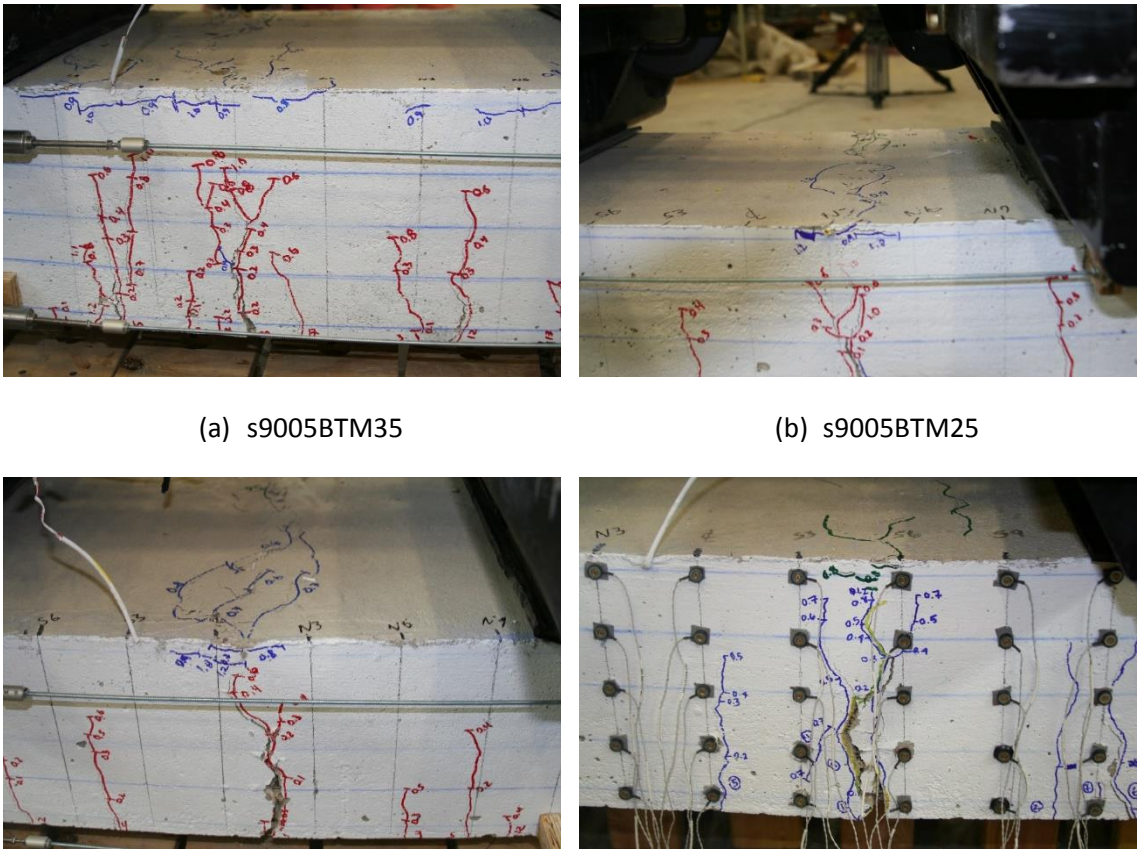

(a) s9005BTM35 (b) s9005BTM25

(c) s9005BTM24 (d) s9005BTM23

Figure 81. Damage for Slab-Strip Specimens 9.0 in Deep with Steel at the Bottom at 1.2 in of Deflection

4.6.1.2 Steel Reinforcement Located at Mid-Depth

The specimens with steel reinforcement located at mid-depth behaved in a manner similar to the specimens with steel located at the bottom. The number of cracks in the constant moment region matched the number of cracks outside the region. The total number of cracks also decreased with a decrease in the area of steel reinforcement. The average crack width did not adhere to any trend in regard to the locations of the crack, in or out of the constant moment region, nor the area of steel reinforcement in the specimen. The first observance of the critical crack width varied by one deflection step amongst the two tests. Table 26 and Table 27 display the properties of the non-critical cracks and failure criteria for these specimens. Figure 82 shows the crack maps at the completion of each test. Relocating the steel resulted in less overall cracks; however, the average crack widths were larger. The deflection step of the failure criteria was not influenced by relocating the steel.

Table 26. Properties of Non-Critical Cracks for Specimens with Steel Reinforcement Located at Center

	Inside Constant Moment Region			Outside Constant Moment Region		
Specimen	**# Of Cracks**	**$\delta_{first\ crack}$ (in)**	**Width (mm)**	**# Of Cracks**	**$\delta_{first\ crack}$ (in)**	**Width (mm)**
s7505CTR35	4	0.1	0.53 (0.021	6	0.15	0.29 (0.011)
s7505CTR25	3	0.13	0.70 (0.028)	3	0.15	0.95 (0.037)

Table 27. Properties of Failure Criteria for Specimens with Steel Reinforcement Located at Center

	Critical Crack				Concrete Crushing		
Specimen	**Location**	**Crack #**	**$\delta_{first\ obs}$ (in)**	**$\delta_{2.50}$ (in)**	**Location**	**$\delta_{first\ obs}$ (in)**	**Width (in)**
s7505CTR35	N6-N3	E5/W4	0.2	1	N12-℄	1.0	12
s7505CTR25	N12-N9	E1/W1	0.10	0.9	N12-N6	0.7	6

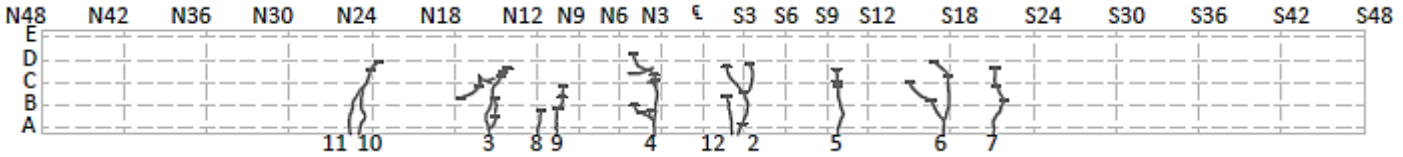

(a) West Face of S7505CTR35

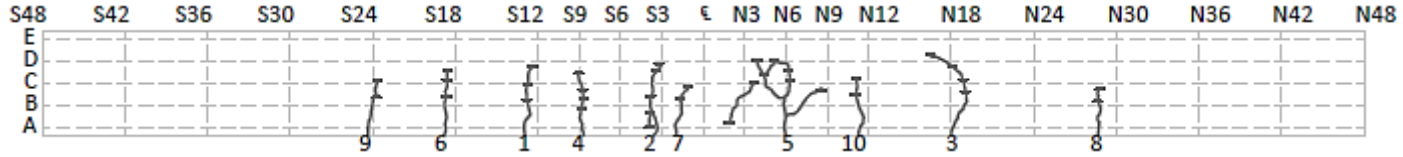

(b) East Face of S7505CTR35

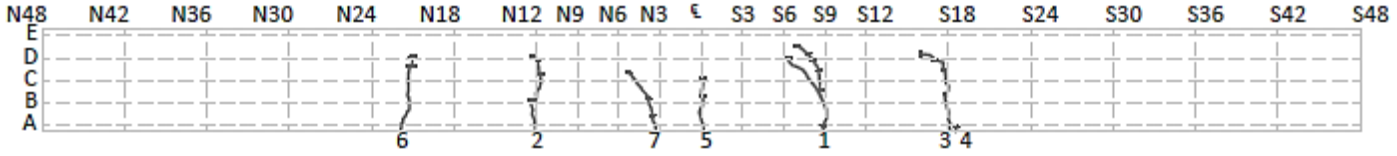

(c) West Face of S7505CTR25

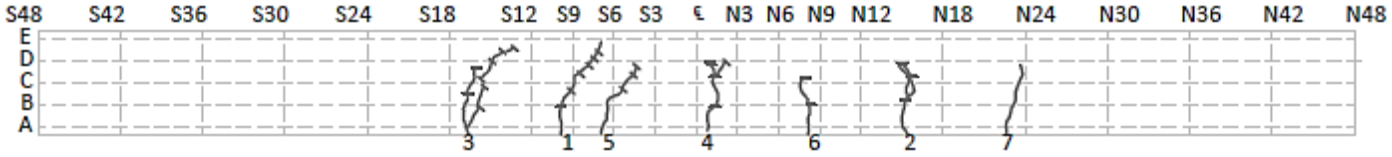

(d) East Face of S7505CTR25

Figure 82. Crack Maps for Slab strips with Steel at Center

4.6.1.3 No Steel

The specimens without steel reinforcement behaved significantly different in comparison to the specimens with steel reinforcement. Each specimen developed a single crack with “accessory” cracks adjacent to it as shown in Figure 83. The location of the primary crack varied significantly. In the deeper slab strips, the failure plane occurred directly beneath the loading point.

The slab strips achieved the maximum allowable crack width of 2.5 mm at a very small deflection step relative to the specimens with steel reinforcement. The specimen with a fiber dosage rate of 0.5 percent by volume and thickness of 7.5 inches exhibited the failure criteria by deflection step 0.3 inches (L/280). Increasing the fiber dosage rate to 2.0 percent by volume delayed the failure crack width by one deflection step to 0.4 inches (L/210).

The SFRC specimens with no steel exhibited crushing at approximately deflection step 0.8 inches (L/105), which is consistent with the deflection step for crushing in the specimens with steel reinforcement. Table 28 details the observance of the failure benchmarks for slab strip specimens without steel reinforcement.

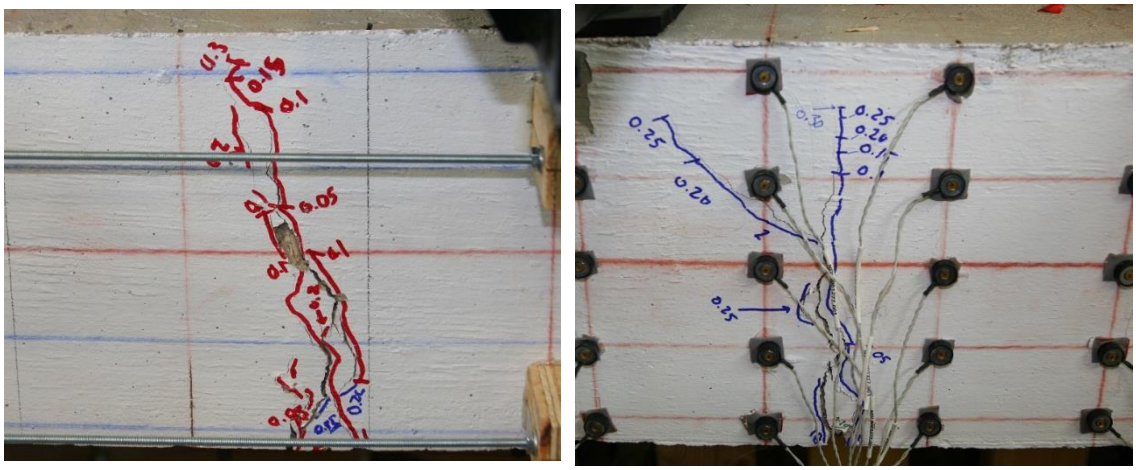

Figure 83. "Accessory" and Branching Cracks of Specimens without Steel Reinforcement S7505NOS00

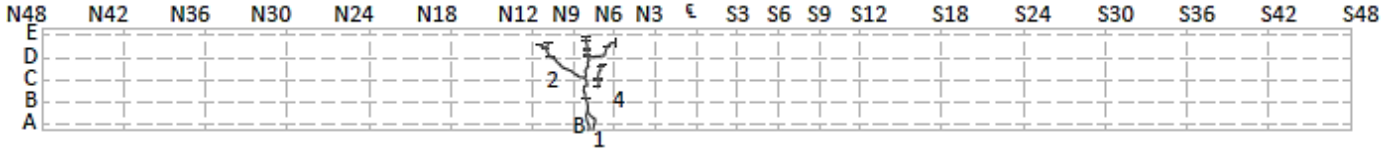

(a) West Face s7505NOS00

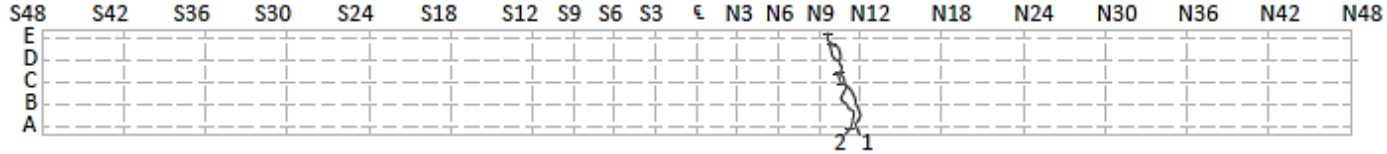

(b) East Face s7505NOS00

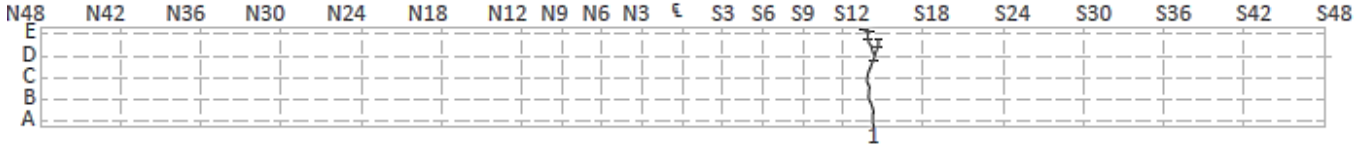

(c) West Face s9005NOS00

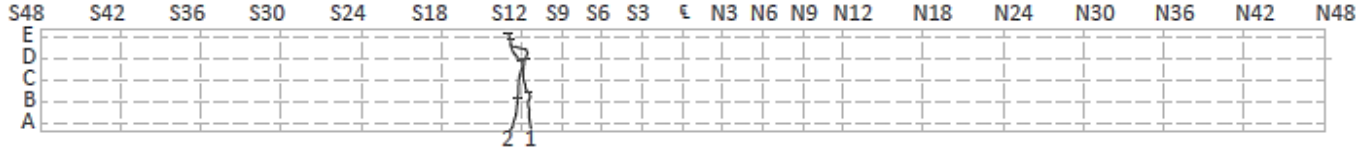

(d) East Face s9005NOS00

Figure 84. Crack Maps for Slab-Strip Specimens without Steel Reinforcement

Table 28. Properties of Failure Criteria for Specimens without Steel Reinforcement

	Critical Crack			Concrete Crushing		
Specimen	**Location**	**$\delta_{first\ obs}$ (in)**	**$\delta_{2.50}$ (in)**	**Location**	**$\delta_{first\ obs}$ (in)**	**Width (in)**
S7505NOS00	N12-N9	0.05	0.3	N12-N9	0.7	1.5
S7520NOS00	S6-S9	0.1	0.4	-	-	-
S9005NOS00	S12-S18	0.05	0.25	N12-N9	0.8	1.5
S9020NOS00	N12	-	-	-	-	-

4.6.2 Service and Capacity Moments

The test results were analyzed in three categories based on their thickness and steel reinforcement ratio: specimens 7.5 inches deep containing steel reinforcement, specimens 9.0 inches deep with steel reinforcement, and finally specimens of both heights without steel reinforcement. Where applicable, the specimen's performance was characterized by moment capacity at service and ultimate loads.

4.6.2.1 Specimens 7.5 Inches Deep with Steel Reinforcement

Figure 85 exhibits the force versus deflection behavior for 7.5 inch deep strips with steel reinforcement. The deflection is based on the readings of the string potentiometer at the center of the specimen. The string potentiometers were removed prior to the completion of the tests to protect them the collapse of the specimen. The end of the force versus deflection curves does not signify failure of the specimens.

The initial stiffness of each test was consistent among the specimens. Each specimen cracked at approximately the same centerline deflection, 0.04 inches, and applied force, 4.5 kips. Utilizing the ACI 318-11 definition for the modulus of rupture for concrete and elastic section analysis, the expected cracking load for the SFRC strips is 5.6 kips. The cracking load of the SFRC specimens was approximately 20 percent lower than the ACI prediction.

The post-crack stiffness of the specimens varied based on the amount and location of steel reinforcement. The specimen with the largest area of reinforcement (3-#5 bars) located near the bottom surface had the largest post-crack stiffness. The post-crack stiffness decreased for specimens with less steel reinforcement. Relocating the steel reinforcement to mid-depth of the specimen resulted in a large decrease in post-crack stiffness.

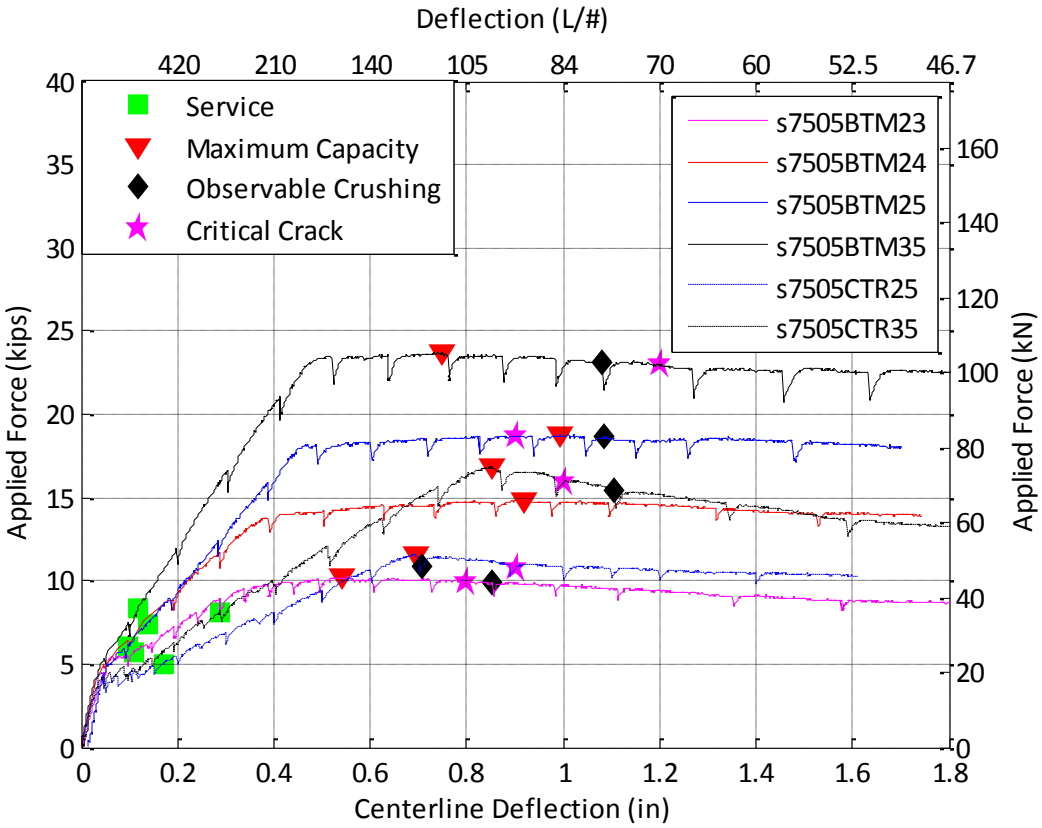

Figure 85. Force versus Deflection of 7.5 in Deep SFRC Slab Strips with Steel

The maximum allowable stress in the steel reinforcement for serviceability, 24 ksi, was achieved after each specimen cracked. The specimens with the steel reinforcement located at mid-depth achieved the largest deflection at this designation. Strip S7505CTR25 has the lowest service load of 5.0 kips while strip S7505BTM35 has the largest service load of 8.3 kips. Relocating the steel reinforcement to the middle, S7505CTR35, decreases the service load to 8.1 kips; however, the specimen with one less steel bar, S7505BTM25, resulted in an even lower service load of 7.4 kips. Table 29 summarizes the service performance of the 7.5 inch deep SFRC slab strips.

Table 29. Summary of S7505 Experimental SFRC Service Capacity

Specimen	Deflection (inch)	Force (kip)	Moment (k-ft)
s7505BTM23	0.11	5.7	7.1
s7505BTM24	0.1	6.2	7.7
s7505BTM25	0.15	7.4	9.3
s7505BTM35	0.12	8.3	10.4
s7505CTR25	0.17	5.0	6.3
s7505CTR35	0.3	8.2	10.2

A similar trend was observed in the maximum capacity of the SFRC strips. Strip S7505BTM35 has the largest capacity at approximately 24 kips and strip S7505BTM23 has the smallest capacity at approximately 10.2 k-ft. The maximum capacity of the specimens did not coordinate with the physical observance of crushing noted in Section 4.6.1. Additionally, the maximum capacity of each specimen occurred at variable deflections. Strip S7505BTM23 achieved its maximum capacity the earliest at a deflection of 0.55 inches while strip S7505BTM25 achieved its maximum capacity the latest at a deflection of 0.99 inches. Table 30 summarizes the maximum capacity of the 7.5 inch deep SFRC slab strips.

Table 30. Summary of S7505 Experimental SFRC Maximum Capacity

Specimen	Deflection (inch)	Force (kip)	Moment (k-ft)
s7505BTM23	0.55	10.2	12.8
s7505BTM24	0.92	14.9	18.59
s7505BTM25	0.99	18.8	23.5
s7505BTM35	0.75	23.7	29.67
s7505CTR25	0.69	11.6	14.48
s7505CTR35	0.85	16.9	21.12

4.6.2.2 Specimens 9.0 Inches Deep with Steel Reinforcement

Figure 86 shows the force versus deflection behavior for each 9.0 inch deep specimen with steel reinforcement. The deeper beams with steel reinforcement exhibited the same trends as

observed in the thinner 7.5 inches deep specimens. The deflection is based on the readings of the string potentiometer at the center of the specimen.

The initial and post-crack stiffness of the 9.0 inch deep specimens was similar to the thinner specimens. The initial stiffness of each test was consistent among the specimens while the post-crack stiffness decreased with a decrease in the area of steel reinforcement. Each specimen cracked at approximately the same centerline deflection, 0.035 inches, and applied force, 6.5 kips. The expected cracking load for plain concrete strips with the same dimensions as the tested specimen is 8.15 kips. Similar to the thinner specimens, the 9.0 inch deep specimens cracked at approximately 20 percent of the ACI prediction.

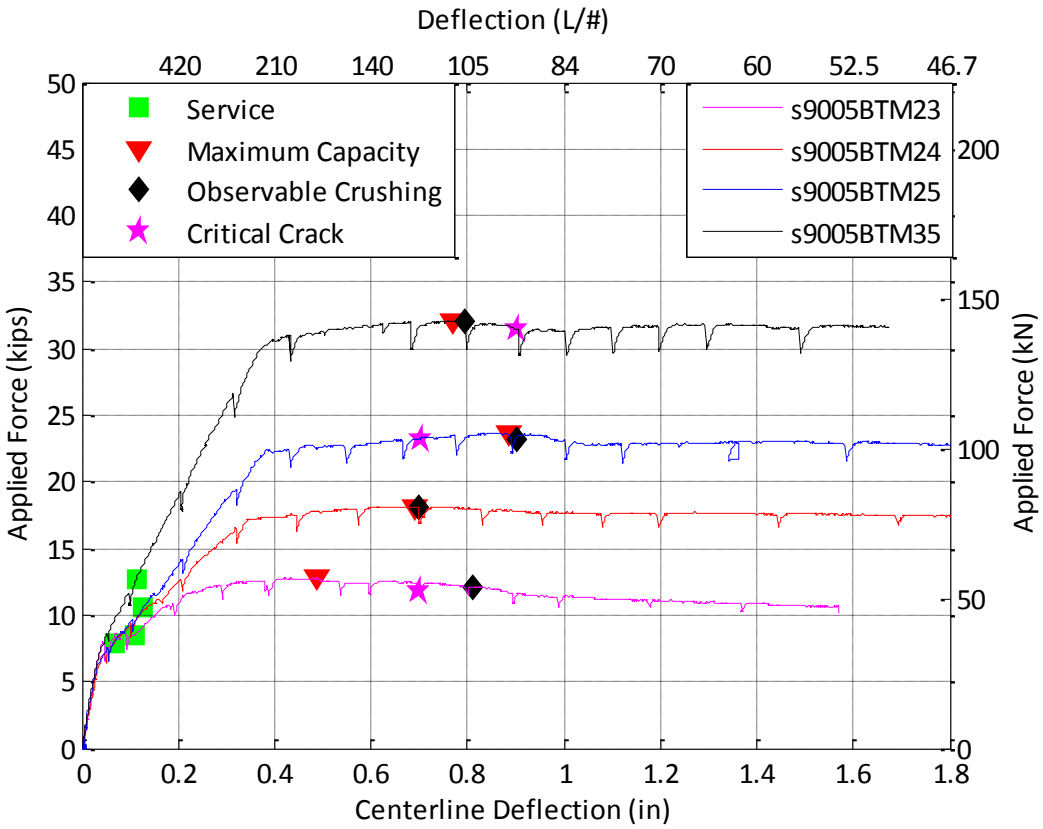

Figure 86. Force vs Deflection for Specimens 9.0 inches Deep with Steel Reinforcement

The maximum allowable stress in the steel reinforcement for serviceability, 24 ksi, was achieved after each specimen cracked. The service stress occurred between deflections 0.07 inches and 0.13 inches. The service capacity was larger in specimens with a larger area of steel reinforcement with the exception of specimen S9005BTM24. The service capacity ranged from 8.5 kips (S9005BTM23) to 12.7 kips (S9005BTM35). Table 31 summarizes the service performance of the 9.0 inch deep slab strip specimens.

Table 31. Summary of S9005 Experimental Service Capacity

Specimen	Deflection (in)	Force (kips)	Moment (k-ft)
s9005BTM23	0.12	8.4	10.6
s9005BTM24	0.07	7.9	9.9
s9005BTM25	0.13	10.6	13.3
s9005BTM35	0.11	12.7	15.9

Strip S9005BTM35 had the largest capacity at approximately 32.0 kips and strip S9005BTM23 had the smallest capacity at approximately 12.8 kips. Unlike the thinner specimens, the maximum capacity of several of the 9.0 inch deep specimens corresponded with the physical observed of crushing noted in Section 4.6.1. The deflection at the maximum capacity was larger in the specimens with a larger area of steel except for strip S9005BTM35. Table 32 summarizes the maximum capacity of the 9.0 inch deep slab strip specimens.

Table 32. Summary of S9005 Experimental Maximum Capacity

Specimen	Deflection (in)	Force (kips)	Moment (k-ft)
s9005BTM23	0.50	12.8	16.1
s9005BTM24	0.69	18.2	22.7
s9005BTM25	0.88	23.7	29.6
s9005BTM35	0.77	32.1	40.1

4.6.2.3 Specimens Without Steel Reinforcement

Figure 87 shows the force versus deflection behavior for each specimen without steel reinforcement. The service limit state is determined based on a steel stress and therefore excluded in the analysis of these sections. The deflection utilized in the figure is the reading of the string potentiometer at the center of the specimen.

The specimens with a fiber dosage volume of 0.5% reached maximum capacity at the cracking moment. During the beginning of test S9005NOS00, the DAQ was erroneously set to record data every five minutes rather than every second. As a result, the true maximum load was not captured by the recorder. When the error was noticed, a screen capture of the DAQ system was taken to capture the data in the system's buffer as shown in Figure 88. The cracking and maximum capacity of the 7.0 and 9.0 inch deep specimens correspond to the cracking load determined in the sections with steel reinforcement, 4.5 kips and 6.5 kips respectively.

The specimens with a fiber dosage volume of 2.0% gained capacity after the initial cracking of the specimen. The additional steel fibers increased the specimens' moment capacity to approximately 170% and 174% of the cracking load. The maximum capacities occurred at approximately the same deflection of 0.10 inches. The test results are summarized in Table 33.

Table 33. Summary of SFRC without Steel Reinforcement Experimental Results

Specimen	Deflection (inch)	Force (kips)	Moment (k-ft)
s7505nos00	0.04	4.6	5.7
s7520nos00	0.13	7.7	9.6
s9005nos00	0.06	4.5	5.6
s9020nos00	0.10	11.3	14.2

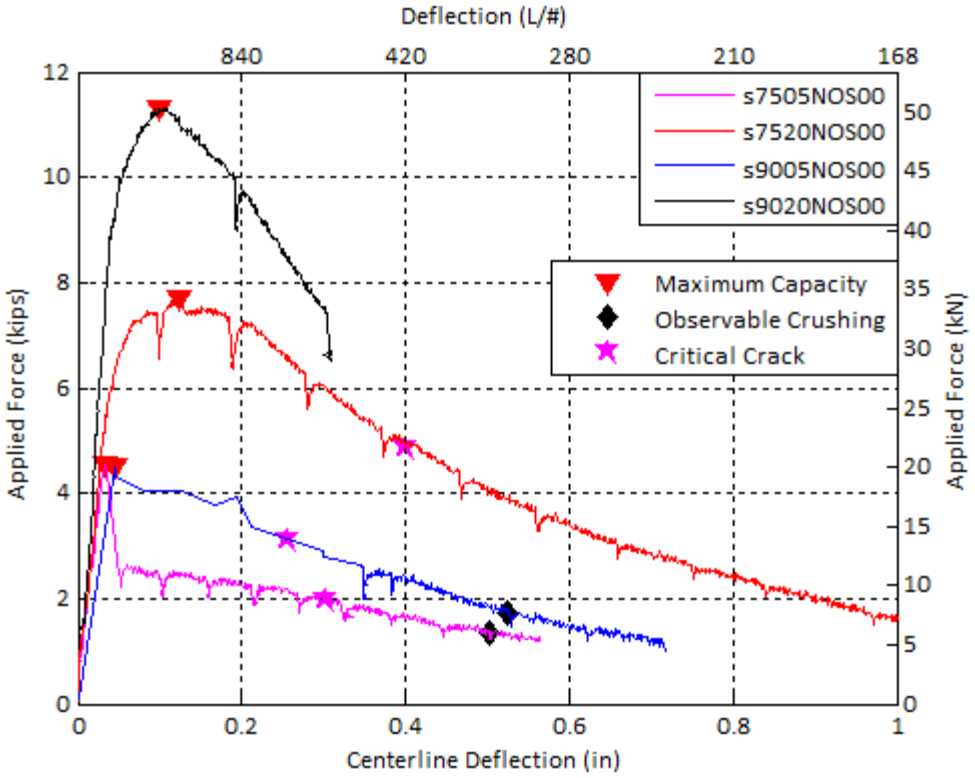

Figure 87. Force vs Deflection for SFRC Specimens without Steel Reinforcement

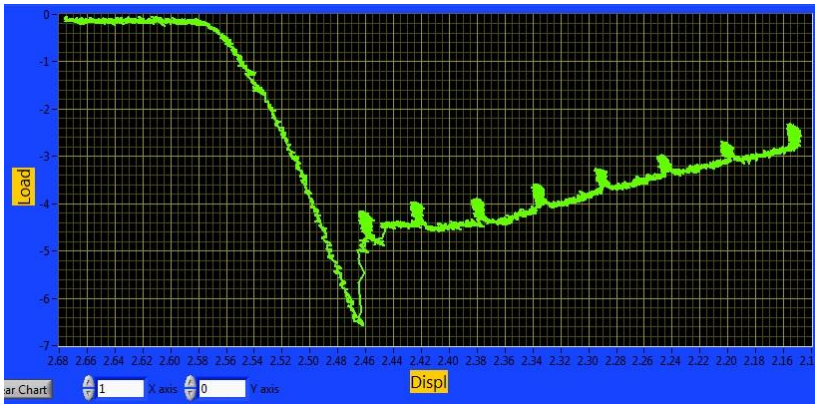

Figure 88. Screen Capture of DAQ During Testing of S9005NOS00

4.7 Discussion

The service capacity of the SFRC strips discussed in Section 4.6.2 corresponds to maximum allowable stress of 24 ksi. Section 4.7.1 examines the performance of the slab strips based on the maximum girder spacing permitted for each strip depth. This is achieved by determining the steel stress under the service limit state based on the experimental results. Section 4.7.2 expands this discussion by determining the maximum permitted girder spacing for each slab strip based only on the service and maximum capacities.

4.7.1 Service Limit State

The maximum girder spacing corresponding to a 7.5 inch deep deck is 7 ft according to the ADOT design requirements. The service demand for girder spacing of 7 ft is used to evaluate the performance of the 7.5 inch deep specimens. The stress in the steel reinforcement at this limit state was predicted for plain concrete using a moment-curvature analysis. The predicted steel stress for plain concrete specimens is compared to the SFRC experimental stress at the service limit state in Table 34. Figure 89 presents the results of Table 34 graphically. The steel stress at the service limit state is plotted for the SFRC tests and plain concrete to demonstrate the effect of adding steel fibers to plain concrete.

Table 34. Service Performance of S7505BTM## at Maximum Girder Spacing, 7 ft

Specimen	PC (Predicted)	SFRC (Experiment)	$\frac{SFRC_{EXP}}{PC_{PRED}}$
s7505BTM23	65	47	0.72
s7505BTM24	38	31	0.82
s7505BTM25	25	21	0.84
s7505BTM35	17	18	1.05
	= Satisfactory steel stress at service limit		

The traditional design for the strength limit state of girder spacing of 7 ft is a 7.5 inch deep plain concrete strip with 2-#5 bars. The service limit state is not satisfied by this steel ratio as the predicted stress in the steel reinforcement is 25 ksi. Specimen s7505BTM25 represents the traditional strength design with steel fibers. As observed from the test results, introducing steel fibers to the traditional strength design reduces the stress in the steel reinforcement to an acceptable 21 ksi. The SFRC strips with a steel reinforcement ratio below the traditional strength

design performed inadequately at the service limit state. Therefore, the service limit state will control the SFRC bridge deck design.

The service stresses presented shows that the benefit of SFRC in comparison to plain concrete diminishes as the area of steel reinforcement increases. The least reinforced SFRC specimen, s7505BTM23, has a steel stress 28% less than the predicted steel stress for a plain concrete strip with the same amount of steel reinforcement. The most reinforced SFRC specimen, s7505BTM35, has a steel stress 5% larger than plain concrete. As the section becomes more heavily reinforced, the steel reinforcement dominates the performance of the specimen. This trend can be observed by the vertical distance between the plain concrete and SFRC data points in Figure 89. The vertical distance between data points decreases until the service stress of the SFRC experiments converge with the predicted service stress of the plain concrete.

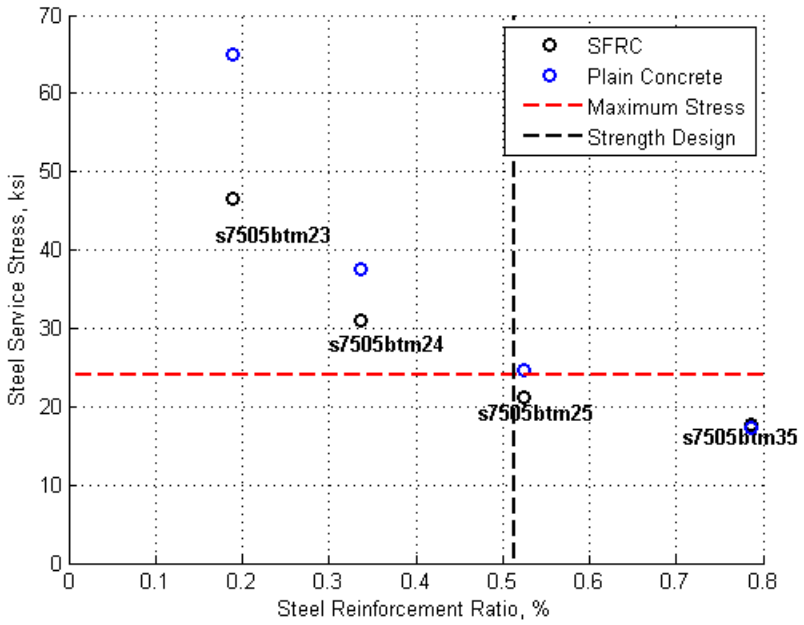

Figure 89. Service Performance of S7505BTM## at Maximum Girder Spacing, 7 ft

The maximum girder spacing corresponding to a 9.0 inch deep deck is 11.5 ft according to the ADOT design requirements. The service demand for girder spacing of 11.5 ft is used to evaluate the performance of the 9.0 inch deep specimens. The stress in the steel reinforcement at this

limit state was predicted for plain concrete using a moment-curvature analysis. The predicted steel stress for plain concrete specimens is compared to the SFRC experimental stress at the service limit state in Table 35. Figure 90 presents the results of Table 34 graphically. The steel stress at the service limit state is plotted for the SFRC tests and plain concrete to demonstrate the effect of adding steel fibers to plain concrete.

The thicker slab strips demonstrate the same trends observed in the 7.5 inch deep strips analyzed based on demands of the maximum allowable girder spacing. The addition of steel fibers to a traditionally strength designed plain concrete section improves the service performance and may satisfy the maximum service stress limit of 24 ksi. As demonstrated by Figure 90, the steel reinforcement ratio required for strength design with plain concrete falls between two of the experimental tests. Test s9005BTM25 does not satisfy the service requirement while s9005BTM35 does satisfy the requirement. Interpolating between the two tests results in a service stress of approximately 26 ksi for the traditional strength designed section with SFRC.

The vertical distance between the SFRC and PC data points in Figure 90 does not exhibit the same trend as the 7.5 inch deep slab specimens. The volume of fibers utilized in the experimental tests does not significantly affect the service stress of the slab strip specimens with the second to least amount of steel reinforcement, s9005BTM24, due to the larger service moment demand.

Table 35. Service Performance of S9005BTM## at Maximum Girder Spacing, 11.5 ft

Specimen	PC (Predicted)	SFRC (Experiment)	$\frac{\mathrm{SFRC_{EXP}}}{\mathrm{PC_{Pred}}}$
s9005BTM23	-	65	-
s9005BTM24	50	49	0.98
s9005BTM25	33	29	0.76
s9005BTM35	23	21	0.81
	= Satisfactory steel stress at service limit		

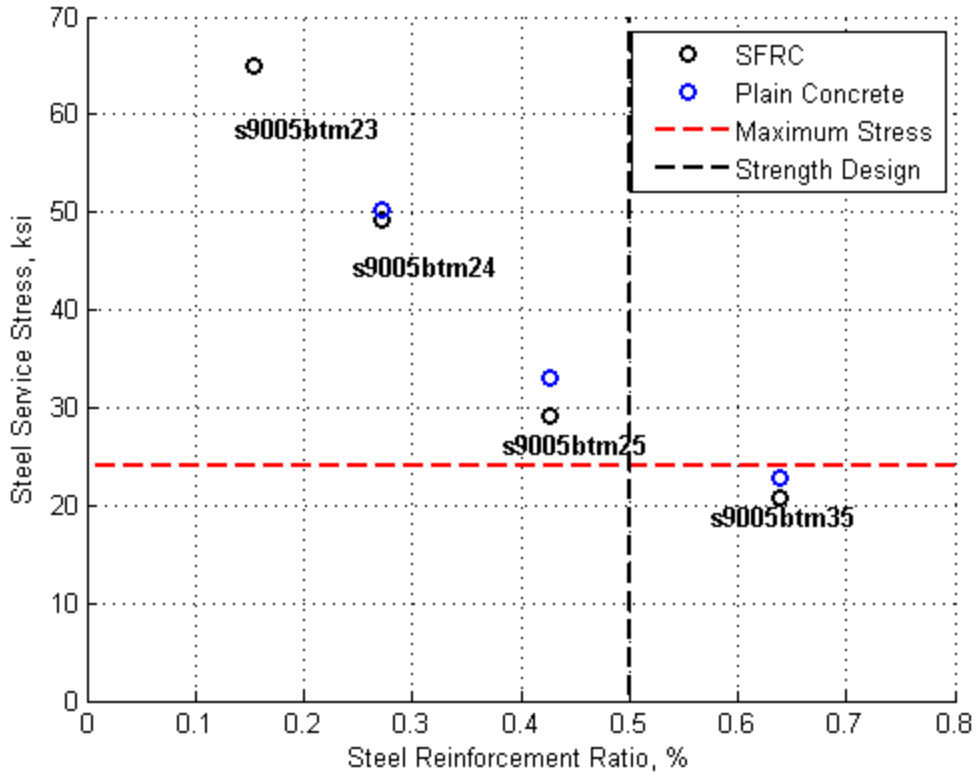

Figure 90. Service Performance of S9005BTM## at Maximum Girder Spacing, 11.5 ft

4.7.2 Maximum Girder Spacing Permitted

SFRC improves the performance of reinforced concrete bridges under both service and strength limit states. An analysis was conducted to determine the maximum permitted girder spacing for the slab-strip specimens. This was achieved by first calculating the service and strength moment demands for girder spacing between 4 ft and 15 ft based on ADOT design requirements. The moment corresponding to the steel service stress of 24 ksi was extracted from the SFRC experimental results. This moment is referred to as the service strength of the specimen. Additionally, the maximum capacity of the SFRC strips was extracted and is referred to as the ultimate strength of the specimen. The service strength and ultimate strength is then compared to the service and strength demands to determine the maximum permitted girder spacing for each specimen. Table 36 summarize the service and strength capacities of each strip SFRC specimen with steel reinforcement and Table 37 demonstrate the maximum allowable girder spacing.

Table 36. Service and Strength Capacities of Plain Concrete (PC) and SFRC

Specimen	Moment (k-ft)			
	Service		Strength	
	PC	SFRC	PC	SFRC
s7505BTM23	2.31	7.12	8.29	12.80
s7505BTM24	4.16	7.65	13.48	18.59
s7505BTM25	6.39	9.29	19.50	23.50
s7505BTM35	9.35	10.40	27.58	29.67
s7505CTR25	2.15	6.29	11.38	14.48
s7505CTR35	2.92	10.15	16.04	21.12
s9005BTM23	2.96	10.56	10.89	16.06
s9005BTM24	5.45	9.91	17.51	22.71
s9005BTM25	8.53	13.29	25.22	29.63
s9005BTM35	11.91	15.85	35.60	40.10

Table 37. Maximum Span Permitted for SFRC Slab strips

Specimen	Max Span (Nearest 0.25 ft)			
	Service		Strength	
	PC	SFRC	PC	SFRC
s7505BTM23	-	-	-	5.00
s7505BTM24	-	5.50	6.00	9.00
s7505BTM25	-	7.50	9.50	11.50
s7505BTM35	7.50	8.50	13.75	14.75
s7505CTR25	-	-	-	6.75
s7505CTR35	-	8.25	7.75	10.25
s9005BTM23	-	8.5	-	7.5
s9005BTM24	-	8	8.25	10.75
s9005BTM25	6.50	10.5	12.00	14.25
s9005BTM35	9.50	12.5	15+	15+

The addition of steel fibers at a rate of 0.5 percent by volume to the 7.5 inch deep slab strip sections increases the number of specimens with a maximum allowable girder spacing greater than 4.0 feet to four in comparison to one for a plain concrete section. The increase in capacity allows for the removal of 1-#5 from S7505BTM35 while still maintain sufficient strength to satisfy

the service requirements for a girder spacing of 7.50 feet. Alternatively, the maximum girder spacing can be increased to 8.50 feet without the removal of any steel from S7505BTM35.

The service moment demand controls the design of the specimen as demonstrated by Table 36. However, the benefits from SFRC are also presented for the ultimate strength capacity. Strip S7505BTM24 with SFRC allows for the maximum girder spacing to be increased by approximately 50 percent from 6.00 feet to 9.00 feet. The increase in ultimate strength capacity is not as great in more heavily reinforced sections. This is likely a result of the section trending toward the balanced steel reinforcement ratio. As the section becomes more compression controlled, the tensile benefits of SFRC are less significant.

According to the ADOT Bridge Design Guidelines, the maximum girder spacing for a plain concrete deck 9.0 inches deep is 11.50 feet. Only two plain concrete specimens with steel reinforcement ratios tested in the 9.0 inches deep SFRC strips provide sufficient capacity for a girder spacing greater than 4.0 feet.

The addition of steel fibers at a rate of 0.5 percent by volume to the 9.0 inch deep slab strip sections increases the number of specimens with a maximum allowable girder spacing greater than 4.0 feet to include all four tests in comparison to two satisfactory plain concrete sections. SFRC increases the capacity the maximum girder spacing for the service limit by 62 percent and 32 percent for S9005BTM25 and S9005BTM35 respectively.

Similar to the 7.5 inch deep sections, the service moment demand controls the design of the specimen. The ultimate capacity also demonstrates an increase with the addition of SFRC; however, the gains are not as significant as observed in the service moment capacities. The increase in the girder spacing for the ultimate limit state is only 19 percent for S9005BTM25 in comparison to its 62 percent increase in the maximum girder spacing for the service limit state.

Ultimately, a fiber dosage rate of 0.5 percent by volume is less influential at the ultimate limit state than the service limit state. However, the service limit state typically controls the design of reinforced concrete bridge decks. The addition of steel fibers would allow for the decrease in the area of steel reinforcement or the increase in girder spacing while still achieving adequate capacity at both the service and ultimate limit states.

4.8 Conclusion

The experimental program followed the philosophy of the case studies conducted in 3. The purpose of the SFRC slab-strip tests was to confirm the observations made in the case studies and investigate the effect of adding steel fibers to structural concrete members. The program offered insight on the damage progression and strength enhancement of SFRC. This was achieved by constructing 14 slab-strip specimens of two different thicknesses and a varying amount and location of steel reinforcement. The varied parameters allow for identification of the impact of

SFRC. Furthermore, the experimental results provide the capacity and service stress of the unit strips to be used in the large-scale bridge deck experiment. The following conclusions are made from the SFRC slab-strip experimental program:

- Steel fibers manage the width of cracks in the concrete prior to the failure criteria. Several cracks developed in the SFRC slab strips, but remained relatively small prior to the onset of crushing in the compression region of the strip and achievement of the specimen's maximum moment.
- The failure of SFRC strips localized in an individual crack. The fibers excel at bridging the cracks and delaying their growth. A hinge forms and the anchorage of the fibers begins to fail. All subsequent rotation and crack opening of the specimen occurs at critical crack.
- SFRC improves the performance of the slab strips under both the service and strength limit states.
- The effect of the steel fibers diminishes at higher ratios of steel reinforcement. The ratio between the residual force of the SFRC and the resultant force of the steel reinforcement decreases as the steel ratio increases. As a result, the influence from the SFRC is smaller.
- The service limit state controls the design of SFRC bridge decks. Adding fibers 0.5% by volume improves the service performance of a plain concrete section designed for the strength limit state. The improvement is sufficient to satisfy the service limit state as well.
- The moment-curvature analysis utilized in the case study analysis, 3, accurately predicts service and strength performance of the slab strips.
- The residual stress has to be determined through an inverse analysis as discussed by Mobasher (2012)

5. FULL SCALE BRIDGE DECK TEST

5.1 Introduction

A full-scale bridge deck was designed and constructed to fully investigate the benefits of adding steel fibers to the concrete matrix when used in a two-way slab. Additional slab strips were also tested to provide one-way bending capacities for the deck bridge deck. This Section details the experimental plan used to evaluate the full-scale specimen and analyze its moment capacity, deflection, cracking pattern, and failure mode. Section 5.2 provides information on the geometry and design philosophy of the bridge deck and companion beam specimens. Section 5.3 summarizes the material properties of the concrete, steel reinforcement, and steel fibers utilized in the experiment. The experimental results of the slab strips will be discussed in section 5.4 followed by the results of the bridge deck in Section 5.5. Finally, conclusions will be made regarding the results of each experiment in Section 5.6.

5.2 Specimens

The experimental program consists of a full-scale bridge deck and four accompanying slab strips. The geometry of the bridge deck was determined based on the constraints of the laboratory and similar tests conducted in the past. The geometry of the bridge deck is representative of the minimum requirements of the ADOT Bridge Design Guidelines (2012). The reinforcement ratio of the full-scale specimen was chosen to satisfy the ADOT requirements for serviceability and strength capacity. Section 5.2.1 details the design philosophy for the full-scale test. Section 5.2.2 details the additional slab strip specimens.

5.2.1 Full-Scale Bridge Deck Specimen

The full-scale specimen is a slab-beam bridge with two equal interior spans and an overhang on each side. The geometry and reinforcement details are shown in Figure 91. The specimen has a footprint of 16 ft (4877 mm) by 18 ft (5486 mm) and is supported by three traditionally reinforced concrete beams without steel fibers. The supporting beams are spaced at 6 ft (1829 mm) on center, and the overhangs are 2.5 ft (762 mm) from the outside face of the beams. The overall dimensions of the full-scale specimen were based on the limitations of the testing facility and previous experimental studies (Mander et al 2009 and Gar et. al 2014) that will serve as reference specimens for the evaluation of the SFRC bridge deck. The deck thickness and steel reinforcement was based on current ADOT design practices. The minimum deck thickness for a 6 ft spacing is 7.5 excluding a mandatory 0.5 inch wearing surface.

The deck is secured to each beam by stirrups spaced at 7.5 inches. The entire specimen was supported directly on the laboratory's strong floor to decouple the longitudinal bending of the support girders from the response of the bridge deck. Each reinforced concrete beam is secured

to the strong floor by three 1 inch threaded rods as shown in Figure 91. A PVC pipe was cast into the reinforced concrete support beams to allow for the installation of the threaded rods prior to the casting of the SFRC bridge deck.

The design of the SFRC bridge deck is based on findings of the tests presented in 0. A live load factor of 1.75 and impact load factor of 1.33 is applied to the moment demand obtained from AASHTO LRFD Section 4 - Appendix A (2014) to determine the moment demand for the strength limit state, 11.2 k-ft/ft. The strength demand and maximum allowable stress, 24 ksi, for the service limit state were utilized in selecting the steel reinforcement for the SFRC bridge deck. The ADOT design with traditional reinforced concrete required to satisfy the service stress is #5 bars at 6.5 inches in the negative moment region and #5 at 8 inches in the positive moment region. The steel reinforcement ratio for the traditional design in the negative moment region is 0.7%. Results from 0 indicate a lower percentage of traditional reinforcement is possible when 0.5% fiber by volume is used. Table 38 summarizes some results from the slab-strip tests. Specimen s7505BTM24 (#4 bar at 9 inches) provides the necessary service and strength performance and was selected for the design in the transverse direction of the SFRC bridge deck. The SFRC design provides a 53% reduction in the amount of traditional reinforcement.

Table 38. SFRC Slab Strip Results at Service and Strength States

	Reinforcement Ratio, ρ (%)	**$Moment_{Strength}$ (k-ft)**	**Service Stress (ksi)**
s7505BTM25	0.5	15.7	17.6
s7505BTM24	0.4	12.4	18.5
s7505BTM23	0.2	8.5	37.8

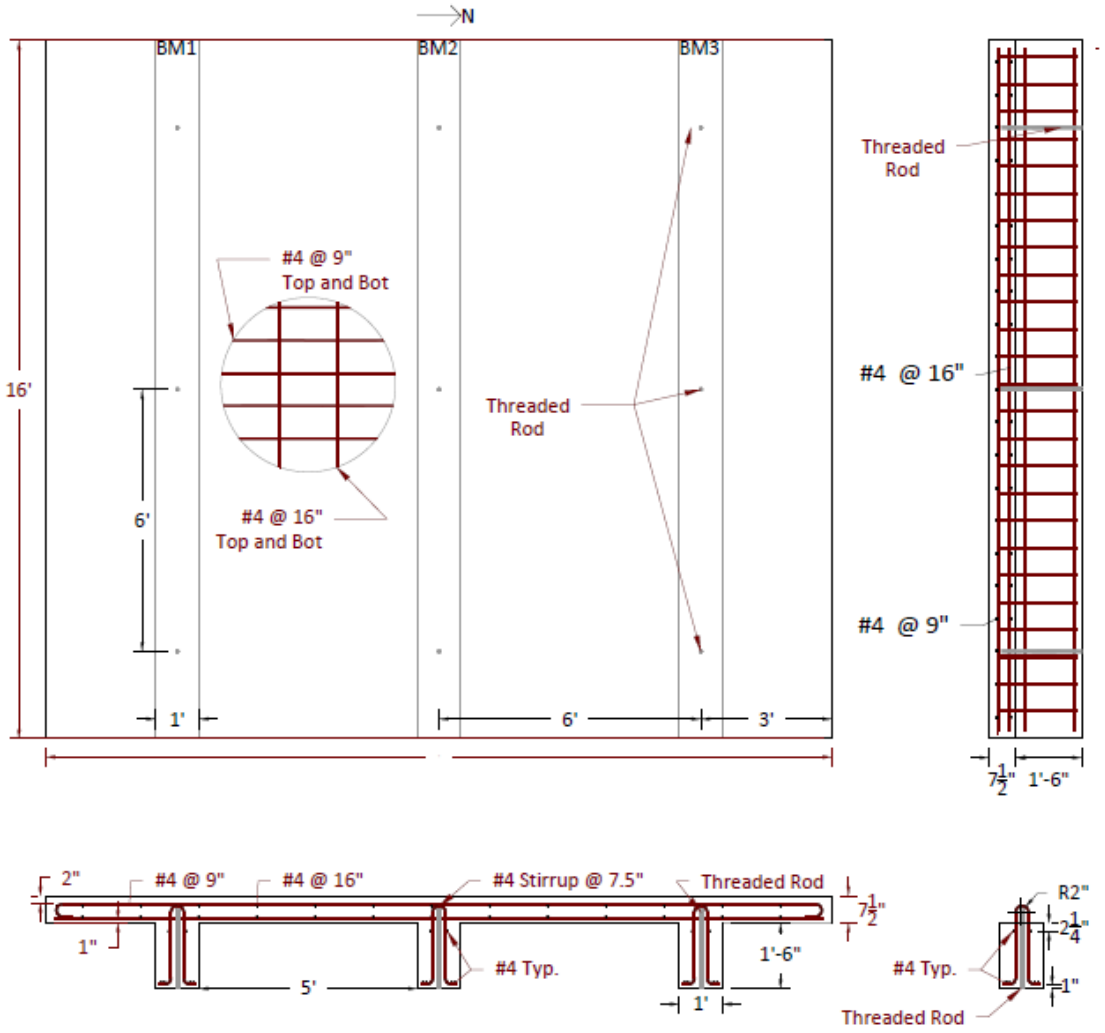

Figure 91. Full-Scale SFRC Bridge Deck Plan

5.2.2 Companion Beam Specimens

Slab strip specimens were cast alongside the SFRC bridge deck to predict the failure capacity of the SFRC bridge deck and to determine the repeatability of the original slab strip experimental program.

The test matrix of the companion beams is shown in Table 39. The naming scheme utilized for the companion beams, shown in Figure 92, is consistent with the scheme used for the slab strips tested with the exception that the companion beams are identified by the first letter, d. Two of the companion beams, d7505BTM24 and d7500BTM24, have the steel ratio utilized in the transverse direction for the bridge deck, a #4 bar spaced at 9 inches. Slab strip d7500BTM24 was cast alongside the bridge deck support beams with plain concrete to provide a direct comparison in strength and behavior to an equivalent specimen cast with SFRC. Section 5.3 discusses the characteristics of the plain and steel fiber reinforced concrete. Additionally, two SFRC specimens without traditional steel reinforcement were cast to provide a direct comparison of the SFRC behavior with the previous experimental program. Specimen d9005NOS00 was cast to supplement the data not recorded by the DAQ during the original experimental program.

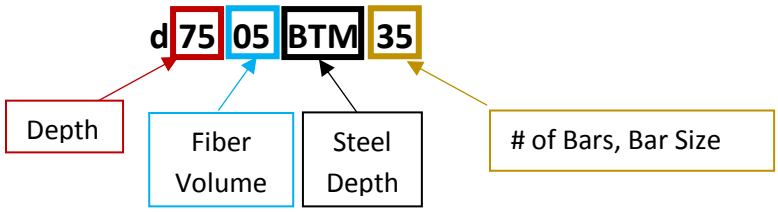

Figure 92. Naming Scheme

Table 39. Testing Matrix for Companion Beams

			Steel Reinforcement		
Specimen	**Concrete**	**Depth (in)**	**Size**	**Spacing (in)**	**ρ (%)**
d7500BTM24	PC	7.5	#4	9	0.57
d7505BTM24	SFRC	7.5	#4	9	0.57
d7505NOS00	SFRC	7.5	-	-	-
d9005NOS00	SFRC	9.0	-	-	-

5.3 Material Properties

The full-scale test program utilized the same concrete requirements as the slab strip test program. Texas Department of Transportation (TxDOT) "Class S" concrete, conventional steel reinforcement with a yield strength of 60 ksi, and Dramix® 3D hooked end fibers were used to design the full-scale bridge deck.

5.3.1 Steel Fiber Material Properties

The steel fibers utilized in the full-scale bridge deck experiment are consistent with the steel fibers used in the slab strip experimental program discussed in Section 3. The fiber has a length of 35 mm and a diameter of 0.55 mm. The aspect ratio, the ratio of length to the diameter, is 65. The fiber has a tensile strength of 1.345 N/mm^2 and modulus of elasticity of 210 N/mm^2.

5.3.2 Concrete Material Properties

Standard tests for compressive (ASTM C39) and flexural (ASTM C1609) strengths were conducted 28 days after the initial casting of the specimens. Direct tension tests were not conducted for the bridge deck experimental program. Plain concrete was utilized for the support beams and SFRC was used for the bridge deck. A total of three specimens were cast for each standard test and concrete type.

Table 40 summarizes the results of test ASTM39 for the SFRC and PC mixtures. Figure 93 and Figure 94 show the stress-strain relationships for the SFRC and PC mixtures. Inaccurate data following the linear elastic stress-strain response was recorded during the Sample 1 test for the PC and therefore excluded from the results.

The average modulus of elasticity for the two mixtures is consistent with each other. The SFRC had an average compressive strength of 6.6 ksi. The strength for the bridge deck is 1.5 ksi larger than the compressive strength of the SFRC used for the original slab strip program and 0.5 ksi stronger than the PC used for the supporting girders. The average results of all concrete mixtures utilized in the slab-strip and bridge deck test programs are summarized in Table 41.

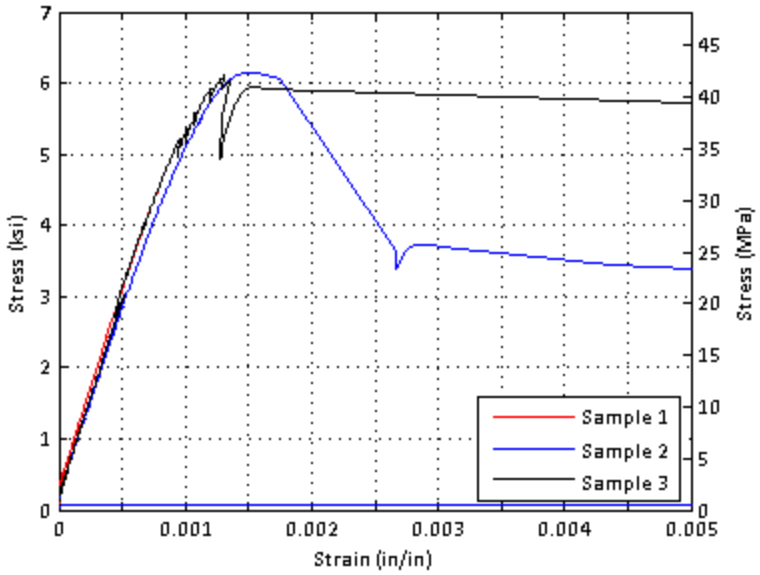

Figure 93. Stress-Strain from ASTM C439 – PC Tests Conducted at 28 Days

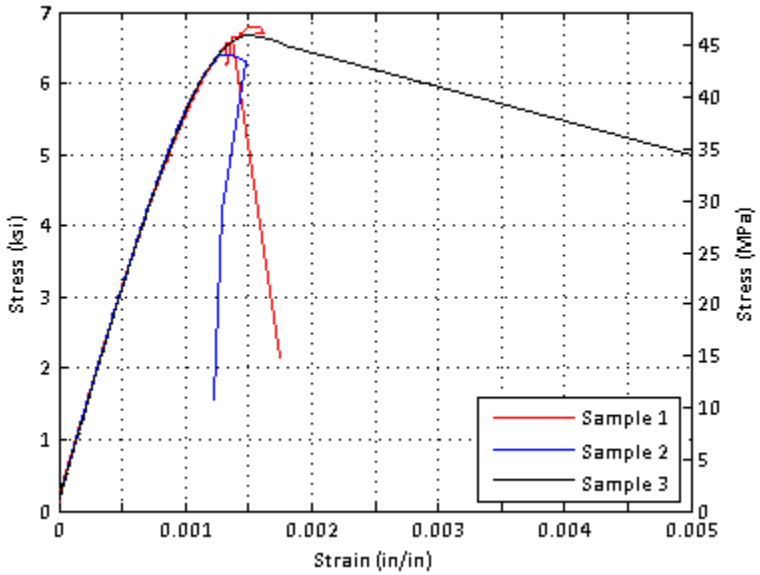

Figure 94. Stress-Strain from ASTM C469 – SFRC Tests Conducted at 28 Days

Table 40. ASTM C39 Test Results for Bridge Deck PC and SFRC

	Plain Concrete		Steel Fiber Reinforced Concrete	
	Modulus of Elasticity (ksi)	**Compressive Strength, f'c (ksi)**	**Modulus of Elasticity (ksi)**	**Compressive Strength, f'c (ksi)**
Sample 1	-	-	6006	6.8
Sample 2	6530	6.1	6017	6.4
Sample 3	5572	6.1	5917	6.7
Average	6051	6.1	5980	6.6

Table 41. Summary of Compression Test Results

Program	Modulus of Elasticity (ksi)	Compressive Strength, f'_c (ksi)
Plain Concrete	6051	6.1
Slab Strip	4027	5.1
Deck	5980	6.6

Figure 95 and Figure 96 show the results of flexure test ASTM C1609 for the PC and SFRC respectively. Table 42 and Table 43 summarize the flexural response of both the PC and SFRC mixtures. The PC specimens lose all tensile strength immediately after the formation of the first crack and fail abruptly. The SFRC specimens continue to have a tensile capacity following the formation of the first crack showing it's enhancement over the PC. The SFRC had a larger first peak stress and modulus of rupture than the PC which is consistent with the results of the compression tests.

The flexural response of both SFRC mixtures with 0.5% fibers by volume and the PC is summarized in Table 44. The SFRC mixture utilized for the bridge deck had a larger cracking stress and modulus of rupture consistent with its larger compressive strength in comparison to the SFRC used for the slab-strips. The SFRC used for the original slab-strip program had a larger post-crack response in comparison.

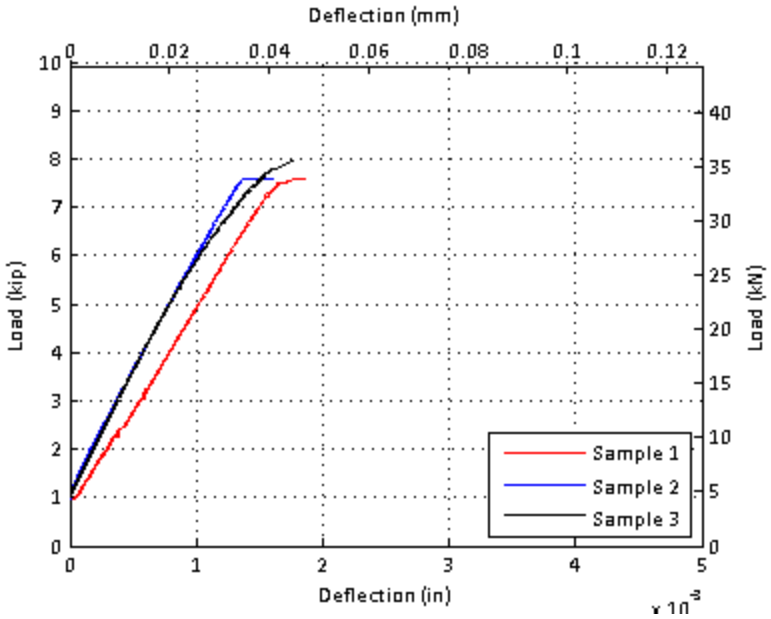

Figure 95. Load-Deflection Response of ASTM C99 – PC Tests Conducted at 28 Days

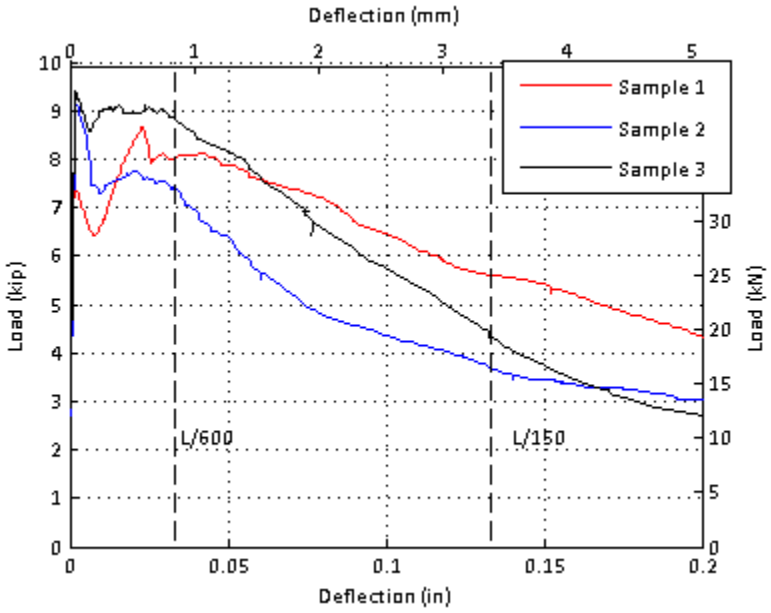

Figure 96. Load Deflection Response of ASTM C1609 - Tests Conducted at 28 Days

Table 42. ASTM C1609 Test Results for Bridge Deck PC

Sample #	P_1 (kips)	f_{cr} (ksi)	P_P (kips)	f_{MOR} (ksi)	P_{600} (kips)	$f_{r,600}$ (ksi)	P_{150} (kips)	$f_{r,150}$ (ksi)
1	7.6	0.70	7.9	0.70	-	-	-	-
2	7.5	0.69	7.5	0.69	-	-	-	-
3	7.9	0.73	7.9	0.73	-	-	-	-
Average	7.7	0.71	7.7	0.71	-	-	-	-

Table 43. ASTM C1609 Test Results for Bridge Deck SFRC

Sample #	P_1 (kips)	f_{cr} (ksi)	P_P (kips)	f_{MOR} (ksi)	P_{600} (kips)	$f_{r,600}$ (ksi)	P_{150} (kips)	$f_{r,150}$ (ksi)
1	8.7	0.81	8.7	0.81	8.0	0.74	5.7	0.53
2	9.2	0.85	9.2	0.85	7.6	0.70	3.7	0.34
3	9.4	0.87	9.4	0.87	8.7	0.81	4.3	0.40
Average	9.1	0.84	9.1	0.84	8.1	0.75	4.6	0.42

Table 44. ASTM C1609 - Average Flexural Tests Results

Program	P_1 (kips)	f_{cr} (ksi)	P_P (kips)	f_{MOR} (ksi)	P_{600} (kips)	$f_{r,600}$ (ksi)	P_{150} (kips)	$f_{r,150}$ (ksi)
PC	7.7	0.71	7.7	0.71	-	-	-	-
Slab Strip	5.1	0.48	7.9	0.73	7.7	0.72	5.9	0.54
Deck	9.1	0.84	9.1	0.84	8.1	0.75	4.6	0.42

5.3.3 Steel Reinforcement Material Properties

A total of four samples were tested for each steel reinforcement size. The tests were conducted in accordance with ASTM A370, “Standard Test Methods and Definitions for Mechanical Testing of Steel Products.” Elongation data was collected via three LVDT’s with a gage length of 8 inches. The results are show in Figure 97and Table 45.

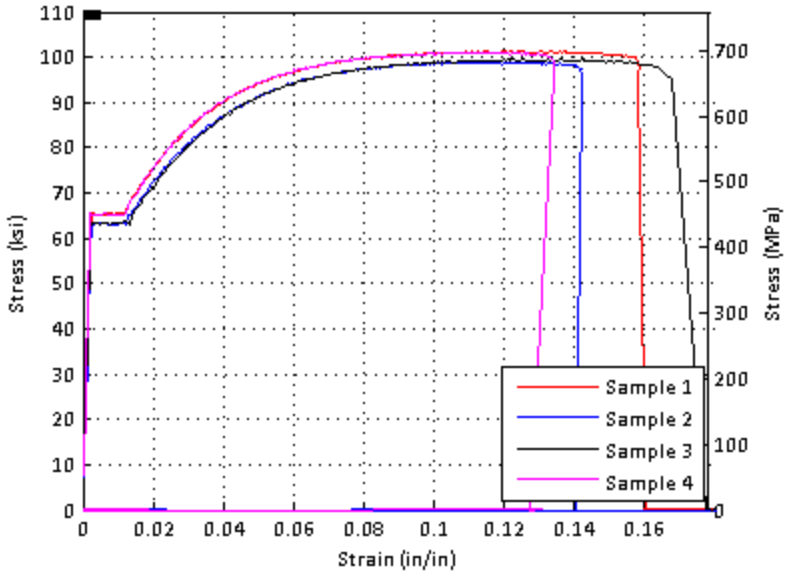

Figure 97. ASTM A370 Test For #4 Steel Reinforcement Bars

Table 45. Summary of Steel Reinforcement Properties

	Yield Stress, f_y (ksi)	Ultimate Stress, f_u (ksi)
Sample 1	65	101
Sample 2	63	99
Sample 3	63	99
Sample 4	65	101
Average	64	100

5.4 Companion Beam Test Results

5.4.1 Test Setup and Instrumentation

The test setup for the companion beams utilized the same configuration as the experimental program discussed in 0 with the exception of the gauge length of the LVDT. The gauge length was

reduced to 1 ft to better determine the strain and curvature profile at the center of the slab strip specimen.

Each companion beam was subjected to a four-point bending flexural tests as shown in Figure 98. A 100 kip (444 kN) actuator was used to load the companion beams to failure. String potentiometers located at 6 inch intervals recorded the deflection profile of each specimen to determine the curvature profile of the specimen. Strain gages were installed on the conventional steel reinforcing bars in each specimen.

Displacement control was utilized for the loading procedure of the specimen. The displacement was increased 0.05 in/min for each specimen. The test was paused at regular intervals to record the cracking damage to the specimen. After reaching a displacement of 1.2 inches, the load was increased until the specimen failed or the actuator achieved its maximum stroke.

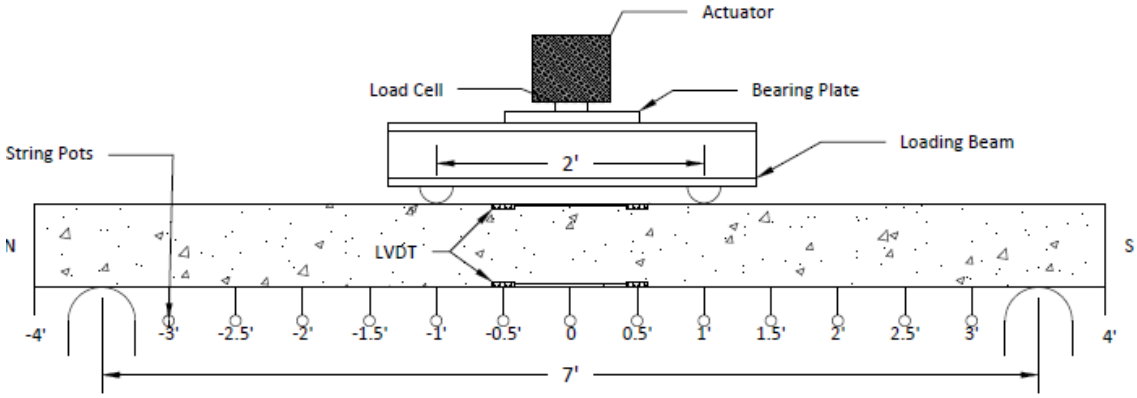

Figure 98. Companion Beam Test and Instrumentation Setup

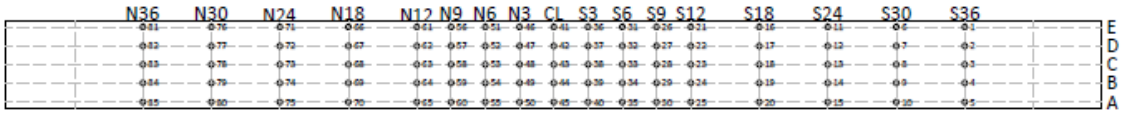

Figure 99. Opotrak Certus Grid Utilized for Test Program

5.4.2 Damage Profile

The damage incurred by each specimen was observed and compared in two groups based on their steel reinforcement layout: bottom or none at all. The damage recorded consisted of the number of cracks, when they formed, their location, width, and height. The data was analyzed to identify trends amongst the groups.

Throughout each experiment, the beams were examined for two failure criteria, the critical crack width and concrete crushing in the compression region. The critical crack width is defined by RILEM (2003) as 2.5 mm (0.1 inches). The failure progression for the SFRC and PC slab-strips behaved in different manners. Several cracks formed in the SFRC specimen with steel, d7505BTM24, prior to one of the cracks becoming critical. The failure localized in an individual crack where all future crack growth occurred. The plain concrete specimen developed fewer cracks and they all continued to grow throughout the entire test. Section 5.4.2 presents the extent of damage incurred by the SFRC and PC specimens with steel reinforcement, d7505BTM24 and d7500BTM24. Section 5.4.2.2 presents the extent of damage for the SFRC specimens without steel reinforcement, d7505NOS00 and d9005NOS00.

5.4.2.1 Reinforced Specimens

The behavior of the SFRC and PC specimen varied significantly. The SFRC specimen, d7505BTM24, developed a single critical crack on each face of the slab strip. The width of the critical crack continued to increase while all other cracks stopped growing at deflection step 0.5 inches. In contrast, every crack that formed in the PC specimen continued to grow. Table 24 summarizes the average properties of the cracks inside and outside the constant moment region. Figure 102 shows the final crack map for each slab strip specimen.

The same number of cracks formed inside and outside the constant moment region for the PC slab strip d7500BTM24. The same behavior occurred in the SFRC specimen. The SFRC specimen developed approximately 1.5 more cracks than its PC counterpart. The average crack width inside and outside the constant moment region is larger in the PC slab strip than the SFRC slab strip. The crack growth of the SFRC slab strip is averaged over a larger number of cracks. The majority of the crack growth for the SFRC specimen occurs in the critical crack that formed in the constant moment region. The SFRC specimen results in one large crack and approximately 9 small cracks while every crack in the PC specimen continues to grow throughout the test.

Table 46. Average Properties of Cracks at Maximum Capacity

	Inside Constant Moment Region			Outside Constant Moment Region		
Specimen	**# of Cracks**	**$\delta_{first\ crack}$ (in)**	**Width, mm (in)**	**# of Cracks**	**$\delta_{first\ crack}$ (in)**	**Width, mm (in)**
d7500BTM24	3	0.05	2.96 (0.116)	3.5	0.3	1.29 (0.051)
d7505BTM24	4.5	0.07	1.70 (0.067)	5	0.2	0.15 (0.006)

Figure 100 shows the average crack width measured on the east and west sides for the SFRC and PC strips for each displacement step. The average crack width of the PC beam is significantly larger than the SFRC specimen due to the number of cracks in each specimen as discussed above. The maximum crack width observed in the SFRC specimen is significantly larger than the PC slab strip as shown in Figure 101. At the beginning of the test, the cracks in the PC slab strip develop much quicker. At deflection step 0.8 inches, the failure localization of the SFRC slab strip resulted in maximum crack width greater than the cracks observed in the PC slab strip. Therefore, the addition of SFRC enhances the performance of the slab strip from a damage progression perspective until the failure localization of the SFRC occurs. This transition point is observed after the critical crack width defined by RILEM (2002) of 2.5 mm is achieved.

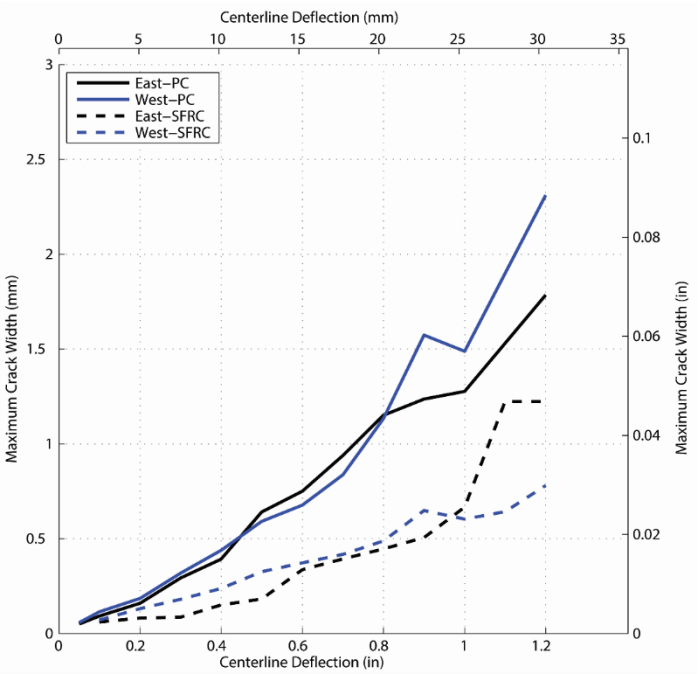

Figure 100. Average Crack Width vs Deflection for SFRC (d7505BTM24) and PC Slab (d7500BTM24) Strips

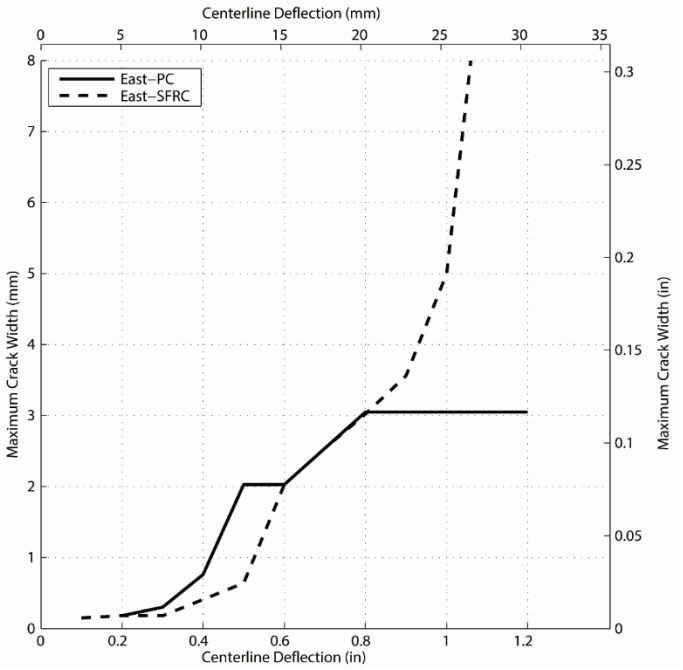

Figure 101. Maximum Crack Width vs Deflection for SFRC (d7505BTM24) and PC Slab (d7500BTM24) Strips

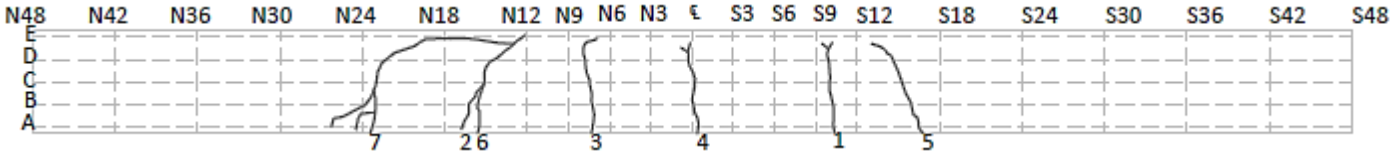

(a) West Face d7500BTM24

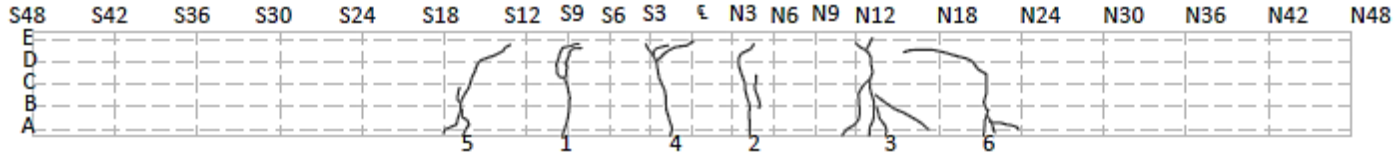

(b) East Face d7505BTM24

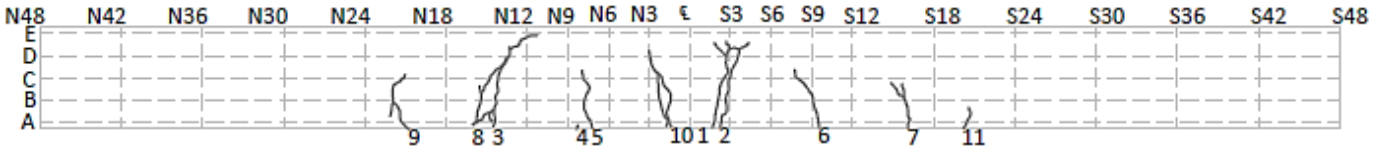

(c) West Face d7500BTM24

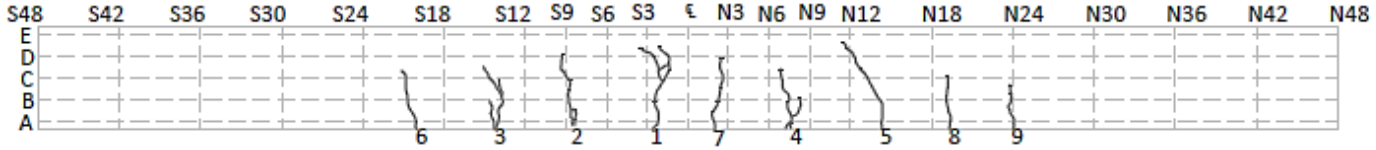

(d) West Face d7505BTM24

Figure 102. Crack Maps for Slab strips with Steel at Bottom

RILEM (2002) and fib (2013) classify failure as a maximum crack width of 2.5 mm. This criteria, along with crushing, was used in identifying failure of the tests. Table 25 demonstrates the damage properties associated with the failure criteria. Figure 103 through Figure 105 show the condition of the each strip at various deflection steps.

The critical crack for the PC slab strip is defined by the first crack to reach 2.5 mm; however, there was not a single critical crack. A total of four cracks on the east face (E1, E2, E3 and E4) and west face (W1, W3, W4, and W6) approached or exceeded the 2.5 mm limit. The critical crack width was achieved for the PC and SFRC specimens at the same deflection step of 0.7 inches.

Crushing was not observed until each specimen was largely deflected. The first observation of crushing on the SFRC slab strip, d7505BTM24, occurred a deflection of 1.6 inches. Conversely, slab strip s7505BTM24 investigated in the original slab strip program exhibited crushing at 1.0 inches.

Table 47. Properties of Failure Criteria for Specimens with Steel Reinforcement Located at Bottom

	Critical Crack				Concrete Crushing		
Specimen	**Location**	**#**	**$\delta_{first\ obs}$ (in)**	**$\delta_{2.50}$ (in)**	**Location**	**$\delta_{first\ obs}$ (in)**	**Width (in)**
d7500BTM24	℄/S12	E4/W5	0.2	0.7	S9 N3-N6	End	6
d7505BTM24	℄-S3	E1/W2	0.05	0.7	℄-S3	1.6	3

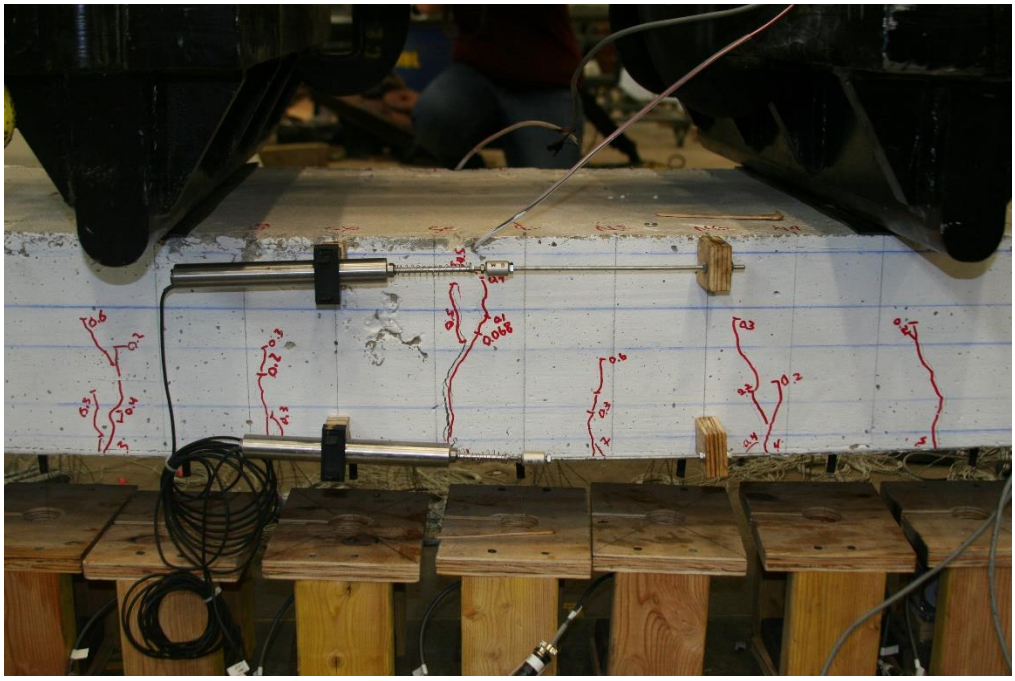

(a) d7505BTM24 – East (SFRC)

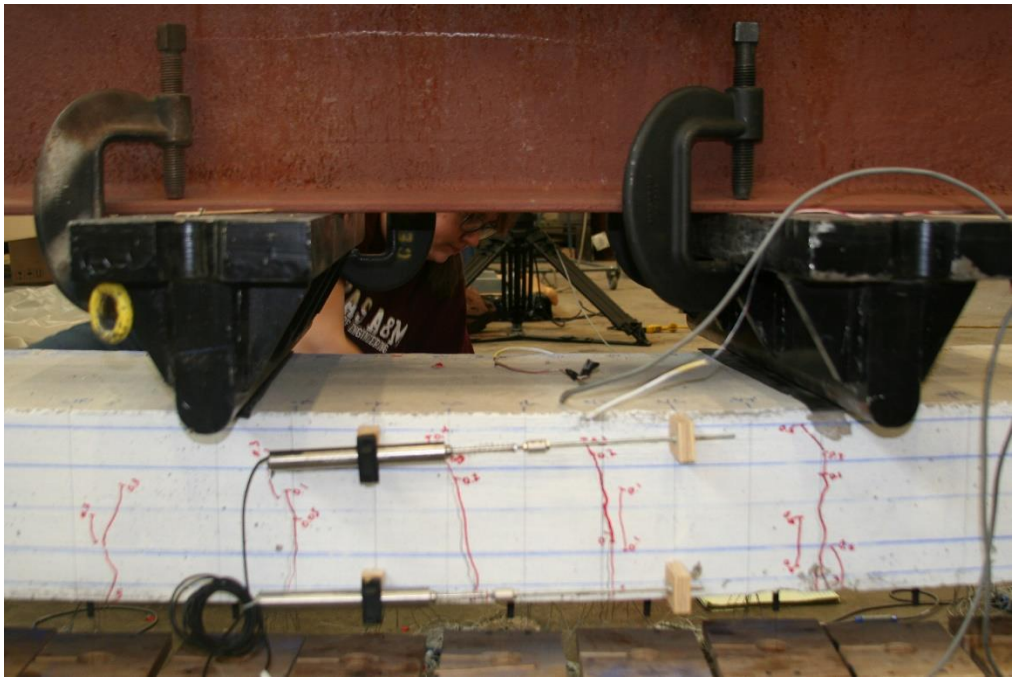

(b) d7500BTM24 (PC)

Figure 103. State of Damage for d7505BTM24 and d7500BTM24 at 0.6in of Deflection

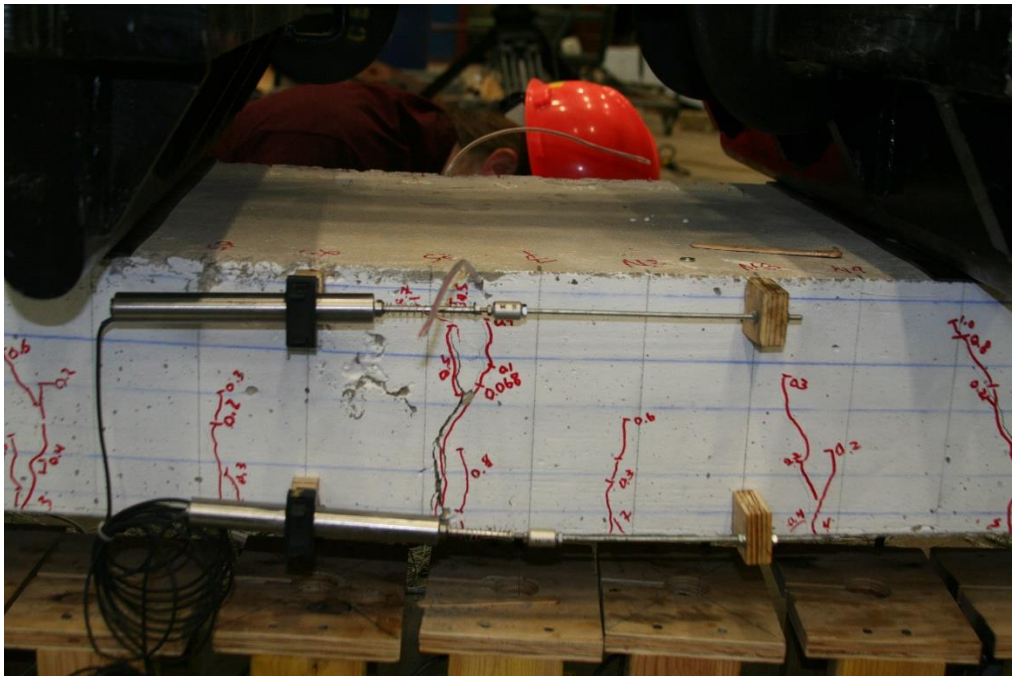

(c) d7505BTM24 – East (SFRC)

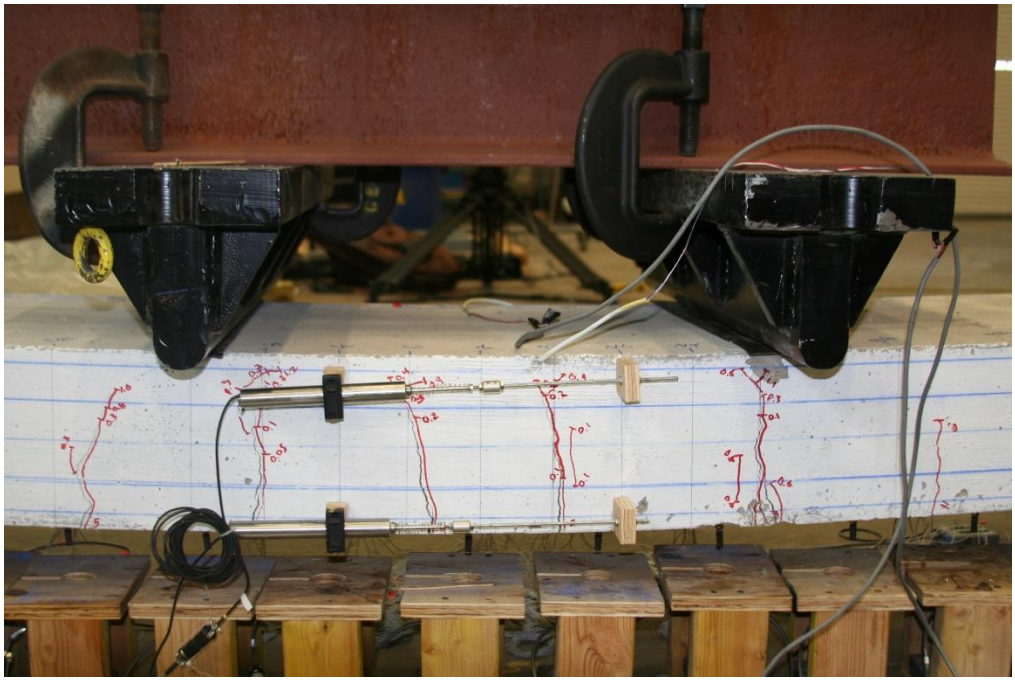

(d) d7500BTM24 – East (PC)

Figure 104. State of Damage for d7505BTM24 and d7500BTM24 at 1.2in of Deflection

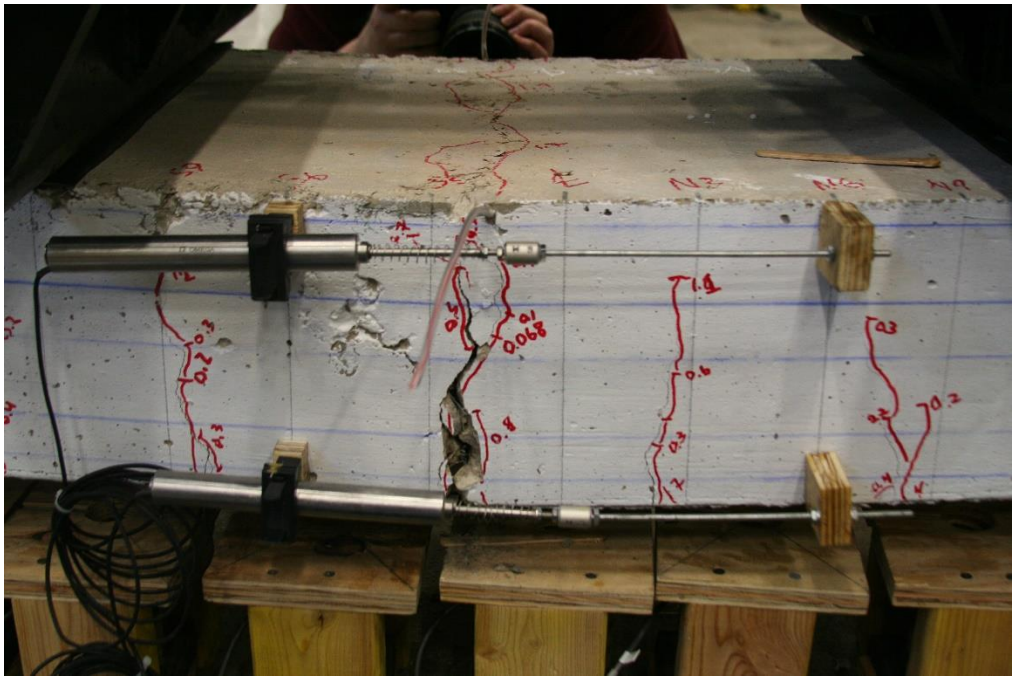

(a) d7505BTM24 – East (SFRC)

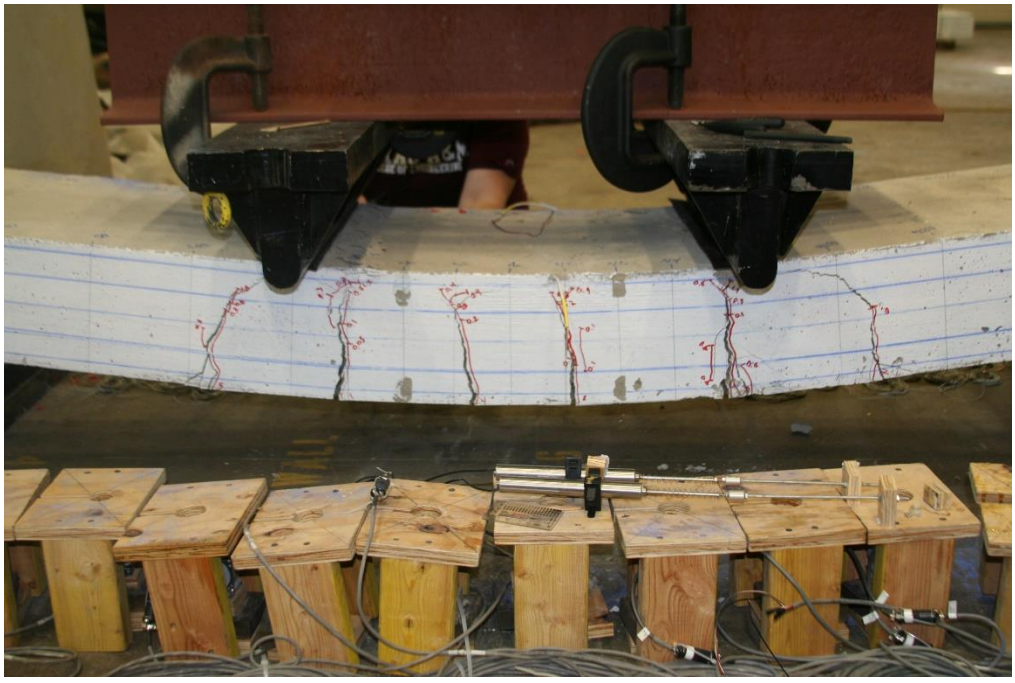

(b) d7500BTM24 – East (PC)

Figure 105. State of Damage for d7505BTM24 and d7500BTM24 at 1.9 inches of Deflection

5.4.2.2 ***No Steel***

The specimens without steel reinforcement behaved significantly different in comparison to the sections with steel reinforcement. Each specimen developed a single crack with "accessory" cracks adjacent to it as shown in Figure 106 and Figure 107.

The slab strips achieved the maximum allowable crack width of 2.5 mm at a very small deflection step relative to the specimens with steel reinforcement. The critical crack width of 2.5 mm was observed at approximately the same deflection step for the deck companion strips and the original slab strips.

Crushing was not observed in the deck companion strips. This varies from the slab strips as shown in Table 28. For all four companion strips, the observation of crushing was either at a larger deflection step in comparison to the original slab strips or did not occur at all.

Table 48. Properties of Failure Criteria for Specimens without Steel Reinforcement

	Critical Crack			Concrete Crushing		
Specimen	**Location**	**$\delta_{first\ obs}$ (in)**	**$\delta_{2.50}$ (in)**	**Location**	**$\delta_{first\ obs}$ (in)**	**Width (in)**
s7505NOS00	N12-N9	0.05	0.3	N12-N9	0.7	1.5
s9005NOS00	S12-S18	0.05	0.25	N12-N9	0.8	1.5
d7505NOS00	S6	0.05	0.4	-	-	-
d9005NOS00	S9-S6	0.05	0.3	-	-	-

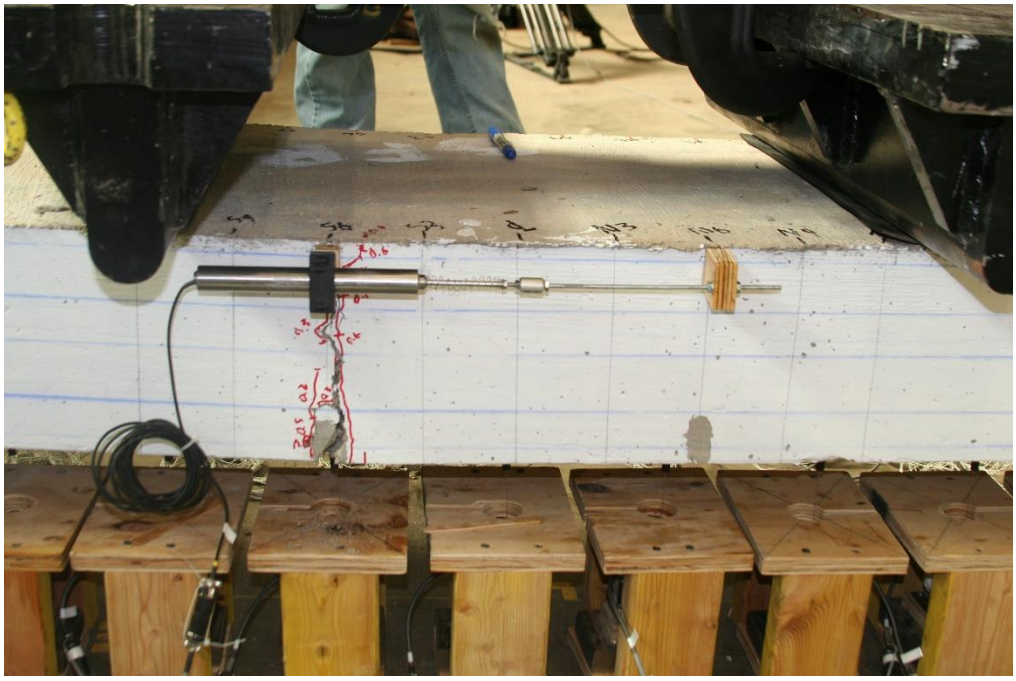

(a) d7505NOS00

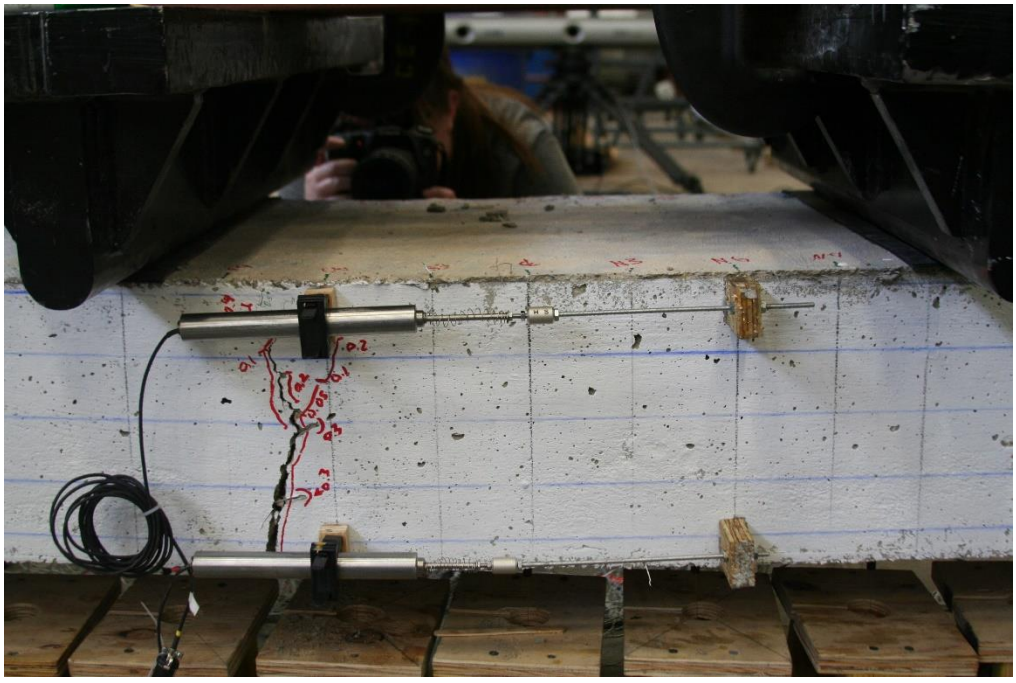

(b) d9005NOS00

Figure 106. Branching Cracks of Specimens without Steel Reinforcement at 0.8 in

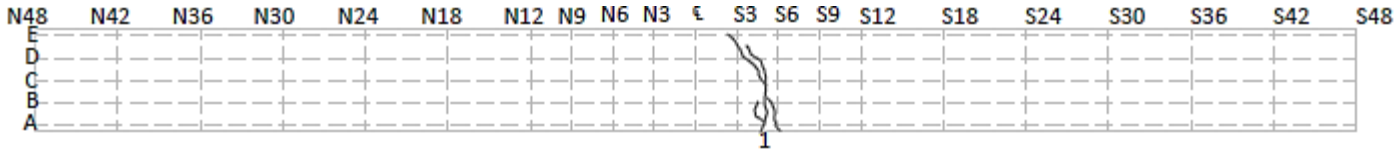

(a) West Face d7505NOS00

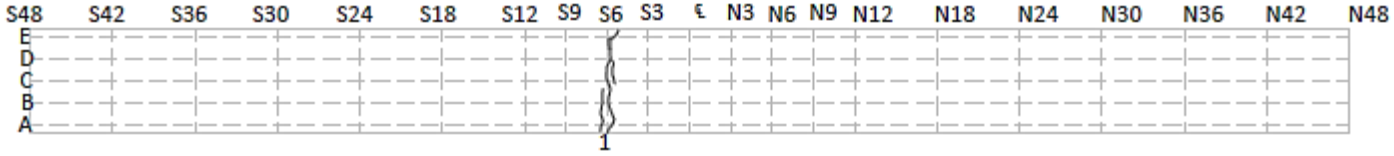

(b) East Face d7505NOS00

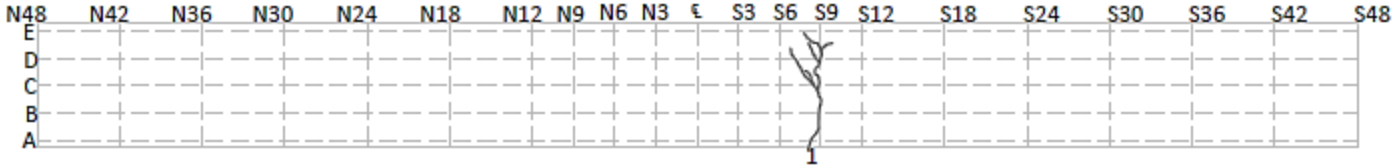

(c) West Face d9005NOS00

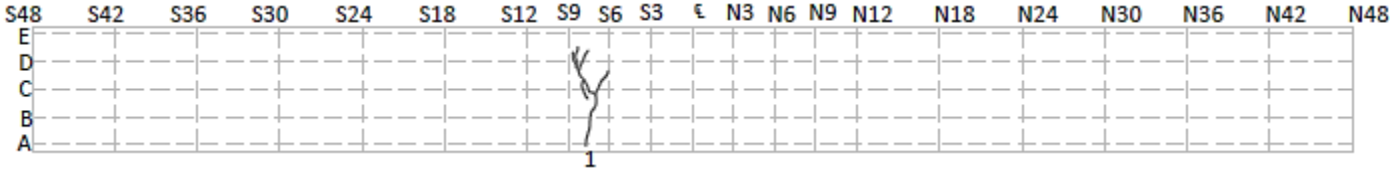

(d) East Face d9005NOS00

Figure 107. Crack Maps for Slab-Strip Specimens without Steel Reinforcement

5.4.3 Moment Capacities

Figure 108 shows the force versus deflection behavior for the bridge deck companion strips. The deflection used in the figure is the string potentiometer at the center of the specimen. The string potentiometers were removed prior to the completion of the tests to protect them from collapse of the specimen. The end of the force versus deflection curves does not signify failure of the specimens.

The initial stiffness of each test prior to cracking was consistent among the specimens. Each 7.5 inch deep specimen cracked at approximately the same centerline deflection of 0.04 inches, and applied force of 6.4 kips. Utilizing the ACI 318-14 definition for the modulus of rupture for concrete and elastic section the expected cracking load for the SFRC strips is 6.75 kips. The cracking load of the SFRC specimens was approximately 5 percent lower than the ACI prediction.

The post-crack stiffness was determined for the two slab strips with steel reinforcement, d7505BTM24 and d7500BTM24. The SFRC strip had a post-crack stiffness of 20.8 k/in and the PC strip had a post-crack stiffness of 11.6 kip/in. The addition of steel fibers increased the post-crack stiffness of the PC slab strip by 9.2 k/in or 80%. The reduced crack widths discussed in Section 5.4.2 supports the increased stiffness of the SFRC slab strip.

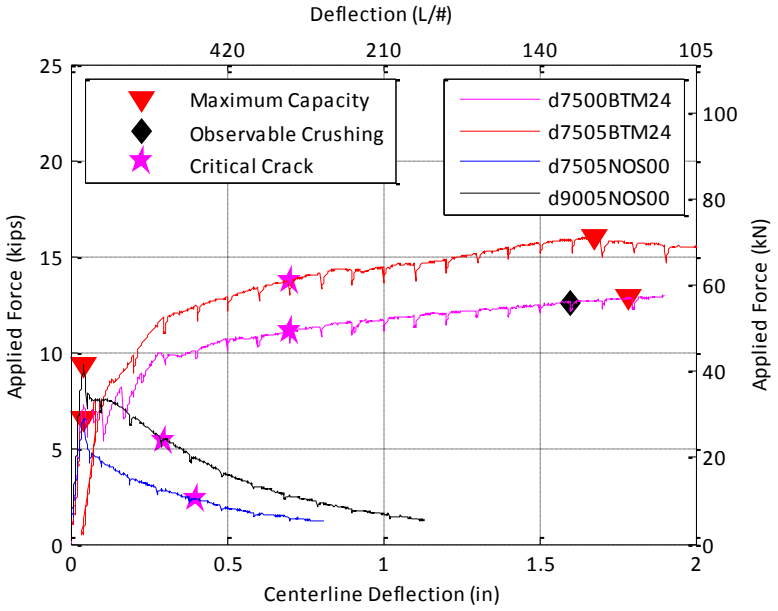

Figure 108. Force versus Deflection of Bridge Deck Companion Strips

5.5 Full-Scale Bridge Test Results

5.5.1 Test Setup and Instrumentation

The size and location of the applied loads were determined based on AASHTO LRFD Bridge Design Specifications (2014) and the HS20 design truck. The wheel footprint of an HS20 truck is 10 by 20 inches. The expected failure pattern for the 10 by 20 inch footprint is shown in Figure 109. The failure pattern consists of a radial-fan mechanism and four rectangular panels. The fan pattern is consistent with the typical failure pattern of a point load on a two-way slab.

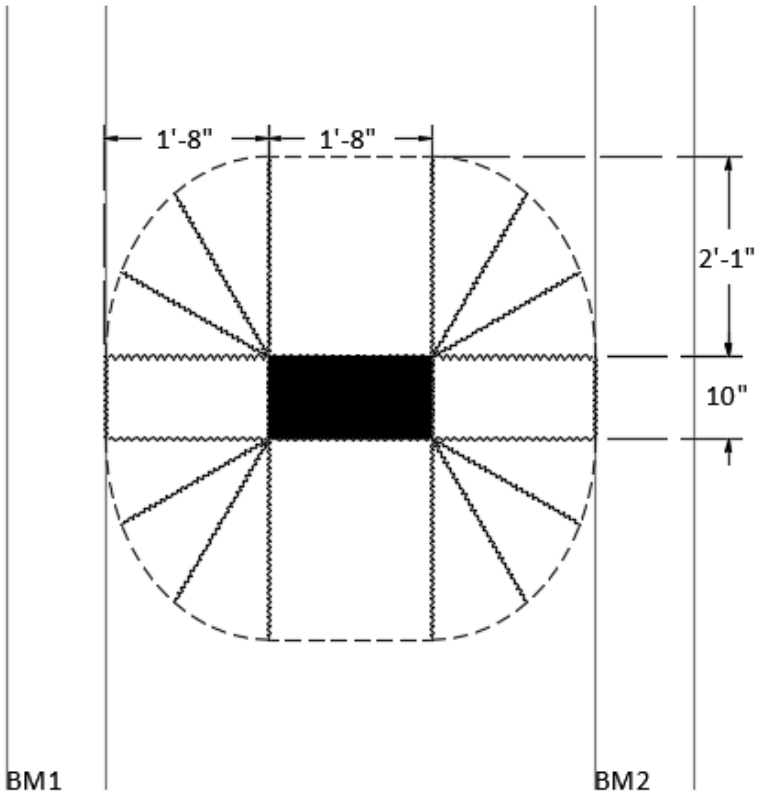

Figure 109. Expected Fan-Mechanism - 10 in by 20 in Wheel (Black)

Four load patterns were applied to the SFRC bridge deck, LP1 through LP4. Each test was conducted by applying a monotonically increasing load using a 600 kip actuator as shown in Figure 110. A load cell was installed in-line with the actuator to record the applied force. A

pressure sensor was included on the pump assembly for after completing LP1 for all subsequent tests to verify the load recorded by the load cell. String potentiometers were installed below each load point at 12 inch intervals in both the longitudinal and transverse directions to record the deflection of the SFRC deck. Strain gauges were also installed on the traditional steel reinforcement to determine the steel stress at locations of high positive and negative moments. Each test location is shown in Figure 111. Strain gauge names and locations are shown in Figure 112.

Both LP1 and LP4 represent an individual wheel applied at the mid span transversely. The loading plate was centered 47 inches from the free edge of the deck longitudinally. Load pattern LP2 represents a tandem axel with wheel footprints spaced 4 ft on center. LP2 was centered in both the longitudinal and transverse directions of the bridge deck. Load pattern, LP3, was applied to the south overhang at the longitudinal center of the bridge. LP3, while not an ADOT design requirement, provides an additional comparison to the two prior bridge tests (Mander et al 2010 and Gar et al 2013).

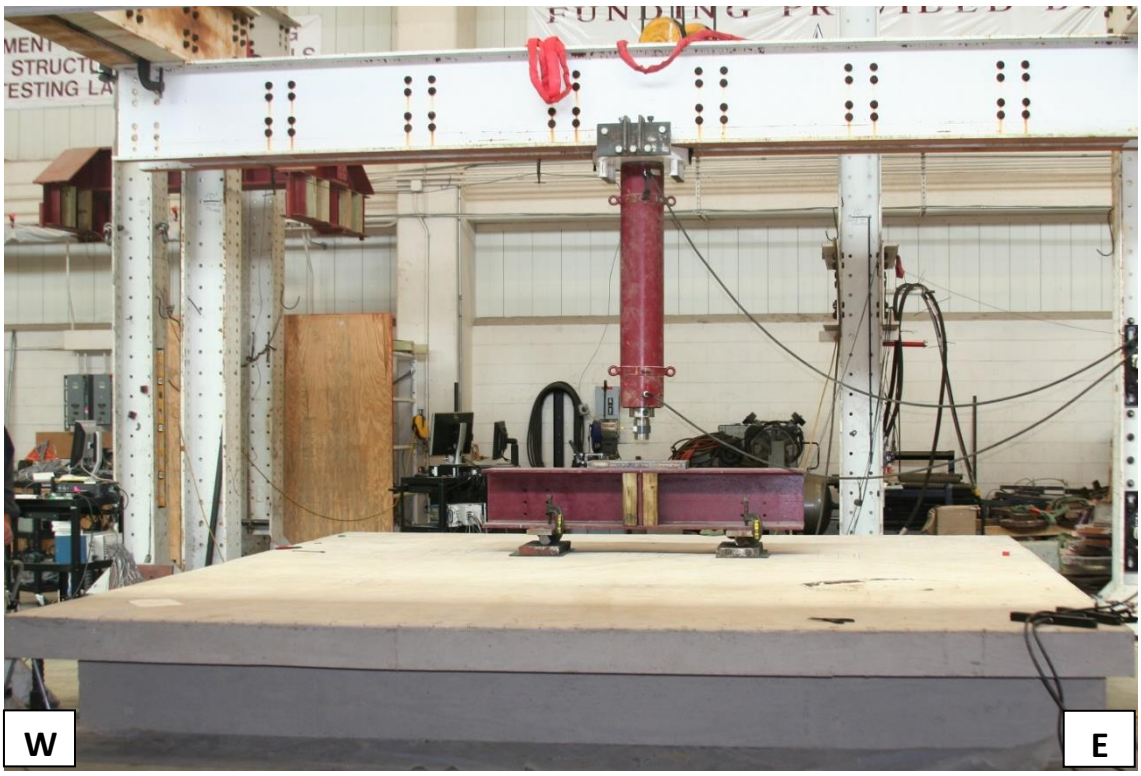

Figure 110. Full-Scale Specimen Test Setup – LP2

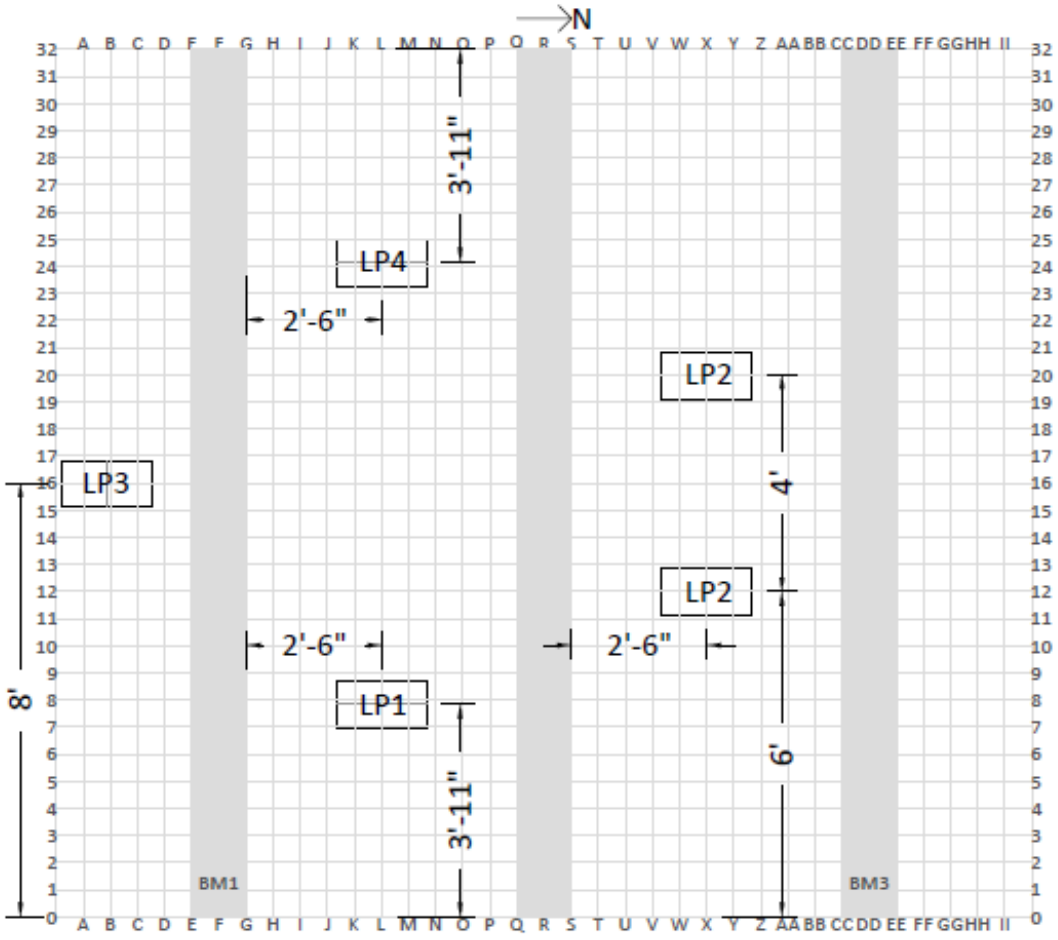

Figure 111. AASHTO Load Patterns Tested on Bridge Deck

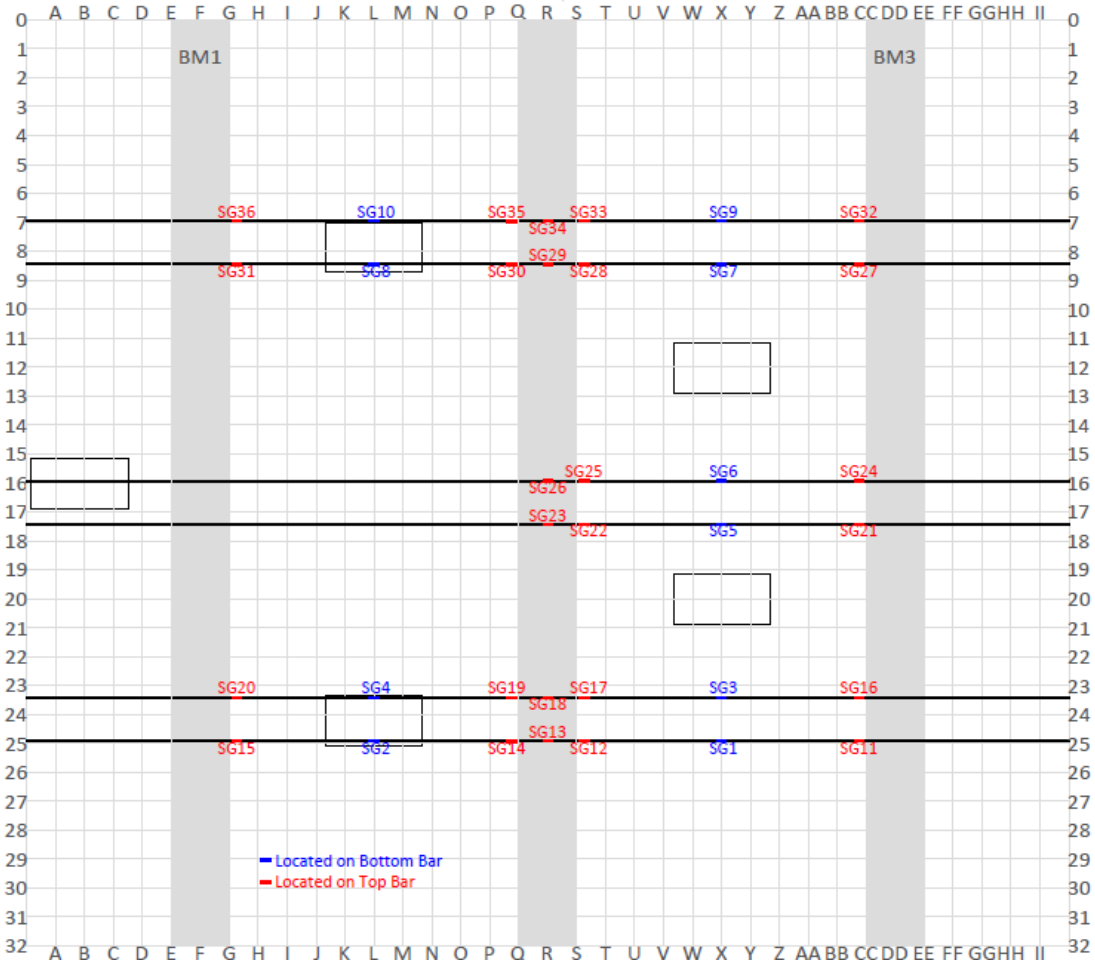

Figure 112. Elevation View of Strain Gauge Locations for Bridge Deck

5.5.2 Testing Adjustments

During the planning phase of the full-scale specimen, the location for LP2 was originally 47 inches from the free edge as shown for LP1; however, the failure mechanism observed following the completion of LP1 dictated the relocation of LP2. The expected fan-mechanism was prevented for LP1 due to a lack of distance between the applied load and free edge. As a result, the strain gauges intended to record the reinforcing steel strain directly below the applied loads are offset from the actual loads points of LP2. The failure mechanism of each load pattern is further discussed in their respective subsections.

At the conclusion of the first session of LP2, a calibration offset was discovered in the data recorded by the load cell. The offset directly affected the results obtained for LP1 and the first testing session of LP2. As a result, the load cell was subjected to a testing and calibration program

to detail the extent of the offset. The testing program applied a known load to the load cell and then recorded the output of the load cell and its current and voltage. The manufacturer's calibration information was used with the current and voltage obtained during testing to verify that the load cell was indeed recording accurate values. The observed calibration offset in the load cell data was attributed to a scaling factor in the data acquisition computer. The reported load at each verification interval was consistently 61% larger than the known applied load. Therefore, a scaling factor was utilized to adjust the values for LP1 and the first session of LP2 to obtain actual load data. The calibration offset was corrected prior to any additional testing. All reported values in this report are corrected data.

5.5.3 LP1 – Individual Wheel

Test LP1 was divided into two sessions to allow for a preliminary analysis of the crack pattern and load before complete failure. The load was increased to approximately 175 kips during the first session. The specimen was completely unloaded at the end of the first session. The test was paused at regular intervals to inspect the specimen for cracks and behavior. The first crack was observed at approximately 100 kips and a deflection of 0.2 inches. As the load increased additional cracks formed and propagated to create an elongated fan failure mechanism. The specimen achieved a maximum load of 203 kips before sudden failure occurred, as defined by a sudden drop in load carrying capacity. Figure 113 shows the final crack pattern observed for LP1. Cracks on the bottom surface were not recorded until the completion of the test. The cracks locations are reported utilizing the Grids 0 through 32 orientated north-south and Grids A through II orientated east-west. Significant cracks are labeled in each figure for the subsequent discussion.

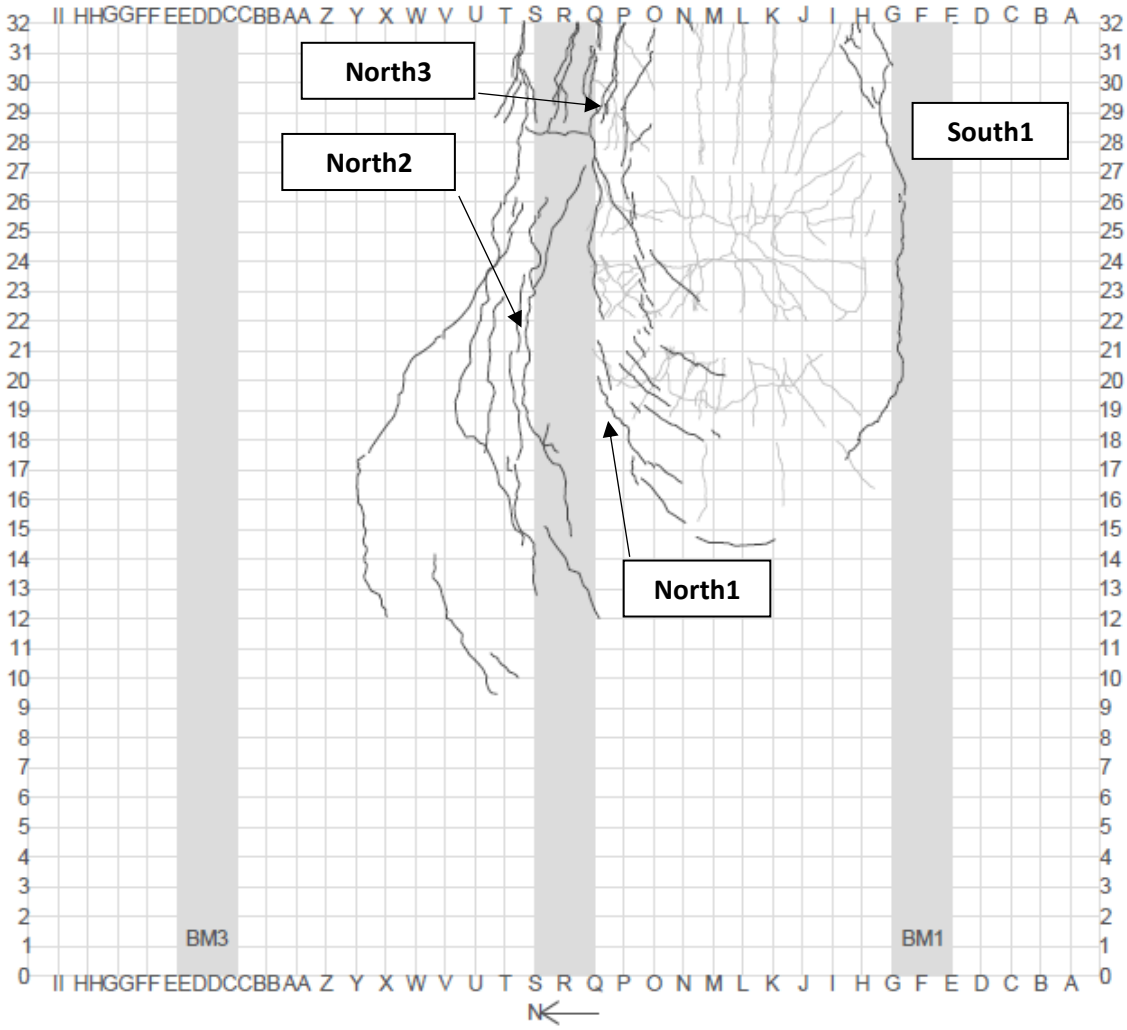

Figure 113. Final Crack Pattern - LP1

5.5.3.1 Crack Pattern

The first cracks initiated at Grid G (crack South1) and Grid Q (crack North1). The cracks formed on the top surface of the deck above the inside face of the adjacent support beams. They initiated adjacent to the steel plate on Grid 25 and propagated east and west as the load was increased. An additional crack was observed north of crack North1 at 125 kips and extended 75 inches from the free edge of the deck to Grid 19. During the final load step of the first session, the crack along Grid S, North2, began to turn south and traverse over the support beam into the loaded span. At the conclusion of the first test session, three primary cracks were observed on the top surface of the deck following Grids G, Q, and S. The cracks originating above the interior face of the support

beam, G and Q, propagated east-west from the free edge to Grid 18, approximately 84 inches while crack along Grid S bent inwards toward the loaded span reaching Grid 14. In addition to the cracks observed on the top surface of the deck, rotation in the support beams was observed despite the beams being anchored to the strong floor with threated rods with a 1 inch diameter. Cracking and minor spalling was observed on the beam faces as a result of the rotation.

No significant changes were observed during the second session prior to reloading the specimen to a load of 160 kips. At this interval, a third crack, North3, on Grid P was observed. As the load was further increased, the four primary cracks continued to propagate in the east-west direction. At a load of 190 kips, the portion of the primary cracks west of the load point began to turn perpendicular to the support beams. The "curving" of the cracks toward the north-south direction is consistent with the expected radial-fan mechanism presented in Section 5.5.1. At the final load step, a crack was observed at Grid 15 and was orientated approximately 90 degrees to the support beam. The portion of the primary cracks to the east side of the load point did not demonstrate this same behavior. They propagated parallel to the support beams until they met the free end of the deck. As a result, the fan mechanism did not occur on the east portion of the failure plane.

After the completion of the test, the cracks on the underside of the bridge deck were mapped and recorded. The bottom cracks were consistent with the observed cracks on the top surface. The bottom cracks outlined the 10 by 20 steel plate and propagate outwards. The cracks on the west side of the load provided the radial cracks for the fan-mechanism while the cracks on the east side of the load continued approximately parallel to the beams as would be expected in a one-way slab.

5.5.3.2 Capacity and Deflection

Figure 114 shows the location of the string potentiometers utilized for LP1. Figure 115 shows the load-deflection relationship for LP1. Three displacements are shown in the figure. The transducer directly below the load, SP4, disengages from the deck surface at a displacement of 0.5 inches. The transducers to the east and west of SP4, SP5 and SP3 respectively, are included to provide data at large displacements. The string potentiometer names are indicated by their direction and distance from the center string potentiometer. Solid lines in Figure 115 indicate the first loading session of the specimen. Dashed lines indicate the second loading session.

The initial stiffness of the full-scale specimen prior to achieving a load of 50 kips is unknown due to a rapid increase in the applied load at the start of the test and the interval at which data was recorded. As a result, the pressure valves used to power the actuator were adjusted to slow the loading rate of the specimen. The force-deflection curve shows a change in its slope at approximately 70 kips indicating a reduction in the specimen's stiffness. This observation is

consistent with the first cracks found during the visual inspection of the deck after this load step. The full-scale specimen deflected approximately 0.1 inches prior to the formation of a crack.

The specimen was unloaded after reaching a load of 175 kips as observed by the decrease in the load and deflection. The second session and reloading of the deck is demonstrated by the dashed line in Figure 115. The full-scale specimen achieved a maximum capacity of 203 kips under the load pattern LP1. The deflection of the specimen directly under the load point is unknown at the maximum load due to SP4 dislodging from the bridge deck during a prior loading cycle. The maximum deflection of the specimen was 0.58 in and occurred at W12 or SP3. After achieving this maximum load the specimen was partially unloaded and then reloaded until complete failure. The applied load increased to approximately 201 kips before the strength began to degrade until the specimen suddenly failed at approximately 0.75 inches embedding into the deck as shown in Figure 116.

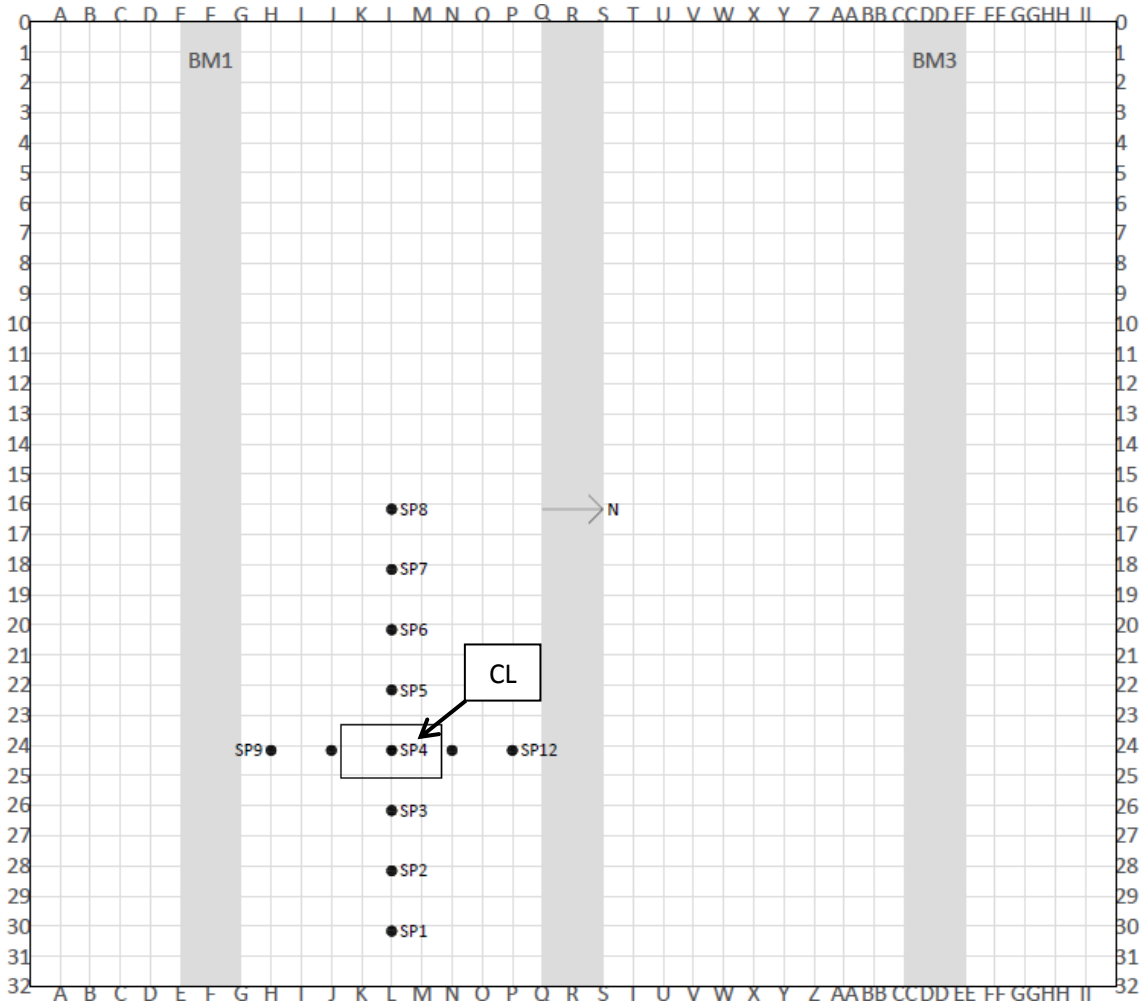

Figure 114. Location of String Potentiometers for LP1

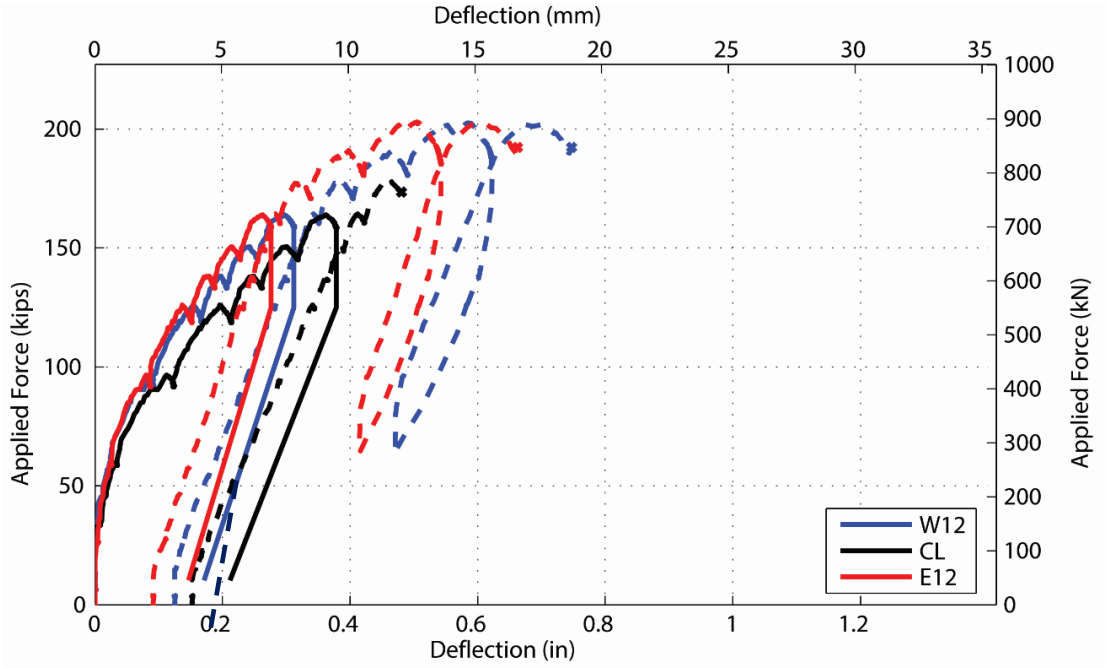

Figure 115. Force vs. Deflection for LP1
Solid for First Session and Dashed Lines for Second Session

Figure 116. SFRC Bridge Deck Failure Due to LP1

Figure 117 and Figure 118 present the deflected shape of the SFRC bridge deck under the influence of LP1 at various load points. The deflected shapes show the stiffness of the bridge deck in both the transverse and longitudinal directions. They provide insight of the condition of the bridge at both service and ultimate loads. At the service demand of 16 kips, the deflection of the specimen is negligible. At the strength demand of 37 kips, the deflection of the specimen is 0.1 inches. As the load increases, the stiffness of the bridge is reduced and cracks begin to open resulting in larger deflections. The slope of the deflected shape in the transverse direction is larger due to the restraint provided by the support beams.

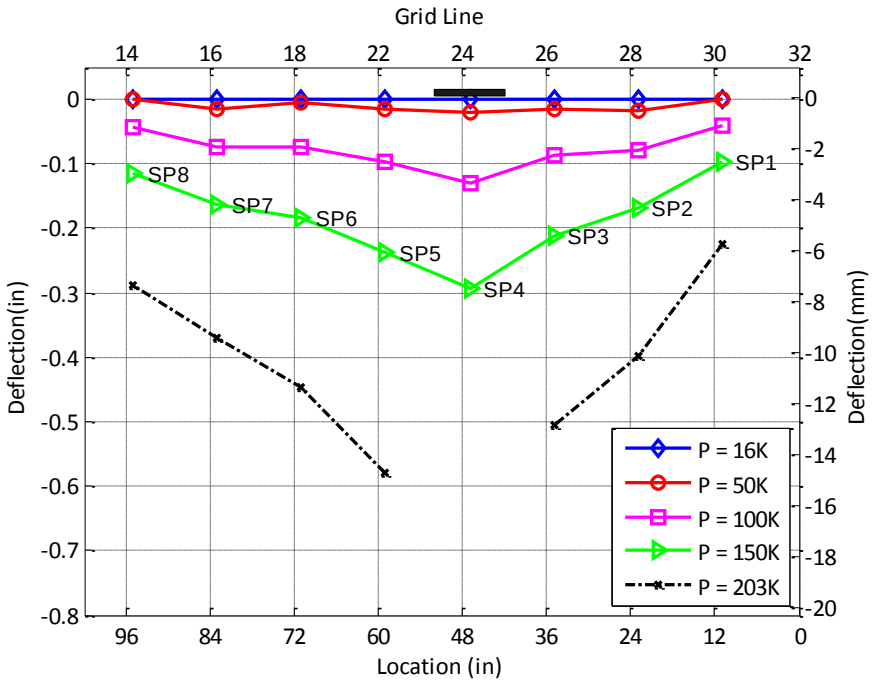

Figure 117. Deflection Profile of LP1 - Longitudinal Direction

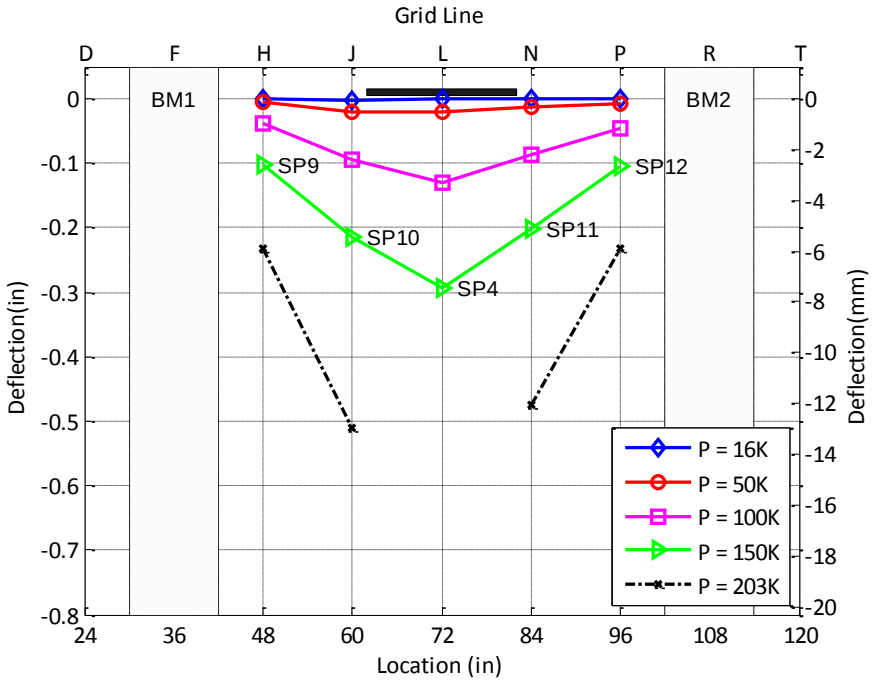

Figure 118. Deflection Profile of LP1 - Transverse Direction (Cross-Section View)

A summary of the performance of the SFRC bridge deck due to LP1 is presented in Table 49. The deflection at both the service and ultimate demands is less than 0.01 inches as a result of the sudden increase in the applied load at the beginning of the test.

The stress in the steel reinforcement at the service demand is 1.6 ksi. Despite the lack of the information collected at both the AASHTO service and ultimate demands, the overall performance of the SFRC bridge deck subjected to LP1 is clear. The maximum load achieved, 203 kips, is approximately 550% larger than AASHTO ultimate demand of 37 kips. At the ADOT allowable stress limit of 24 ksi, the applied load is 64 kips, or 400% of the AASHTO service demand of 16 kips.

Table 49. Load and Deflection Capacities of LP1

	Service (16 kips)		**Demand** (37 kips)	**Service Stress Limit** (24 ksi)	**Cracking**		**Maximum**	
	$\Delta_{service}$ in(mm)	σ_{steel} ksi (MPa)	Δ_{demand}, in(mm)	$P_{fs=24ksi}$ Kips (kN)	P_{crack} kips (kN)	Δ_{crack}, in(mm)	P_u kips (kN)	Δ_u in(mm)
LP1	0.0 (0.0)	1.6 (11.0)	0.01 (0.25)	64 (284)	70 (311)	0.03 (0.76)	203 (903)	0.58 (14.73)

5.5.4 LP2 – Tandem Axel

The location of LP2 was adjusted as a result of the crack locations and progression of LP1. LP2 was shifted west to the longitudinal center of the bridge deck to ensure the full radial-fan mechanism formed on each side of the load. Figure 119 shows the setup and location for LP2. The force was applied to a steel wide flange beam that distributed the load between two load points spaced 4 ft apart. All data reported for LP2 is for each individual load point. Test LP2 was also divided into two sessions due to the calibration offset discovered with the load cell. The first session was concluded at approximately 105 kips. The SFRC bridge deck was gradually unloaded so that data concerning the load cell's electrical current and voltage could be recorded. The specimen was loaded until failure occurred at 185 kips during the second session. Figure 120 presents the final crack pattern of LP2. Existing cracks from LP1 are not included in the figure. Significant cracks are labeled in each figure for the subsequent discussion.

Figure 119. Load Pattern LP2

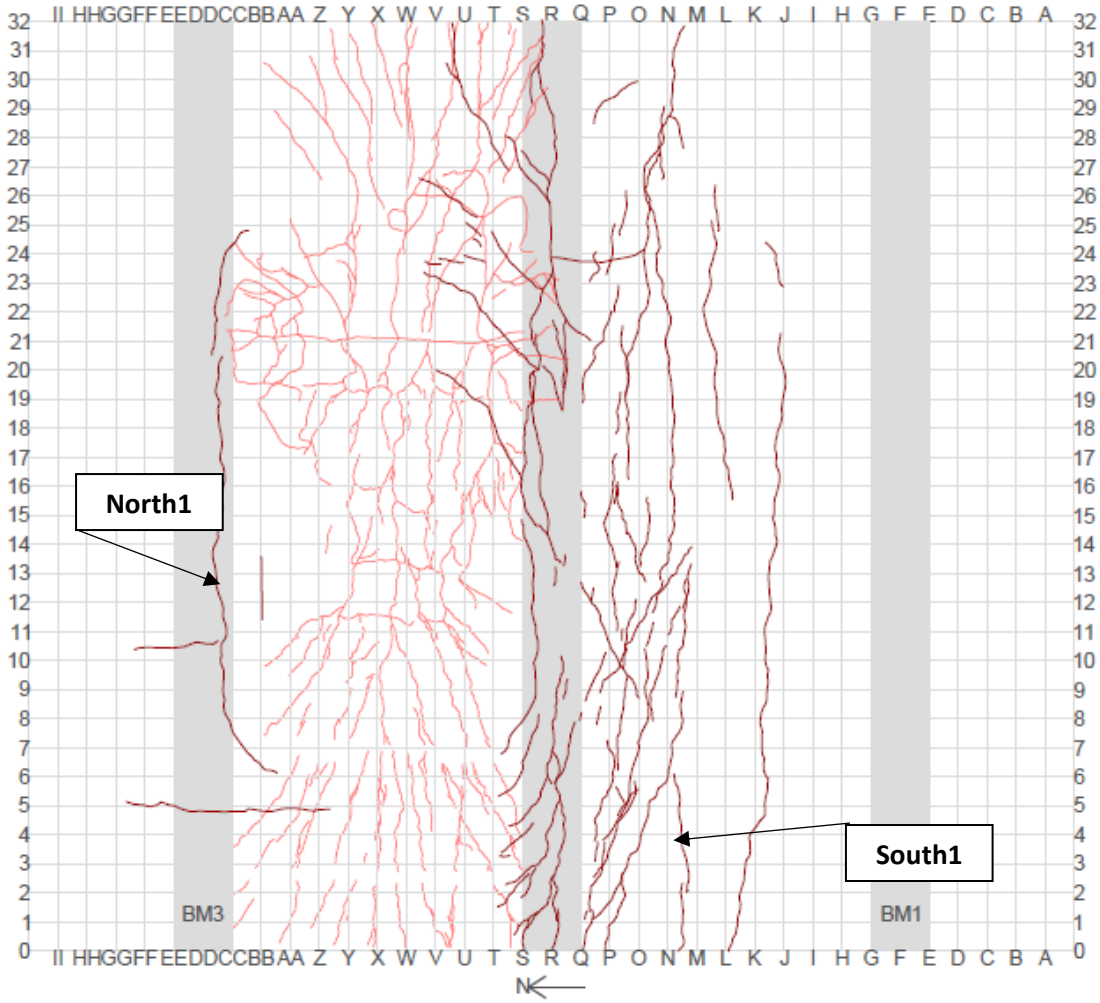

Figure 120. Final Crack Pattern – LP2

5.5.4.1 Crack Pattern

The extent of cracking from the first test, LP1, impacted the onset of cracking and deflection of LP2. At the conclusion of LP1, a crack on the north side of the middle beam had extended through the mid-point of LP2. In addition, a crack on Grid S, or the north face of beam 2, had extended beyond LP2 as shown in Figure 121. The first new crack on the top surface of the deck, crack South1, was observed at 75 kips and a deflection of 0.27 inches. The crack initiated south of the load point at the free edge of the deck and Grid Q and extended 102 inches to Grids M and 17. The first crack north of the load points, North1, was observed at approximately 100 kips and extended 48 inches. The test was ceased after the next load step and unloaded. At this time, only one propagating crack was observed north of the load point while several cracks from both LP1 and LP2 were present south of the load point. Cracks were also observed in beam 3.

During the second session, no changes to the deck were observed prior to achieving a load of approximately 110 kips. A slight extension of the existing cracks was observed at this time. The cracks continued to propagate east-west as the load increased. During the next load step, several string potentiometers adjacent to the loading points began to dislodge from the deck due to damage of the bottom side of the deck. At 130 kips, the cracks south of the load point began to turn perpendicular to the support beams. This behavior became more apparent at 160 kips as shown in Figure 124. Finally the load was increased until the specimen failed at approximately 185 kips. At the conclusion of the test, significant deformation of the specimen was noted. Additionally, the north and center supporting beams exhibited significant rotation.

Crushing was observed beneath the steel beam at a load of 171 kips as shown in Figure 122. By the conclusion of the test, the crushed region of concrete extended 24 inches west of the west load point.

After the failure of the specimen under LP2, the cracks on the bottom of the deck were mapped. The failure pattern observed on both the top and bottom surfaces are consistent with the expected fan pattern. The negative moment cracks on the top surface propagated parallel to the load points before “curving” inwards to the east and west of the load points forming the outer edge of the fan-mechanism. Radial cracks were observed on the bottom surface east and west of the load points while cracks parallel to the support beams connected the two load points in the positive moment region.

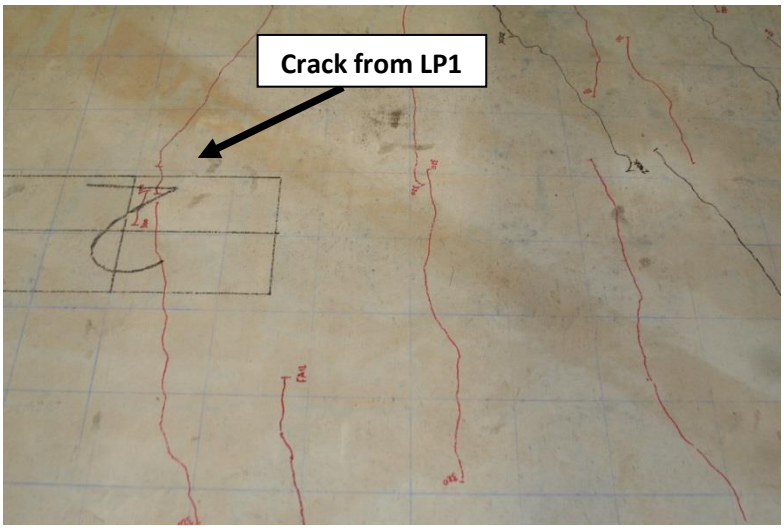

Figure 121. Influence of LP1 Cracks on LP2 - Crack Extends Through LP2

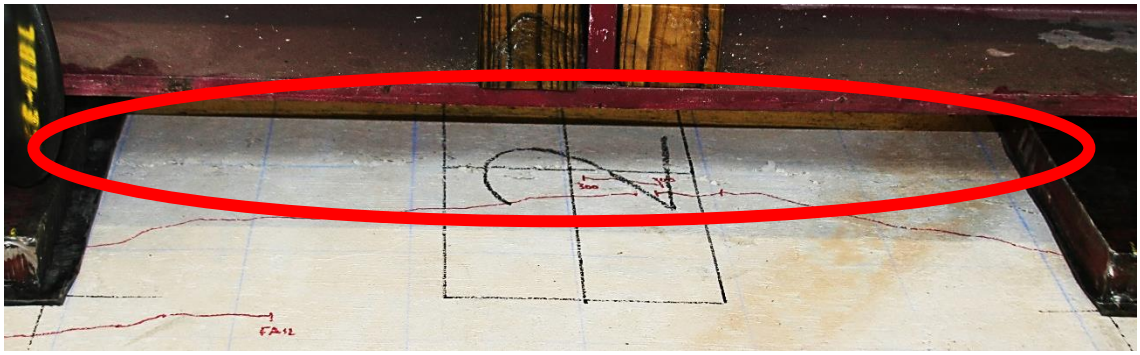

Figure 122. Crushed Region Extends Between Both Load Points

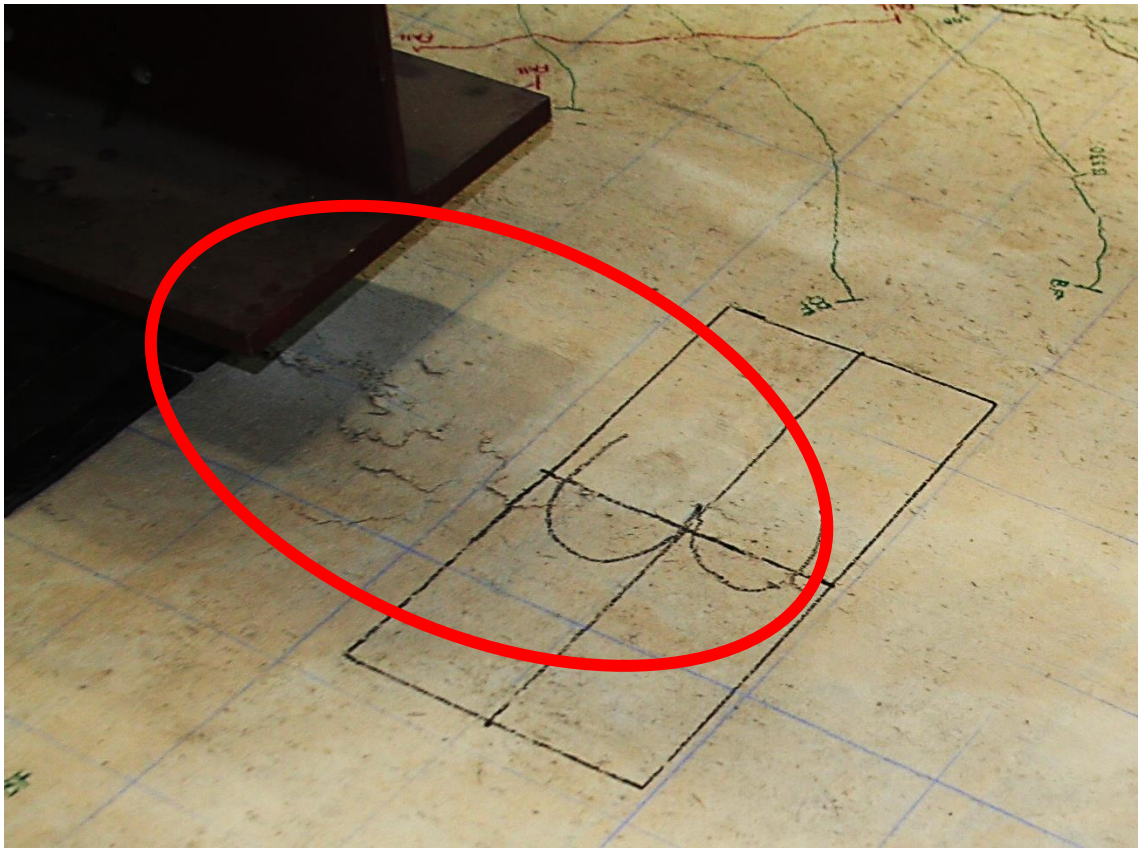

Figure 123. Crushing Failure Extends 24 in Passed LP2

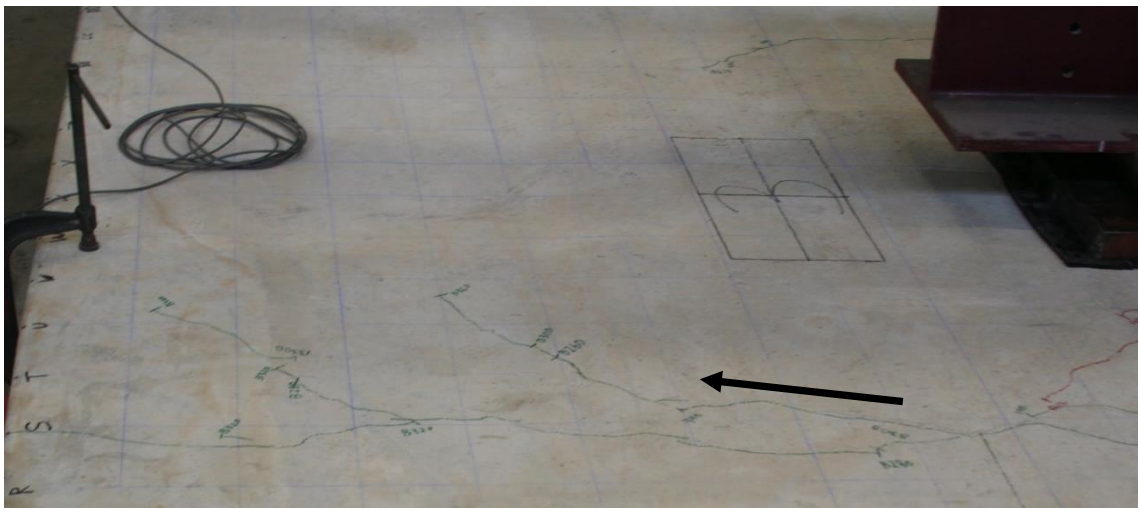

Figure 124. "Turning" of Negative Moment Cracks – LP2

5.5.4.2 Capacity and Deflection

Figure 125 shows the location of the string potentiometers for LP2. Figure 126 shows the load-deflection relationship for LP2. Three displacements are shown in the figure. The transducer directly below the load, SP6, dislodges from the deck surface at a displacement of 0.5 inches. The transducers to the east and west of SP6, SP5 and SP7 respectively, are included to provide data at large displacements. The string potentiometer names are indicated by their direction and distance from the center string potentiometer. Solid lines in Figure 126 indicate the first loading session of the specimen. Dashed lines indicate the second loading session.

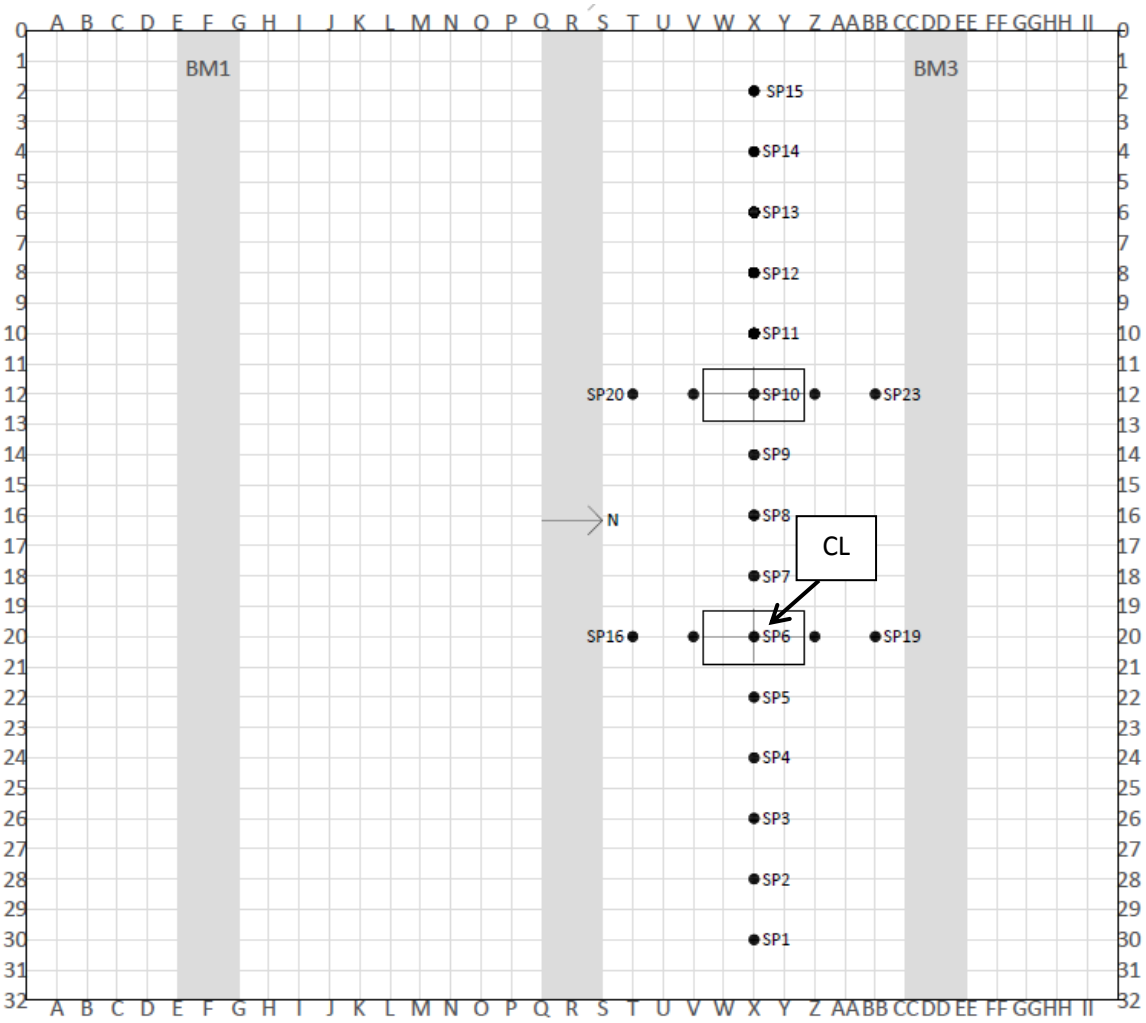

Figure 125. Location of String Potentiometers for LP2

The initial stiffness of the bridge deck is approximately 700 kip/in and changes at approximately 23 kips. The loading was paused at 30 kips for observations and no new cracks were observed. The change in slope is attributed to the opening of the cracks resulting from LP1. The stiffness of the SFRC bridge deck reduced to 290 kip/in following the opening of LP1 cracks. The slope of the force-deflection curve changes again at approximately 70 kips. The change in stiffness is consistent with the formation of new cracks observed during the pause immediately after 70 kips. As the load was increased, string potentiometer SP6, or CL, dislodged from the deck prior to the completion of the first session.

The specimen was unloaded after reaching a load of 105 kips as observed by the decrease in the load and deflection. The second session and reloading of the deck is shown by the dashed line in Figure 126. The bridge deck achieved a maximum capacity of 185 kips under the load pattern LP2. The deflection of the specimen directly under the load point is unknown at the maximum load due to SP6 dislodging from the bridge deck during a prior loading cycle. The deflection at the maximum load was 1.9 inches and occurred at E12 or SP5. Further deflecting the specimen did not result in a change in its load capacity. The deflection increased until the specimen suddenly failed at 2.25 inches.

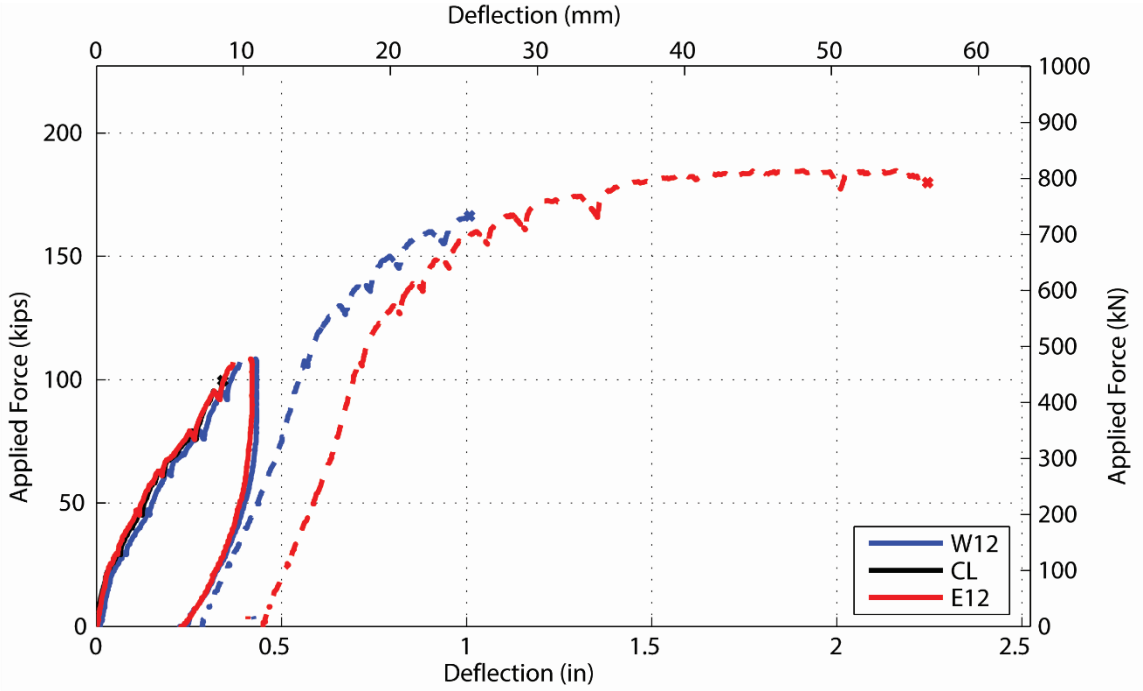

Figure 126. Force vs. Deflection for LP2
Solid for First Session and Dashed Lines for Second Session

Figure 127 through Figure 129 present the deflected shape of the SFRC bridge deck under the influence of LP2 at various load points. The deflected shapes show the stiffness of the bridge deck in both the transverse and longitudinal directions. They provide insight of the condition of the bridge at both service and ultimate loads. At the service demand of 16 kips, the deflection of the specimen is approximately 0.03 inches. As the load increases, the stiffness of the bridge is reduced and cracks begin to open resulting in larger deflections. The slope of the deflected shape in the transverse direction is larger due to the restraint provided by the support beams. Numerous string potentiometers dislodged from the bridge deck after achieving 100 kip.

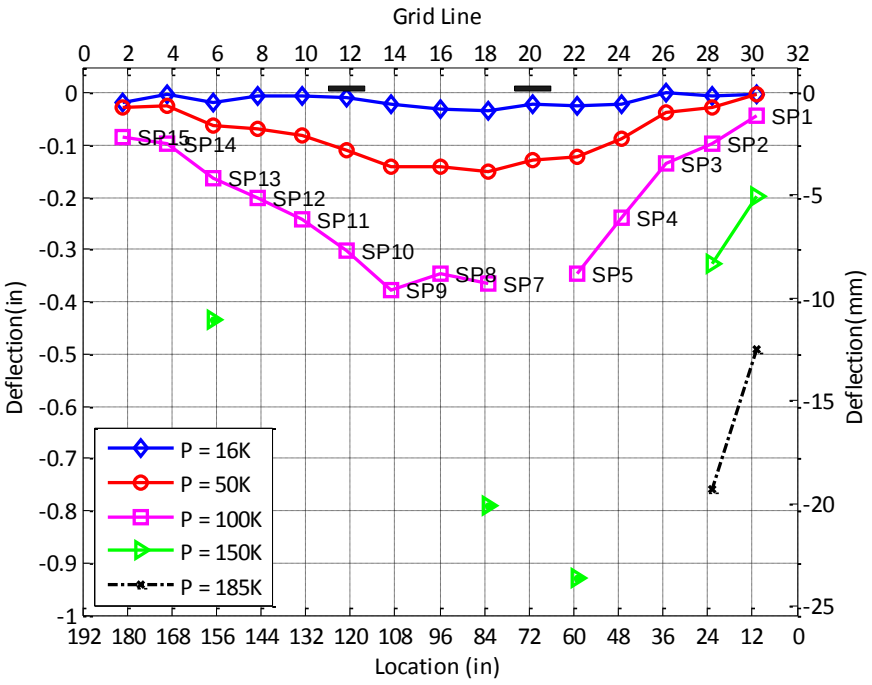

Figure 127. Deflection Profile of LP2 - Longitudinal Direction

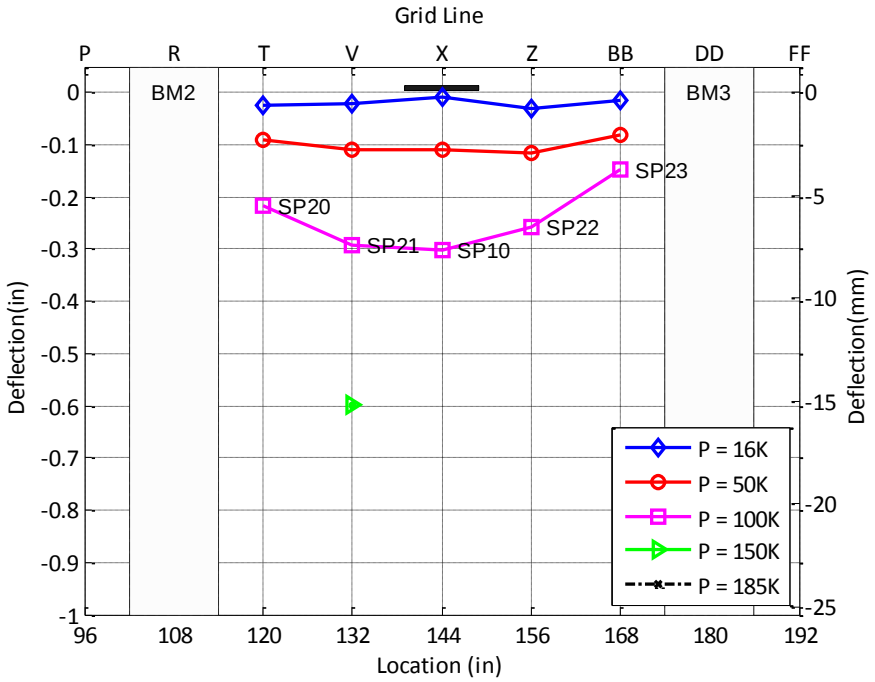

Figure 128. Deflection Profile of LP2 - Transverse Direction, West Load Point

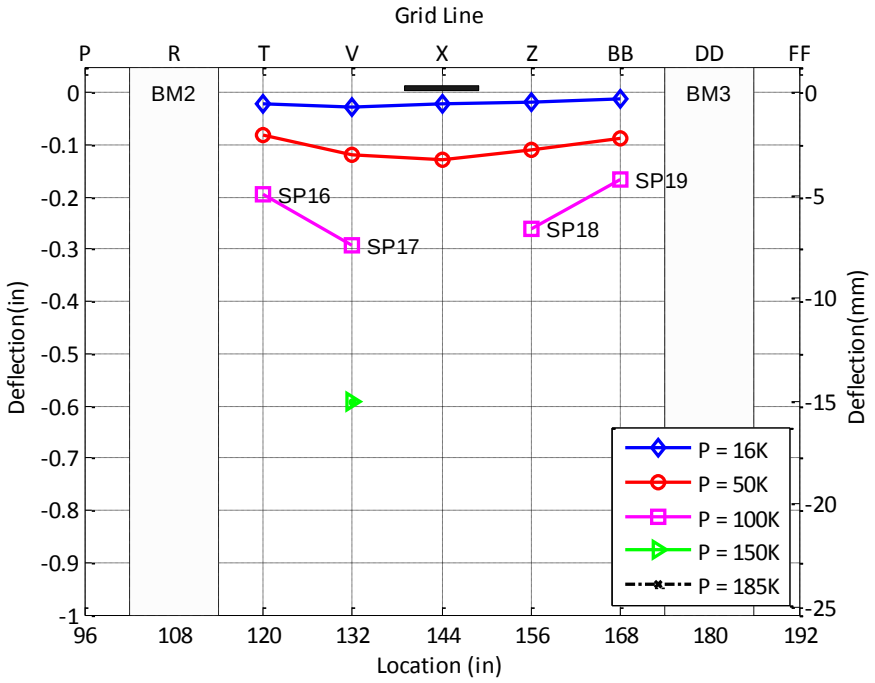

Figure 129. Deflection Profile of LP2 - Transverse Direction, East Load Point

A summary of the performance of the SFRC bridge deck due to LP2 is presented in Table 50. The deflection at both the service and ultimate demands is 0.03 inches and 0.07 inches respectively. The deflections at the service and ultimate demands for LP2 are marginally larger in comparison to LP1.

The stress in the steel reinforcement at the service demand is 12 ksi. The maximum load achieved, 185 kips, is 500% larger than AASHTO ultimate demand of 37 kips. At the ADOT allowable stress limit of 24 ksi the applied load is 33 kips, or 200% of the AASHTO service demand of 16 kips.

Table 50. Load and Deflection Capacities of LP2

	Service (16 kips)		**Demand** (37 kips)	**Service Stress Limit** (24 ksi)	**Cracking**		**Maximum**	
	$\Delta_{service}$ in(mm)	σ_{steel} ksi (MPa)	Δ_{demand}, in (mm)	$P_{fs=24ksi}$ Kips (kN)	P_{crack} kips (kN)	Δ_{crack}, in (mm)	P_u kips (kN)	Δ_u In (mm)
LP2	0.03 (0.76)	12 (82.7)	0.07 (1.78)	33 (147)	70 (311)	0.21 (5.33)	185 (823)	1.91 (48.51)

5.5.5 LP3 – Overhang Single Axel

Test LP3 is located on the center of the south overhang of the specimen as shown in Figure 130. The test occurred in a single session and continued until the specimen exhibited significant damage. The location of the test was selected to limit the influence of LP1 on the results. The information obtained from LP3 is not directly relatable to a given AASHTO LFRD load pattern; however, LP3 offers information on the strength and ductility of the specimen as it relates to identical tests conducted by others using different reinforcing systems (Mander et al 2009 and Gar et al 2014).

Test LP3 achieved a maximum load of approximately 96 kips. The test was concluded due to the extreme damage of the specimen and not a sudden failure of the concrete like the previous tests as shown in Figure 133. Concentric cracks formed at support beam 1 and propagated at approximately 45 degrees towards the free edge of the deck as shown in the final crack map in Figure 131.

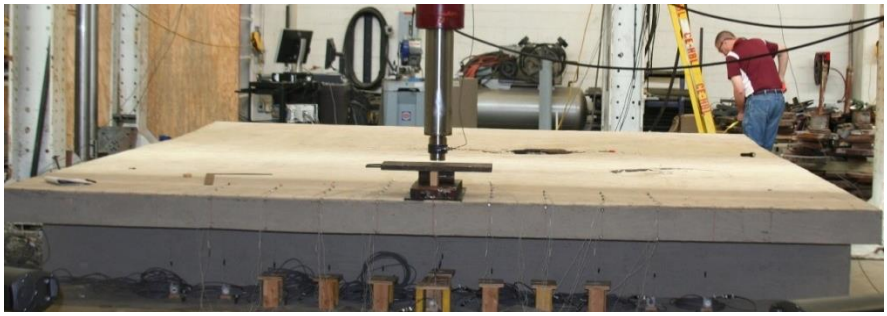

Figure 130. Location of LP3 on SFRC Bridge Deck

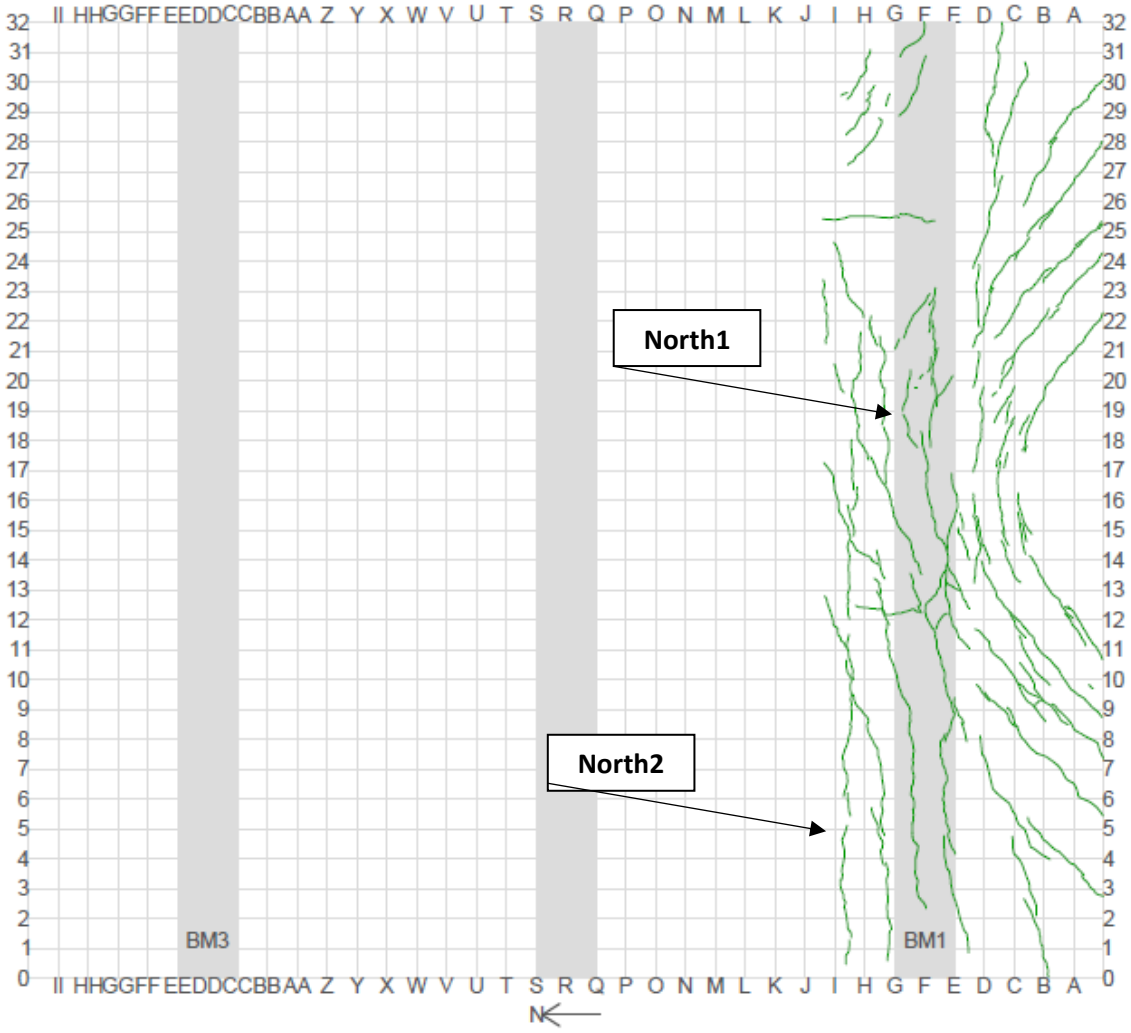

Figure 131. Final Crack Pattern – LP3

5.5.5.1 Crack Pattern

Crack North1 was observed during the first loading phase to 16 kips and deflection of 0.05 inches. The crack originated at Grids F and 18 and extended approximately 3 inches. Cracks developed on the edge of the specimen directly beneath the load point at 40 kips as shown by Figure 132. Crack North2 formed on Grid H north of the beam 1. The crack propagated almost the entire length of the deck with the exception of approximately 3 ft at the center of the deck. West of the load point the crack North2 connected with the cracks from LP1. Once the load and deflection was increased to 60 kips and 0.36 inches respectively, diagonal cracks formed orientated at an approximately 45 degree angle from beam 1. The diagonal cracks "fanned out" similar to the radial cracks observed on the bottom surface of the SFRC bridge deck in LP1 and LP2. Further increasing the load resulted in a proliferation and extension of the diagonal cracks and the formation of additional cracks on the edge of the deck. The test continued until the cracks on the edge of the deck opened significantly and the panel directly beneath the steel plate was only connected via the steel reinforcement bars as shown in Figure 133. A sudden failure or rupture of the concrete did not occur.

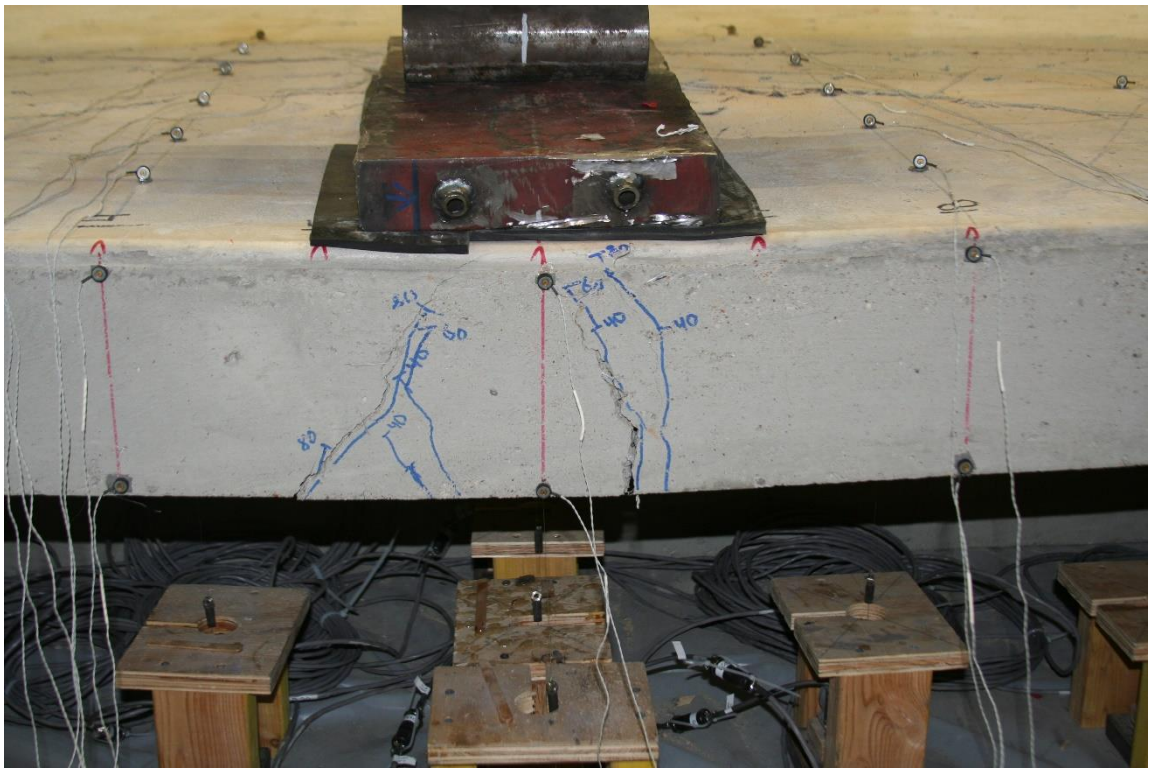

Figure 132. Cracks Beneath Load Point on Edge of Deck - LP3

Figure 133. Completion of LP3

5.5.5.2 Capacity and Deflection

Figure 125 shows the location of the string potentiometers for LP2. Figure 135 shows the load-deflection relationship for LP3. Three displacements are shown in the figure: SP5 (E12), SP6 (CL), and SP7 (W12).

The initial stiffness of the full-scale specimen is approximately 225 kip/in and changes at approximately 30 kips. The first crack that was observed extended a total of 3 did not affect the stiffness of the structure. The change in the stiffness at 30 kips is consistent with the observation of the first major cracks observed when the test was paused at 40 kips for inspection. The load increased steadily in relation to the deflection following the cracking event until approximately 70 kips and 0.45 inches of deflection. At this time the diagonal cracks spanned the entire overhang and crack North2 at Grid H extended the entire length of the deck. The level of damage resulted in a large decrease in stiffness as the bridge deflected more significantly without achieving an equivalent gain in load. The specimen achieved a maximum load of 96 kips at approximately 1.4 inches of deflection before slowly losing capacity. Test LP3 was concluded after significant damage to the concrete was observed.

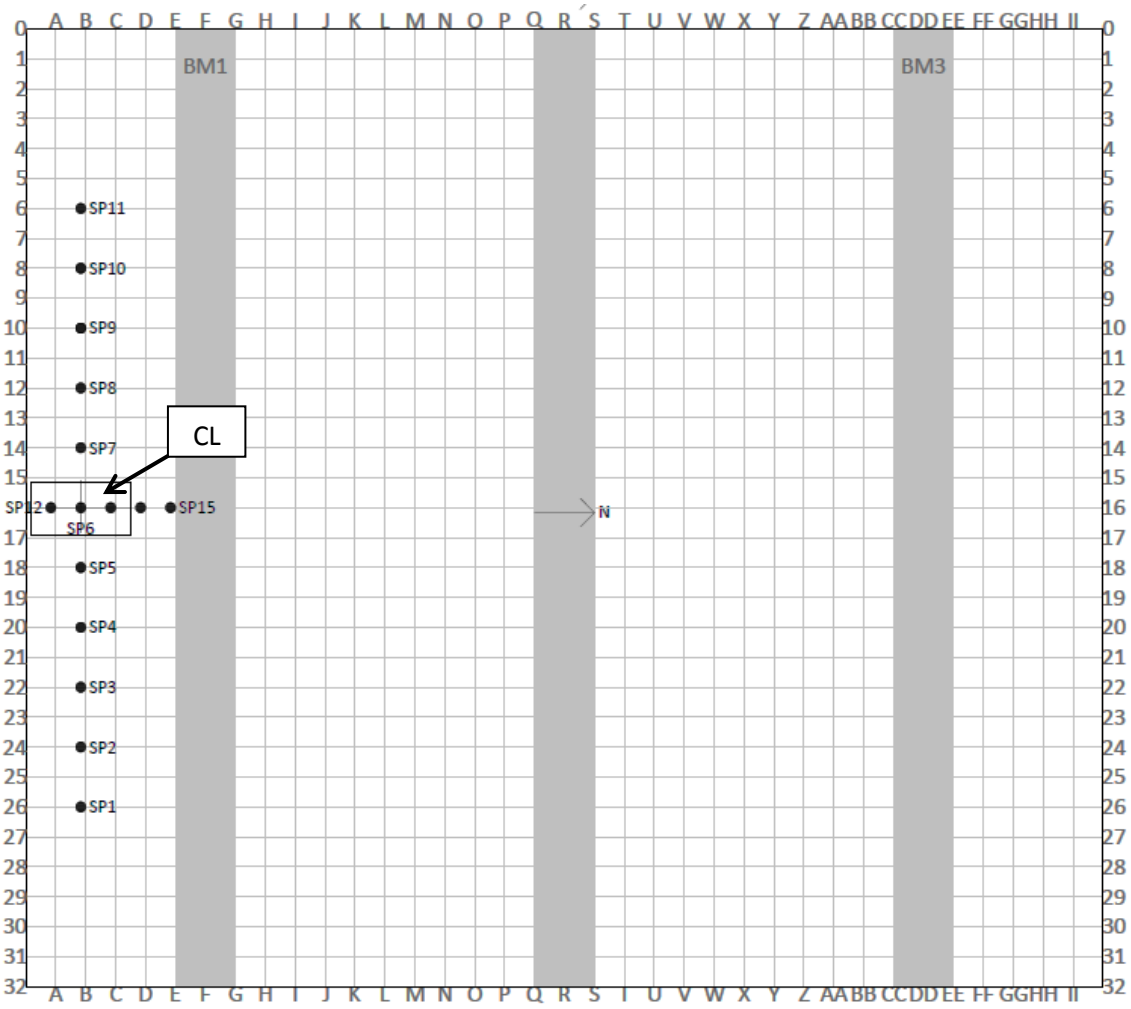

Figure 134. Location of String Potentiometers for LP3

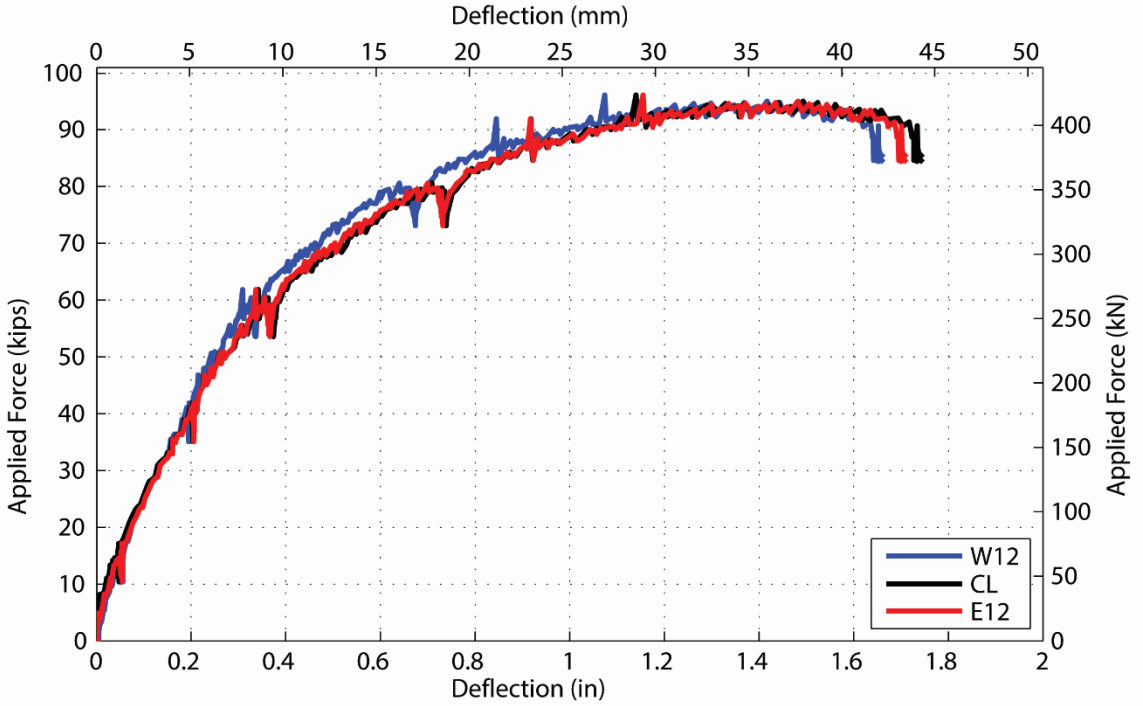

Figure 135. Force vs. Deflection for LP3

Figure 136 and Figure 137 present the deflected shape of the SFRC bridge deck under the influence of LP3 at various load points. The deflected shapes show the stiffness of the bridge deck in both the transverse and longitudinal directions. They provide insight of the condition of the bridge at both service and ultimate loads. At the service demand of 16 kips, the deflection of the specimen is approximately 0.06 inches. As the load increases, the stiffness of the structure decreases due to the opening of the cracks resulting in larger deflections. In comparison to LP1 and LP2, significant deflection is observed due to the lack of restraint at the free-edge of the deck.

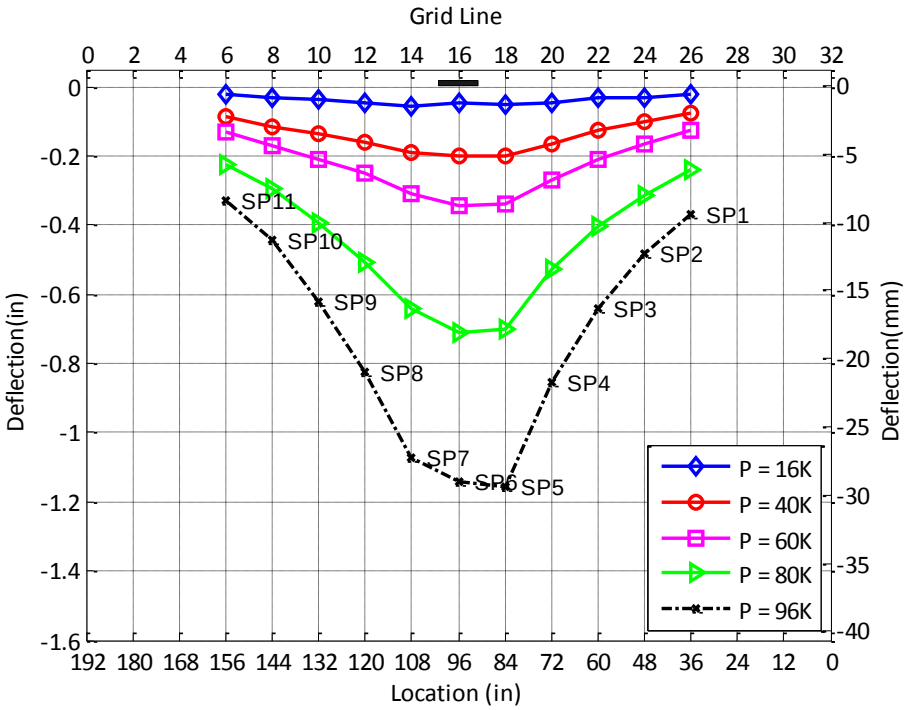

Figure 136. Deflection Profile of LP3 - Longitudinal Direction

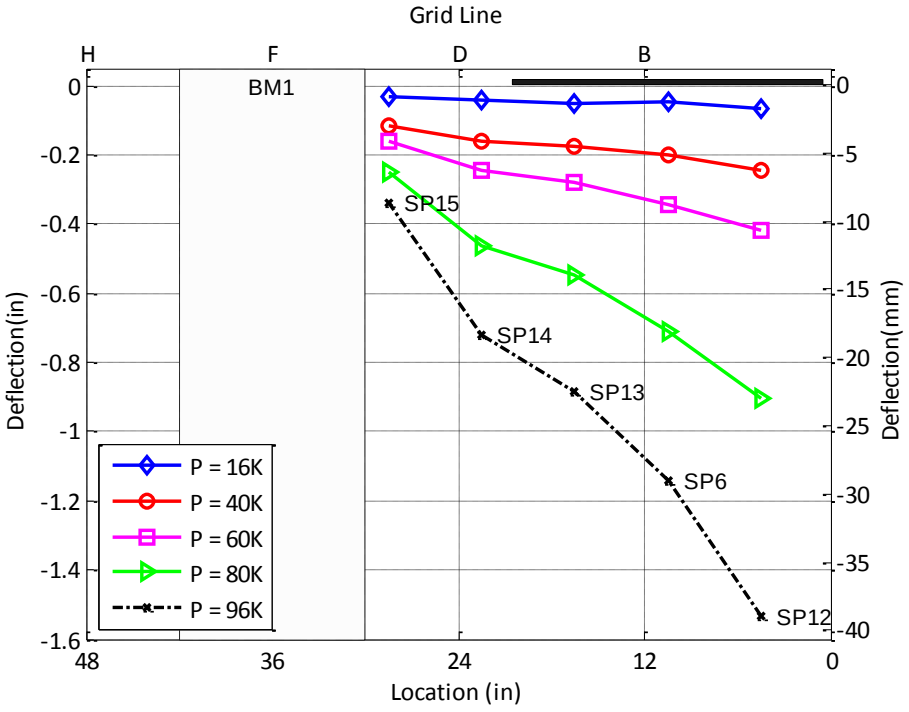

Figure 137. Deflection Profile of LP3 - Transverse Direction

A summary of the performance of the SFRC bridge deck due to LP3 is presented in Table 51. The deflection at both the service and ultimate demands is 0.05 inches and 0.13 inches respectively. The deflections at the service and ultimate demands for LP3 are significantly larger than LP1 and LP2 due to the lack of restraint. The maximum load achieved, 96 kips, is 260% larger than AASHTO ultimate demand of 37 kips.

Table 51. Load and Deflection Capacities of LP3

	Service (16 kips)		**Demand** (37 kips)	**Service Stress Limit** (24 ksi)	**Cracking**		**Maximum**	
	$\Delta_{service}$ in(mm)	σ_{steel} ksi (MPa)	Δ_{demand}, in(mm)	$P_{fs=24ksi}$ Kips (kN)	P_{crack} kips (kN)	Δ_{crack}, in(mm)	P_u kips (kN)	Δ_u in(mm)
LP3	0.05 (1.27)	-	0.18 (4.57)	-	30 (133)	0.13 (3.30)	96 (427)	1.74 (44.20)

5.5.6 LP4 – Individual Wheel

Figure 138 shows the final test, LP4, conducted on the bridge deck. LP4 is the same loading pattern tested in LP1, but at the opposite end of the SFRC bridge deck. Test LP4 was conducted to demonstrate both the repeatability of the results and the effect of pre-cracking on the performance of the bridge deck. Pre-existing cracks contributed to LP2 and LP3 as a result of the significant crack formation resulting from LP1.

The first new crack due to LP4 was not observed until 100 kips. The existing cracks from LP1, LP2, and LP3 reopened prior to initiation of the first crack. Increasing the load resulted in extension of existing cracks until a failure mechanism similar to LP1 formed as shown in Figure 139. LP4 achieved the same maximum load as LP1, 203 kips. The deflection of LP4 at 203 kips was approximately double the deflection of LP1 at 1.1 inches. The test concluded at the maximum load with the concrete suddenly failed. Figure 139 demonstrates the final crack pattern observed for LP4. The final crack pattern was consistent with the failure-mechanism observed for LP1.

Figure 138. Location of LP4 on SFRC Bridge Deck

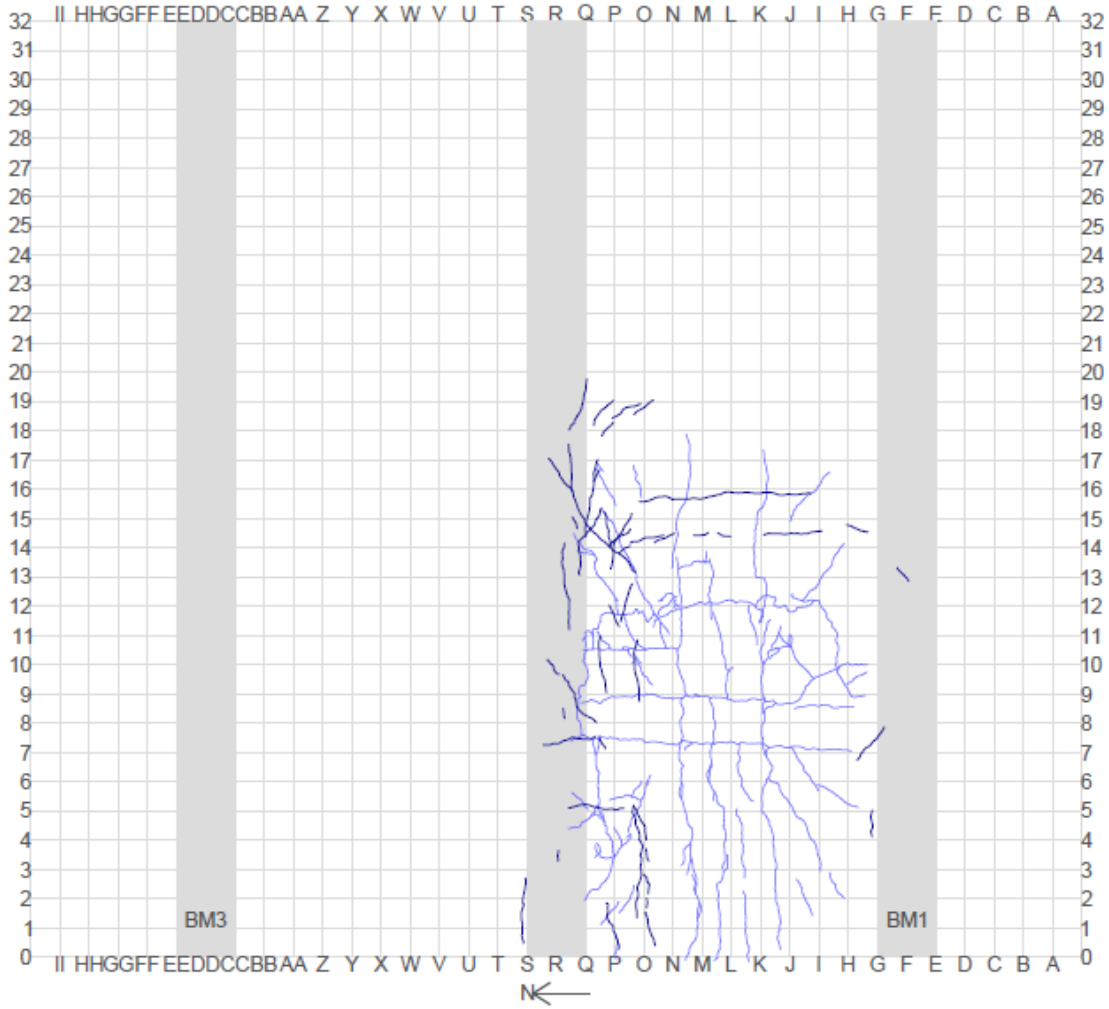

Figure 139. Final Crack Pattern for LP4

5.5.6.1 Crack Pattern

No new cracks were observed during the first load steps. Pre-existing cracks resulting from the previous tests likely opened during the early loading stages. At 100 kips the first new cracks were observed north of the load point; however, each of the cracks observed were extensions of the earlier tests' cracks. As the load increased, the web of cracks continued to connect, yet no new isolated cracks formed. During the loading phase up to 180 kips, a crack perpendicular to the supporting beams formed at Grid 15 adjacent to the north-south cracked formed during LP1. The longitudinal influence of LP4 appeared to match the influence of LP1. The north-south crack at grid 15 continued to propagate as the load increased until it connected the longitudinal cracks of the south and center beams. Crushing directly underneath the load point was observed during the final load step of 200 kips and 1.01 inches of deflection. The load was increased until failure of 203 kips.

After the completion of the test, the cracks on the underside of the bridge deck were mapped and recorded. The bottom cracks were consistent with the observed cracks on the top surface. The bottom cracks outlined the 10 by 20 steel plate and propagate outwards. The cracks on the west side of the load provided the radial cracks for the fan-mechanism while the cracks on the east side of the load continued approximately parallel to the beams as would be expected in one-way slab.

5.5.6.2 Capacity and Deflection

Figure 125 shows the location of the string potentiometers for LP2. Figure 141 shows the load-deflection relationship for LP4. Three displacements are shown in the figure: SP7 (E12), SP8 (CL), and SP9 (W12).

The initial stiffness of the full-scale specimen is approximately 585 kip/in and changes at approximately 75 kips. The first extension of existing cracks was observed during the load step to 100 kips; however, significant cracking was also present due to the prior tests. The string potentiometer at E12 dislodged from the specimen prior to reaching 150 kips. Further increasing the load resulted in a shallower force-deflection curve as the specimen approached its peak capacity. The level of damage resulted in a large decrease in stiffness as the bridge deflected more significantly without achieving an equivalent gain in load. The specimen achieved a maximum load of 203 kips at approximately 1.1 inches of deflection. The bridge deck suddenly failed after reaching this capacity.

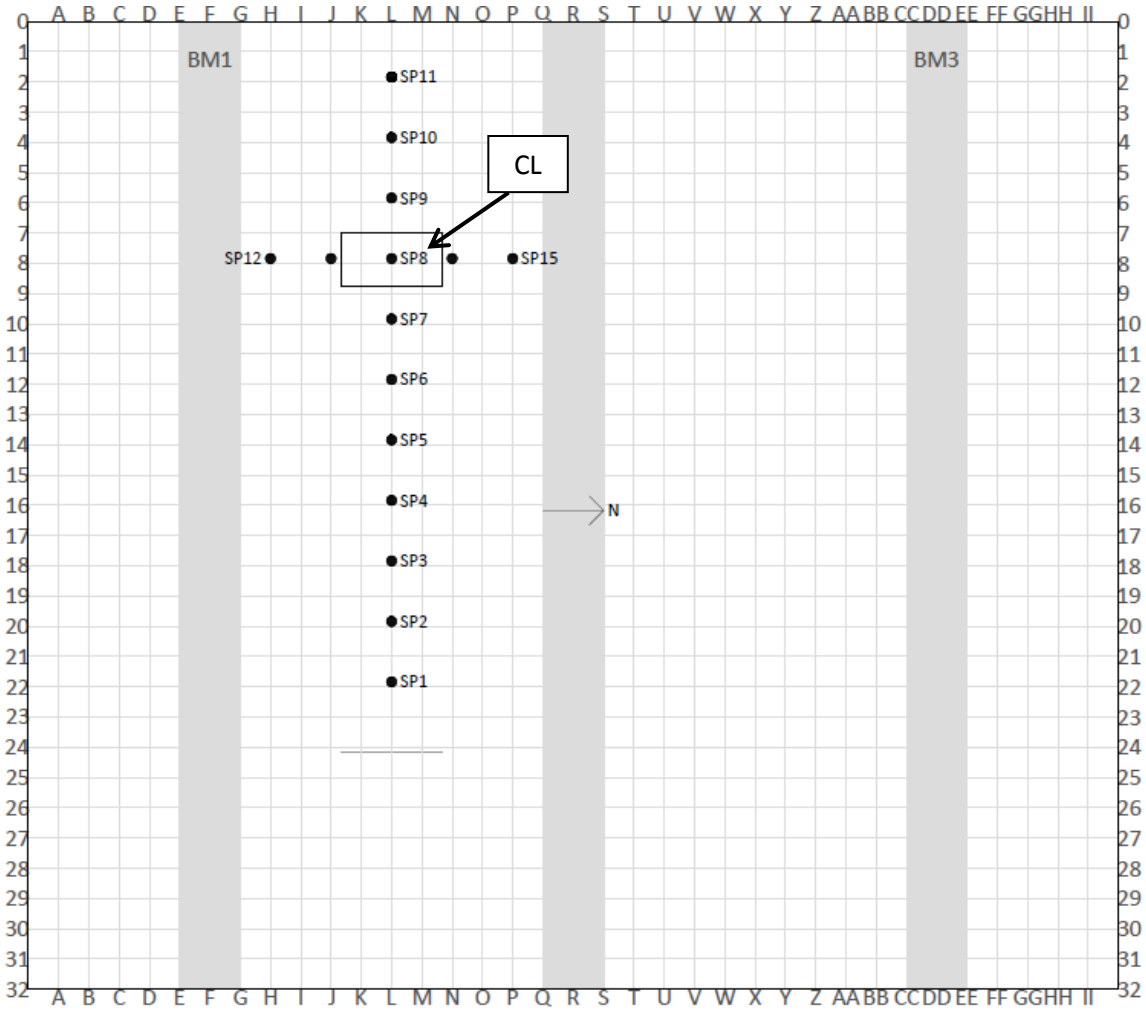

Figure 140. Location of String Potentiometers for LP4

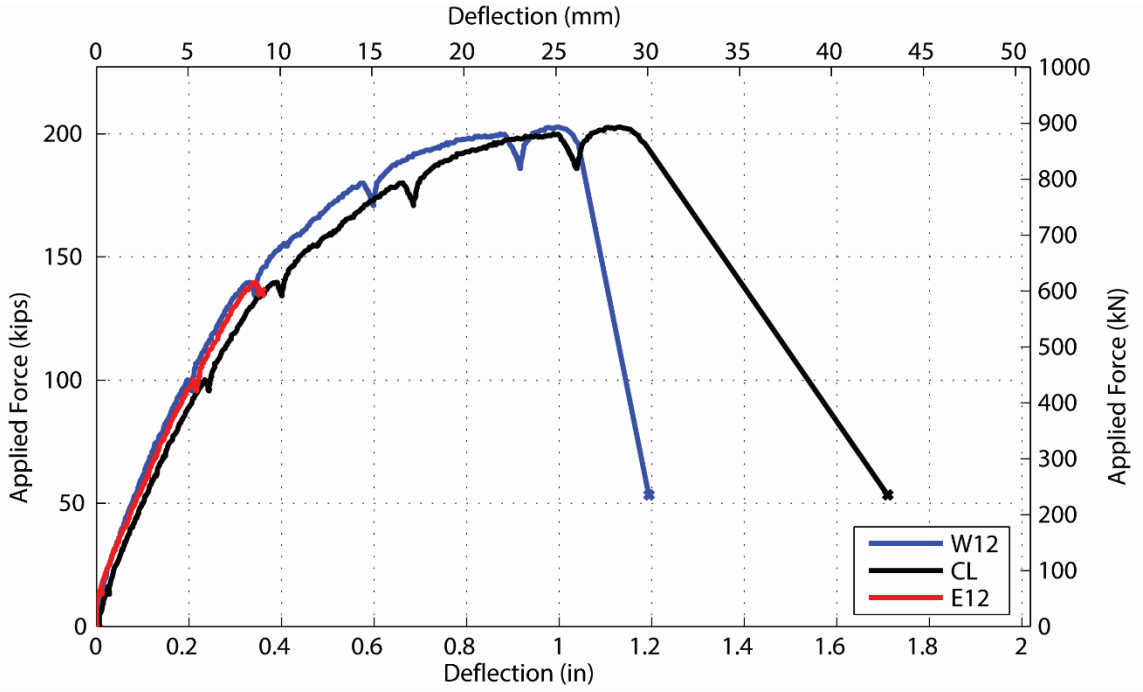

Figure 141. Force vs. Deflection for LP4

Figure 142 and Figure 143 present the deflected shape of the SFRC bridge deck under the influence of LP4 at various load points. The deflected shapes show the stiffness of the bridge deck in both the transverse and longitudinal directions. They provide insight of the condition of the bridge at both service and ultimate loads. At the service demand of 16 kips, the deflection of the specimen is approximately 0.06 inches. As the load increases, the stiffness of the structure decreases due to the opening of the cracks resulting in larger deflections. The deflections observed from LP4 are approximately 60% larger than those measured during LP1 at the same load points.

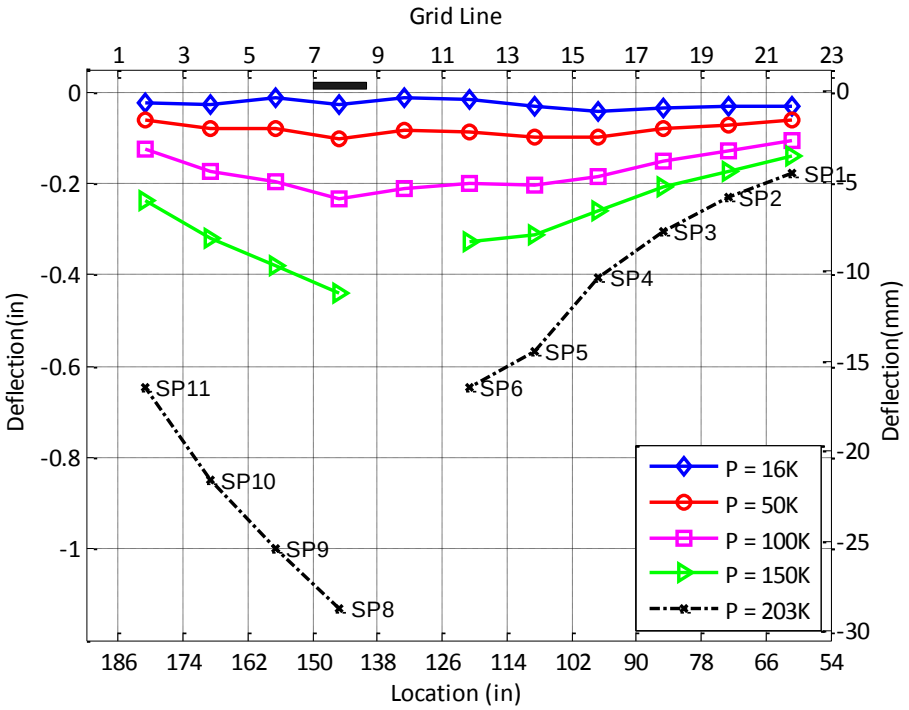

Figure 142. Deflection Profile of LP4 - Longitudinal Direction

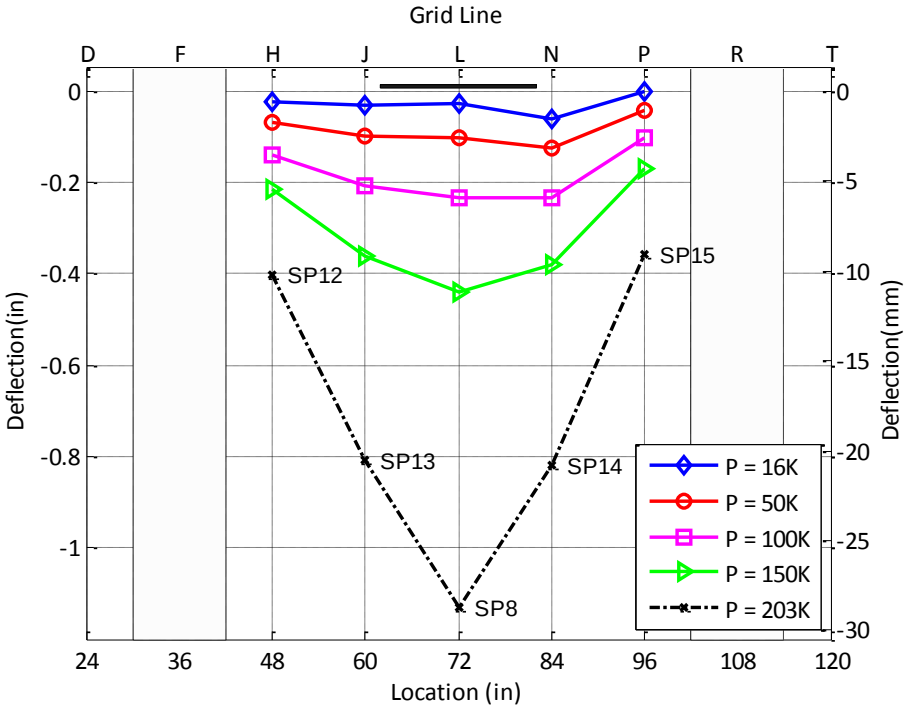

Figure 143. Deflection Profile of LP4 - Transverse Direction

A summary of the performance of the SFRC bridge deck due to LP4 is presented in Table 49. The deflection at both the service and ultimate demands is 0.01 and 0.05 respectively.

The stress in the steel reinforcement at the service demand is 20.8 ksi. The maximum load achieved, 203 kips, is approximately 550% larger than AASHTO ultimate demand of 37 kips. At the ADOT allowable stress limit of 24 ksi, the applied load is 61 kips, or 400% of the AASHTO service demand of 16 kips.

Table 52. Load and Deflection Capacities of LP4

	Service (16 kips)		**Demand** (37 kips)	**Service Stress Limit** (24 ksi)	**Cracking**		**Maximum**	
	$\Delta_{service}$ in(mm)	σ_{steel} ksi (MPa)	Δ_{demand}, in(mm)	$P_{fs=24ksi}$ Kips (kN)	P_{crack} kips (kN)	Δ_{crack}, in(mm)	P_u kips (kN)	Δ_u in(mm)
LP4	0.01 (0.25)	20.8 (143.4)	0.05 (1.27)	61 (271)	75 (333)	0.14 (3.56)	203 (903)	1.1 (27.94)

5.5.7 Discussion

5.5.7.1 Overall

Table 53 summarizes the results for each test. All reported strengths represent individual wheel loads. The SFRC specimen satisfied both the service and strength demands required by ADOT and AASHTO LRFD (2014). Under the influence of the service limit state of LP4, the stress in the steel reinforcement reaches a maximum of 21 ksi, or 87% of the stress permitted by ADOT design guidelines. The failure capacity of the SFRC specimen is 500% of the ultimate limit state defined by ADOT and AASHTO LRFD (2014).

The final crack pattern observed from each test is consistent with the expected flexural failure mechanism. The interior loads exhibit the typical fan-radial failure mechanism while the overhang test, LP3, yielded a trapezoidal failure mechanism. Every test, with the exception of the overhang test failed, in a sudden manner. However, the failures occur beyond the usable limit of the SFRC bridge deck. Furthermore, concrete crushing on the top surface was observed during LP2 and LP3 before the sudden failure occurred.

Each test conducted after LP1 presented evidence of their interaction with the initial test. The interaction is evident in the smaller pre-crack stiffness of LP2 through LP4 and the increased

ductility observed at both the service and strength limit states. The shared cracked regions did not affect the ultimate capacity of the structure as evident in comparing the capacity of LP1 and LP4.

Table 53. Summary of Results from SFRC Bridge Deck Test Program

	Service (16 kips)		**Demand** (37 kips)	**Service Stress Limit** (24 ksi)	**Cracking**		**Maximum Capacity**	
	$\Delta_{service}$ in(mm)	σ_{steel} ksi (MPa)	Δ_{demand}, in(mm)	$P_{fs=24ksi}$ Kips (kN)	P_{crack} kips (kN)	Δ_{crack}, in(mm)	P_u kips (kN)	Δ_u in(mm)
LP1	0.0 (0.0)	1.6 (11.0)	0.01 (0.25)	64 (284)	70 (311)	0.03 (0.76)	203 (903)	0.58 (14.73)
LP2	0.03 (0.76)	12 (82.7)	0.07 (1.78)	66 (147)	70 (311)	0.21 (5.33)	185 (823)	1.91 (48.51)
LP3	0.05 (1.27)	-	0.18 (4.57)	-	30 (133)	0.13 (3.30)	96 (427)	1.74 (44.20)
LP4	0.01 (0.25)	20.8 (143.4)	0.05 (1.27)	61 (271)	75 (333)	0.14 (3.56)	203 (903)	1.1 (27.94)

5.5.7.2 Comparison to Former Tests

Similar tests were conducted by others utilizing different reinforcing systems. Mander et al (2009) constructed a similar specimen utilizing precast, prestressed panels on one half of the bridge while the other half of the bridge was designed as cast-in-place with traditional reinforcement. Gar et al (2014) tested a deck prestressed AFRP full depth panels. Both investigation teams tested load patterns LP2 and LP3. Load pattern LP1 was tested by only Gar et al The bridge deck constructed by both research groups had a slightly thicker bridge deck at 200 mm (7.87 inches). Figure 144 through Figure 146 compare the force-deflection curves of each reinforcing system and Table 54 numerically summarizes the results.

Figure 144 compares the results from Gar et al (2014) and the SFRC full-scale test program for LP1. The general shape of the SFRC and AFRP specimens are similar; however, the SFRC specimen exhibits a larger pre-cracking stiffness. Additionally, the AFRP specimen cracks at a smaller applied load, 56kips, than the SFRC specimen, 70 kips. The post-cracking response of each

specimen yield a similar stiffness and peak load, 200 kips. The SFRC specimen achieves a larger deflection that the AFRP specimen before failure, 0.87 inches and 0.5 inches respectively.

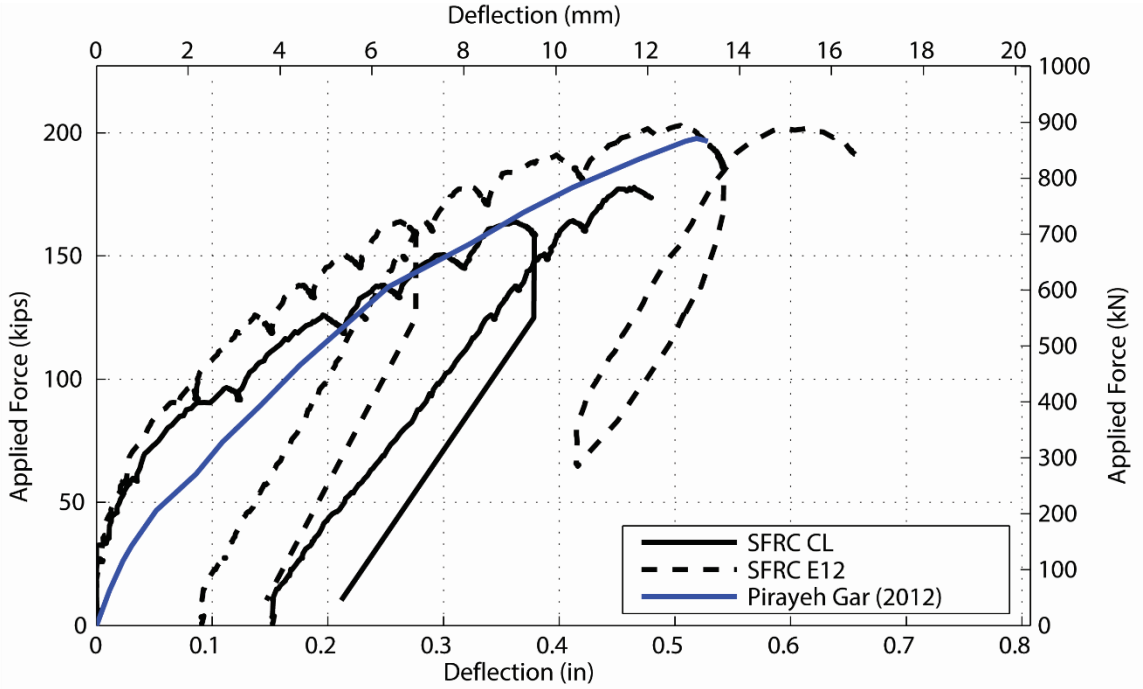

Figure 144. Force vs Deflection Comparison of SFRC and Others – LP1

Figure 145 compares LP2 for Mander et al (2009) and Gar et al (2014). The pre-cracking stiffness for both tests conducted by others are similar while the pre-cracking stiffness of the SFRC specimen is smaller. The reduced stiffness may be a result of the interaction of LP2 and LP1 and the thinner deck. Applying load pattern LP2 resulted in the opening of the existing cracks from LP1 prior to the propagation of new cracks due to LP2. The ultimate capacity of the SFRC specimen, 185 kips, is significantly larger than both prior tests, 127 kips and 157 kips for Mander et al and Gar et al, respectively.

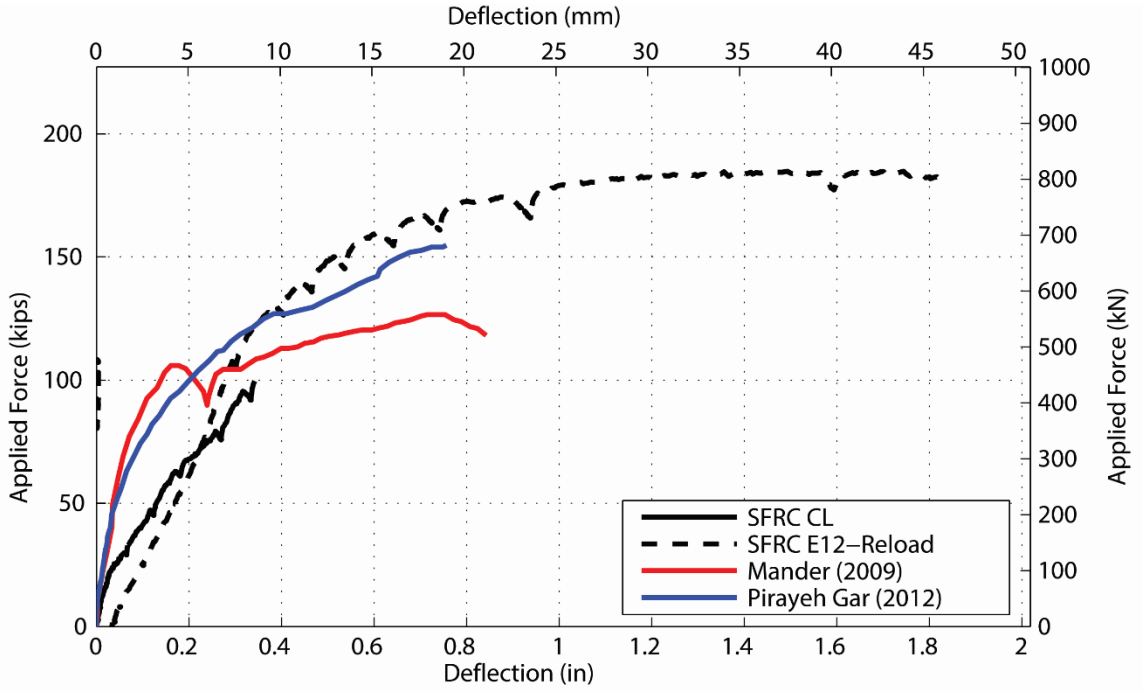

Figure 145. Force vs Deflection Comparison of SFRC and Others – LP2

The response of the SFRC specimen to the single wheel load on the overhang, LP3, is enveloped by the response of the test conducted by Mander et al and Gar et al as shown in Figure 146. The pre-crack stiffness of the SFRC and AFRP specimens are similar while the stiffness of the traditionally reinforced specimen is larger. Similar to LP2, an interaction between LP3 and LP1 is likely due to the extent of cracking resulting from LP1. The post-cracking stiffness of the SFRC specimen is larger than both of the other specimens. The SFRC specimen achieved the largest wheel load and deflection under this load pattern at 96 kips and 1.7 inches.

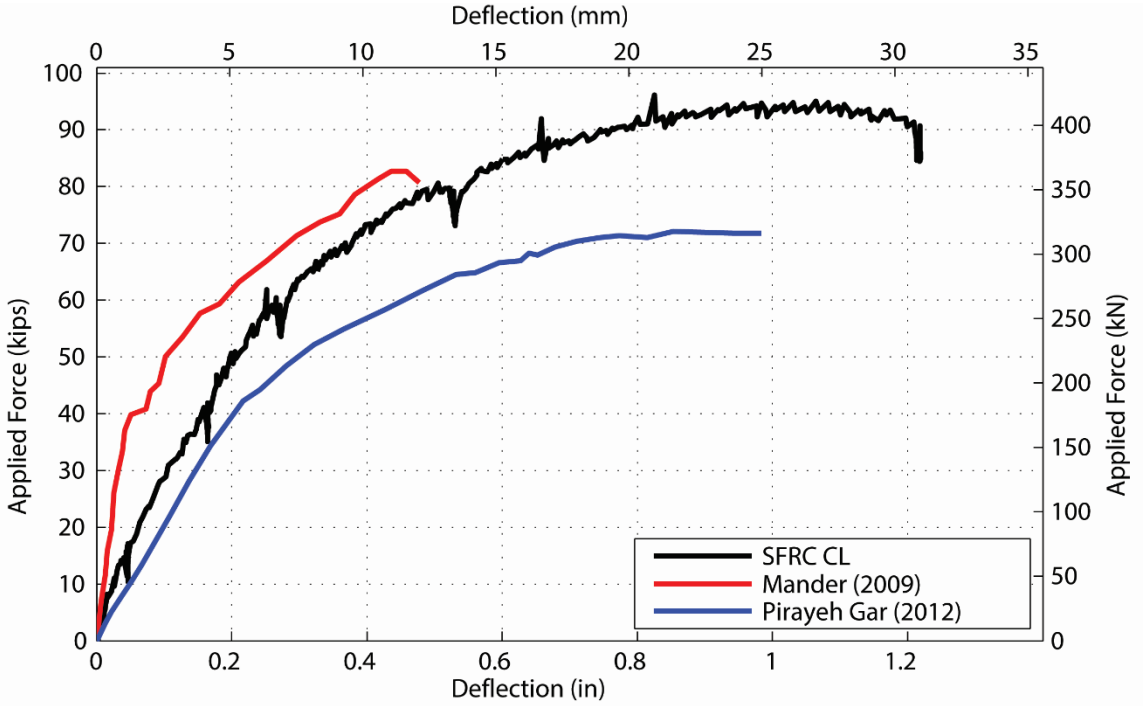

Figure 146. Force vs Deflection Comparison of SFRC and Others - LP3

Table 54. Comparison for Full-Scale Specimen and Tests by Others

	Failure Capacity kips (kN)			**Deflection at Failure** In (mm)		
	LP1/LP4	LP2	LP3	LP1/LP4	LP2	LP3
Mander et al (2009)	-	127 (565)	84 (374)	-	0.8 (21)	0.5 (12)
Gar et al (2014)	197 (880)	157 (700)	71 (320)	0.5 (13.5)	0.7 (19)	1.0 (25)
Full-Scale Specimen	203 (903)	185 (823)	96 (427)	0.84	1.91 (48.5)	1.7 (44.2)

5.6 Conclusion

The purpose of the full-scale SFRC bridge test was to demonstrate the effect of adding steel fibers to a two-way slab. The experimental program offered insight on the stiffness, deformability, failure mechanisms, and load capacity of a concrete bridge deck reinforced with steel bars and steel fibers. This was achieved by designing and constructing a full-scale specimen with SFRC and a reduced area of steel reinforcement to achieve a service and ultimate limit state consistent with a traditionally designed reinforced concrete bridge deck. Furthermore, the geometry was chosen to both represent actual bridges in use as well as conform to tests conducted in the past by other researchers. The similar geometries facilitate the additional comparison to actual data and observations recorded from controlled experiments. The following conclusions are made from the full-scale bridge test program:

- The overall performance of the SFRC bridge deck satisfies the serviceability and strength requirements of ADOT and AASHTO LRFD (2014). Under the influence of the service limit state, the stress in the steel reinforcement reaches a maximum of 21 ksi, or 87% of the stress permitted by ADOT design guidelines. The failure capacity of the SFRC specimen is 500% of the ultimate limit state defined by ADOT and AASHTO LRFD (2014).
- Comparing the experimental results to similar tests conducted by others demonstrate the benefits of adding steel fibers to the concrete matrix. The post-cracking stiffness of the SFRC specimen is superior to using prestressed AFRP strands or plain concrete with traditional reinforcement. The larger stiffness is an expected result of the “crack-bridging” behavior of the steel fibers. Furthermore, the addition of steel fibers resulted in larger ultimate capacities and maximum deflection before failure.
- The failure mechanism of SFRC matches the crack patterns expected from plain reinforced concrete. The only difference in the failure mechanism is the proliferation of cracks. Numerous cracks developed parallel to the interior beam due to the restraint provided and the “crack-bridging” effect of SFRC.
- The cracks and their location exhibit a flexural failure. Sudden failure of the bridge deck occurred well beyond the usable state of the bridge. Significant cracking and deflection had already been achieved prior to the failure of the specimen.

6. ANALYSIS OF EXPERIMENTAL RESULTS – SLAB STRIPS

6.1 Introduction

Reinforced concrete bridge decks are commonly designed based on the effective strip method prescribed in the AASHTO LFRD Bridge Design Guidelines (2014). The effective strip method distributes the wheel load parallel to traffic, or in the longitudinal direction of the deck, a distance determined based on the girder spacing and location of the span relative to the supporting girders, interior or exterior. The design of a reinforced concrete bridge deck is directly related to the capacity of the section per unit width as a result of the AASHTO procedure.

The aim of this Section is to provide an analysis of each slab strip tested in both experimental test programs. The moment-curvature response of the experimental results is computed and evaluated in Section 6.2. The analysis will provide the basis for a design procedure utilizing SFRC for bridge decks. Material data determined from standard ASTM testing is compared to traditional constitutive models in Section 6.3 where theoretical moment-curvature relationships are and compared to the experimental relationships. Finally, Section 6.5 compares the experimental results to the conclusions made in the case study analysis presented in 3.

6.2 Experimental Moment Curvature

The moment-curvature relationship of the slab-strip specimens were computed at midspan utilizing two methods: finite difference and the strain profile.

To compute curvature with the finite difference method, the deflection measured by the string pots is utilized. The second derivative of the deflection profile yields the curvature profile of the specimen. The second derivative is computed numerically using the finite difference method as follows:

$$\varphi = \frac{d^2 z}{dx^2} \tag{27}$$

$$\varphi_j = \frac{z_{j-1} - 2z_j + z_{j+1}}{\Delta x^2} \tag{28}$$

Where φ is the curvature at string potentiometer j, z is the vertical deflection measured by string potentiometer j, and Δx is the horizontal spacing of string potentiometers.

The curvature was also computed using the strain profile inferred from the LVDTs attached to the east face of the specimen. The strain at the top and bottom of the specimen is determined based on the horizontal displacement measured by each LVDT and the gauge length of the LVDTs.

The slope of the strain profile is used to compute the curvature of the specimen at the midspan. This method provides the average curvature over the entire gauge length of the LVDT.

$$\varepsilon_j = \frac{\Delta x_j}{x} \quad (29)$$

$$\varphi = \tan\frac{y}{\varepsilon_1 + \varepsilon_2} \quad (30)$$

Where ε_j is the strain at LVDT j, x is the LVDT gauge length, and y is the vertical distance between top and bottom LVDTs.

Figure 147 through Figure 150 show the moment-curvature relationship for the strips tested in the slab strip experimental program presented in 0. The experimental moment-curvature relationships are consistent with physical observations and the measured force-deflection relationships. The curves demonstrate a change in stiffness at the cracking moment and plateau when the steel yields and failure localizes in the critical crack. After yielding occurs, the moment capacity of the specimens with steel reinforcement located at the bottom of the specimen remains nearly constant with a very slight decrease. The moment capacity of the specimens with steel reinforcement located at the center gradually declines as the curvature increases. The decrease in the moment capacity is likely a result of the decrease in the tension capacity of the SFRC. The effect is more pronounced in the specimens with the steel reinforcement located at the center than the specimens with steel at the bottom due to the smaller moment arm to the center of the specimen. The end of the moment-curvature relationships signifies the removal of the string potentiometers from the slab-strips to prevent them from damage.

The experimental moment-curvature relationship determined by both methods show an overall consistency between each other. The curves from both methods show agreement in the pre-crack and plateau portion of the curves. However, a slight difference is observed in the post-crack stiffness between the two methods. The LVDT curve resulted in a smaller post-crack stiffness in five specimens: s7505BTM24, s7505BTM25, s7505BTM35, s9005BTM25, and s9005BTM35. The LVDT response for specimen s9005BTM23 resulted in a larger post-crack stiffness compared to the string pot response.

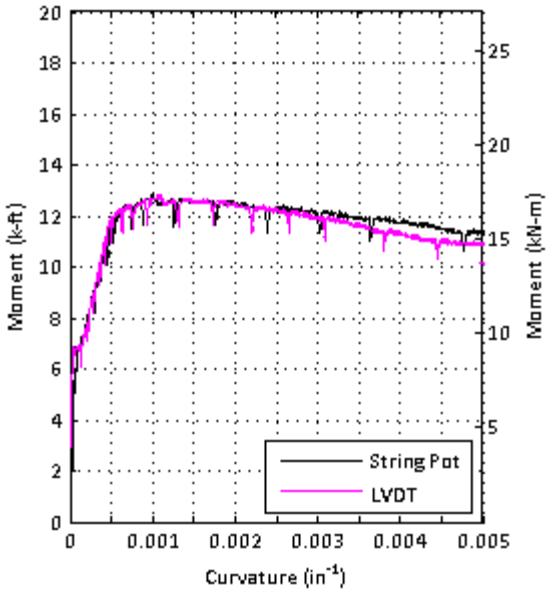

(a) s7505BTM23

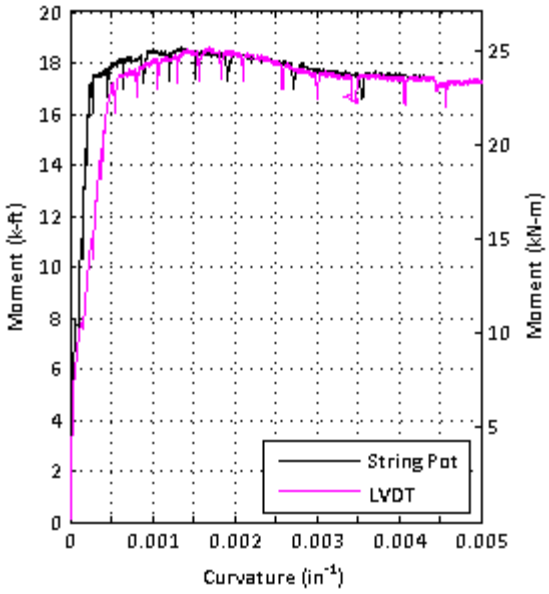

(b) s7505BTM24

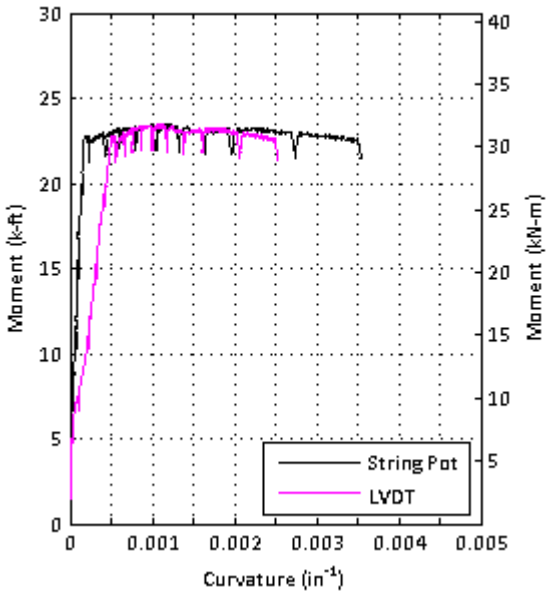

(c) s7505BTM25

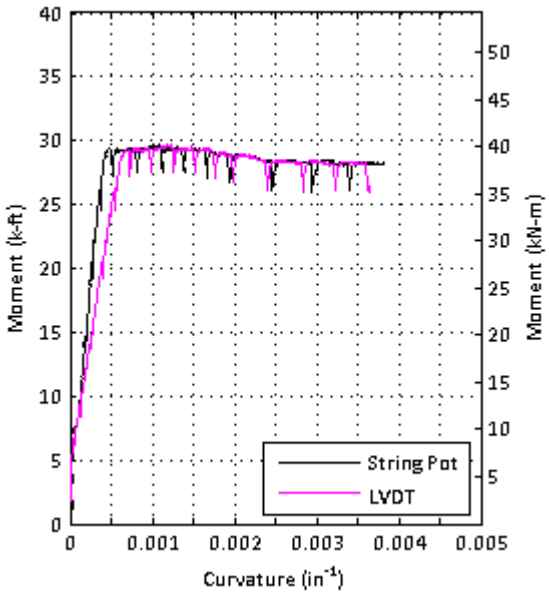

(d) s7505BTM35

Figure 147. Experimental Moment Curvature Relationship for s7505BTM##

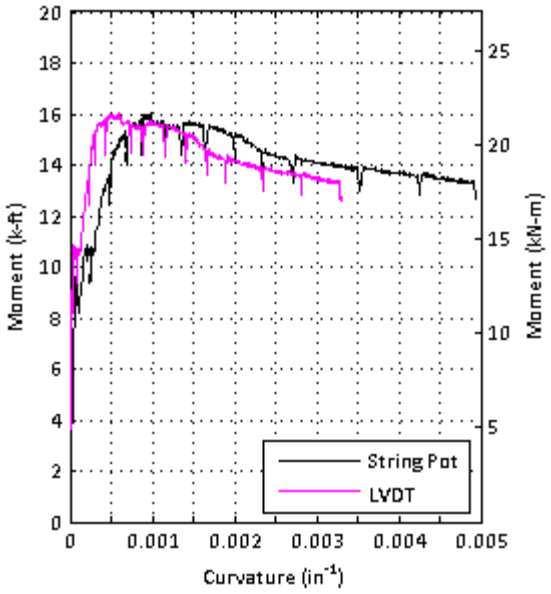

(a) s9005BTM23

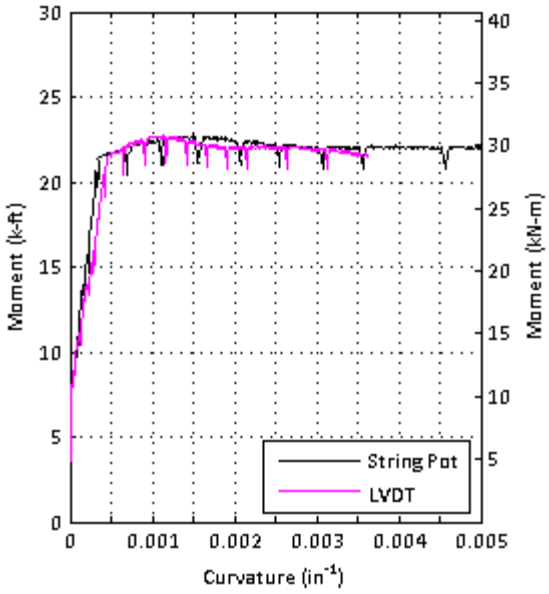

(b) s9005BTM24

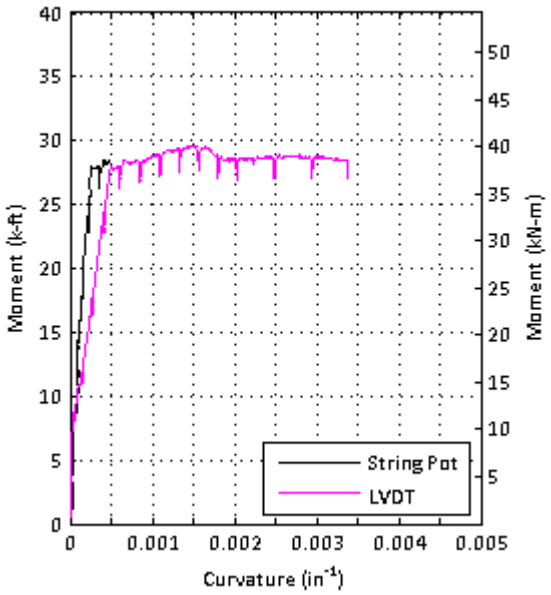

(c) s9005BTM25

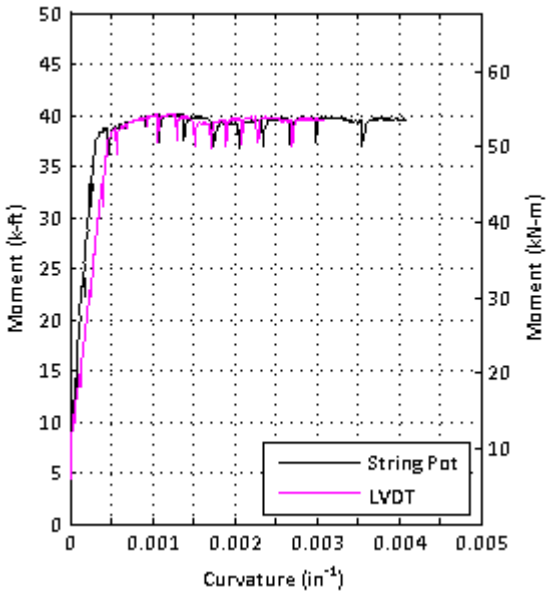

(d) s9005BTM35

Figure 148. Experimental Moment Curvature Relationship for s9005BTM##

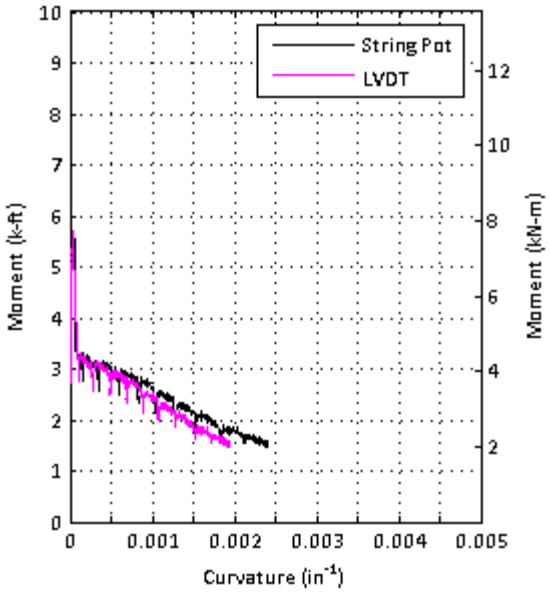

(a) s7505NOS00

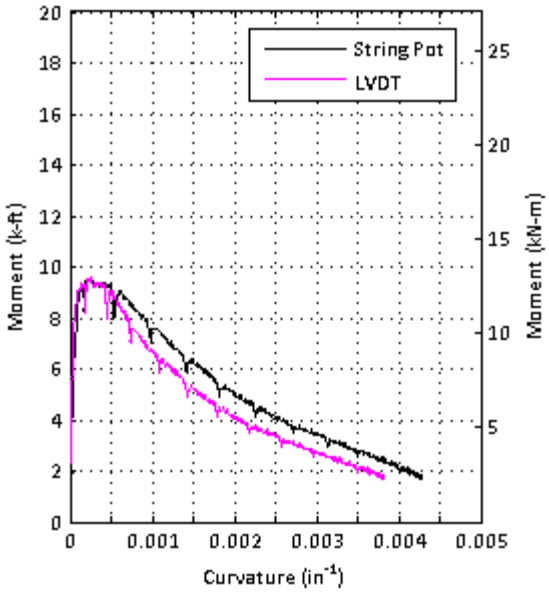

(b) s7520NOS00

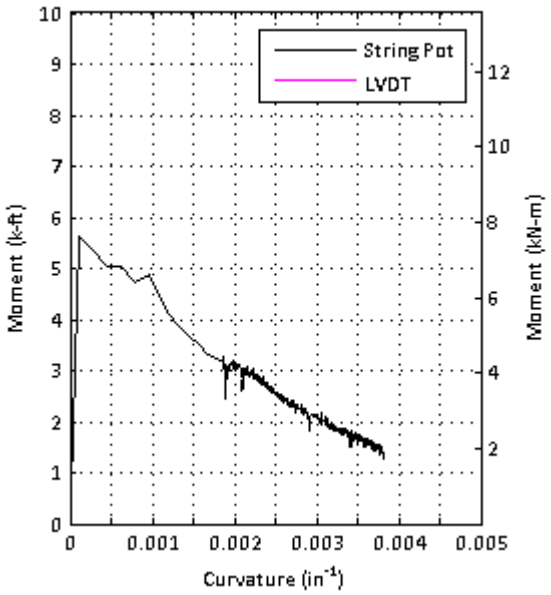

(c) s9005NOS00

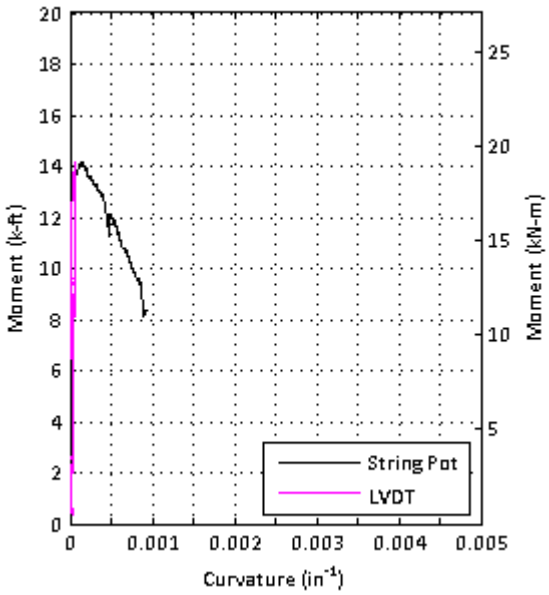

(d) s9020NOS00

Figure 149. Experimental Moment Curvature Relationship for s####NOS00

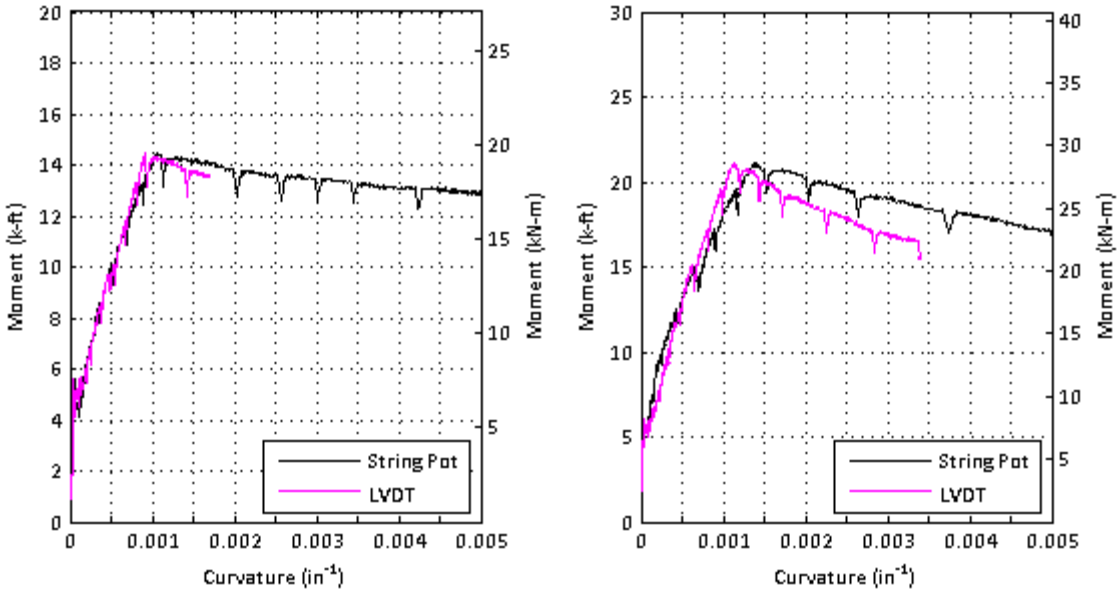

(a) s7505CTR25 (b) s7505CTR35

Figure 150. Experimental Moment Curvature Relationship for s7505CTR##

Figure 151 show the moment-curvature relationship for the companion strips tested in the bridge deck experimental program presented in 5. Deck strip specimen d7505BTM24 was partially unloaded and then reloaded during its testing. Only the reloading portion of the moment-curvature relationship is shown for the string potentiometers due to excessive “noise” captured during the unloading phase.

The moment-curvature response determined by the LVDT and string potentiometer are in agreement until the bend-over point, or yield moment. Beyond the yield moment, the LVDT curve is stiffer than string potentiometer curve resulting in a left shift of the moment-curvature relationship. The deflection profile of d7505BTM24 and d7500BTM24 shown in Figure 152 show the specimen deformed unsymmetrically about its centerline likely resulting in the discrepancy between the moment-curvature curves.

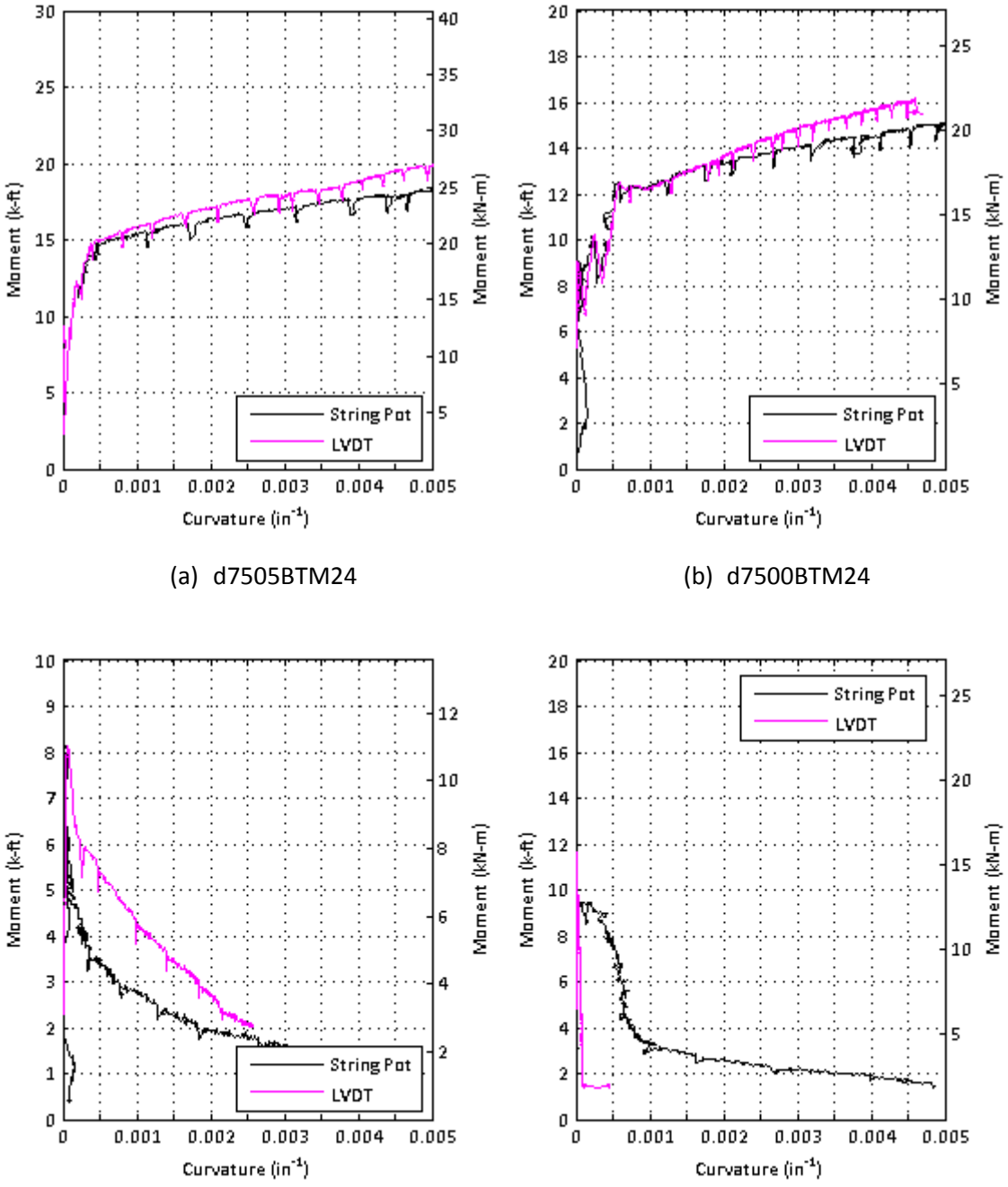

(a) d7505BTM24

(b) d7500BTM24

(c) d7505NOS00

(d) d9005NOS00

Figure 151. Experimental Moment Curvature Relationship for Deck Companion Strips

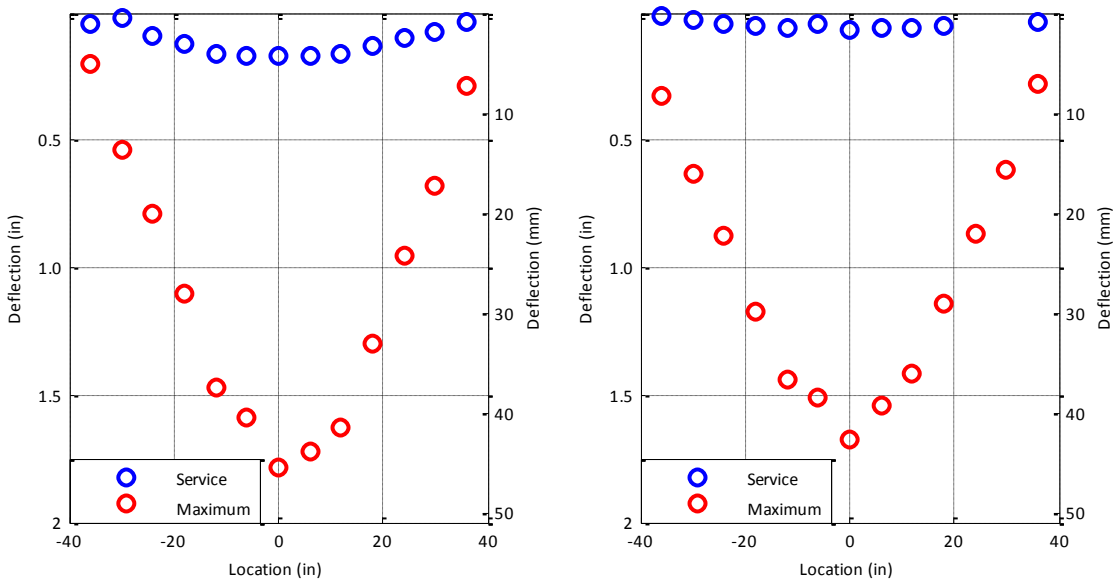

(a) d7500BTM24 (b) d7505BTM24

Figure 152. Deflection Profile of Deck Companion Strips

6.3 Theoretical Moment Curvature

Standard ASTM tests were conducted to determine the constitutive models that are used in a moment-curvature analysis of the slab strip specimens. The compressive response for SFRC is determined by test ASTM C39 and then compared with the constitutive model utilized in the case studies presented in Section 3. A standard test does not exist to determine the tensile response of SFRC directly. The general response proposed by others, RILEM (2003), Soranakom and Mobasher (2007), and fib (2013) is used in an inverse analysis to determine the residual strength of the concrete. The residual strength parameter in the general response is adjusted until the resulting theoretical moment-curvature response fits the experimental moment-curvature.

6.3.1 Compression Models

Table 55 summarizes the results of test ASTM C39 for each SFRC and plain concrete mixture used in the experimental programs. The reported values are the average 28-day response of three specimens for each test. The modulus of elasticity as determined by AASHTO (2014) is presented to demonstrate the effect of fibers on the plain concrete response. Figure 153 compares the measured compression response of SFRC to the modified Kent-Park model for plain concrete with a post-peak descending slope, Z, of 50 computed as follows:

$$f_c = f_c'\left(\frac{2\varepsilon_c}{\varepsilon_0} - \left(\frac{\varepsilon_c}{\varepsilon_0}\right)^2\right) for\ \varepsilon_c < \varepsilon_0, \quad (31)$$

$$f_c = f_c'\left(1 - Z(\varepsilon_c - \varepsilon_0)\right) for\ \varepsilon_c > \varepsilon_0 \quad (32)$$

Where ε_c is the strain at any point, f_c is the stress at any point, ε_0 is the strain at maximum compressive strength, f_c' is the maximum compressive strength, and Z is the slope of descending branch of the stress-strain response.

The compression model was chosen to be consistent with the analysis performed in the case studies presented in 3. Figure 153 shows that the theoretical compression model accurately represents the experimental compression response determined from ASTM C39. Therefore, the modified Kent-Park model shown in Section 3 is used as the SFRC compression model for the moment-curvature analysis.

Table 55. Average Response of ASTM C39

Program	Modulus of Elasticity, Experimental (ksi)	Modulus of Elasticity, AASHTO (2014) (ksi)	Compressive Strength, f'c (ksi)
Slab Strip V_f = 0.5%	4027	4071	5.1
Slab Strip V_f = 2.0%	4170	4341	5.8
Bridge Deck V_f = 0.5%	5980	4630	6.6

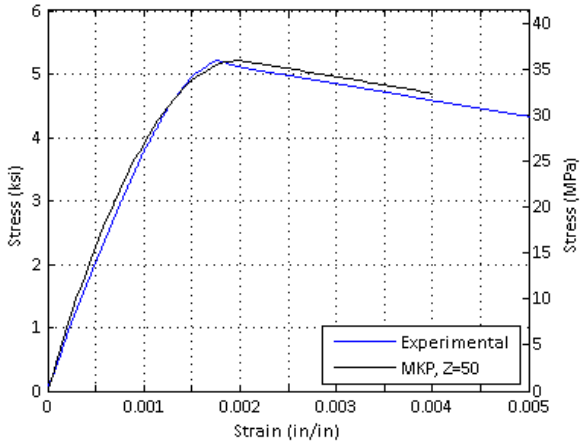

Figure 153. ASTM C39 Average Compression Results (0.5% Beam Program) and Modified Kent Park

6.3.2 Tension Models

A standard test to directly determine the tensile behavior of SFRC has not been adopted by ASTM. Flexural test ASTM C1609 indirectly characterizes the tensile behavior of SFRC; however, a translation of the flexural data to a tensile stress-strain response has not been adopted. As a result, the SFRC tensile response for the moment-curvature is determined utilizing a curve-fitting approach with the general parameters of RILEM (2003), Soranakom and Mobasher (2007), and fib (2013).

The elastic pre-crack response of plain concrete is also used for SFRC. After cracking, the residual stress of the SFRC decreases linearly similar to the model utilized by fib (2013) shown in Figure 154. The residual stress decreases until it has lost all capacity at 0.025. The tensile model used in the moment-curvature analysis is defined by the three parameters, modulus of elasticity, cracking stress, and residual stress. Standard test ASTM C1609 provides the modulus of elasticity and cracking stress for the SFRC mix. An inverse analysis is used to determine the final parameter required to describe the generalized tension response of SFRC.

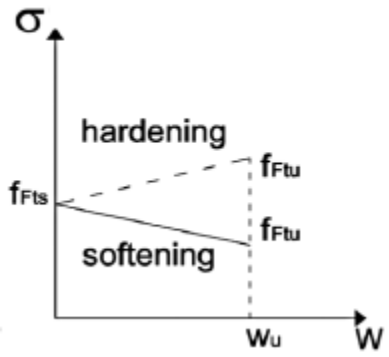

Figure 154. Pre-Crack Constitutive Model for SFRC (fib 2013)

Specimens s7505NOS00 and s9005NOS00 were utilized in determining the SFRC tensile model for the slab-strip program. Figure 155 and Figure 156 show the tensile model for the SFRC used for the inverse analysis. The inverse analysis was conducted by changing the initial residual stress of the SFRC model and performing a theoretical moment-curvature analysis of the two SFRC specimens without steel reinforcement. The fit of the tensile model was evaluated based on the moment curvature response after cracking occurs. The theoretical moment capacity was

compared to the experimental moment capacity at 15 different curvatures following the peak moment.

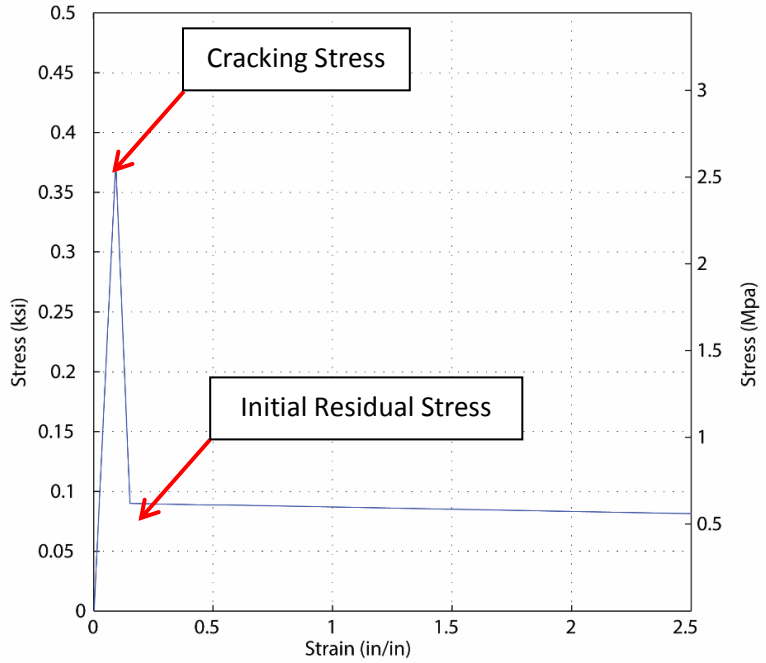

Figure 155. SFRC Tensile Model - Elastic Region and Initial Residual Stress

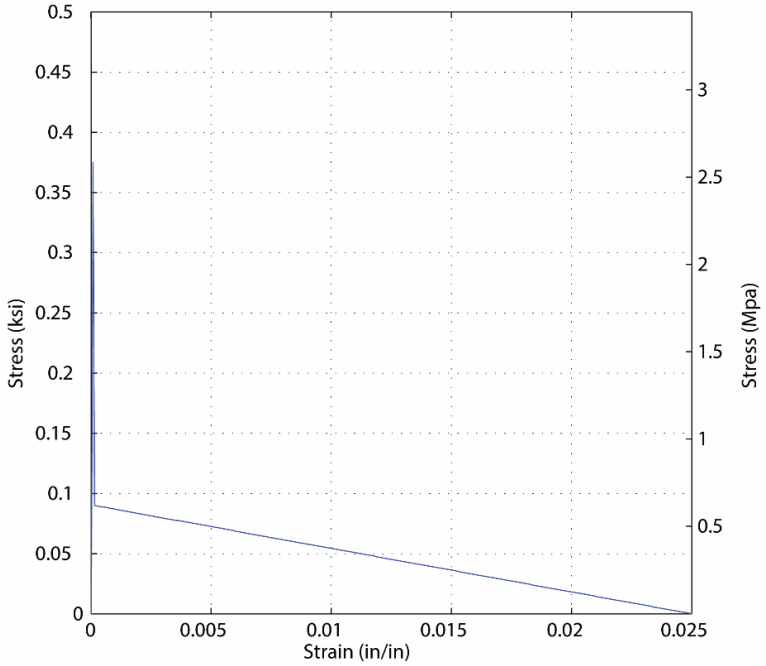

Figure 156. Post-Crack Constitutive Models for SFRC

Figure 157 and Figure 158 show the theoretical moment-curvature response for s7505NOS00 and s9005NOS00 using the tensile model shown in Figure 156. A residual tensile stress of 90 psi minimized the error of the portion of the curve bound by the red lines in the figures.

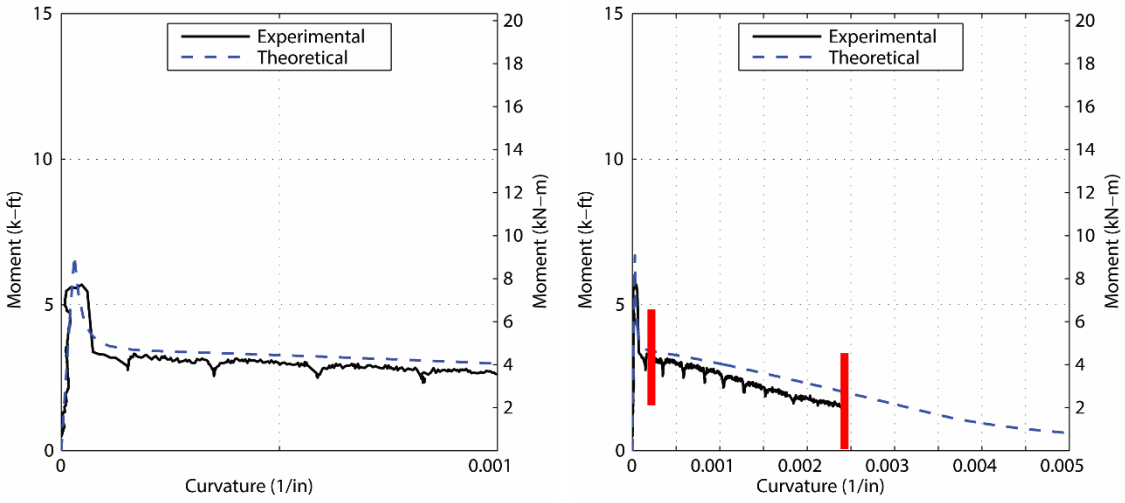

(a) Pre-Crack Response (b) Entire Response

Figure 157. Theoretical and Experimental Moment-Curvature Response - s7505NOS00

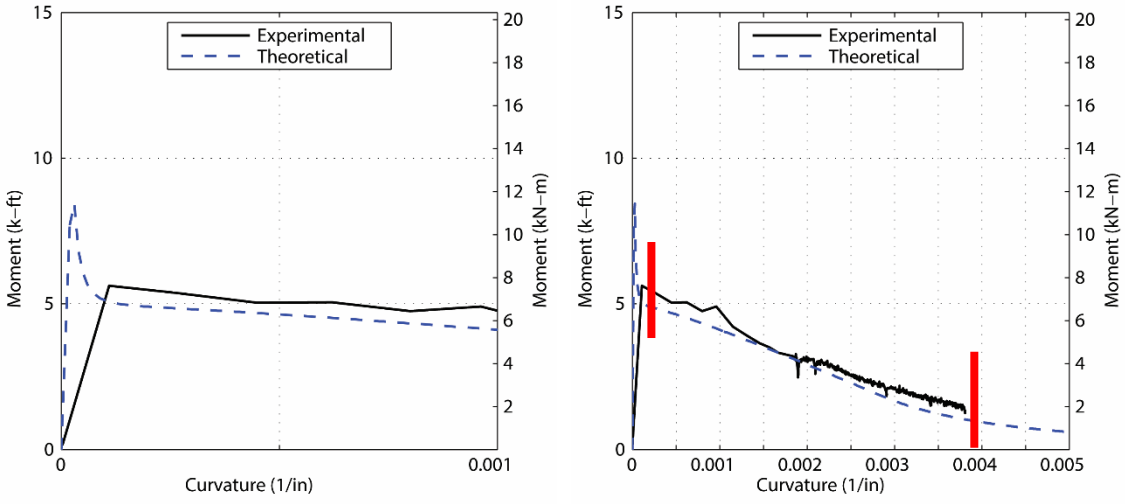

(a) Pre-Crack Response (b) Entire Response

Figure 158. Theoretical and Experimental Moment-Curvature Response – s9005NOS00

The inverse analysis was also conducted for the slab-strips with 0.5% fibers by volume cast alongside the bridge deck and the slab-strips with 2.0% fibers by volume shown in Figure 159 and Figure 160 respectively. The SFRC tensile model used for the deck strips with 0.5% fiber had a consistent residual strength of 90 psi and a larger cracking stress of 810 psi as a result of its larger compressive strength. The residual stress of the SFRC specimen with 2.0% fibers had a residual stress of 230 psi. The tensile models are summarized in Table 56.

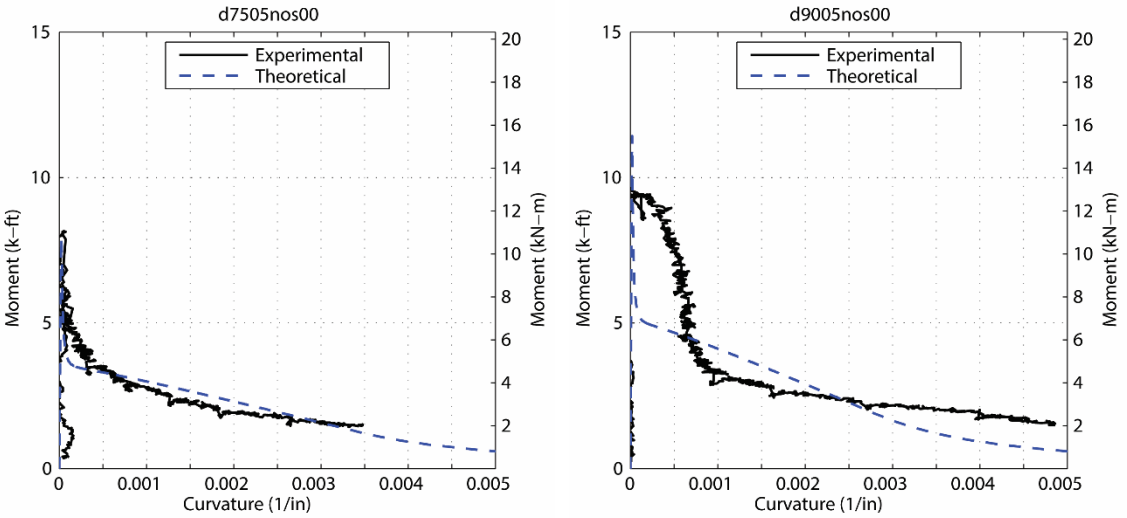

Figure 159. Theoretical and Experimental Moment-Curvature Response for d7505NOS00 and d9005NOS00

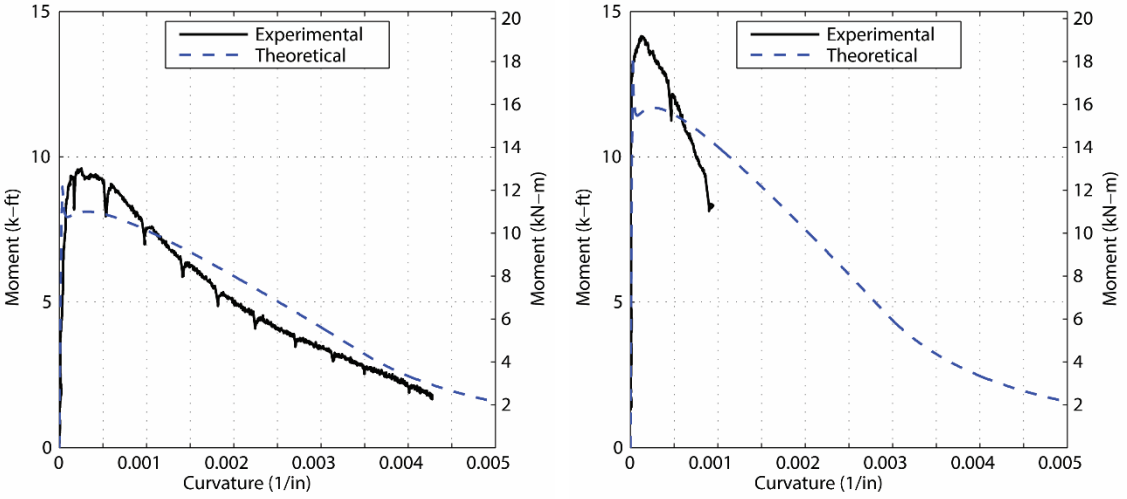

Figure 160. Theoretical and Experimental Moment-Curvature Response for s7520NOS00 and s9020NOS00

Table 56 summarizes the tensile model and residual strength used to determine the theoretical moment-curvature relationship. The residual strength for each SFRC concrete mix was determined based on the experimental results.

Table 56. Summary of ASTM C1609 Results and Tension Models

Dosage Rate	E (ksi)	f_{cr} (ksi)	f_r (ksi)
Slab Strip Program			
0.5%	4027	0.48	0.09
2.0%	4170	0.68	0.23
Bridge Deck Program			
0.5%	5980	0.81	0.09

6.3.3 Moment-Curvature

Figure 165 through Figure 166 show the moment-curvature relationship for each slab strip specimen with steel reinforcement. The experimental moment-curvature relationship determined based on the string potentiometers is represented by a solid black line. The theoretical relationship is shown by a dashed blue. Finally, a solid gray line is included on each plot showing the theoretical moment-curvature response for a plain concrete section with the same steel reinforcement. The theoretical models are compared to the experimental models based on pre-crack stiffness, post-crack stiffness to yield, and the moment plateau.

Figure 165 shows the theoretical and experimental moment-curvature response for the slab-strip specimens with 0.5% fiber by volume, steel reinforcement at the bottom of the specimen, and a depth of 7.5 inches. The theoretical model accurately captures the experimental behavior of each slab strip prior to the moment plateau with the exception of s7505BTM24 and s7505BTM25. The post-crack stiffness of s7505BTM24 and s7505BTM25 are larger than the stiffness of the theoretical models. This trend was also observed between the moment-curvature response determined from string potentiometers and the LVDT. The string potentiometers resulted in a larger post-crack stiffness of the slab strip than the LVDT. The deflection profiles of s7505BTM24 and s7505BTM25 show an unsymmetrical deflection of the specimen about its centerline. The uneven bending of the specimen shown in Figure 162 is the probable cause for the increased stiffness reported by the string potentiometers.

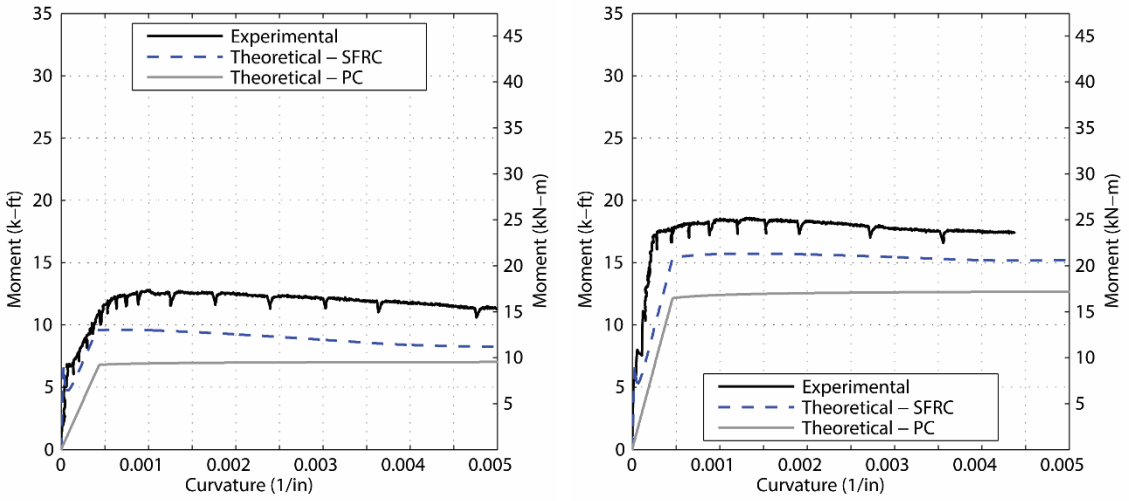

(a) s7505BTM23

(b) s7505BTM24

(c) s7505BTM25

(d) s7505BTM35

Figure 161. Theoretical Moment-Curvature Relationship for Slab Strips s7505BTM##

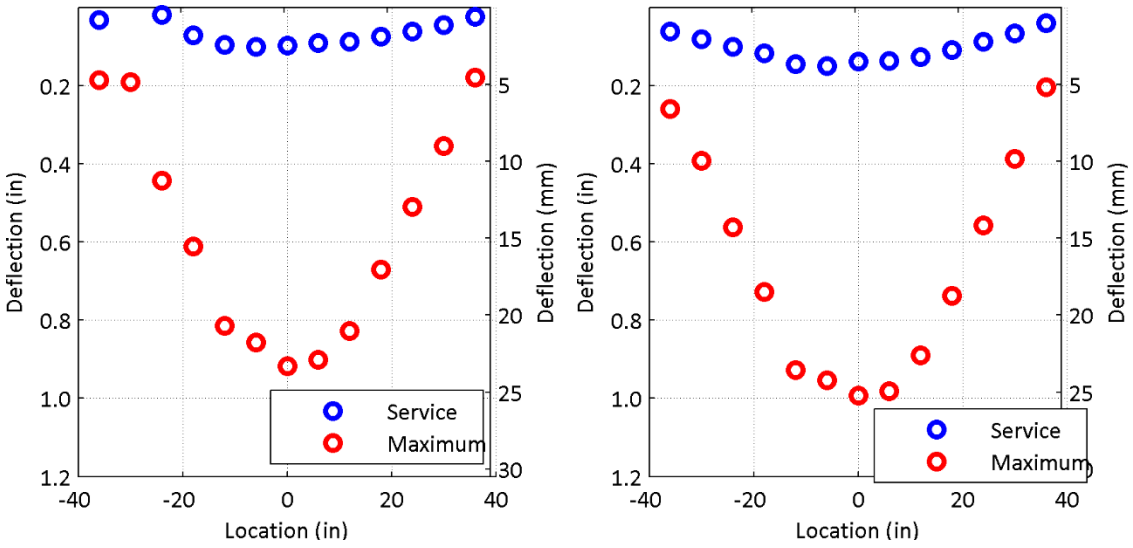

(a) s7505BTM24 (a) s7505BTM25

Figure 162. Deflection Profiles of s7505BTM24 and s7505BTM25

The behavior, or shape, of the theoretical moment-curvature response after yielding occurs is consistent with the behavior of the experimental results. The moment in the theoretical model gradually declines as the curvature of the specimen increases. At a large curvature the tension capacity in the theoretical model achieves the maximum tensile strain for SFRC and the moment begins to decline ultimately converging with the PC model.

While the general behavior of the theoretical responses adheres to the behavior of the experimental results, the moment at yield and beyond is different. The theoretical model underpredict the moment capacity of the SFRC specimens with a low steel reinforcement ratio. The underprediction of the capacity decreases as the reinforcement ratio increases. As demonstrated by specimen s7505BTM35, a critical reinforcement ratio exists at which point the theoretical models begin to overpredict the moment capacity of the specimen. At low reinforcement ratios, the steel fibers contribute significantly to the moment-curvature response of the specimen increasing its yield and nominal moment. As the reinforcement ratio increases, the benefits of the steel fibers diminish as the moment-curvature response is dominated by the steel reinforcement ratio.

This trend can be explained by examining the resultant tension force and moment contributions of the SFRC and steel reinforcement as shown in Figure 163. The neutral axis depth is not largely

affected by adding steel reinforcement resulting in a near constant SFRC resultant force while the steel resultant force sees a significant increase. Therefore, the moment-curvature response of the SFRC specimen will begin to converge to the response of a PC specimen as the steel reinforcement ratio increases. This can be observed in Figure 161 as the PC curve represented by the gray line begins to accurately capture the experimental response of the SFRC best shown by s7505BTM35.

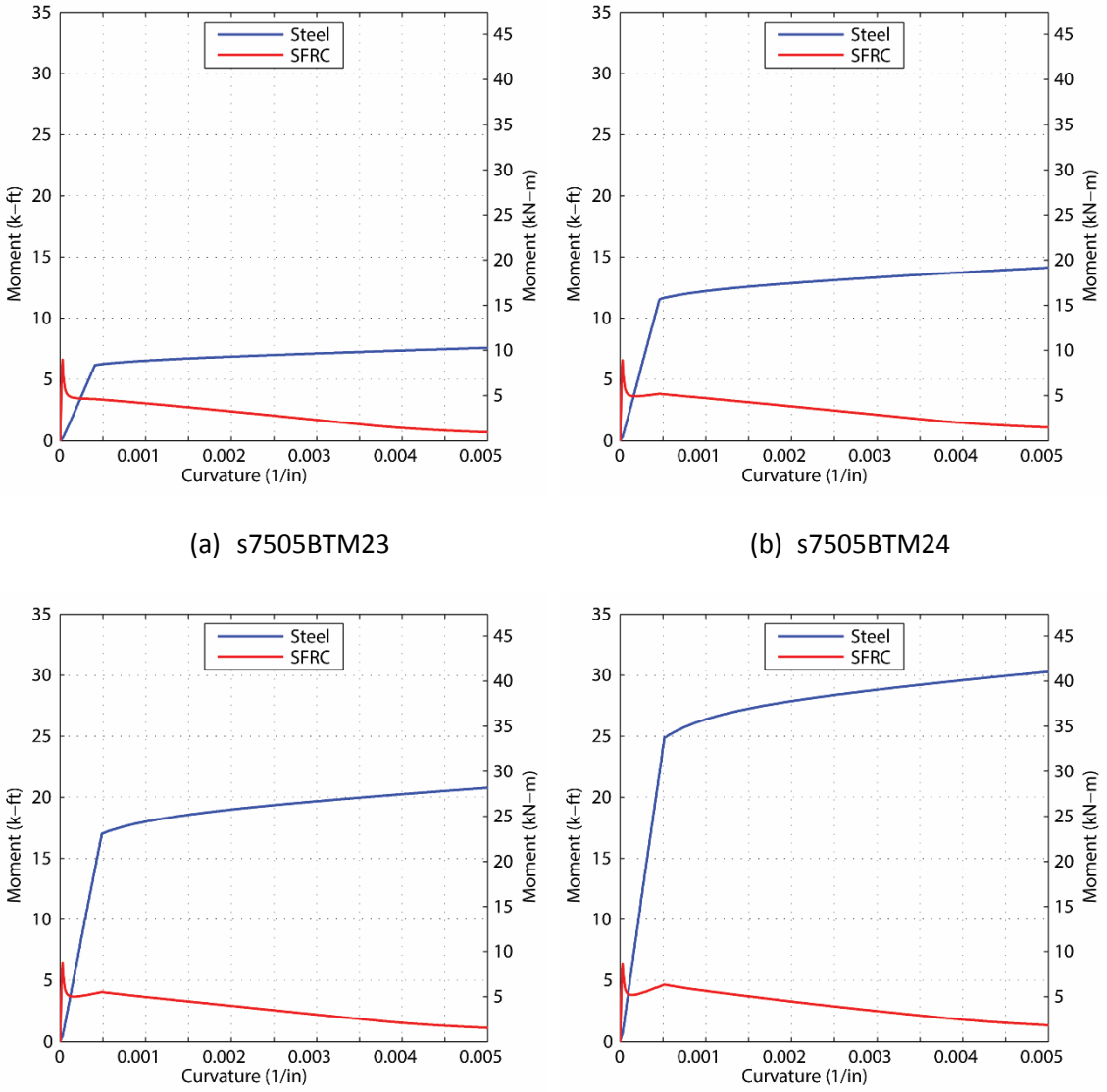

Figure 163. Steel and SFRC Contribution to Moment Capacity

The theoretical moment-curvature relationships were also determined for the deeper 9 inch slab-strips with 0.5% and are shown in Figure 164. The trends between the theoretical and experimental moment-curvature relationships made for the 7.5 inch strips are also observed in the 9 inch sections. The theoretical model captures the behavior of the SFRC specimens before the steel reinforcement yields. Following the yield of the steel, the theoretical models underpredict the capacity for specimens with low ratios of steel reinforcement. The underprediction is not as significant for specimens with larger reinforcement ratios.

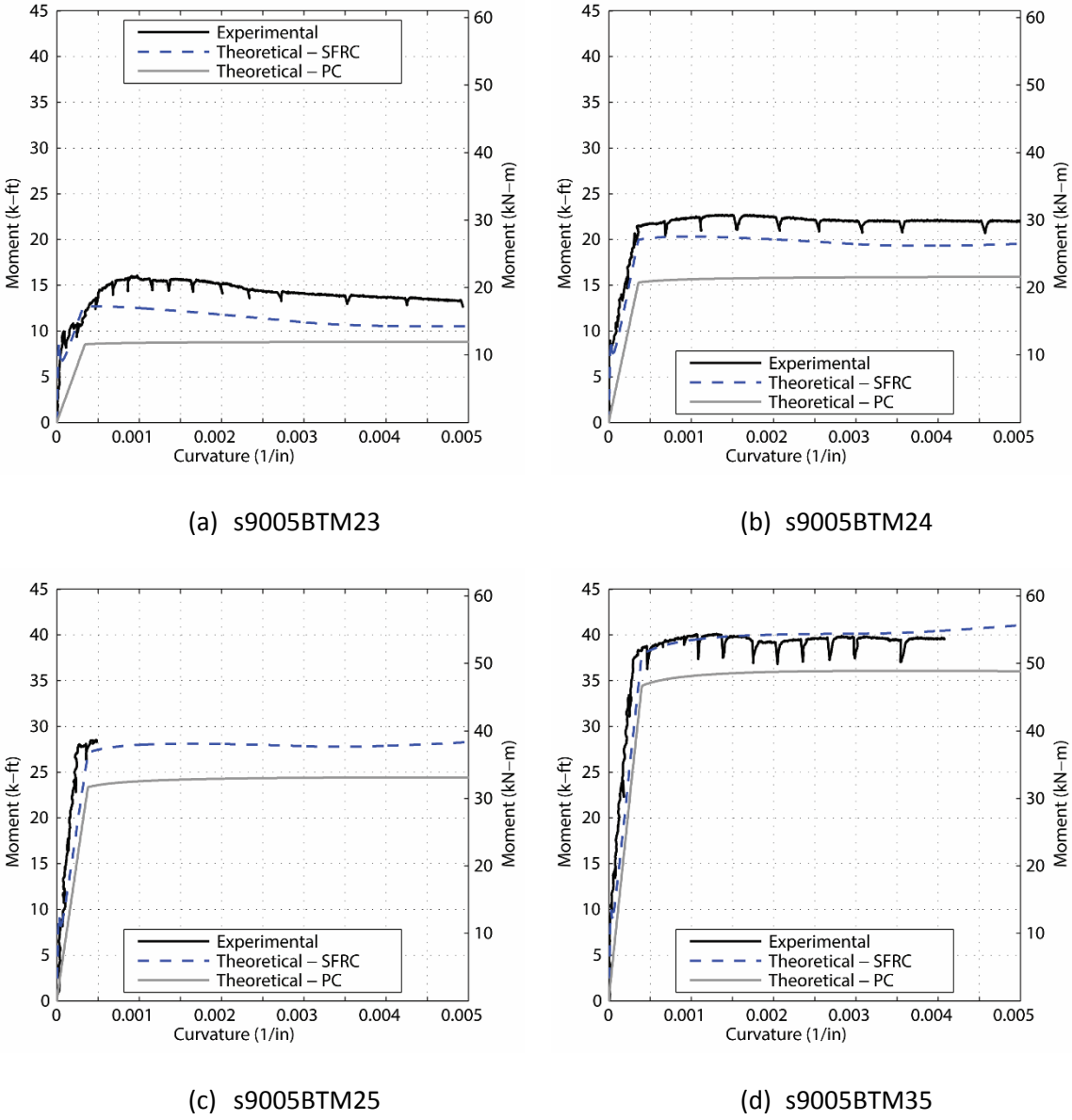

Figure 164. Theoretical Moment-Curvature Relationship for Slab Strips s9005BTM##

The theoretical model accurately captures the behavior of the specimens with the steel reinforcement located at the center depth of the specimen as shown in Figure 165. The decreased moment-arm for the steel reinforcement decreases its influence in the overall response of the specimen. Additionally, the SFRC in the lower half of the specimen is free to act more like the specimens without steel reinforcement that was used in determining the steel tensile properties.

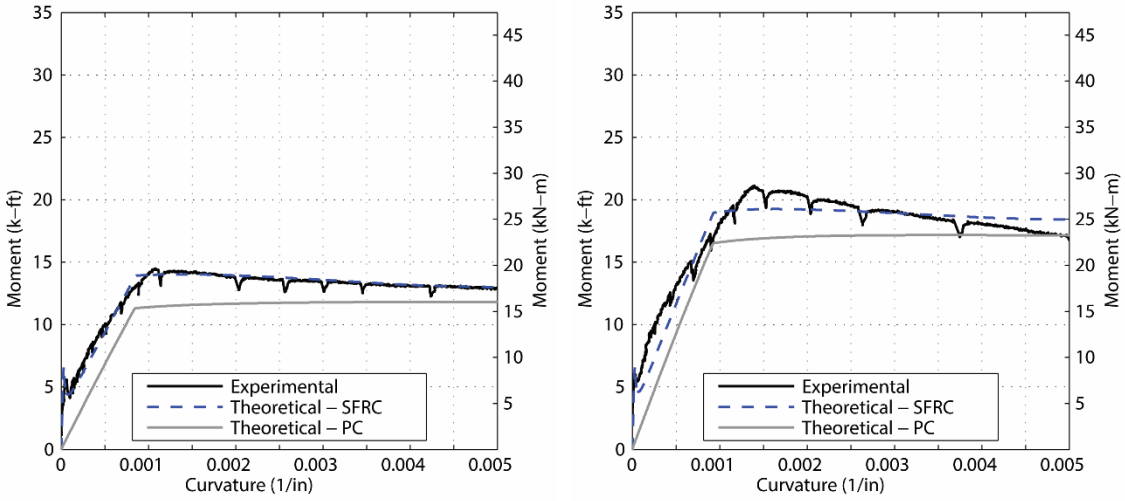

(a) s7505ctr25 (b) s7505CTR35

Figure 165. Theoretical Moment-Curvature Relationship for Slab Strips s7505CTR##

The theoretical and experimental moment-curvature response for the SFRC deck strip with steel reinforcement, d7505BTM24, is shown in Figure 166. The SFRC strip had the same reinforcement and fiber dosage as s7505BTM24 tested during the first experimental program of the project. As expected, the theoretical response of d7505BTM24 in comparison to the experimental results is consistent with the comparisons made for s7505BTM24. The theoretical model captures initial stiffness and capacity up to yield. Afterwards, the theoretical model continues to underpredict the response of the SFRC specimens.

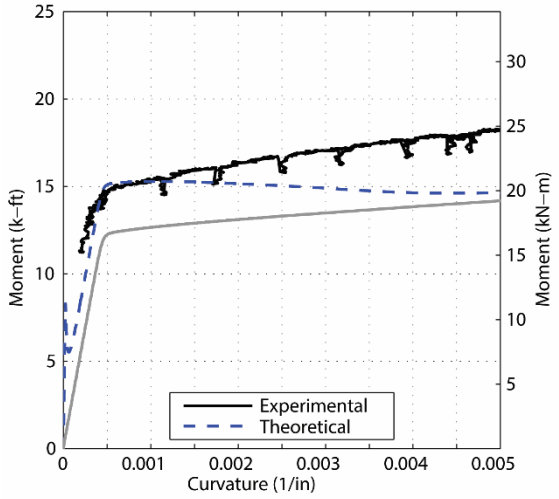

Figure 166. Theoretical Moment-Curvature Relationship for Slab Strips d7505BTM24

The moment capacity of the theoretical and experimental models was compared to each other to determine the accuracy of the theoretical models. Table 57 shows the difference in the theoretical and experimental models. The theoretical model under predicts the capacity specimen with the smallest reinforcement ratio, s9005BTM23, by 27% and over predicts the capacity of the specimen with the largest reinforcement ratio, s7505BTM35, by 11.3%. Both specimens with steel reinforcement at the center are over predicted by as much as 10%.

Table 57. Percent Difference between Experimental Results and Theoretical model

Slab-Strip	P (%)	% Difference
s7505BTM23	0.20	-33.1
s7505BTM24	0.37	-13.4
s7505BTM25	0.57	0.4
s7505BTM35	0.86	11.3
s9005BTM23	0.16	-26.6
s9005BTM24	0.30	-4.6
s9005BTM25	0.46	3.5
s9005BTM35	0.69	10.0
s7505CTR25	0.92	3.3
s7505CTR35	1.4	9.7

6.4 Comparison Of Deck And Slab Strip

The reinforcement ratio used in three of the companion deck strips was also tested in the slab strip program, x7505BTM24, x7505NOS00, and x9005NOS00. The redundancy of the tests show the repeatability of the experimental results with SFRC. Figure 167 shows the average response of the standard ASTM material tests conducted for each test program. The SFRC for the bridge deck program had a larger compressive strength and cracking stress. The increased cracking stress is evident in the flexural response of the material samples. The average response of the slab strip SFRC samples become larger than the deck's response at larger strains and deflections.

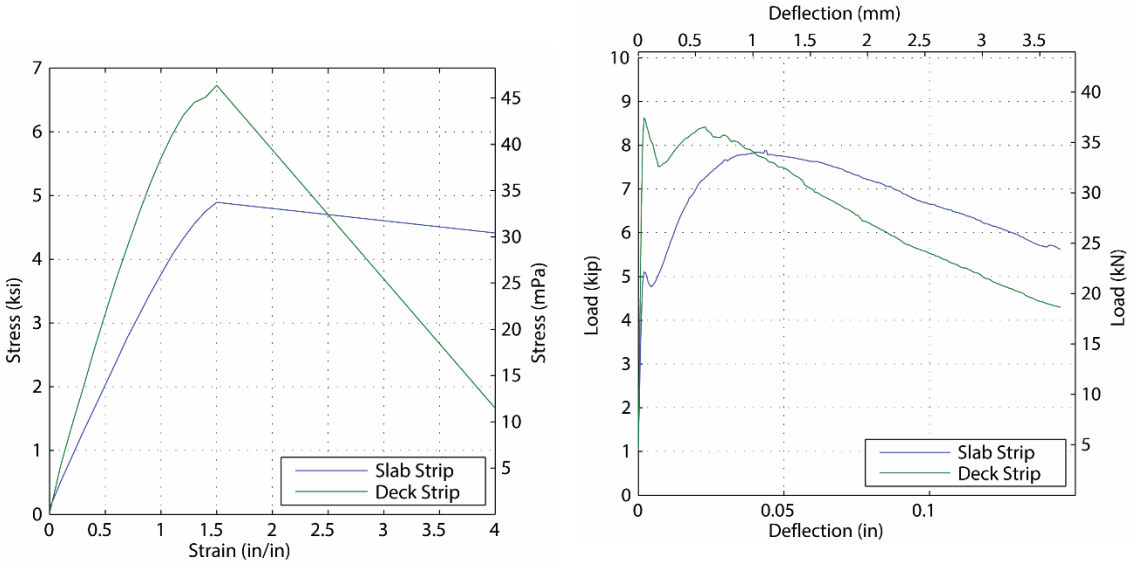

(a) ASTM C39 – Compression (c) ASTM C1609 – Flexural

Figure 167. Average Material Response for SFRC Slab and Deck Programs

Figure 168 shows the force-deflection and moment-curvature responses for strip specimens 7.5 inch deep without steel reinforcement, d7505NOS00 and s7505NOS00. The strip from both programs have the same initial stiffness. The increased cracking stress is prominent in both the force-deflection and moment-curvature response of the deck companion strip. The slope of the post-crack response of the d7505NOS00 is larger than the slope of s7505NOS00. This is consistent with flexural material test ASTM C1609. The behavior of both slab strips with the same dosage of fibers is similar; however, the compressive strength and cracking stress are significant in the response SFRC specimens without steel reinforcement.

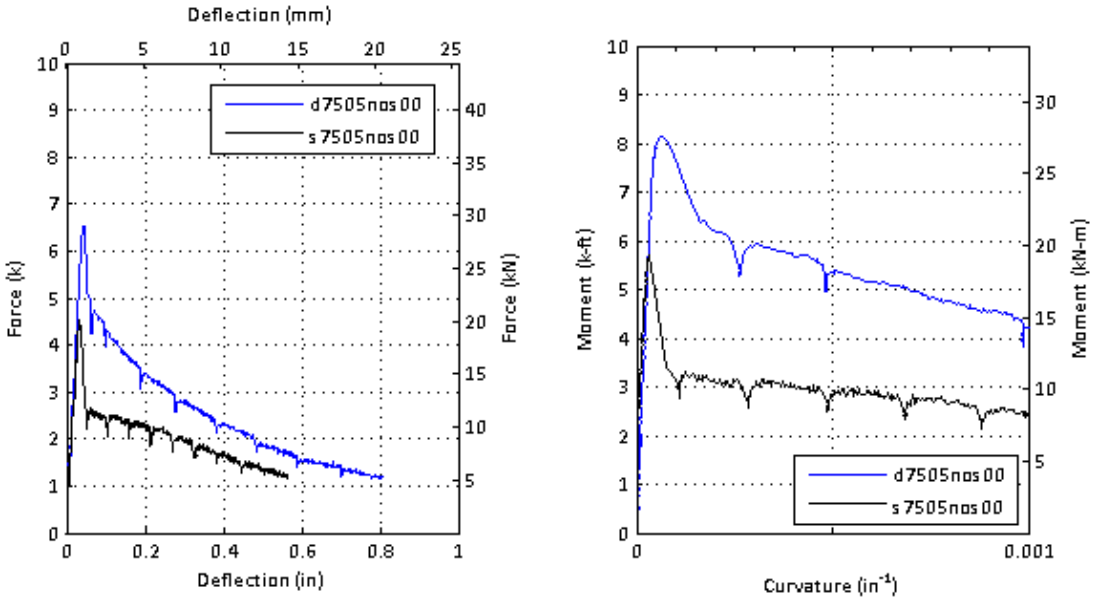

(a) Force vs Deflection (b) Moment vs Curvature

Figure 168. Comparison of Slab Strip Program and Bridge Deck Program – x7505NOS00

Figure 169 shows the force-deflection and moment-curvature responses for strip specimens 7.5 inches deep with two #4 bars, d7505BTM24 and s7505BTM24. Both strips have the same stiffness prior to cracking. However, after cracking occurs d7505BTM24 is less stiff and has a shallow force-deflection and moment-curvature response. The yield moment for the for the deck companion strip is lower as a result of the smaller stiffness. As the deflection and curvature increases, the moment capacity of the deck companion strip surpasses the original slab strip. The improved compression strength and larger modulus of rupture shown by the SFRC material tests provide the enhancement of the SFRC deck companion strip. The maximum moment capacity of the strips from each program is comparable, but the overall behavior, or shape, of the force-deflection and moment-curvature relationships is not. The difference in their behavior is manifested in the ASTM material tests.

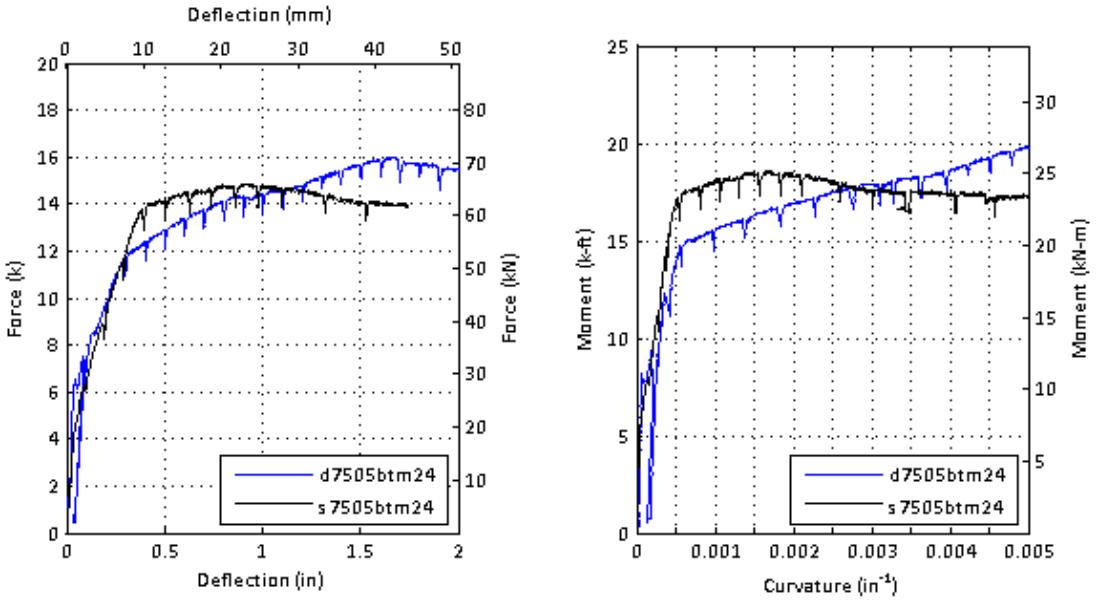

(a) Force vs Deflection (b) Moment vs Curvature

Figure 169. Comparison of Slab Strip Program and Bridge Deck Program – x7505BTM24

6.5 Case Study Comparison

Several case studies were conducted and presented in Section 3. The goal of the parameter studies was to examine the effects of SFRC on the behavior of each system by varying their material and geometric properties, such as the compressive strength of concrete, the post-crack strength of the SFRC and the location and area of traditional steel reinforcement.

The slab strip experimental program recreated the case study analysis with fewer parameters; specifically, the area of traditional steel reinforcement and the depth of the section. The maximum recorded moment for the experimental program is normalized by the moment demand for a 6 ft span. Figure 170 through Figure 171 shows the relationship between the steel reinforcement ratio and the sections moment capacity and service stress. Each figure has a vertical line representing the steel reinforcement ratio for the traditional strength and service designs. Figure 170 and Figure 165 have horizontal lines signifying a ratio of capacity to demand of 1. The black horizontal line does not take into account strength reduction factors while the red horizontal line does. The trends observed in the slab strip program are consistent with the trends noted in the theoretical case study analysis:

- Increasing the area of traditional steel reinforcement results in a proportional increase in the moment capacity. The effect of the SFRC is more pronounced in the deeper section as shown by the steeper trend line for the 9 inch sections. The increased effectiveness is a result of a larger area of concrete being in tension for the deeper section and therefore a larger resultant force and moment arm.
- The case study showed that a moderate amount of steel fibers and the AASHTO empirical steel design may be used to satisfy the moment demand. The AASHTO empirical steel is equivalent to #4 rebar spaced at 9 inches.
- Figure 170 shows that the a section with 0.5% fibers by volume and less steel than the AASHTO empirical design, #3 spaced at 9 inches (s7505btm23), provides sufficient strength to satisfy the moment demands of a 6 ft girder spacing.
- The case study concluded that a large amount of fibers may be used instead of steel reinforcement to satisfy the moment demand. According to the case study analysis, a section using SFRC with a significant amount of strain hardening provided approximately 40% more strength than required by the ultimate strength design. This trend was also observed in the slab strip program. Section s9020nos00 provided sufficient strength to meet the strength moment demands; however, the section did not produce as large of an over strength as observed in the case study. Including fiber 2.0% by volume is not sufficient to achieve the levels of strain hardening utilized in the case study.
- Current ADOT design procedures for concrete bridge decks is based on the elastic analysis of the deck under service loads. This design is accomplished by limiting the stress in the steel reinforcement to 24 ksi. Based on the case study analysis and the slab strip program, the use of strength design with 0.5% fibers by volume satisfies the service design as shown by Figure 172. Additionally, the amount of steel reinforcement may further be decreased as shown by section s7505btm23.

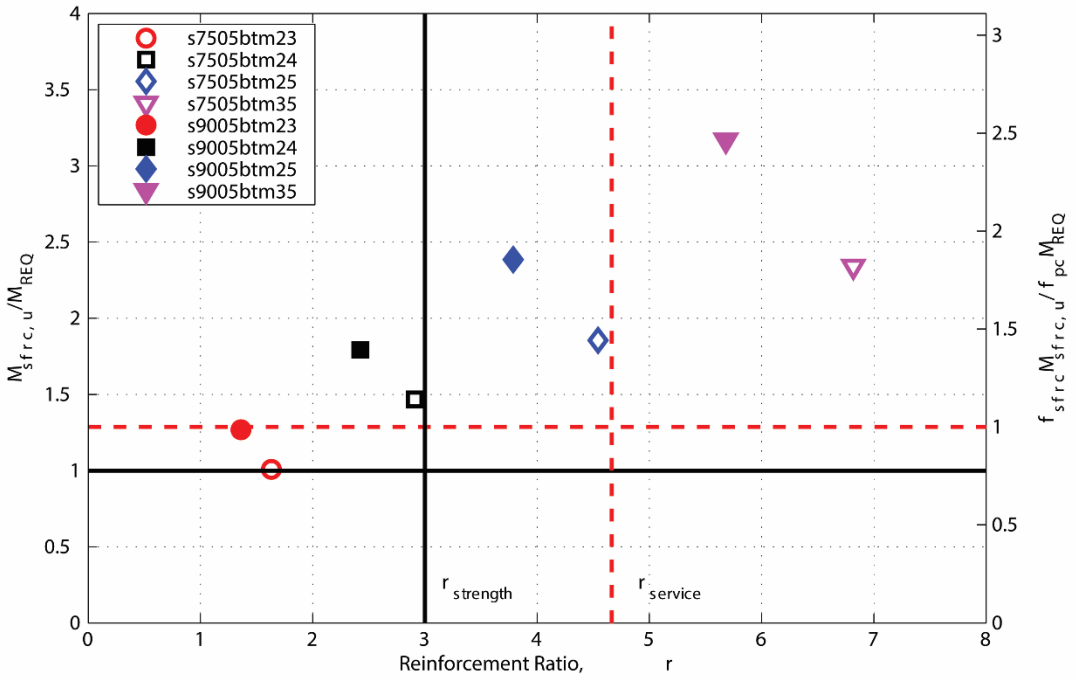

Figure 170. Normalized Moment vs Steel Reinforcement Ratio - 6 ft Girder Spacing and Steel at Bottom

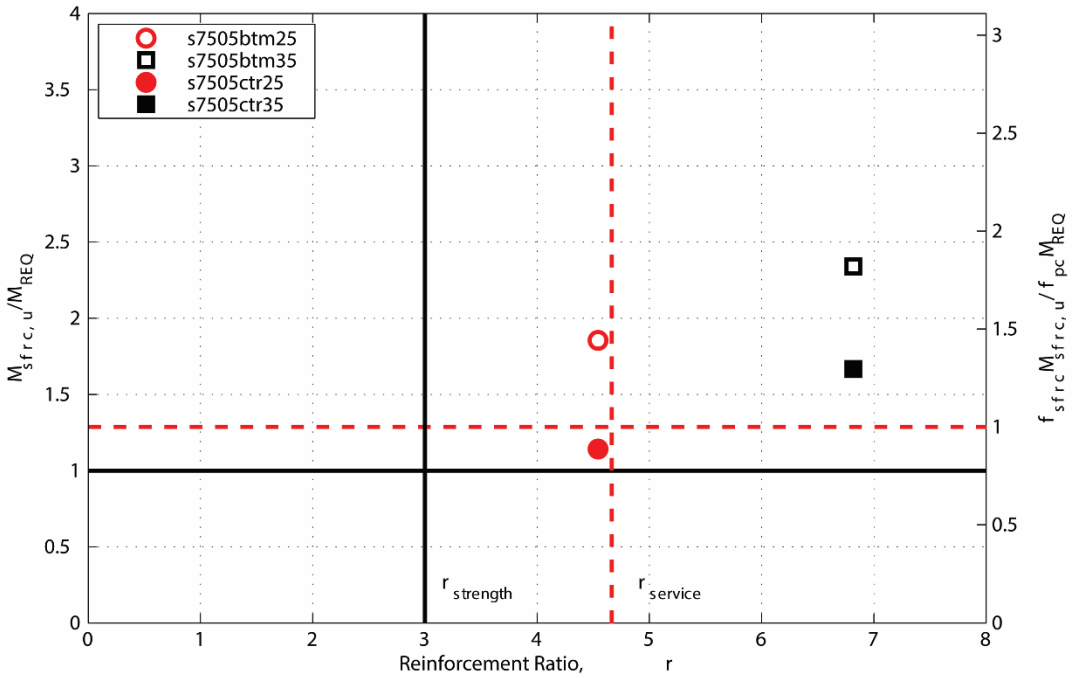

Figure 171. Normalized Moment vs Steel Reinforcement Ratio - 6 ft Girder Spacing and Steel at Cetner

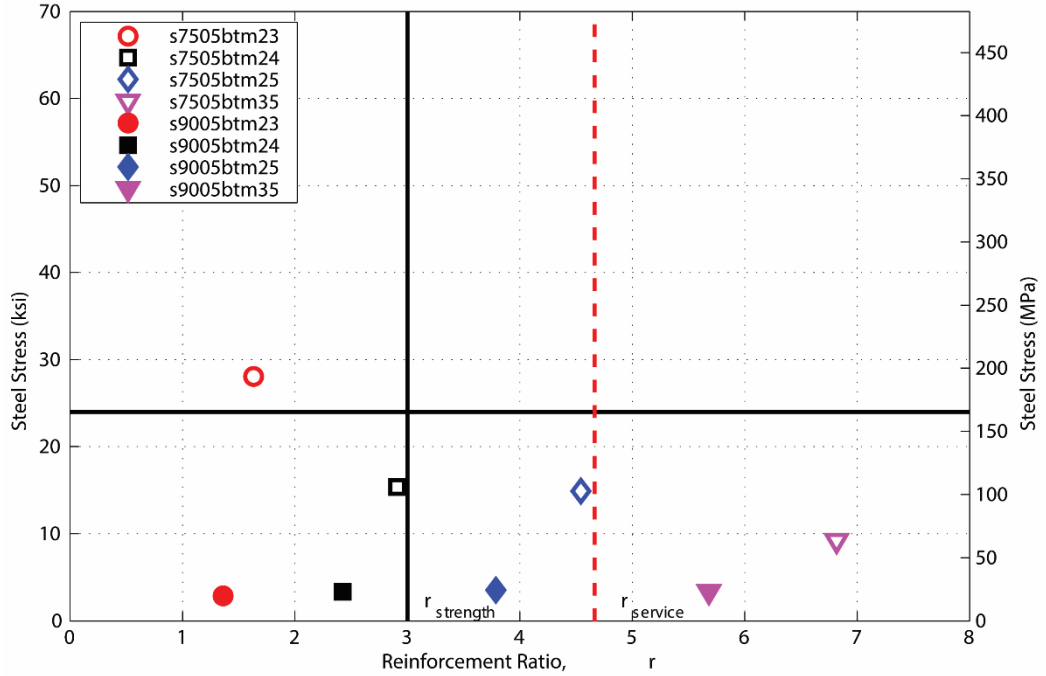

Figure 172. Service Stress vs Steel Reinforcement Ratio - 6 ft Girder Spacing and Steel at Bottom

6.6 Conclusion

The moment-curvature analysis presented in this Section is intended for the development of design procedures for SFRC in concrete bridge decks. The analysis provides a means to inversely determine the constitutive model for the tensile response of SFRC after the initial crack occurs. Furthermore, the analysis presents a comparison between the theoretical and experimental moment-curvature relationships and overall behavior. Verification of trends observed in the parameter study presented in Section 2 is also made. Finally, the repeatability of SFRC structural members is examined in the two experimental programs. The following conclusions are made from the moment-curvature analysis:

- The compression response is not affected by the presence of steel fibers in the concrete matrix. The modified Kent-Park model with a post-peak slope, Z, of 50 closely models the response of SFRC.
- The tension response can be modeled with a piecewise curve. An elastic response is used prior to the formation of the first crack. Following cracking, the response can be modeled with a linearly decreasing curve or a constant stress until the maximum strain of 0.025. The post-crack models are consistent with responses presented by other researchers: RILEM (2003), Soranakom and Mobasher (2007), and fib (2013).
- The residual stress used in the tension response can be determined using an inverse analysis to create the best-fit curve of the moment-curvature response.
- The effectiveness of the steel fibers decreases as the area of steel reinforcement increases. Increasing the area of steel reinforcement directly increases the tension force carried by steel reinforcement; however, the maximum tension force carried by the fibers remains unchanged. Therefore, at low levels of steel reinforcement, the tension capacity of the fibers and the steel reinforcement are similar.
- The response of the companion beams cast alongside the bridge deck varied slightly from the slab strip specimens cast during the original experimental program.
    - Further researcher needs to be conducted on the repeatability of SFRC experiments and the development of the post-crack tension response from standard test ASTM C1609.
- The results of the slab strip experimental program are consistent with the trends observed in the parameter study conducted in Section 2.
    - Increasing the area of traditional steel reinforcement results in a proportional increase in the moment capacity.
    - Add fibers 0.5% by volume to the AASHTO empirical design satisfies both strength and service criteria.
    - Traditional steel reinforcement can be excluded from a SFRC section with 2.0% by volume fibers while satisfying strength requirements.

7. ANALYSIS OF EXPERIMENTAL RESULTS – BRIDGE DECK

7.1 Introduction

The experimental results of the SFRC bridge deck presented in 5 are evaluated using a yield line analysis and a two-way shear analysis. The analyses are based on the results of the slab-strip experiments presented in 0 and 5. The yield line analysis is presented in Section 7.2 and evaluates the flexural capacity of the bridge deck based on crack patterns and the moment capacity of a unit strip. The two-way shear analysis is presented in Section 7.3 and is based on design equations formulated by other researchers.

7.2 Yield Line Theory

Yield line theory is an upper-bound method that determines the failure load of a slab system. The method assumes that regions of plastic deformation or hinges form in the slab to create a failure pattern or mechanism. The failure pattern forms slab panels that rotate as a unit about each yield line or axis of rotation. Because the theory is an upper-bound method, all possible failure mechanisms must be investigated, with the lowest providing the true collapse load. The method utilizes the conservation of work and energy principle. The internal and external work of the slab are calculated and equated to each other to determine the failure capacity of the specimen. The internal and external work are calculated by:

$$IW = \sum ml\theta \quad (33)$$

$$EW = \sum P\delta + w_d A_d \delta_c \quad (34)$$

Where IW and EW are the internal and external work, respectively, m is the moment capacity per linear foot, θ is the angle of rotation for deflected shape, P is the externally applied load, δ is the deflection measured at the applied load, w_d is the self-weight of concrete slab, A_d is the area encompassed by failure mechanism, and δ_c is the deflection measured at the centroid of the failure mechanism.

7.2.1 Affinity Theorem

The affinity theorem is a transformation of an orthotropic failure mechanism to an isotropic mechanism (Park and Gamble 2000). The transformation modifies the length and external loads of the failure mechanism using a ratio, denoted μ, of the moment capacities in the strong and weak direction. The affinity transformation ratio is determined as follows:

$$\mu = \frac{m_y}{m_x} \quad (35)$$

Where μ is the affinity transformation ratio of moment capacity in the strong and weak directions and m_x and m_y are the moment capacity per linear foot in the strong and weak directions.

The length in the weak direction and external load is normalized by the square root of the affinity transformation ratio to determine the equivalent isotropic mechanism, or affine slab. The transformed length and load for the affine slab is determined as follows:

$$l_{y,a} = \frac{l_y}{\sqrt{\mu}} \quad (36)$$

$$P_{u,a} = \frac{P_u}{\sqrt{\mu}} \quad (37)$$

Where $l_{y,\alpha}$ is the length of affine slab in the weak direction, l_y is the length of real slab in the weak direction, $P_{u,a}$ is the external load for the affine slab, and P_u is the external load for the real slab.

The affinity theorem is particularly useful for fan failure mechanisms in orthotropic slabs. A circular fan is a common failure mechanism for an isotopically reinforced slab. The circular failure mechanism is "stretched" into an ellipse in the orthotropic slab due to the unequal moment capacities. Applying the affinity theorem to the orthotropic slab transforms the ellipse failure mechanism to a circular fan as shown in Figure 173.

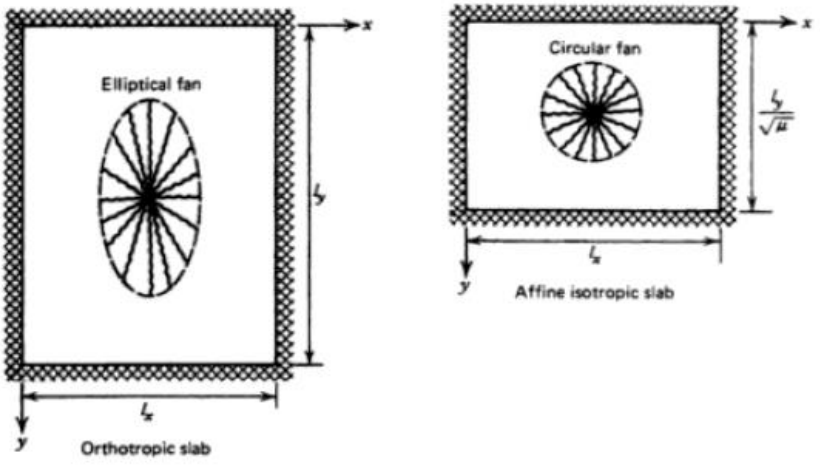

Figure 173. Affinity Theorem - Transformed Fan Mechanism (Park and Gamble 2000)

The affine slab is solved by the simple equation for the internal and external work of a circular fan mechanism with the following affine transformation:

$$P_{u,a} = \frac{P_u}{\sqrt{\mu}} = 2\pi(m_x^+ + m_x^-) \quad \textbf{(38)}$$

7.2.2 Unit Moment Capacities

The unit moments utilized for the yield line analysis were determined based on the moment-curvature relationship for d7505BTM24 presented in 6. The constitutive model utilized for the SFRC post-crack response was the plastic model with a residual strength of 0.14 ksi. The nominal moment was extracted from the theoretical moment-curvature relationship determined for each direction of the SFRC bridge deck. Figure 174 and Table 58 show the theoretical moment curvature relationships and summarize the unit capacities.

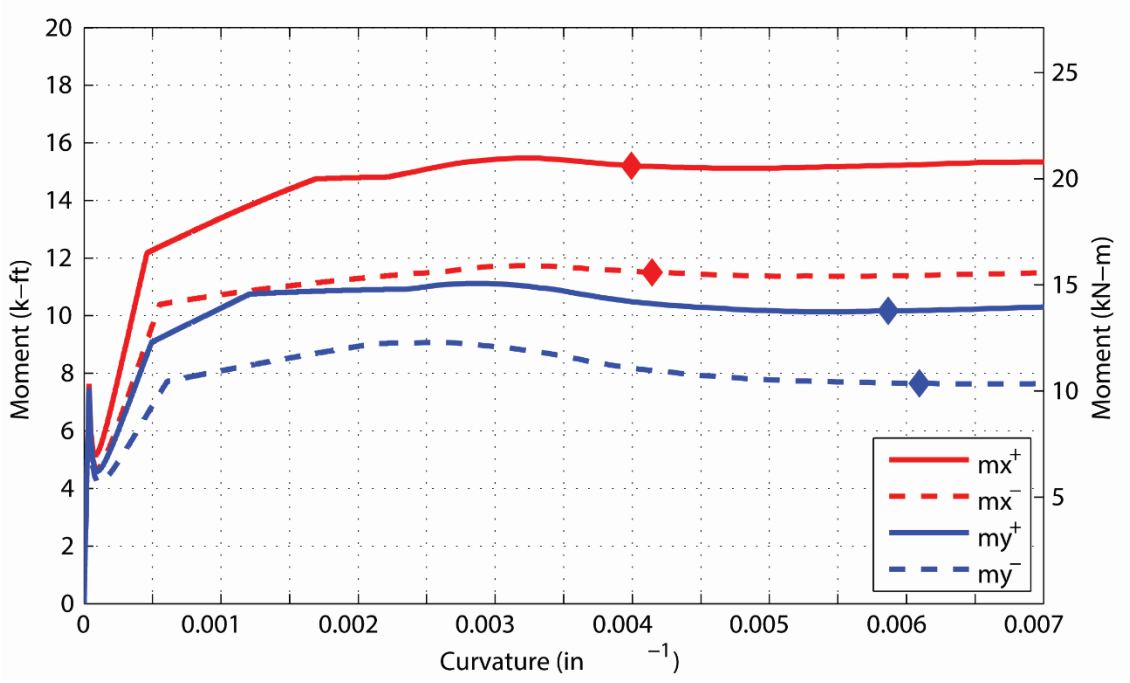

Figure 174. Moment-Curvature Relationship for SFRC Bridge Deck - Both Directions

Table 58. Moment Capacities Utilized for Yield Line Analysis

	Positive (k-ft)	Negative (k-ft)
m_x	15.21	11.51
m_y	10.16	7.65

7.2.3 LP1 and LP4 – Individual Wheel

Figure 175 and Figure 176 show the crack pattern observed at the conclusion of testing for LP1 and LP4. Tests LP1 and LP4 achieved the same maximum capacity and failure pattern. Negative yield lines originated on the top surface of the deck adjacent to the support beams and propagated east and west. Both load cases had negative yield lines that propagated toward the longitudinal middle of the deck prior to orientating perpendicular to the support beams extending north and south. The portion of the bridge deck between the load point and the free edge of the deck behaved in a one-way manner. The negative yield lines extended directly towards the free edge of the deck with very minimal signs of re-orientating perpendicular to the support beams. Positive yield lines form on the bottom surface of the deck adjacent to the wheel load and propagate east and west parallel to the support beams. After extending beyond the load point the positive yield lines radiate outwards diagonal completing the formation of the elliptical fan failure pattern at the longitudinal middle of the deck. The yield pattern consists of half of an elliptical fan mechanism and four rectangular panels. These regions are labeled in Figure 175 and Figure 176**.** The darker lines in each of these figures are the cracks that were observed on the top surface of the deck and the lighter lines are the cracks observed on the bottom surface.

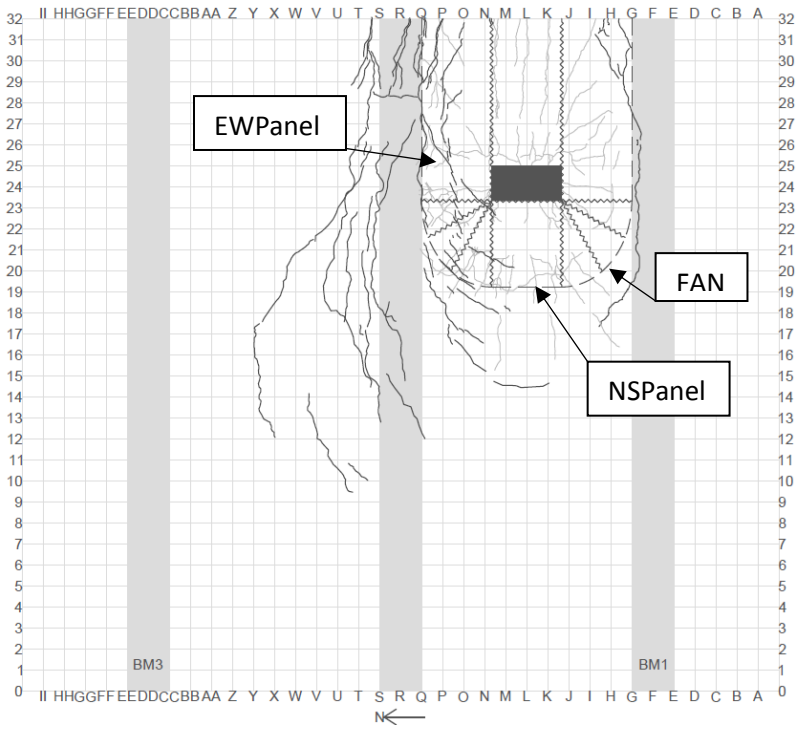

Figure 175. Failure Mechanism for LP1

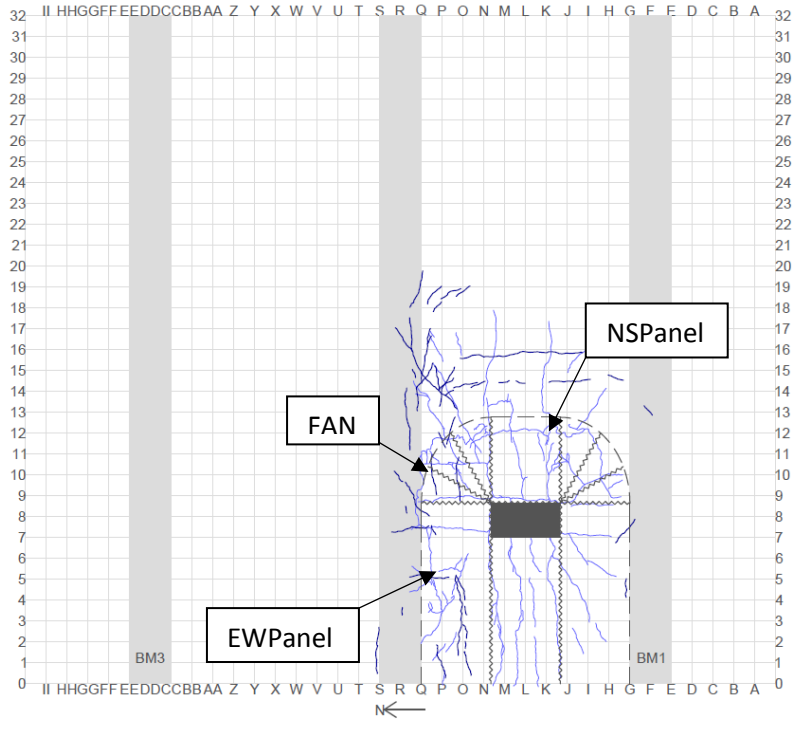

Figure 176. Failure Mechanism for LP4

An elliptical fan mechanism formed as a result of the concentrated load and orthotropic reinforcement. An affinity transformation is applied to the deck to simplify the elliptical fan mechanism into a circular fan as shown in Figure 177. The deck is transformed by the following:

$$EW = \underbrace{\frac{P}{\sqrt{\mu}}\delta + q\left(\frac{\pi r^2}{3}\right)\delta}_{\text{FAN}} + \underbrace{3(52qr^2\delta)}_{\text{EWPanel}} + \underbrace{\frac{20}{\sqrt{\mu}}qr^2\delta}_{\text{NSPanel}} \quad (39)$$

$$IW = \underbrace{2\pi\delta(m_x^- + m_x^+)}_{\text{FAN}} + \underbrace{\frac{20}{\sqrt{\mu}}\frac{\delta}{r}(m_x^- + m_x^+)}_{\text{EWPanel}} + \underbrace{2\left(52\frac{\delta}{r}(m_x^- + m_x^+)\right)}_{\text{NSPanel}} \quad (40)$$

Where m_x is the moment capacity in the strong direction, r is the radius of circular fan pattern, μ is the affine ratio of moment capacity in weak direction to moment capacity in the strong direction, q is the self-weight of concrete, and P_u is the external load.

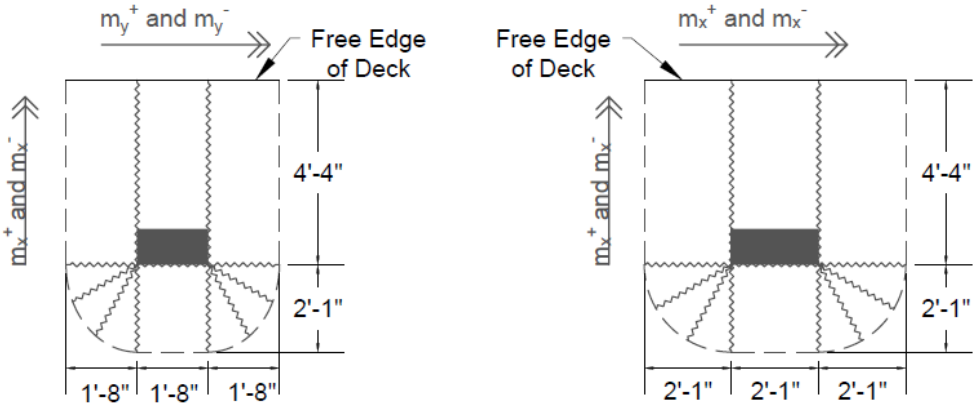

(a) Physical Slab (b) Affine Slab

Figure 177. Transformation of Physical Slab to Affine Slab – LP1/LP4

The moment-curvature analysis conducted in 6 was used to determine the moment capacities. The theoretical collapse load for the SFRC bridge deck under the influence of LP1/LP4 is 161 kips, 11% higher than the estimated collapse load for the same deck without SFRC. The actual collapse

load of the bridge deck experiment was 203 kips. The theoretical collapse load conservatively underestimated the load by 26%.

7.2.4 LP2 – Tandem Axel

Figure 178 shows the crack pattern observed at the conclusion of testing for LP2 and its associated failure mechanism or yield line. Negative yield lines originated on the top surface of the deck adjacent to the support beams and propagated east and west. After extending beyond each loading point, the yield line curves forming the outside edge of an elliptical failure pattern. Positive yield lines form on the bottom surface of the deck adjacent to the wheel loads and propagate east and west parallel to the support beams. After extending beyond the load points the positive yield lines radiate outwards diagonal completing the formation of the elliptical fan failure pattern. The yield pattern consists of a complete elliptical fan mechanism and four rectangular panels. These regions are labeled in Figure 178**.** The darker lines in the figure are the cracks that were observed on the top surface of the deck and the lighter lines are the cracks observed on the bottom surface.

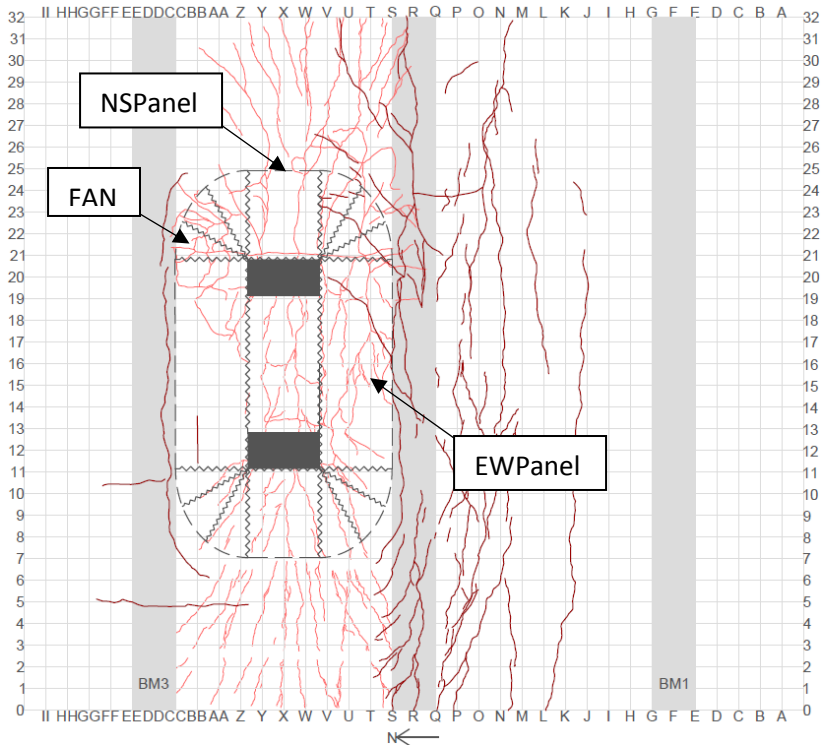

Figure 178. Failure Mechanism for LP2

An elliptical fan mechanism formed as a result of the concentrated load and orthotropic reinforcement. An affinity transformation is applied to the deck to simplify the elliptical fan mechanism into a circular fan as shown in Figure 179. The deck is transformed by the following:

$$EW = \frac{P}{\sqrt{\mu}}\delta + \underbrace{q\left(\frac{\pi r^2}{3}\right)\delta}_{\text{FAN}} + \underbrace{3(58qr^2\delta)}_{\text{EWPanel}} + \underbrace{\frac{20}{\sqrt{\mu}}qr^2\delta}_{\text{NSPanel}} \quad (41)$$

$$IW = \underbrace{2\pi\delta(m_x^- + m_x^+)}_{\text{FAN}} + \underbrace{2\left(\frac{20}{\sqrt{\mu}}\frac{\delta}{r}(m_y^- + m_y^+)\right)}_{\text{EWPanel}} + \underbrace{2\left(58\frac{\delta}{r}(m_x^- + m_x^+)\right)}_{\text{NSPanel}} \quad (42)$$

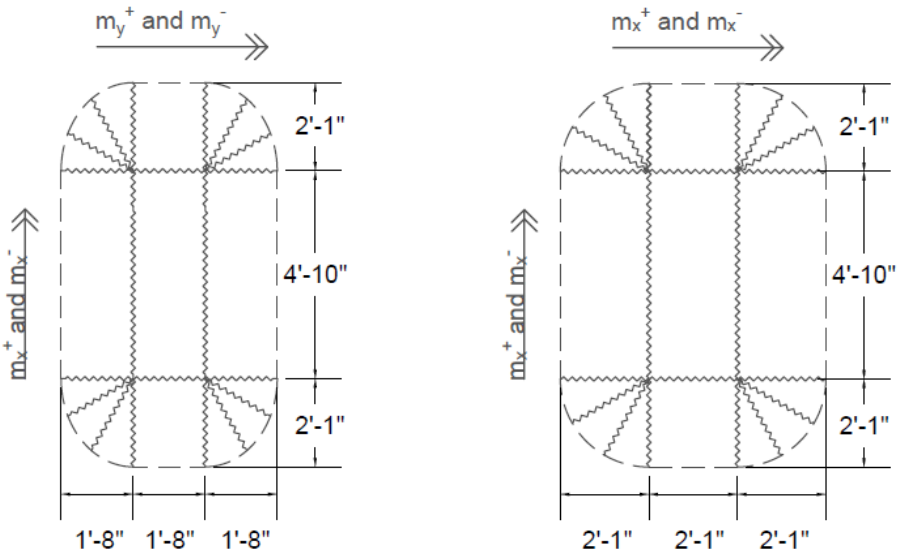

(c) Physical Slab (d) Affine Slab

Figure 179. Transformation of Physical Slab to Affine Slab – LP2

The moment-curvature analysis conducted in 6 was used to determine the moment capacities. The theoretical collapse load for the SFRC bridge deck under the influence of LP2 is 128 kips for each individual wheel footprint, 5% higher than the estimated collapse load for the same deck without SFRC. The actual collapse load of the bridge deck experiment was 185 kips. The theoretical collapse load conservatively underestimated the load by 44%.

7.2.5 LP3 – Overhang Single Axel

Figure 180 shows the crack pattern observed at the conclusion of testing for LP3 and its associated failure mechanism or yield line. Negative yield lines originated on the top surface of the deck adjacent to the support beams and propagated diagonally southwest and southeast. Positive yield lines form on the bottom surface of the deck adjacent to the wheel loads and propagated north until extending to the support beams. The yield pattern consists of two triangular panels and one rectangular panel. An affinity transformation was not necessary for this load pattern. The conservation of work was determined by the following (Mander et al 2009):

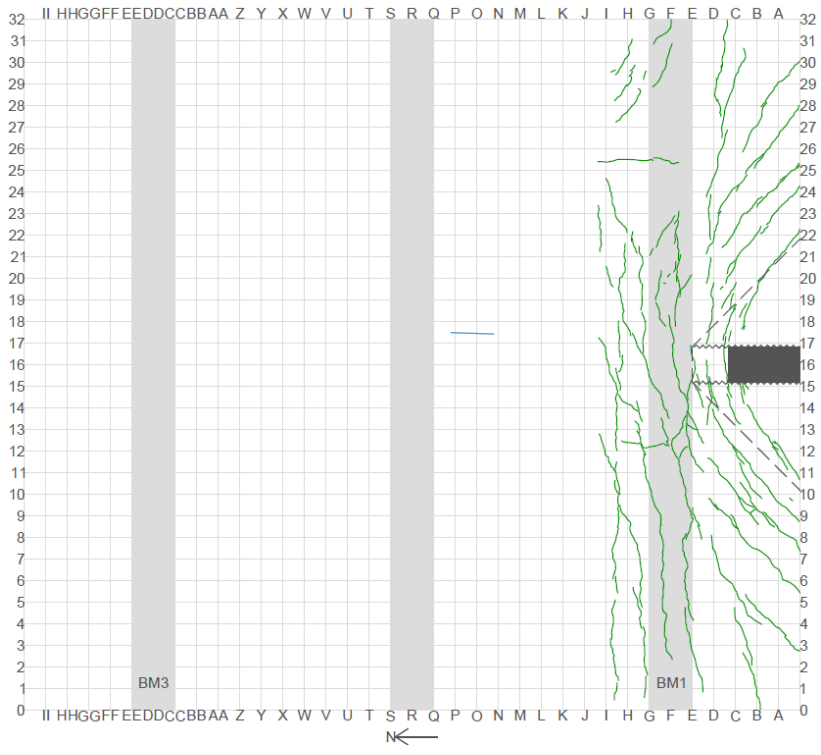

Figure 180. Failure Mechanism and Deflection Profile for LP3

$$EW = P\delta + q\left(l_x l_y \frac{\delta}{3} + b_1 l_x \frac{\delta}{2}\right) \quad (43)$$

$$IW = \frac{2m_x^-}{l_x - .5(20)}\left(l_y + 0.5(10)\right)\delta + 2\left(m_y^+ + m_y^-\right)\frac{l_x^2}{l_y\left(l_x - .5(20)\right)} \quad (44)$$

Where l_x and l_y are the length of yield lines in the strong and weak directions.

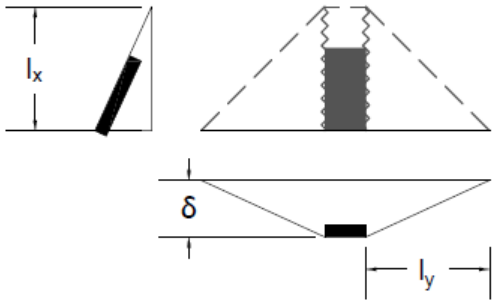

Figure 181. Failure Mechanism for LP3

The moment-curvature analysis conducted in 6 was used to determine the moment capacities. The theoretical collapse load for the SFRC bridge deck under the influence of LP3 is 91 kips, 15% higher than the estimated collapse load for the same deck without SFRC. The actual collapse load of the bridge deck experiment was 96 kips. The theoretical collapse load conservatively underestimated the load by 6%. A significant underprediction of the collapse load was not observed by LP3 as was with the other tests due to the lack of restraint necessary to allow for the load redistribution and compressive membrane action.

7.2.6 Discussion

Table 59 summarizes the results for the yield line analysis conducted on the SFRC bridge deck. The theoretical strength of the SFRC bridge deck is approximately 11% larger than the theoretical strength of a plain concrete bridge deck with the same area of traditional steel reinforcement. The addition of fibers increases the unit moment capacity of the bridge deck and allows for a redistribution of the stresses in the bridge deck. The theoretical strength for the SFRC and PC

bridge deck was computed using an identical failure mechanism; therefore, only the increase moment capacity of the SFRC is accounted for in the theoretical values reported in Table 59. As a result, the experimental results vary significantly from the theoretical strength.

Table 59. Summary of Yield Line Analysis for SFRC Bridge Deck

	Exp_{SFRC}	Theo_{SFRC}	$\frac{\text{Exp}_{SFRC}}{\text{Theo}_{SFRC}}$	Theo_{PC}	$\frac{\text{Theo}_{SFRC}}{\text{Theo}_{PC}}$
LP1/LP4	203	161	1.26	145	1.11
LP2	185	128	1.44	122	1.05
LP3	96	91	1.06	83	1.09

*All collapse loads are for individual wheels.

The experimental failure capacity of the interior load patterns, LP1, LP2, and LP4, is approximately 35% larger than the theoretical capacity determined utilizing the yield line analysis. Numerous other potential failure patterns were investigated based on the observed crack patterns. The failure pattern presented here resulted in the lowest collapse load. The under-prediction of the failure capacity is not observed in LP3. The south overhang lacks the restraint necessary to redistribute the load and provide membrane action.

The significant under-prediction of yield line analysis for SFRC slabs has been observed by other researchers. Fall et al (2014) tested simply supported two-way slabs with SFRC made with approximately 0.35 percent by volume of double-hooked that performed significantly better than the yield line analysis predicted. Destree and Mandl (2008) investigated elevated flat slabs with SFRC. The flat slab had a maximum capacity of up to five times the yield line capacity.

The under-prediction of the collapse load is a factor of the redistribution of the load. The indeterminacy and restraint of the structure allows the SFRC to significantly spread the load as observed by the larger areas of cracking on the SFRC bridge deck. Compressive and tension membrane action has been demonstrated to also play a significant role. Mufti et al (1993) investigated the use of exterior struts and synthetic fibers on bridge decks. The researchers reduced the area of steel reinforcement to a single layer due to the restraint provided by the exterior struts and the resulting compressive membrane action.

7.3 Two-Way Shear Analysis

The concentrated foot print of the applied wheel load and restraints of the supporting concrete beams can result in a two-way or punching shear failure. The shear capacity of the bridge deck must also be evaluated.

7.3.1 Shear Capacity of SFRC

Naaman et al (2007) evaluated the shear capacity of high-performance fiber-reinforced cementitious composite slabs and found that FRC had nearly double the capacity of plain reinforced concrete. The slabs evaluated by Naaman et al had fiber percentages between 1.75% and 2.0%. Nguyen-Minh et al (2011) evaluated the existing equations proposed by Choi (2007), Harajili et all (1995), and Choi (2007) for the two-way shear capacity of FRC. Nguyen-Minh et al concluded that the proposed methods are inadequate because they do not account for the length, shape, or aspect ratio of the fibers included in the concrete matrix. Furthermore, the authors found that the scatter of the proposed equations was significant with a coefficient of variance of greater than 24% as shown in Figure 182.

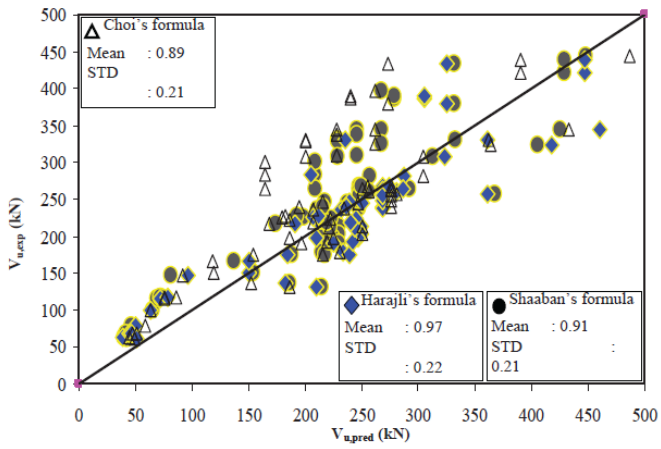

Figure 182. Comparison of Theoretical and Experimental Two-Way Shear Capacity (Nguyen-Minh et al 2011)

The design philosophy proposed by Harajili et al (1994) is used to determine the two-way shear capacity of the SFRC utilized in this test program due to the lack of a code approved method for calculating the capacity of SFRC. The method proposed by Harajli et al is currently the most

accurate method as demonstrated by Nguyen-Minh et al (2011). The additional two-way shear capacity of an SFRC slab can be accounted for by adding an additional term to the existing equation for punching shear of a plain reinforced concrete slab as follows:

$$V = V_{PC} + V_{FRC} \quad (45)$$

$$V_{FRC} = 1.15 v_f b_0 d \sqrt{f_c'} \quad (46)$$

$$= \left(0.063 + \frac{0.126}{\beta_c}\right) b_0 d \sqrt{f_c'} \quad (47)$$

Where V the total shear strength of composite material is, V_{PC} is the shear strength of plain concrete for critical failure plane in accordance with AASHTO (2014), V_{FRC} is the shear strength of FRC for critical failure plane (Harajli et al 1994), v_f is the dosage of fiber by volume, $b_0$is the perimeter of critical failure plane shown in Figure 183, d is the depth to bottom layer of steel, f_c' is the compressive strength of concrete, and β_c is the ratio of long side to short side of concentrated load.

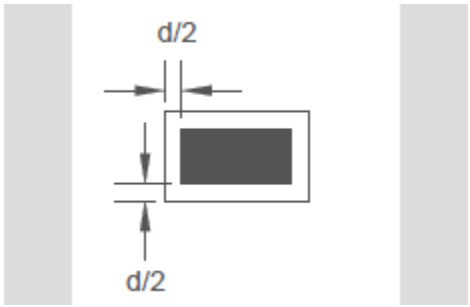

Figure 183. Critical Shear Perimeter due to Wheel Load

The two-way shear capacity is calculated using equations 45 through 47 for the 10 by 20 inch wheel load utilized for the bridge deck tests. The SFRC bridge deck has a shear capacity of 243 kips, approximately 40 kips larger than the failure load recorded for LP1 and LP4.

7.4 Conclusion

The analyses performed in this section are intended to demonstrate and predict the two-way behavior of an orthotropic SFRC bridge deck. The analysis provides a means to predict the failure capacity of the SFRC bridge deck based on its moment capacity and shear strength. The yield line analysis relates the slab strips presented in 0 and 5 to the ultimate capacity of the SFRC bridge deck. The yield line analysis is compared to the experimental tests of the bridge deck presented 5. A two-way shear analysis was conducted to relate the moment capacity of the SFRC to its shear capacity. The following conclusions are made from the two-way analysis:

- The failure capacity of the SFRC specimen is significantly underpredicted by the yield line theory. This result is consistent with conclusions made by other researchers (Fall et al, 2014 and Destree and Mandl, 2008). The membrane action and load redistribution provided by the steel fibers adds significant strength to the ultimate limit state of the structure not accounted for by yield line analysis.
- The predicted failure capacity from yield line analysis is five times larger than the AASHTO HS20 design truck wheel load with strength limit state load factors.
- A satisfactory method for determining the two-way, or punching shear strength of SFRC has not been developed. Utilizing the design philosophy proposed by Harajili et al (1994), the punching shear capacity of the SFRC bridge deck is 243 kips. The punching shear strength is 40 kips larger than the highest experimental collapse load and 80 kips larger than the highest theoretical collapse load from yield line analysis.

8. DESIGN RECOMMENDATIONS

8.1 Introduction

The experimental tests have shown the benefits of SFRC on the performance of reinforced concrete bridge decks. The aim of this Section is to provide insight and recommendations for designing bridge decks with SFRC. In Section 8.2 and 0 the traditional design procedures for the service and strength limit states will be modified to account for the addition of steel fibers. In Section 8.5 the shortcomings of the proposed design recommendations will be discussed.

8.2 Service Limit State

The traditional design for the service limit state was discussed in detail in Section 4.2.2. The design of conventionally reinforced concrete bridge decks is typically controlled by the service limit state. The service limit state utilizes the allowable stress design and a maximum allowable tensile stress of 24 ksi (165 Mpa) in the conventional steel. This design is achieved using Hooke's law in an elastic analysis of the cross-section. The steel area is transformed into an equivalent concrete area to permit the analysis. The service condition is assumed to occur after the cross-section has cracked and the tension capacity of the plain concrete is ignored.

The proposed service state design procedure for SFRC utilizes the same principles of the traditional design for PC. An elastic analysis with transformed sections is performed. An additional component is added to the stress and strain profiles as shown in Figure 184 to account for the contribution of the SFRC. The residual tensile force of the SFRC will be accounted for in a manner similar to the traditional steel reinforcement by "lumping" the resultant force at the mid-depth of the cracked region and transforming its area so that the elastic stress corresponding to the strain at the mid-depth is the residual stress.

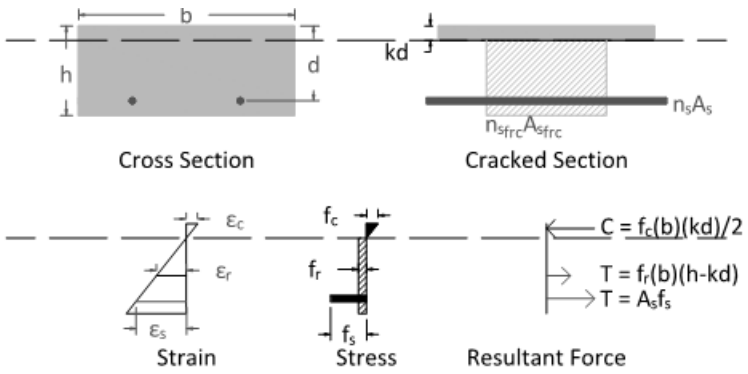

Figure 184. Service Limit State - SFRC

Two additional variables need to be determined to facilitate the modified service analysis of SFRC, the strain at the mid-depth of the section and the transformation factor for the SFRC. Similar triangles, strain compatibility, and the specified service stress of the steel reinforcement are used to determine the strain at the mid-depth of the tension region:

$$f_s \frac{\varepsilon_r}{\frac{h-kd}{2}} = \frac{\varepsilon_s}{d-kd} \quad \textbf{(48)}$$

$$\varepsilon_r = \frac{(h-kd)\varepsilon_s}{2(d-kd)} \quad \textbf{(49)}$$

Where ε_r is the residual strain of the SFRC at mid-depth of the cracked region, ε_s is the service strain of the steel reinforcement, h is the height of the cross-section, d is the depth to the steel reinforcement, and k is the ratio of the compression region to the height of the cross-section.

The transformation factor of the SFRC is determined based on Hooke's law and the transformed section. The stress at the mid-depth of the section must be the SFRC residual stress determined from material tests and inverse analysis:

$$n_{sfrc} = \frac{E_{sfrc}}{E_c} \quad \textbf{(50)}$$

$$\varepsilon_r E_{sfrc} = f_r \quad \textbf{(51)}$$

Where n_{sfrc} is a factor transforming the cracked SFRC into an equivalent "lumped" concrete section.

With the residual strain of the SFRC and transformation factor defined, sufficient information is available to determine the depth of the neutral axis by the following quadratic equation:

$$\left(\frac{bd^2(n_{sfrc}-1)}{2}\right)k^2+\left(\frac{d(n_{sfrc}bh+n_sA_s)}{2}\right)k+\left(\frac{n_{sfrc}bh^2}{2}-n_sA_sd\right)=0 \quad \textbf{(52)}$$

Finally, the service capacity of the section can be determined by summing the moment of the resultant forces about the neutral axis depth:

$$T_{Steel}=f_sA_s \quad \textbf{(53)}$$

$$T_{sfrc}=f_rb(h-kd) \quad \textbf{(54)}$$

$$M_{Service}=T_{Steel}\left(d-\frac{kh}{3}\right)+T_{sfrc}\left(\frac{h-kd}{2}-\frac{kd}{3}\right) \quad \textbf{(55)}$$

The proposed procedure has all of the same components of the traditional service design for SFRC. Determining the depth of the neutral axis is more involved due to the transformed area for the SFRC tension region and its resultant stress. However, once the neutral axis is known, the procedure returns to the traditional service equation with the addition of a single term for the SFRC contributions to the service capacity. The proposed method is also unorthodox as the procedure utilizes the maximum allowable service stress to find the maximum allowable service moment while the traditional procedure utilizes the service moment demand to check the stress in the steel reinforcement.

The error of the proposed method is summarized in Table 60. The theoretical model accurately predicted the service moments within 8% for five of the slab-strips with steel reinforcement located in the bottom of the cross-section. The service moments of slab strips with the steel located at mid-depth were within 15% of the theoretical model. The model underpredicted the experimental service moment of s9005BTM23 by 36%. The under prediction is consistent with the trends between the theoretical and experimental moment capacities observed in the moment-curvature analysis. The trend is also observed in the overprediction of 21% for the slap-strip with the largest reinforcement ratio, s7505BTM35. Overall, the average difference between the theoretical and experimental service moment is 12.3%.

Table 60. Service Moment

Using Proposed Procedure

	Experimental (k-ft)	Theoretical (k-ft)	Error
s7505BTM23	7.1	5.8	-0.22
s7505BTM24	7.7	7.7	0.00
s7505BTM25	9.3	10	0.07
s7505BTM35	10.4	13.2	0.21
s9005BTM23	10.6	7.8	-0.36
s9005BTM24	9.9	10.2	0.03
s9005BTM25	13.3	13.1	-0.02
s9005BTM35	15.9	17.2	0.08
s7505CTR25	6.3	7.4	0.15
s7505CTR35	10.2	9.3	-0.10
Max Error, %		36.0	
Min Error, %		0.0	
|Average|, %		12.3	
Average, %		2.0	
STD		17.2	

8.3 Strength Limit State

The proposed procedure to verify the strength of an SFRC specimen utilizes the traditional approach for PC with the addition of a component to account for the SFRC. Figure 185 shows the stress and strain profiles for an SFRC section at the strength limit state. A simplification is made to both the compression and tension stress blocks of the SFRC consistent with current practice. The compression block is identical to current design for plain concrete while the tensile stress block is represented by a constant residual stress the entire height of the tensile region of the cross section.

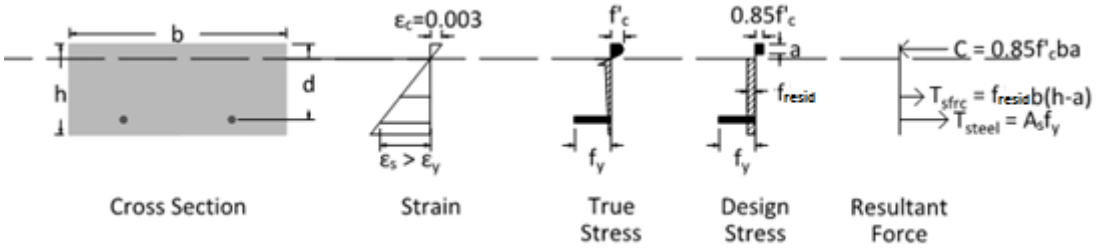

Figure 185. Strength Limit State – SFRC

The depth of the neutral axis is calculated based on static equilibrium of the cross-section:

$$T_s = A_s f_y \quad \textbf{(56)}$$

$$C_C = 0.85 f_c' \text{ba} \quad \textbf{(57)}$$

$$T_{sfrc} = (h - c) f_{resid} b \quad \textbf{(58)}$$

$$a = \frac{A_S f_y + h f_{resid} b}{0.85 f_c' b + \frac{f_{resid} b}{\beta_1}} \quad \textbf{(59)}$$

Once the depth of the neutral axis is determined, the moment capacity of the section is determined by summing the moments of the cross-section:

$$M_n = A_s f_y \left(d - \frac{a}{2}\right) + (h - c) f_{resid} \left(h \left(1 - \frac{1 - c}{2}\right) - \frac{a}{2}\right) \quad \textbf{(60)}$$

The procedure for determining the strength capacity of an SFRC section is nearly identical to the traditional design equation with the exception of an additional term in the equation to determine the depth of the neutral axis and moment capacity.

The error of the proposed method is summarized in Table 60. The theoretical model over predicts the experimental moment capacity for every slab-strip specimen. The largest over prediction, 8.5%, occurs on slab-strip s9005BTM25. The smallest over prediction occurs on slab-strip specimen s7505BTM35. Overall, the average difference between the theoretical and experimental service moment is 5.5%.

Table 61. Nominal Moment Using Proposed Procedure

	Experimental	Theoretical	Error
s7505BTM23	12.2	13	0.06
s7505BTM24	17.6	18.1	0.03
s7505BTM25	23.5	24.5	0.04
s7505BTM35	32.8	33.4	0.02
s9005BTM23	15.1	16.3	0.07
s9005BTM24	20.2	21.2	0.05
s9005BTM25	16.1	17.6	0.09
s9005BTM35	22.7	24	0.05
s7505CTR25	29.6	31.9	0.07
s7505CTR35	40.1	43.3	0.07
Max Error, %		8.5	
Min Error, %		1.8	
|Average|, %		5.5	
Average, %		-5.5	
STD, %		2.2	

8.4 Other Recommendations

Obtaining material properties for SFRC is the primary challenge in designing with SFRC. Direct tension tests of concrete are unreliable and under predict the residual stress of SFRC. Flexural tests offer insight on the post-crack behavior of SFRC; however, without a direct translation of flexural data to tension data, the material test is insufficient for determining the constitutive model for SFRC. As a result, other methods are proposed in Sections 8.4.1 and 8.4.2.

8.4.1 Empirical Strength Design

ACI 318 provides guidelines for the minimum dosage of steel fibers to behave as shear reinforcement in SFRC beams. The dosage requirements are based upon ASTM C1609, the weight of fiber added to the concrete matrix, and collection of experimental results.

The same philosophy can be adopted for the flexural design of SFRC as supplement reinforcement. Both the theoretical case studies and experimental slab-strip programs showed that adding fibers to the traditional strength design for plain concrete elevates its service

performance to adequate levels. Based on the experimental results of the slab-strip specimens and large scale bridge deck, reinforced concrete bridge decks could be designed for the strength limit state. Rather than increasing the area of steel reinforcement to also satisfy the service requirement, the designer can specify the minimum dosage of fibers cited in ACI 318 to enhance the service performance of the reinforced concrete section. Additional research needs to be conducted to determine the maximum span length that the proposed procedure is adequate.

8.4.2 Design Aids

Design aids can be developed by researchers and fiber manufacturers to facilitate the empirical design with SFRC. Soranakom and Mobasher (2007) presented design aids relating the capacity of plain concrete with SFRC sections.

Figure 186 and Figure 187 utilize the strain-softening model proposed by Soranakom and Mobasher (2007). The strain-softening model was also used for the theoretical analysis conducted in this thesis. The figures provide service and strength capacities for three levels of residual strength and three different depths. Designers with a required moment demand, known residual stress, and depth of the section may use the design aid to determine the area of steel reinforcement necessary to satisfy both the service and strength demands.

The proposed design aids does not solve the issue of obtaining the residual stress for SFRC. The aids simplify the design procedure once the material properties are known. Additional research to relate the tension response of SFRC to repeatable material tests is crucial to the adoption of SFRC as supplemental reinforcement.

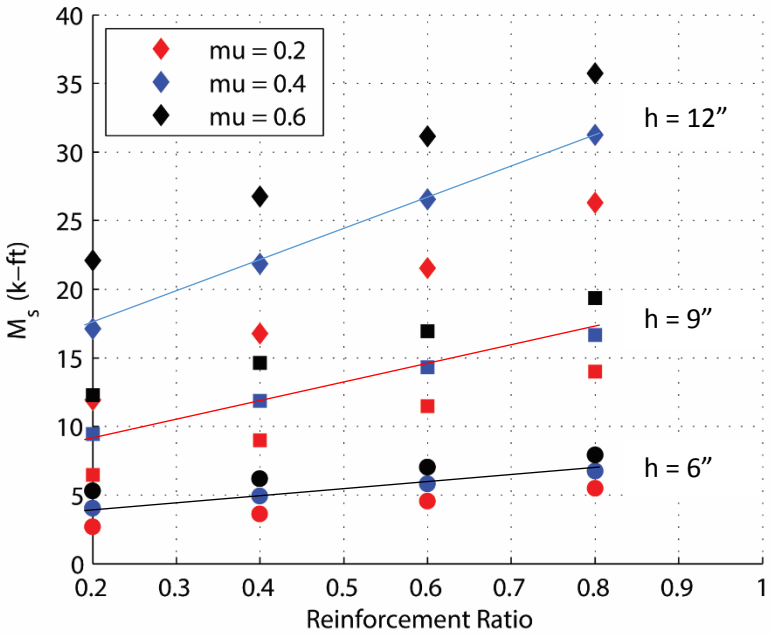

Figure 186. Design Aid - Service Moment vs. Reinforcement Ratio

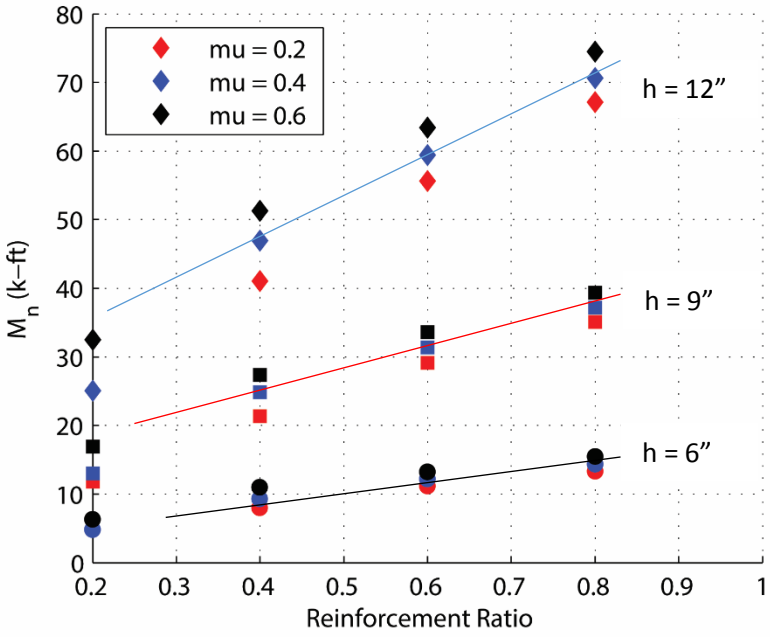

Figure 187. Design Aid - Strength Moment vs. Reinforcement Ratio

8.5 Conclusion

Steel fiber reinforced concrete enhances both the service and strength performance of plain concrete. Designers must be able to determine the tension properties of SFRC to fully utilize the benefits of SFRC. Other researchers have demonstrated the effectiveness of an inverse analysis to determine key properties of the tension response while international organizations have developed notched flexural tests to determine the SFRC response. In this section an inverse analysis and moment-curvature results of experimental data were utilized to verify a simplified method for determining the service and strength performance of SFRC.

- The contributions of SFRC to the service limit state performance can be accounted for by adding an additional stress block to the traditional elastic design. The tension response of the SFRC is "lumped" at its mid-depth similar to the design of plain concrete sections with multiple layers of steel reinforcement. The stiffness of the SFRC stress block is transformed so that Hooke's law may apply to the cross-section and facilitating an elastic analysis. The transformation is conducted such that the tension response at the mid-depth is equal to the residual stress. The neutral axis of the transformed section is determining resulting in the moment capacity at the maximum allowable service stress of the steel reinforcement.
- The proposed procedure varies from the traditional method as it assumes the steel reinforcement is at its maximum allowable stress of 24 ksi. The method calculates the moment capacity at this critical state yielding the service moment capacity.
- Trends observed in the theoretical moment-curvature analysis presented in 6 are also present in the proposed method. The theoretical service moment capacity is under predicted for specimens with a low reinforcement ratio and over predicted for specimens with a large reinforced ratio.
- The average error of the proposed method for service design is 12.3%.
- Similar to the proposed method for the service limit state, the proposed design method for the strength limit state utilizes the traditional analysis with an added component to account for the SFRC. A constant residual stress is assumed for the entire depth of the section in tension. The resultant tension force is computed for the SFRC and included in the static analysis of the cross-section.
- The proposed procedure consistently over predicted the strength capacity of the SFRC specimens by as much as 8.5%
- The average error of the proposed method for strength design is 5.5%.
- An empirical method utilizing the ACI 318 minimum dosage of steel fibers for shear reinforcement was proposed. The theoretical and experimental results show that adding fibers to a plain concrete section design for the strength limit state enhances the performance of the reinforced concrete specimen to adequate service levels.

- Design aids proposed by manufacturers and other researchers can be used to design with SFRC. Two design aids are presented in this thesis relating the service and strength performance of SFRC. Designers with a known residual strength and section depth can utilize the design aids to determine the required steel reinforcement to satisfy their moment demands. The design aids were developed using an theoretical analysis and the general tension response proposed by Soranakom and Mobasher (2007).

9. CONCLUSIONS

9.1 Summary

This thesis investigated the effectiveness of utilizing SFRC as supplemental reinforcement in reinforced concrete bridge decks. The investigation was achieved by first conducting a case study analysis. The information and conclusions of the case studies were utilized to construct and test simply-supported slab strips. The slab-strips provided information in conjunction with the case study analysis to design a large-scale bridge deck utilizing SFRC and a reduced area of traditional steel reinforcement to determine the overall effectiveness of SFRC in a large scale structure.

9.1.1 Case Study

The case study analysis investigated the effectiveness of SFRC using a fiber model and a moment-curvature analysis. The constitutive relationships used in the case studies were based upon the literature. The modified Kent-Park compression model was used in the case study analysis as the additional of steel fibers does not affect the compression response of concrete significantly. The tension model utilized was a bilinear curve proposed by Soranakom and Mobasher (2007). The case study investigated the relationship between SFRC and the girder spacing, thickness of the concrete deck, the concrete compressive strength, the post-crack tensile strength, and the traditional steel reinforcing layout. A total of 486 models were investigated.

The models were evaluated based on their service performance and nominal moment. The service performance is characterized by the stress in the steel reinforcement at the service limit state. Both the service stress and nominal moment of each model was normalized with respect to a traditionally designed and reinforced concrete section.

The addition of steel fiber to the traditional design resulted in a service performance enhancement and a strength increase, but also a reduced curvature at the nominal moment. The use of SFRC adds to the reinforcement of a section and must be balanced by a reduction in conventional steel or depth. Otherwise, the section will begin to become over-reinforced resulting in a lower curvature at nominal and potentially a brittle failure.

9.1.2 Slab-Strip Experiments

The slab-strip experimental program investigated the relationship between SFRC and ratio of steel reinforcement in a specimen. The program was conducted by constructing 14 unique slab-strips using two different depths, two volume dosages of steel fibers, and four different amounts of steel reinforcement. The goal of the experiment was to identify the failure progression of SFRC

and determine the effect of SFRC on the performance of reinforced concrete bridge decks under the service and strength demands.

The loading cycle on each test was paused numerous times to monitor and record the level of damage incurred by the SFRC specimens. Several trends were identified as a result of the steel fibers. Steel fibers controlled the width of cracks in the concrete prior to the crushing or crack width failure criteria. Several cracks developed in the SFRC slab strips, but remained relatively small prior to the onset of crushing in the compression region of the strip and achievement of the specimen's maximum moment. Eventually, the anchorage of the steel fibers failed in a single crack creating a hinge allowing all subsequent rotation and crack opening of the specimen occurs in the critical crack.

The tests provided information regarding the service and strength performance of SFRC sections. SFRC improves the performance of the slab strips under both the service and strength limit states. Adding 0.5% fibers to a section with traditional reinforcement and concrete designed for the strength limit state elevates the performance of the concrete bridge deck to satisfy the service limit state.

An inverse analysis was conducted utilizing a simplified tensile model similar to the linear model used by fib (2013) and the slab-strip specimens without steel reinforcement. The theoretical tensile model was used in a moment-curvature analysis. The residual stress in the tensile model used in the analysis was adjusted to reduce the error between the theoretical and experimental moment-curvature relationships after cracking occurs. The theoretical models showed that the effect of the steel fibers diminishes at higher ratios of steel reinforcement. The ratio between the residual force of the SFRC and the resultant force of the steel reinforcement decreases as the steel ratio increases. As a result, the influence from the SFRC is smaller.

Ultimately, the conclusions of the slab-strip experimental program were consistent with the findings of the case study analysis. An increase in the area of traditional steel reinforcement in a concrete specimen results in a proportional increase in the moment capacity. Adding fibers 0.5% by volume to the AASHTO empirical design satisfies both strength and service criteria. Traditional steel reinforcement can be excluded from a SFRC section with 2.0% by volume fibers while satisfying strength requirements.

9.1.3 Bridge Deck Experiment

The purpose of the full-scale SFRC bridge test was to demonstrate the effect of adding steel fibers to a two-way slab. The experimental program offered insight on the stiffness, deformability, failure mechanisms, and load capacity of a concrete bridge deck reinforced with steel bars and steel fibers. The geometry was chosen to both represent actual bridges in use as well as conform to tests conducted in the past by other researchers.

The deck was subjected to four tests consistent with traditional AASHTO (2014) load patterns: a single wheel load, a trailing axel design truck, and a single axel on the overhang of the bridge deck. The tests failed in a flexural manner with several cracks forming on the top surface parallel to the supporting girders. These cracks are consistent with negative bending experienced by the SFRC bridge deck at the girders. Directly under the load point, cracks formed on the bottom surface that radiated outwards in an elliptical radial fan mechanism. Multiple negative and positive bending cracks formed for each load pattern exhibiting the load redistribution of the SFRC. The fibers "bridged" the first cracks to form allowing other cracks to form prior to the eventual formation of a hinge in the critical cracks. The SFRC bridge deck achieved deflections of up to 2 inches prior to the failure of the bridge deck. In comparison, similar tests conducted by others using either traditionally designed and reinforced concrete or prestressed concrete with AFRP tendons achieved a deflection of 1 inch prior failure.

The overall performance of the SFRC bridge deck satisfies the serviceability and strength requirements of ADOT and AASHTO LRFD (2014). The bridge's maximum strength was 450% greater than the factored AASHTO demand. The largest stress measured in the steel reinforcement at the service limit state was 21 ksi.

Yield line and punching shear analysis was conducted to determine the theoretical collapse load of the SFRC specimens. The slab-strips cast and tested alongside the large scale specimen were used in determining the unit moment capacity for the analyses.

The punching shear strength of the SFRC bridge deck is larger than the deck's flexural strength based on these analyses. The yield line analysis significantly underpredicted the failure capacity of the SFRC bridge deck restrained on either side by girders. The analysis underpredicted the capacity of the single wheel load by 26%. The capacity of the trailing axel load was underpredicted by 44%. This result is consistent with conclusions made by other researchers (Fall et al 2014 and Destree and Mandl (2008). The membrane action and load redistribution provided by the steel fibers adds significant strength to the ultimate limit state of the structure not accounted for by yield line analysis.

The yield line analysis did not significantly underpredict the load in the overhang. The theoretical collapse load was 6% smaller than the experimental failure. Test LP3 was conducted on the overhang without restraint on one side. The lack of restraint prevents membrane action from occurring and increasing its moment capacity similar to the results for the other tests.

9.2 Design Recommendations

Steel fiber reinforced concrete enhances both the service and strength performance of plain concrete. Designers must be able to determine the tension properties of SFRC to fully utilize the benefits of SFRC. Other researchers have demonstrated the effectiveness of an inverse analysis

to determine key properties of the tension response while international organizations have developed notched flexural tests to determine the SFRC response. This thesis has utilized an inverse analysis and moment-curvature results of experimental data to develop a method for determining the service and strength performance of SFRC.

A procedure for determining the service and strength performance of an SFRC section has been proposed. The theoretical capacities are within 12.3% of the experimental results. Each method utilizes the traditional strain, stress, and resultant force section profiles. An additional component is added to each figure to account for the contributions of SFRC to the performance of the specimen. The proposed method for the service limit state differs from the traditional methods as it provides the maximum allowable moment capacity rather than verifying the steel stress at the service moment.

An empirical method utilizing the ACI 318 minimum dosage of steel fibers for shear reinforcement was proposed. The theoretical and experimental results show that adding fibers to a plain concrete section design for the strength limit state enhances the performance of the reinforced concrete specimen to adequate service levels.

Design aids proposed by manufacturers and other researchers can be used to design with SFRC. Two design aids are presented in this thesis relating the service and strength performance of SFRC. Designers with a known residual strength and section depth can utilize the design aids to determine the required steel reinforcement to satisfy their moment demands. The design aids were developed using a theoretical analysis and the general tension response proposed by Soranakom and Mobasher (2007).

9.3 Recommendations For Future Work

A design guideline has not yet been adopted in the United States for SFRC. Currently there is not a way to accurately determine the residual stress associated with SFRC. Material tests proposed adopted by ASTM provide information regarding the post-crack behavior of SFRC; however, a direct translation of the force-deflection data to stress-strain data has not been developed. An inverse analysis similar to the one used in this thesis have been shown by other researchers to provide adequate information to design. The lack of a material test with a direct correlation to the tensile stress-strain response prevents the widespread use and adoption of a design procedure for fiber reinforced concrete in the United States. Future work to develop and adopt material test to determine the stress-strain response of FRC is critical to the use of enhanced concrete.

Additional research needs to be conducted for concrete systems using both fibers and traditional steel reinforcement. As shown in 6, an inverse analysis with a generally accepted SFRC tensile model and unreinforced concrete beams can be used to determine the tensile constitutive

relationship for strain-softening SFRC. However, the interaction of the steel fibers and steel reinforcement results in theoretical models that under predict the capacity of lightly reinforced sections and over predict heavily reinforced sections. Further experimentation of the dual reinforcement system will provide insight on the tension hardening of the SFRC and its contribution to the capacity of the section.

The yield line analysis under predicted the capacity of the SFRC bridge deck. In particular, the under prediction was observed in the portions of the bridge that were the most restrained. The yield line analysis failed to capture 26% capacity of the individual wheel load patterns. Further work investigating the effect of membrane action and the significant redistribution of load due to the excessive cracking can allow for designers to use the full potential of SFRC.

REFERENCES

American Association of State Highway and Transportation Officials (AASHTO). 2014. AASHTO LRFD Bridge Design Specifications, U.S. Customary Units. Washington, DC: Print.

American Concrete Institute (ACI) Committee 318. 2011. *Building code requirements for structural concrete (ACI 318-11) and commentary*. Edited by I. American Concrete, *2011 building code and commentary*. Farmington Hills, MI: Farmington Hills, MI : American Concrete Institute.

ACI Committee 544. 1988. *Design considerations for steel fiber reinforced concrete*, *Steel fiber reinforced concrete*. Farmington Hills, Mich.: Farmington Hills, Mich. : American Concrete Institute.

ACI Committee 544. 1998. *Guide for specifying, proportioning, mixing, placing, and finishing steel fiber reinforced concrete*, *Specifying, proportioning, mixing, placing, and finishing steel fiber reinforced concrete*. Farmington Hills, Mich.: Farmington Hills, Mich. : American Concrete Institute.

ACI Committee 544. 1999. *Measurement of properties of fiber reinforced concrete*, *Properties of fiber reinforced concrete*. Farmington Hills, Mich.: Farmington Hills, Mich. : American Concrete Institute.

ACI Committee 544. 2016. *Report on Indirect Method to Obtain Stress-Strain Response of Fiber-Reinforced Concrete (FRC)*. Farmington Hills, Mich.: Farmington Hills, Mich. : American Concrete Institute.

Arizona Department of Transportation (ADOT). 2006. *ADOT Construction Manual - Section 6: Structures*.

Arizona Department of Transportation (ADOT). 2011. *ADOT Bridge Design Guidelines - Section 5: Concrete Structures*.

Aviram, A., Stojadinovic, B., and Parra-Montesinos, G. J. 2014. "High-Performance Fiber-Reinforced Concrete Bridge Columns under Bidirectional Cyclic Loading." *ACI Struct. J.* 111 (2): 303-312.

Bae, Han-Ug, Oliva, Michael G., and Bank, Lawrence C. 2010. "Obtaining Optimal Performance with Reinforcement-Free Concrete Highway Bridge Decks." *Engineering Structures* 32 (2010): 2300-2309.

Bae, H. U., Oliva, M. G., and Bank, L. C. 2011. "Reinforcement-Free Decks Using Modified Strut-and-Tie Model." *ACI Struct. J.* 108 (5): 562-571.

Campione, Giuseppe. 2002. "The Effects of Fibers on the Confinement Models for Concrete Columns." *Canadian Journal of Civil Engineering* 29: 742-750.

Chandrangsu, Kulsiri. 2003. *Innovative Bridge Deck with reduced Reinforcement and Strain-Hardening Fiber Reinforced Cementitious Composites*, Department of Civil and Environmental Engineering, University of Michigan, Ann Arbor, Mi.

Choi KK, Reda Taha MM, Park HG, and Maji AK. 2007. “Punching Shear Strength Of Interior Concrete Slab–Column Connections Reinforced With Steel Fibers.” *Cement & Concrete Composites.* 29, pp. 409–420.

Destrée, X. 2009. "Steel-Fibre-Only Reinforced Concrete In Free Suspended Elevated Slabs." *Concrete Engineering International* 13 (1): 47-49.

Destrée, Xavier, and Mandl, Jürgen. 2008. “Steel Fibre Only Reinforced Concrete In Free Suspended Elevated Slabs.” In *Tailor Made Concrete Structures*: CRC Press.

Dhonde, Hemant B., Mo, Y.L., Hsu, Thomas T.C. 2005. *Fiber Reinforcement in Prestressed Concrete Beams.* FHWA/TX-06/0-4819-1. Houston, Tx: Department of Civil and Environmental Engineering Cullen College of Engineering University of Houston

Dinh, Hai H., Parra-Montesinos, Gustavo J., and Wight, James K. 2011. "Shear Strength Model for Steel Fiber Reinforced Concrete Beams without Stirrup Reinforcement." *Journal of Structural Engineering* 137 (No. 10): 1039-1051.

Dunn, Mark, Brehm, Lyle, Engineer, Tama County, Klaiber, F Wayne, Phares, Brent M, and Wood, Douglas L. 2005. *Tama County’s Steel Free Bridge Deck.* Paper read at Proc., Mid-Continent Transportation Research Symposium, Ames, Iowa.

Fall, D., Shu, Jiangpeng, Rempling, Rasmus, Lundgren, Karin, Zandi, Kamyab. 2014. "Two-Way Slabs: Experimental Investigation Of Load Redistributions In Steel Fibre Reinforced Concrete." *Engineering Structures* 80: 61-74.

fédération internationale du béton (fib). 2013. *fib Model Code for Concrete Structures 2010,* Wiley.

Harajli MH, Maalouf D, and Khatib H. 1995. “Effect Of Fibers On The Punching Shear Strength Of Slab–Column Connections.” *Cement & Concrete Composites.* 17, pp.161–170.

Hillerborg, M. Modéer, P.-E. Petersson. 1976. “Analysis Of Crack Formation And Crack Growth In Concrete By Means Of Fracture Mechanics And Finite Elements.” *Cement Concrete Res.*, 6 (6) (1976), pp. 773–782

Kim, D. J., Naaman, Antoine E., El-Tawil, Sherif. 2008. "Comparative Flexural Behavior of Four Fiber Reinforced Cementitious Composites." *Cement and Concrete Composites* 30(2008): 917-928.

Kwak, Yoon-Keun, Eberhard, Marc O., Kim, Woo-Suk, and Kim, Jubum 2002. "Shear Strength of Steel Fiber-Reinforced Concrete Beams without Stirrups." *ACI Structural Journal* 99 (No. 4): 530-538.

Lequesne, R., Setkit, M., Kopczynski, C., Ferzli, J., Cheng, M. Y., Parra-Montesinos, G., and Wight, J. K. 2011. “Implementation Of High-Performance Fiber Reinforced Concrete Coupling Beams In High-Rise Core-Wall Structures.” *ACI Special Publication 280.*

Lequesne, R. D., Parra-Montesinos, G. J., and Wight, J. K. 2013. "Seismic Behavior and Detailing of High-Performance Fiber-Reinforced Concrete Coupling Beams and Coupled Wall Systems." *J. Struct. Eng.-ASCE* 139 (8): 1362-1370.

Liao, W.-C., Chao, Shih-Ho, Park, Sang-Yeol, and Naaman, Antoine E. (2006). Self-Consolidating High Performance Fiber Reinforced Concrete - Preliminary Investigation. Ann Arbor, MI, University of Michigan.

T. Y. Lim, P. P. and S. L. Lee. 1987. "Bending Behavior of Steel-Fiber Concrete Beams." *Structural Journal* 84(6): 524-536.

Mander, T., Henley, M., Scott, R., Head, M., Mander, J., and Trejo, D. (2010). "Experimental Performance of Full-Depth Precast, Prestressed Concrete Overhang, Bridge Deck Panels." *J. Bridge Eng.*, 10.1061/(ASCE)

Michels, Julien, Waldmann, Daniele, Maas, Stefan, and Zurbes, Arno. 2011. "Steel Fibers as only Reinforcement for Flat Slab Construction - Experimental Investigation and Design." *Construction and Building Materials* 26 (2012): 145-155.

Mobasher, Barzin. 2012. *Mechanics of Fiber and Textile Reinforced Cement Composites*: Taylor and Francis Group.

Mobasher, B., and Destrée, X. 2010. “Design And Construction Aspects Of Steel Fiber-Reinforced Concrete Elevated Slabs.” *Special Publication 270.*

Mufti, Aftab A., Jaeger, Leslie G., Bakht, Baidar, and Wegner, Leon D. 1993. "Experimental Investigation of Fibre-Reinforced Concrete Deck Slabs without Internal Steel Reinforcement." *Canadian Journal of Civil Engineering* 20: 398-406.

Naaman, Antoine E., and Chandrangsu, Kulsiri. 2004. "Innovative Bridge Deck System Using High-Performance Fiber-Reinforced Cement Composites." *ACI Structural Journal* 101 (No. 1): 57-64.

Naaman, Antoine E., Likhitruangsilp, Visit, Parra-Montesinos, Gustavo. 2007. "Punching Shear Response of High-Perofrmance Fiber-Reinforced Cementitious Composite Slabs." *ACI Structural Journal* 104 (No. 2): 170-179.

Naaman, A. E. and H. W. Reinhardt (2006). "Proposed Classification of HPFRC Composites Based on Their Tensile Response." *Materials and Structures* 39(5): 547-555.

Niwa, Junichiro, Shakya, Kabir, Matsumoto, Koji, and Watanabe, Ken. 2012. "Experimental Study on the Possibilty of Using Steel Fiber-Reinforced Concrete to Reduce Conventional rebars in Beam-Column Joints." *Journal of Materials in Civil Engineering* 24 (12): 1461-1473.

Nguyen-Minh, L., Rovňák, M., Tran-Quoc, T., Nguyen kim, K. 2011. "Punching Shear Resistance of Steel Fiber Reinforced Concrete Flat Slabs." *Procedia Engineering* 14: 1830-1837.

Ostertag, C. P. and Blunt, J. 2008. *Use of Fiber Reinforced Concrete in Bridge Approach Slabs.* CA09-0632. Berkeley: Civil and Environmental Engineering Department University of California

Park, Philip, Xijun Shi, and Younho Rew. 2015. "October 2015 TAC Meeting: Applications of Fiber Reinforced Concrete". Presentation.

Pirayeh Gar, S., Head, M., Hurlebaus, S., and Mander, J. 2013. "Experimental Performance of AFRP Concrete Bridge Deck Slab with Full-Depth Precast Prestressed Panels." *J. Bridge Eng.*

RILEM TC 162-TDF. 2002. "Test and Design Methods for Steel Fibre Reinforced Concrete." *Materials and Structures* 35 (June 2002): 262-278.

RILEM TC 162-TDF. 2003. "Test and Design Methods for Steel Fibre Reinforced Concrete - Stress-Strain Design Method, Final Recommendation." *Materials and Structures* 36 (October 2003): 560-567.

Roesler, Jeffery R., Lange, David A., Altoubat, Salah A., Reider, Klause-Alexander, and Ulreich, Gregory R. 2004. "Fracture of Plain and Fiber-Reinforced Concrete Slabs under Monotonic Loading." *Journal of Materials in Civil Engineering* 16 (No. 5): 452-460.

Soranakom, Chote and Mobasher, Barzin. 2009. "Flexural Design of Fiber-Reinforced Concrete." *ACI Materials Journal* 106 (No. 5): 461-469.

Texas Department of Transportation (TxDOT). 2014. *Standard Specifications for Construction and Maintenance of Highways, Streets, and Bridges.*

Wille, K., El-Tawil, S., Naaman, A. E. (2014). "Properties of Strain Hardening Ultra-high Performance Fiber Reinforced Concrete (UHP-FRC) under Direct Tensile Loading." *Cement and Concrete Composites* 48: 53-66.

Woods, A.P. “Double-Punch Test for Evaluating the Performance of Steel Fiber-Reinforced Concrete,” M.S. Thesis, May 2012. University of Texas at Austin, Austin, TX.

APPENDIX A DAMAGE PROFILES OF SLAB STRIP SPECIMENS

A.1 S7505BTM35

Slab strip specimen S7505BTM35 has 3-#5 steel bars located with a clear cover of 1 inch from the bottom of the specimen. The specimen has an overall depth of 7.5 inches and a fiber volume of 0.5%. The specimen achieved a maximum capacity of 23.55 kips at a deflection of 0.7 inches (L/120). At this time, all observed cracks had already formed.

A total of 14 cracks formed on the east face of the specimen, eight inside the constant moment region, and 15 on the west face of the specimen, nine inside the constant moment region. The first crack for each side occurred at a deflection of 0.1 inches (L/840). The majority of the cracks extended to the mid-depth of the specimen by a deflection of 0.3 inches (L/280). Beyond this deflection, little upward extensions was observed in the cracks outside of the constant moment region. At 0.7 inches (L/120) of deflection, the extension of cracks in the constant moment region slowed or stopped. The cracks approached referenced elevation E, but did not extend passed it. Figure 1 through Figure 4 the vertical progression of the cracks on the east and west faces.

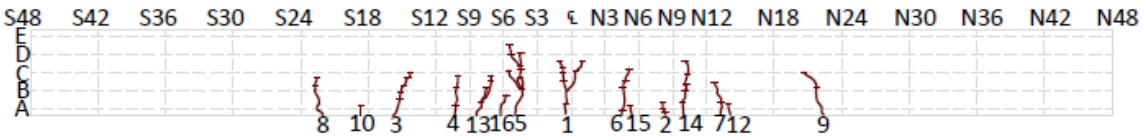

Figure 1. Crack Profile of the East Face (LVDT)

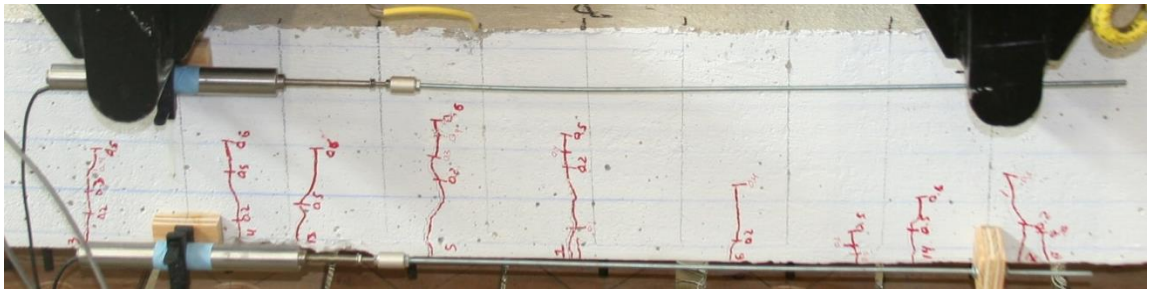

Figure 2. Crack Profile of East Face in Constant Moment Region

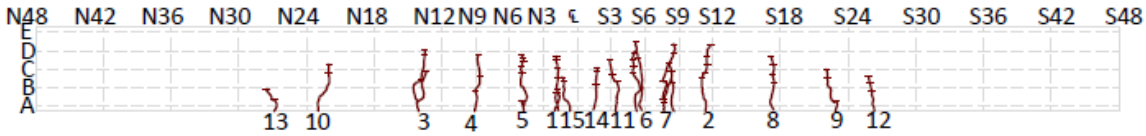

Figure 3. Crack Profile of the West Face (Optotrak)

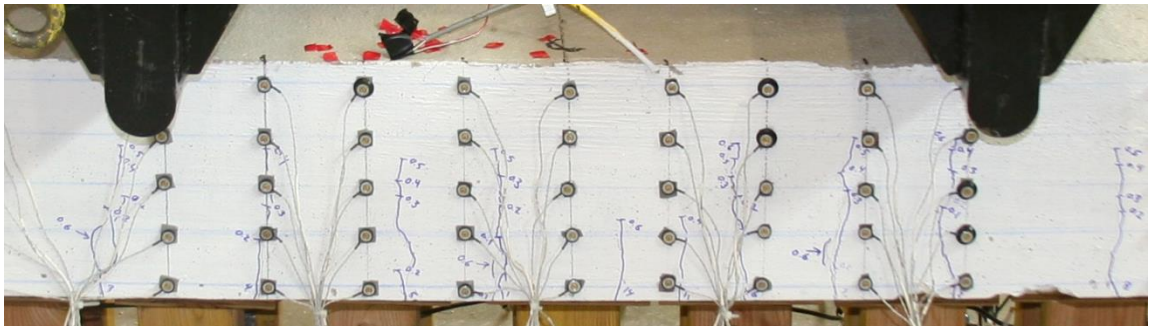

Figure 4. Crack Profile of West Face in Constant Moment Region

The average non-critical crack width on the east and west face is 0.19 mm 0.37 mm respectively. Ultimately, cracks E5 and W7 created the primary failure plane of the specimen. At 0.8 inches of deflection, the rate of increase in the width of E5 exceeded the rate of all other cracks. The crack width of E5 was 1.27 mm while the next largest crack on the east face, E1, had a width of 0.64 mm. On the west face, adjacent cracks W6 and W7 maintained a steady width increase. At a deflection of 1.2 inches and capacity of 22.6 kips, E5 surpassed the maximum crack width allowed by RILEM (2002) and fib (2010), 2.5 mm. Figure 5 demonstrates the relationship between crack opening and deflection for each face.

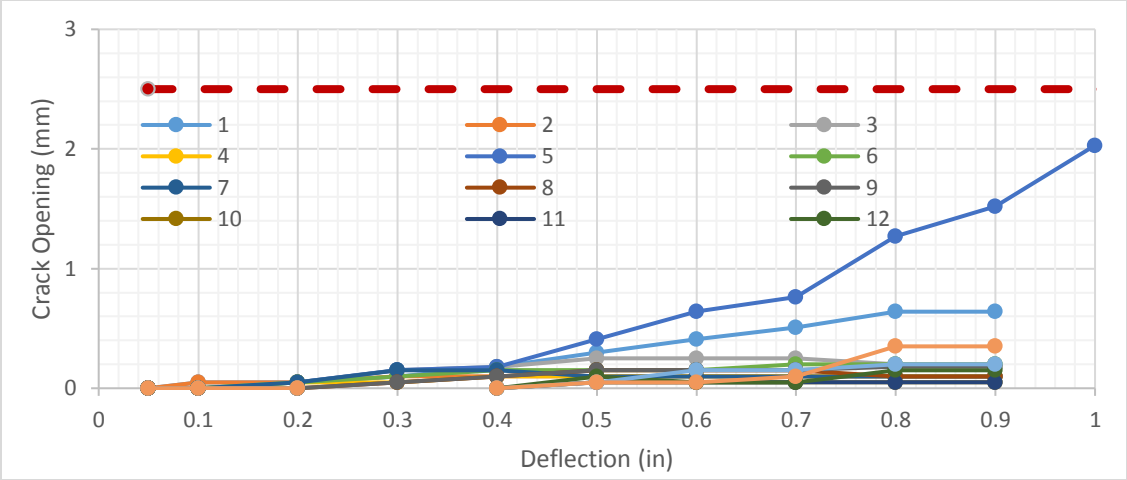

(a)

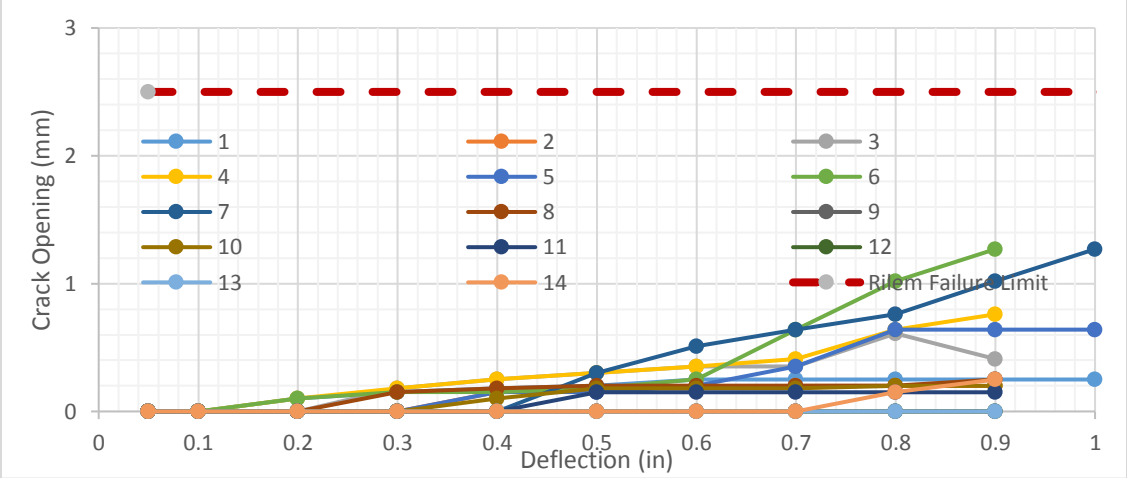

(b)

Figure 5. Crack Opening vs Strip Deflection for (a) East Face and (b) West Face

Figure 6 and Figure 7demonstrate the progression of critical cracks on the east and west faces. E5 and W6 first formed at deflection step 0.2 inches (L/480). By 0.3 inches, they both extended to the mid-depth of the section. At deflection step 1.0 inch each crack had reached its highest point above reference point D. As shown, both E5 and W6 exhibited spalling related to the crack, aggregate, and fibers. A “wedge” of concrete corresponding to a small coarse aggregate was dislodged from both E5 and W6 while fibers near the surface of the specimen resulted in spalling at reference elevation B on W7.

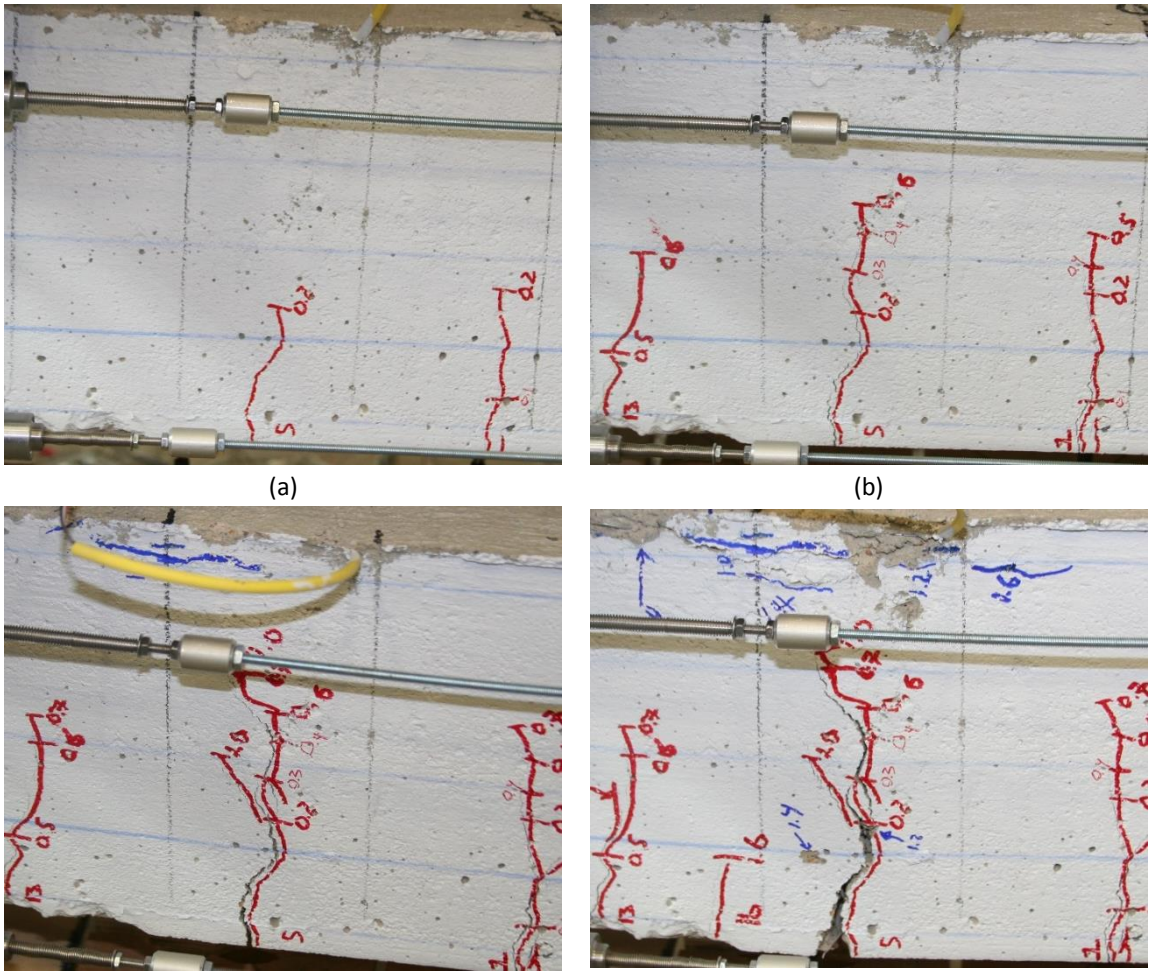

(a) (b)

(c) (d)

Figure 6. Crack Progression of E5 at deflection:
(a) 0.2 inches, (b) 0.6 inches, (c) 1.0 inches, and 1.6 inches.

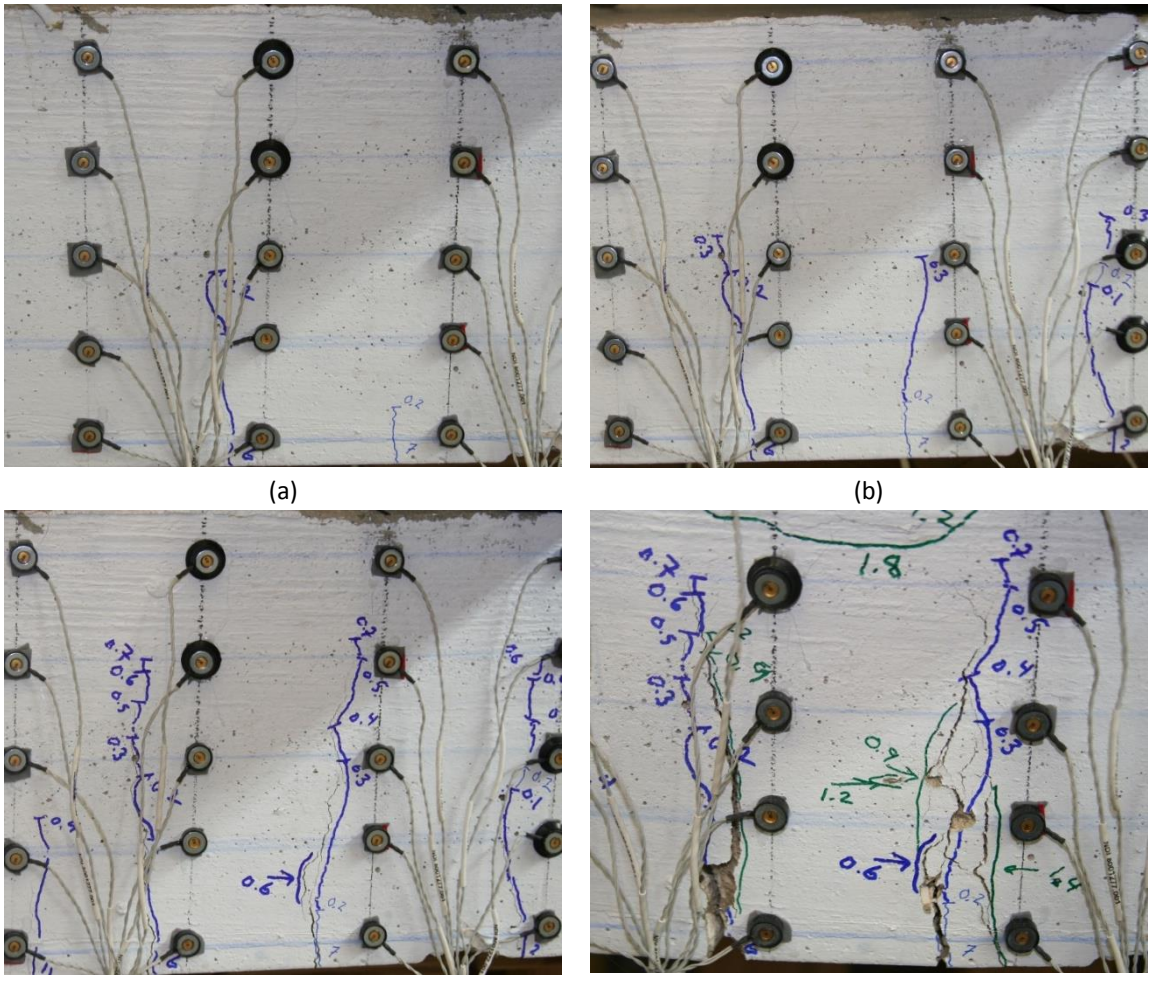

(a) (b)

(c) (d)

Figure 7. Crack Progression of W6 and W7 at deflection:
(a) 0.2 inches, (b) 0.3 inches, (c) 0.7 inches, and 1.8 inches.

Crushing was first observed on both sides at a deflection of 1 inch or a capacity of 23.1 kips. The crushing occurred between references S3 and S6. By the conclusion of the test, the crushed region expanded to include the entire south region of the constant moment region and approached vertical reference D. At the completion of the test, the specimen had not collapsed. Figure 8 demonstrates the progression of crushing damage in specimen S7505BTM35.

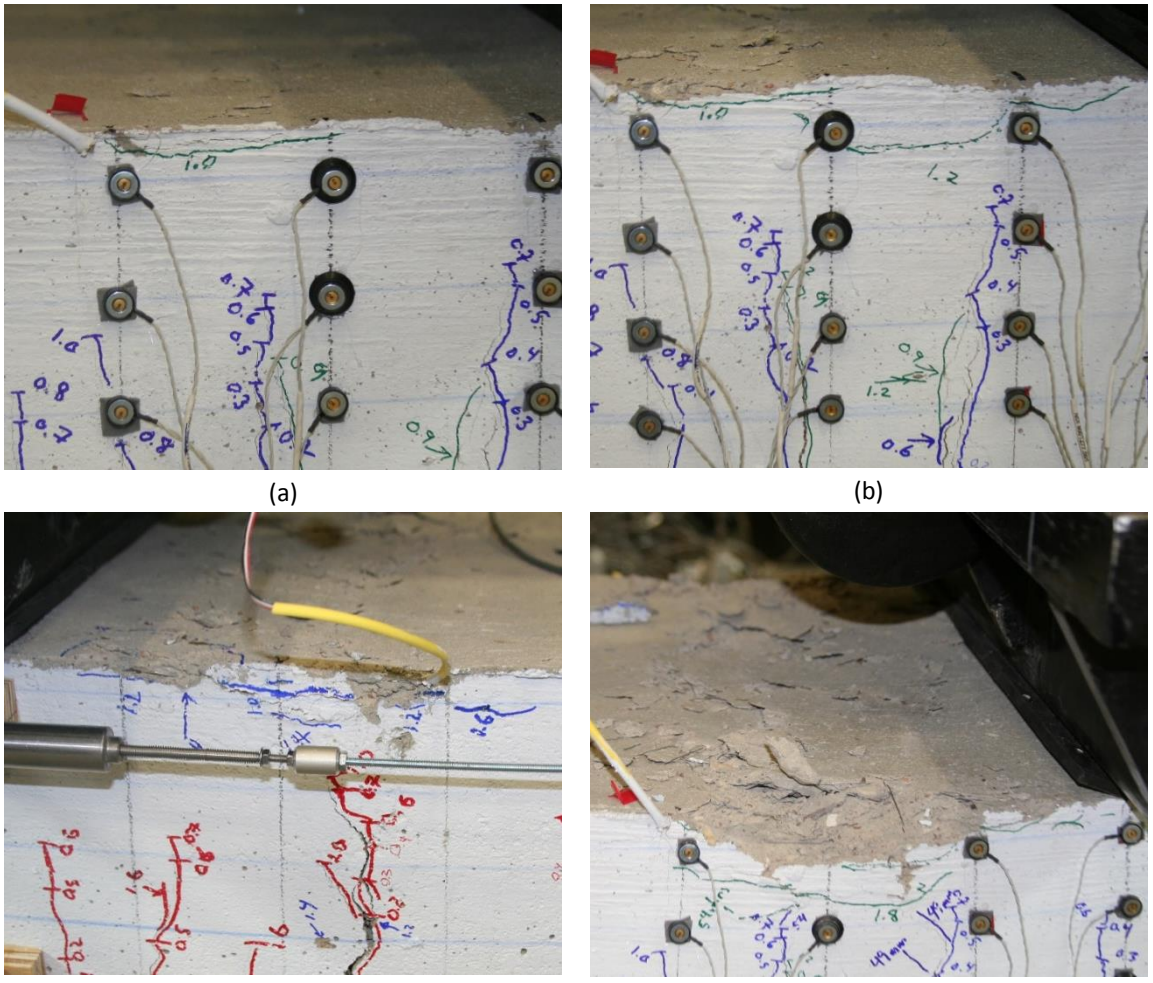

(a) (b)

(c) (d)

Figure 8. Crushing Progression of S7505BTM35

A.2 S7505BTM25

Slab strip specimen S7505BTM25 has 2-#5 steel bars located with a clear cover of 1 inch from the bottom of the specimen. The specimen has an overall depth of 7.5 inches and a fiber volume of 0.5%. The specimen achieved a maximum capacity of 18.58 kips at a deflection of 0.8 inches (L/105). At this time, all observed cracks had already formed.

A total of 12 cracks formed on the east face of the specimen, six inside the constant moment region, and 13 on the west face of the specimen, seven inside the constant moment region. The first crack for each side occurred at a deflection of 0.1 inches (L/840). The majority of the cracks extended to the mid-depth of the specimen by a deflection of 0.6 inches (L/140). Beyond this deflection, little upward extensions were observed in the cracks outside of the constant moment region. At 0.8 inches (L/105), the extension of cracks in the constant moment region slowed or stopped. Between 0.8 and 1.1 inches, some cracks in the constant moment region extended approximately an inch beyond reference elevation D. The cracks approached reference elevation E, but did not extend passed it. Figure 9 through Figure 12 demonstrate the vertical progression of the cracks on the east and west faces.

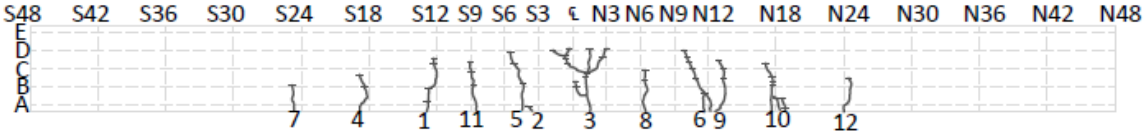

Figure 9. Crack Profile of the East Face (LVDT)

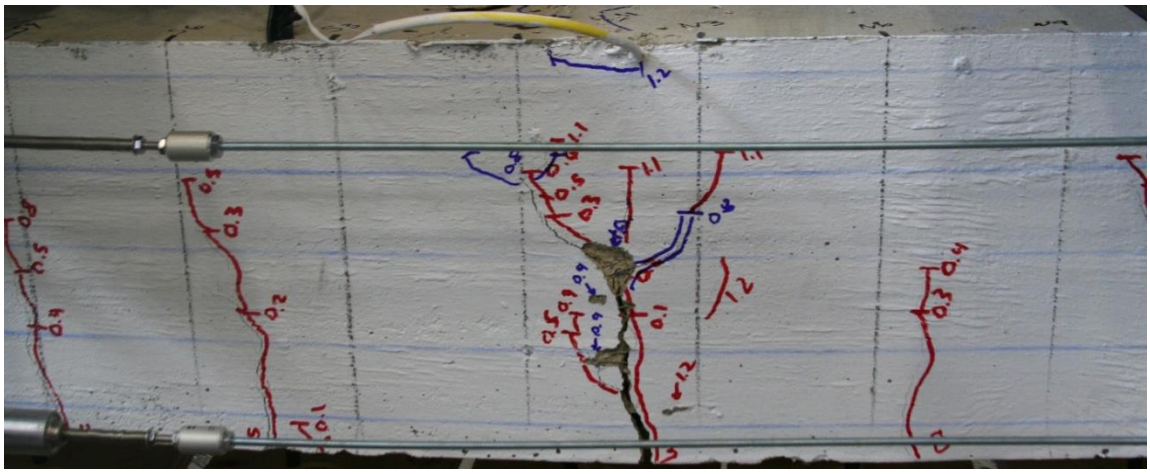

Figure 10. Crack Profile of East Face in Constant Moment Region

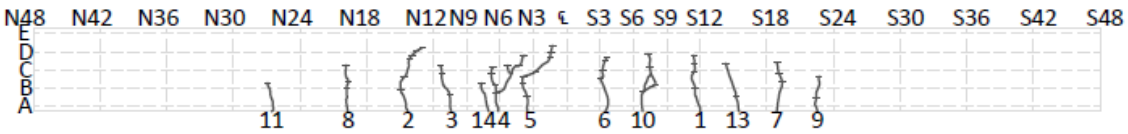

Figure 11. Crack Profile of the West Face (Optotrak)

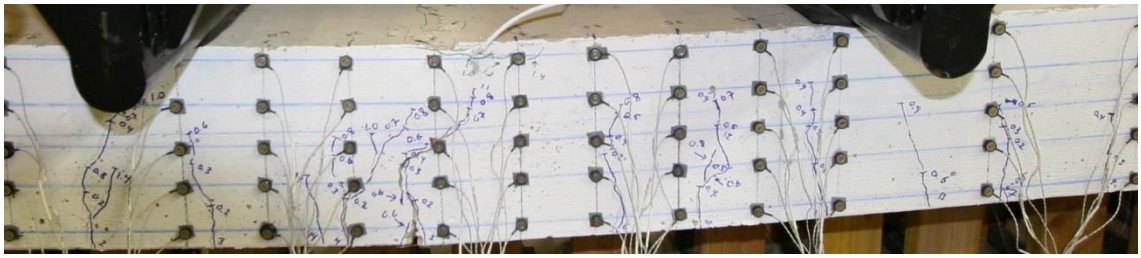

Figure 12. Crack Profile of West Face in Constant Moment Region

The average non-critical crack width on the east and west face is 0.28 mm 0.47 mm respectively. Ultimately, cracks E3 and W5 created the primary failure plane of the specimen. At a deflection of 0.8 inches, the rate of increase in the width of E5 exceeded the rate of all other cracks. The crack width of E3 was 2.54 mm while the next largest crack on the east face, E1, had a width of 1.02 mm. On the west face, adjacent cracks W4 and W5 maintained a steady width increase. At a deflection of 0.9 inches and capacity of 18.55 kips, E3 surpassed the maximum crack width allowed by RILEM (2002) and fib (2010), 2.5 mm. Figure 13 and Figure 14 demonstrate the relationship between crack opening and deflection for each face.

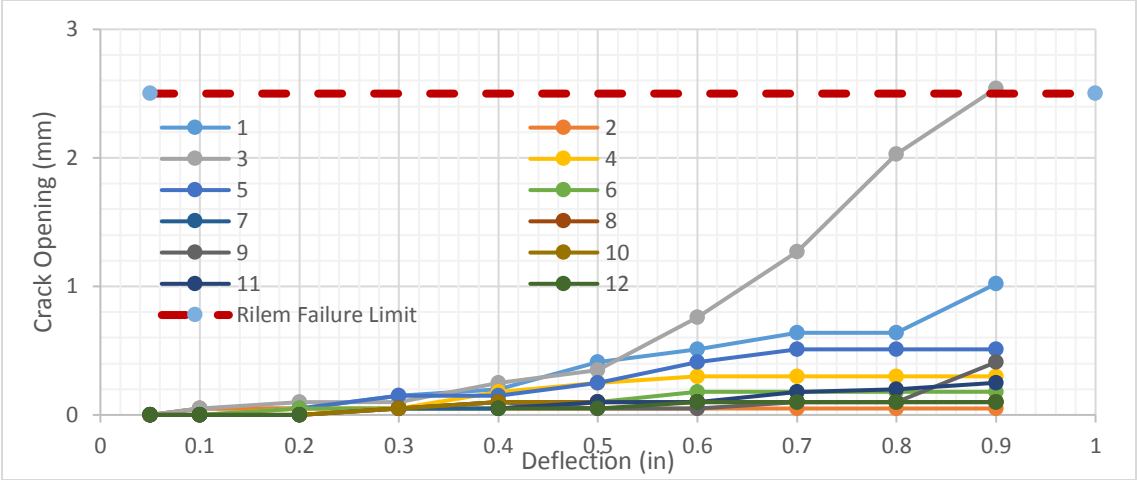

(a)

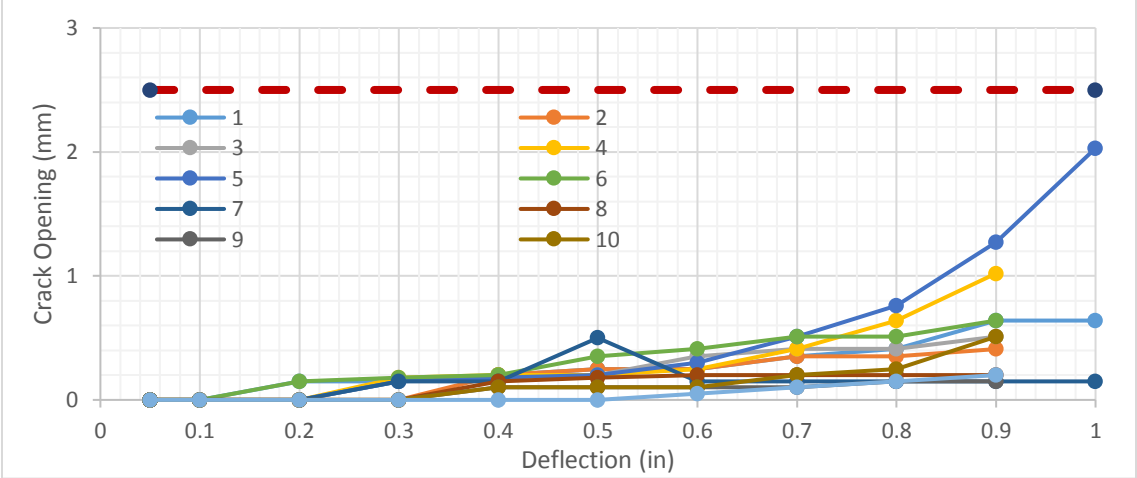

(b)

Figure 13. Crack Opening vs Strip Deflection for (a) West Face and (b) East Face

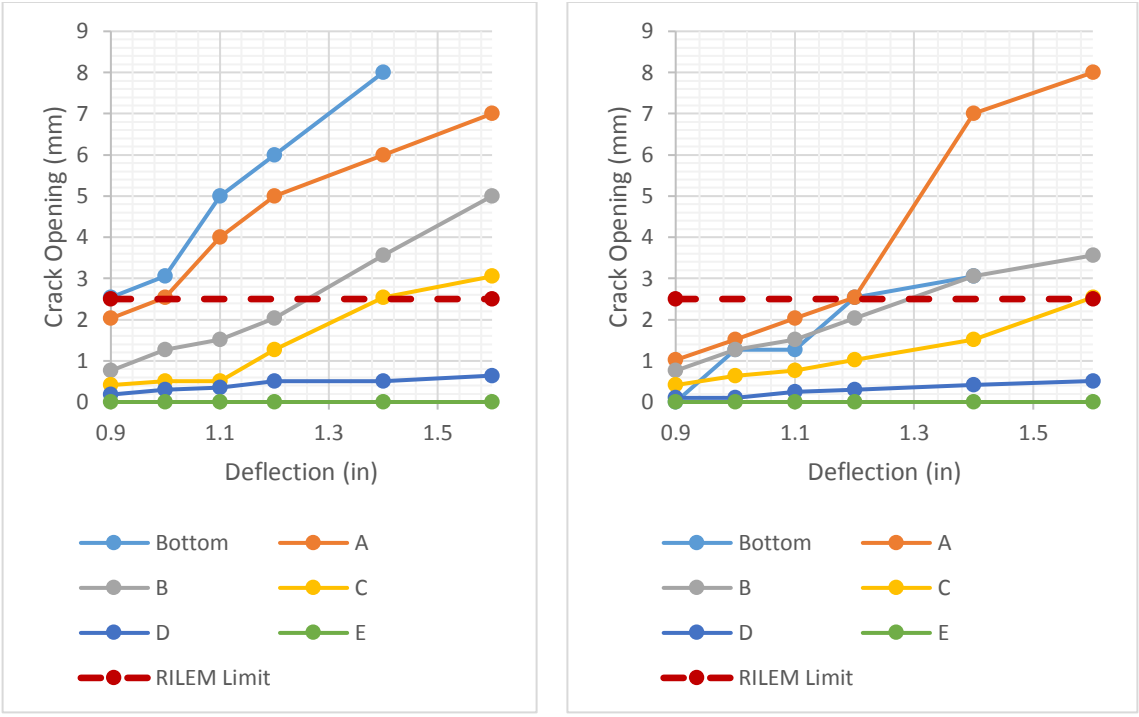

Figure 14. Crack Opening vs Strip Deflection for Primary Crack at Each Reference Elevation (a) E3 and (b) W5

Figure 15 and Figure 16 demonstrate the progression of critical cracks on the east and west faces. E3 first formed at deflection step 0.1 inches (L/840) while W3 formed did not form until the next deflection step, 0.2 inches (L/420). By 0.3 inches, they both extended to the mid-depth of the section. At deflection step 1.1 inches (L/76), both cracks had reached its highest point above reference point D. Severe spalling was observed in E3 at reference elevation C. The spalling was directly related to steel fibers located near the surface due to their hooked ends not having sufficient cover.

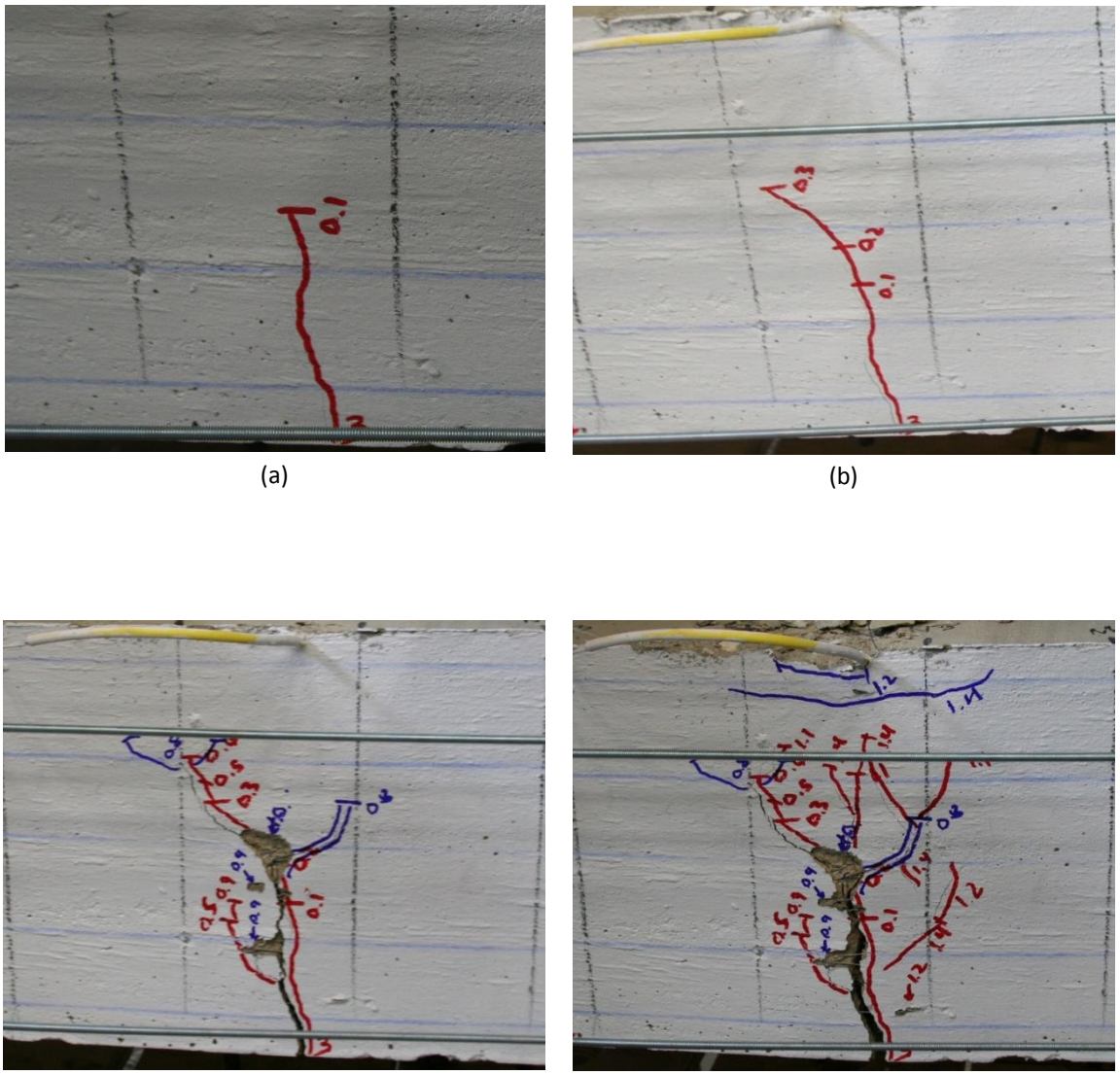

(a) (b)

(c) (d)

Figure 15. Crack Progression of E3 at deflection:
(a) 0.1 inches, (b) 0.3 inches, (c) 1.0 inches, and 1.4 inches.

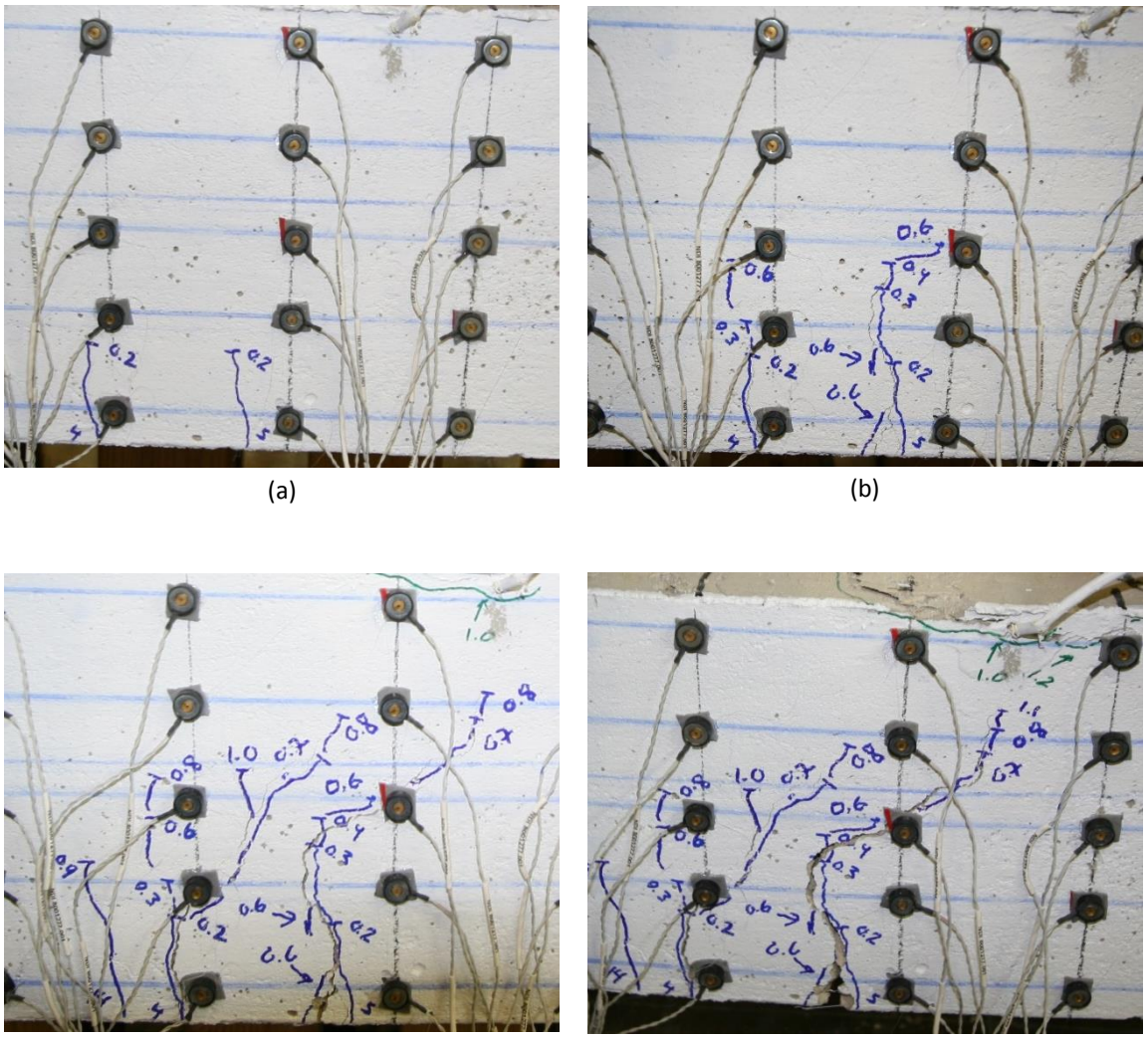

(a) (b)

(c) (d)

Figure 16. Crack Progression of W5 at deflection:
(a) 0.2 inches, (b) 0.6 inches, (c) 1.0 inches, and 1.4 inches.

Crushing was first observed on both sides at a deflection of 1.0 inch (L/84) or a capacity of 18.63 kips. The crushing occurred between references centerline and N3. By the conclusion of the test, the crushed region expanded south to include S3 to N3, approximately 6 inches wide. At the conclusion of testing, the specimen had not collapsed. Figure 17 demonstrates the crushed region of concrete for specimen S7505BTM25.

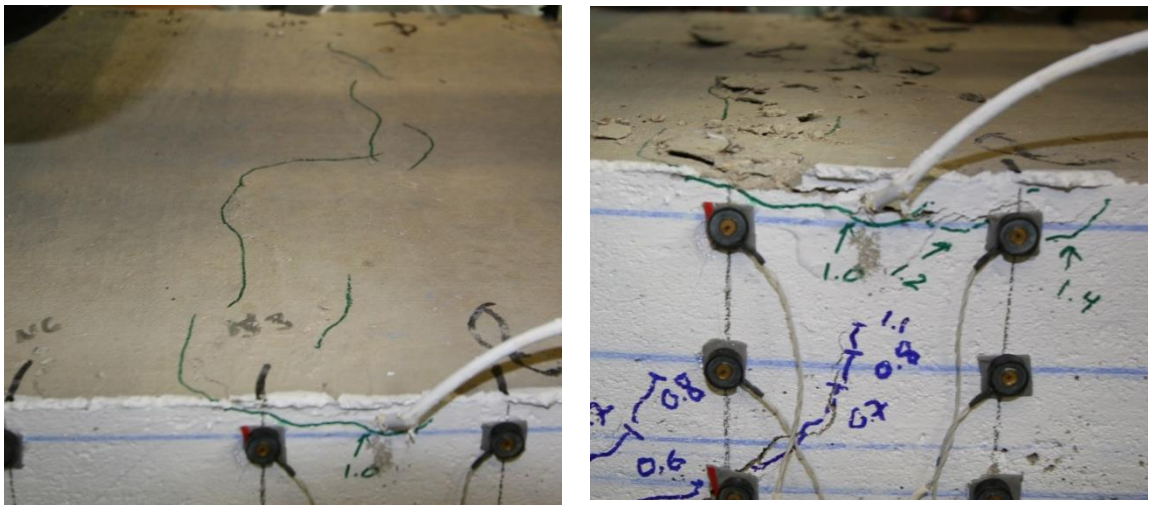

(a) (b)

Figure 17. Crushing Progression of S7505BTM25 deflection of (a) 1.0 inch and (b) 1.4 inch

A.3 S7505BTM24

Slab strip specimen S7505BTM24 has 2-#4 steel bars located at the mid-depth of the specimen. The specimen has an overall depth of 7.5 inches and a fiber volume of 0.5%. The specimen achieved a maximum capacity of 14.70 kips at a deflection of 0.9 inches (L/93). At that time, all observed cracks had already formed.

The bottom edge on the east face was damaged in the demolding of the specimen between N3 and S9. Cracks E1, E5, and E10 formed at the base of this damaged region as shown in Figure 18.

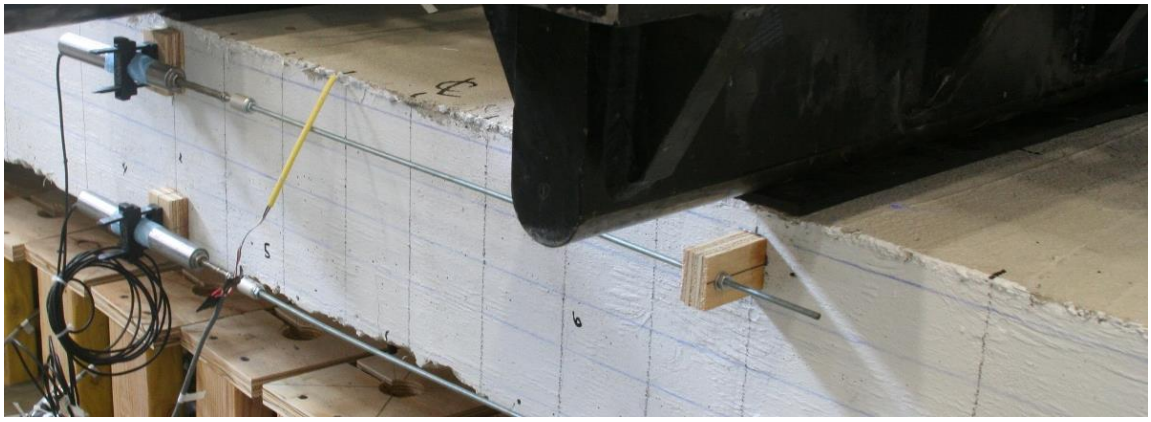

Figure 18. Damaged Corner of S7505BOT24 Where 4 Cracks Have Formed

A total of 12 cracks formed on the east face of the specimen, seven inside the constant moment region, and 13 on the west face, five inside the constant moment region. The first crack for both the east and west face occurred during the 0.1 inch deflection step, (L/840). All cracks formed by the 0.50 inch deflection step (L/168). Cracks outside the constant moment region progressed vertically to reference elevation D, or approximately 1.9 inches from the top surface. Cracks inside the constant moment region progressed vertically to reference elevation E, or approximately 0.5 inches from the top surface. Vertical progression of cracks ceased at deflection step 0.7 inches (L/120). Further increasing the deflection of the specimen resulted in widening of the primary crack and crack branching.

The critical cracks on the east face and west face are E12 and W7. Crack E1 formed during the 0.5 inch deflection step (L/168) while crack W7 formed during the 0.2 inch deflection step (L/420). Both cracks formed between the centerline and horizontal reference S3. The maximum allowable crack width, 2.5 mm, for each crack was observed at deflection step 1.0 inches (L/84). Critical crack E12 formed a wedge with crack E1 at the bottom edge allowing a large piece of

concrete to fall away. Figure 19 and Figure 20 demonstrate the progression of each crack throughout the test.

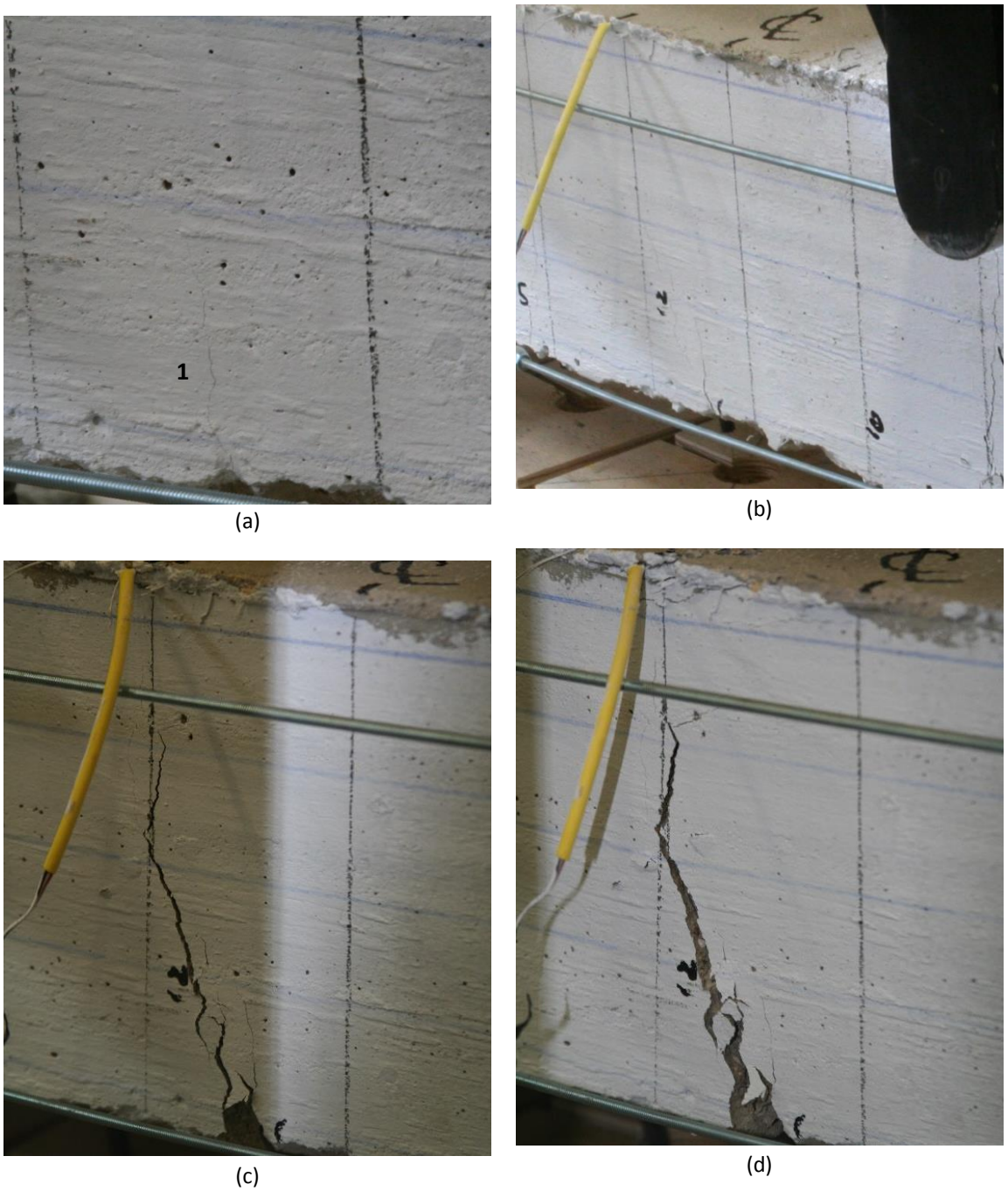

(a) (b)

(c) (d)

Figure 19. Crack Progression of E1 and E12 at Deflection Step: (a) 0.1 inches, (b) 0.6 inches, (c) 1.0 inches, and 1.4 inches

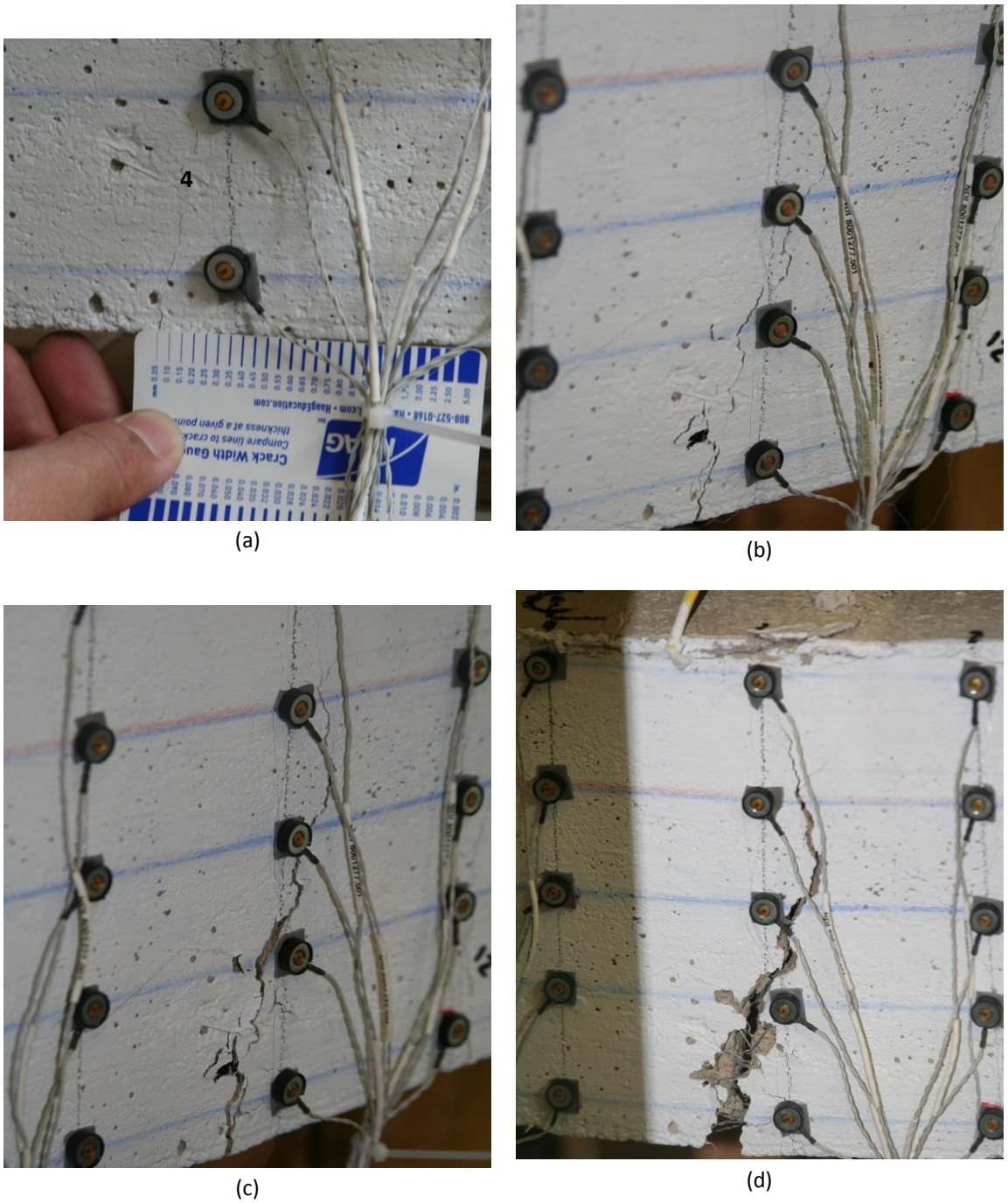

(a) (b)

(c) (d)

Figure 20. Crack Progression of W4 at Deflection Step:
(a) 0.2 inches, (b) 0.7 inches, (c) 1.0 inches, and 1.6 inches

Crushing was first observed on the east, west, and top surface at deflection step 1.0 inches (L/84). The crushing began at horizontal reference S3 above each critical crack. As the test continued, the crushing extended horizontally extending to centerline and S6. The crushed

concrete region extended downward and joined the tension cracks prior to completion of the test. The specimen did not collapse due to the steel reinforcement; however, a complete fracture plane of the concrete was observed. Figure 21 exhibits the progression of concrete crushing and the extent of the damage prior to removal of the specimen.

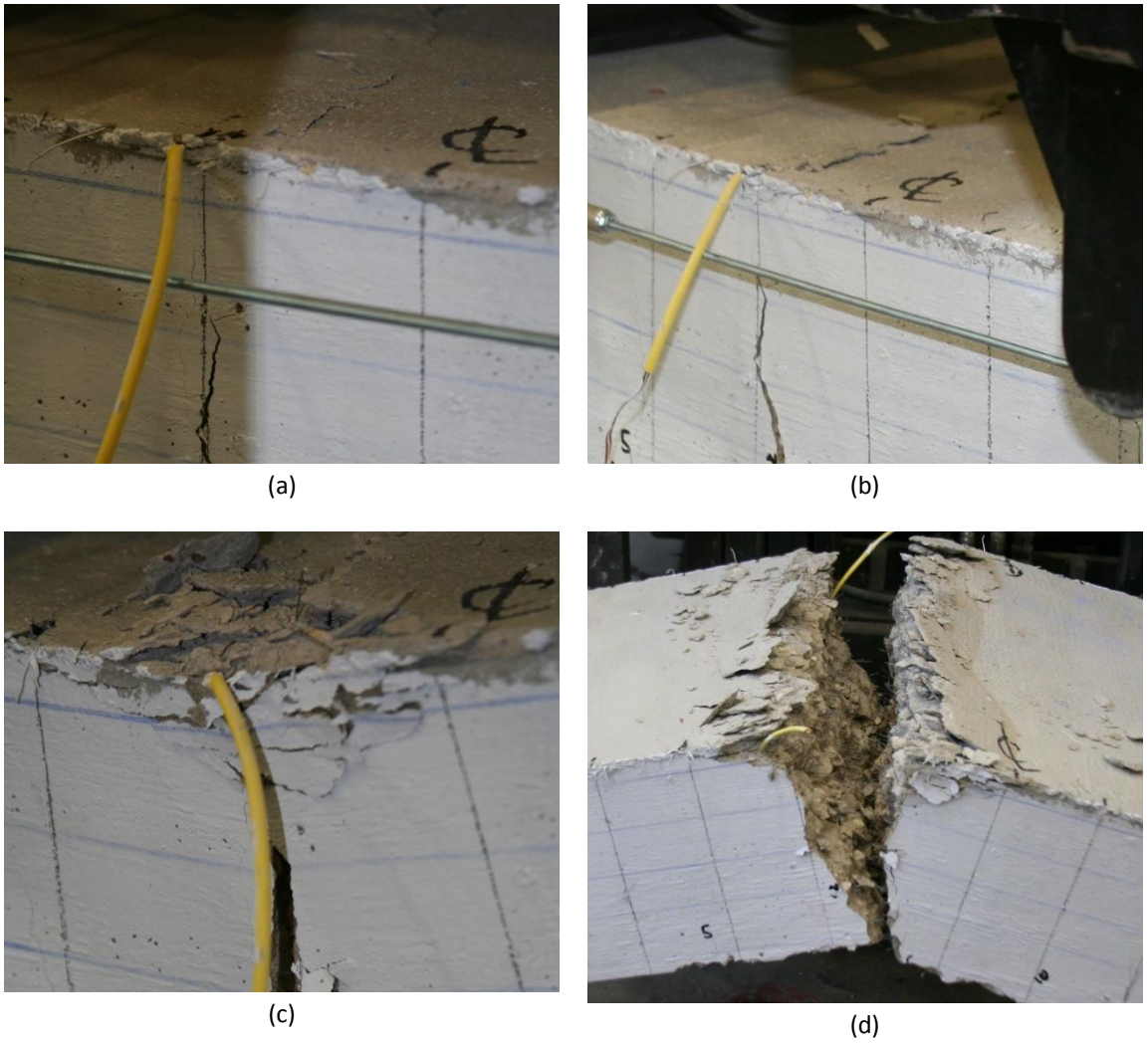

(a) (b)

(c) (d)

Figure 21. Crushing Progression of S7505BTM24 deflection:
(a) 1.2 inch, (b) 1.6 inch, (c) After Removal of Instrumentation and (d) Completion of Test

A.4 S7505BTM23

Slab strip specimen S7505BTM23 has 2-#3 steel bars located with a clear cover of 1 inch from the bottom of the specimen. The specimen has an overall depth of 7.5 inches and a fiber volume of 0.5%. The specimen achieved a maximum capacity of 10.0 kips at a deflection of 0.5 inches (L/168). At that time, all observed cracks had already formed.

On the east face of the specimen, the bottom corner was damaged throughout the constant moment region. Cracks E1, E2, E8, and E10 formed in this damaged region as shown in Figure 22.

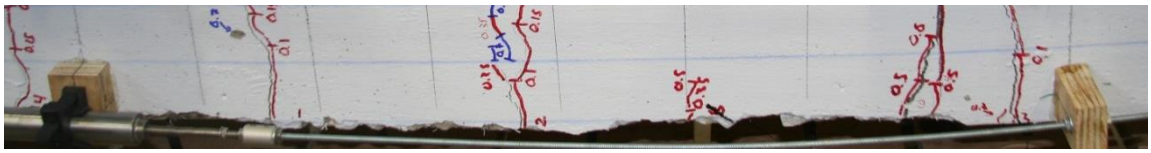

Figure 22. Damaged Corner of S7505BTM23 Where 4 Cracks Have Formed

A total of 10 cracks formed on the east face of the specimen, four inside the constant moment region, and 11 on the west face of the specimen, six inside the constant moment region. The first crack for both the east and west face occurred during the 0.1 inch deflection step, (L/840). At the 0.35 inch deflection step, (L/240), the majority of the formed cracks had extended to the mid-depth of the specimen. Cracks outside of the constant moment region had little to no vertical extensions beyond the 0.35 inch deflection step. Cracks inside the constant moment region continued to extend vertically until the 0.7 inch deflection step, (L/120). At this deflection, further deflecting the specimen resulted in minor vertical extensions and significant widening of the critical cracks. The critical cracks approached reference elevation E while non-critical cracks extended slightly beyond reference elevation D. Figure 23 through Figure 26 demonstrate the progression of each crack throughout the test.

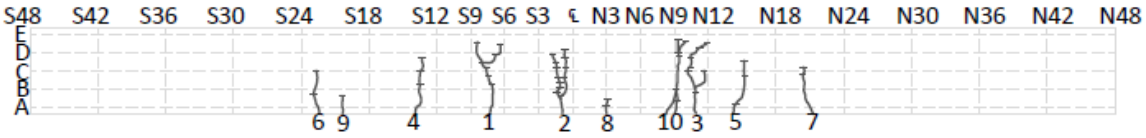

Figure 23. Crack Profile of the East Face (LVDT)

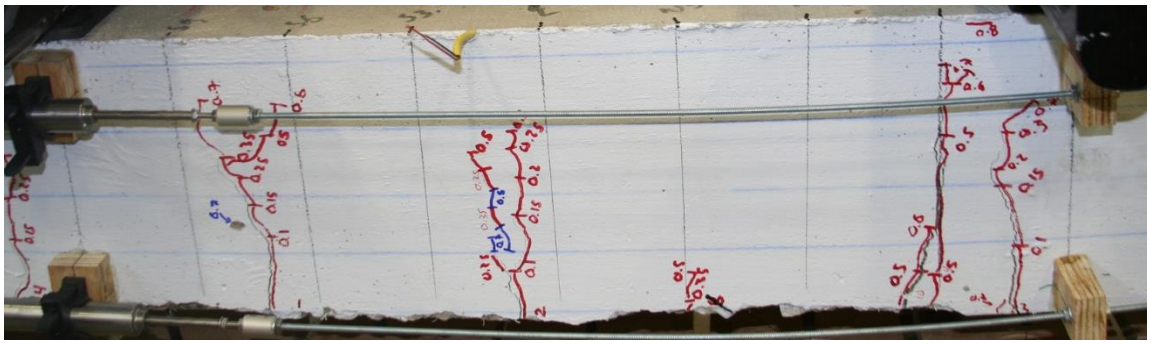

Figure 24. Crack Profile of East Face in Constant Moment Region

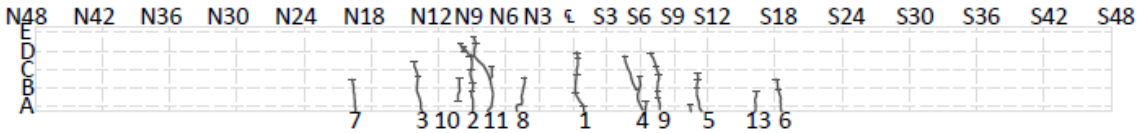

Figure 25. Crack Profile of the West Face (Optotrak)

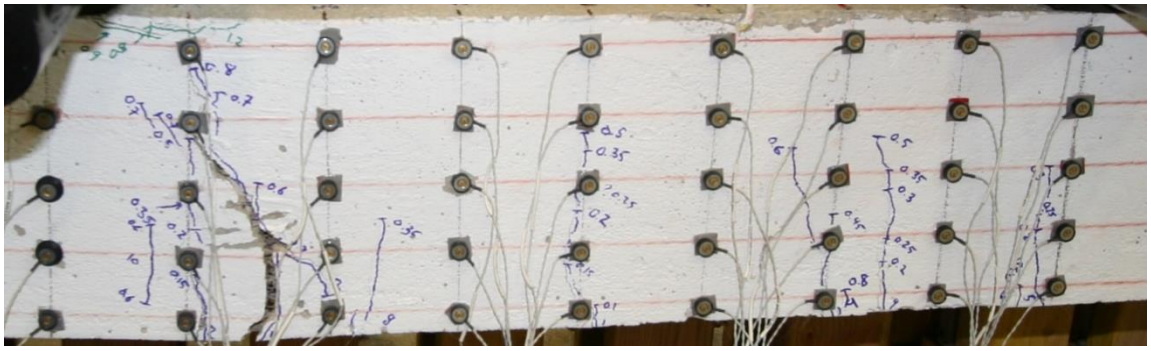

Figure 26. Crack Profile of West Face in Constant Moment Region

The average non-critical crack width on the east and west face was 0.4 mm 0.36 mm respectively. Ultimately, cracks E10 and W11 created the critical failure plane of the specimen. From deflection step 0.7 inches to 0.8 inches (L/150), the crack width of E10 doubled to 2.54. In comparison, all other cracks on the east face did not change in width except the second largest crack, E3 with a width of 1.27mm. The same behavior was observed on the west face; W11 doubled in width to 3.05. Figure 29 displays the critical crack on each side of the specimen. Both E10 and W11 surpassed the maximum allowed crack width at the 0.8 inch deflection step,

capacity of 9.82 kips. (RILEM 2002, fib 2010) Figure 27 and Figure 28 demonstrate the relationship between the crack opening and strip deflection for each face.

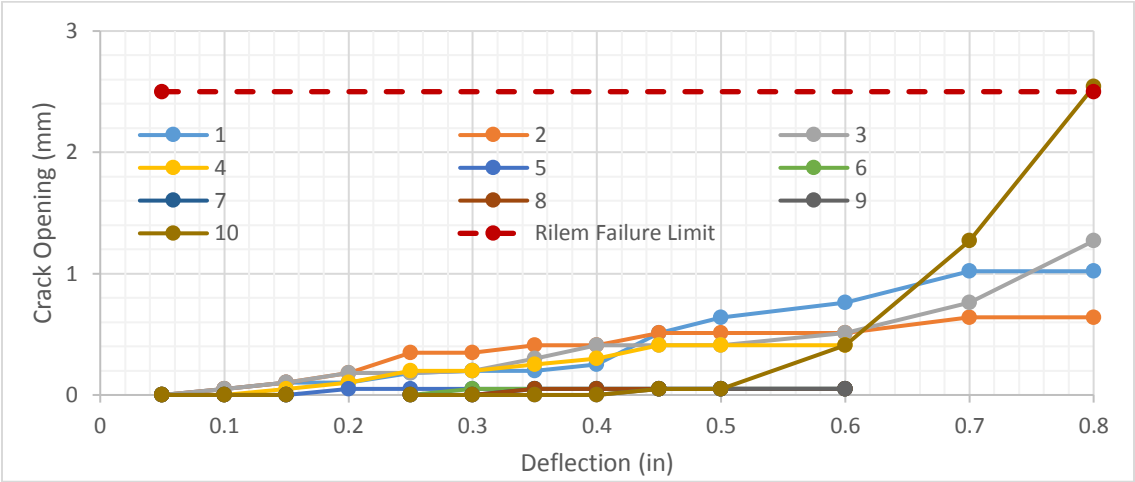

(a)

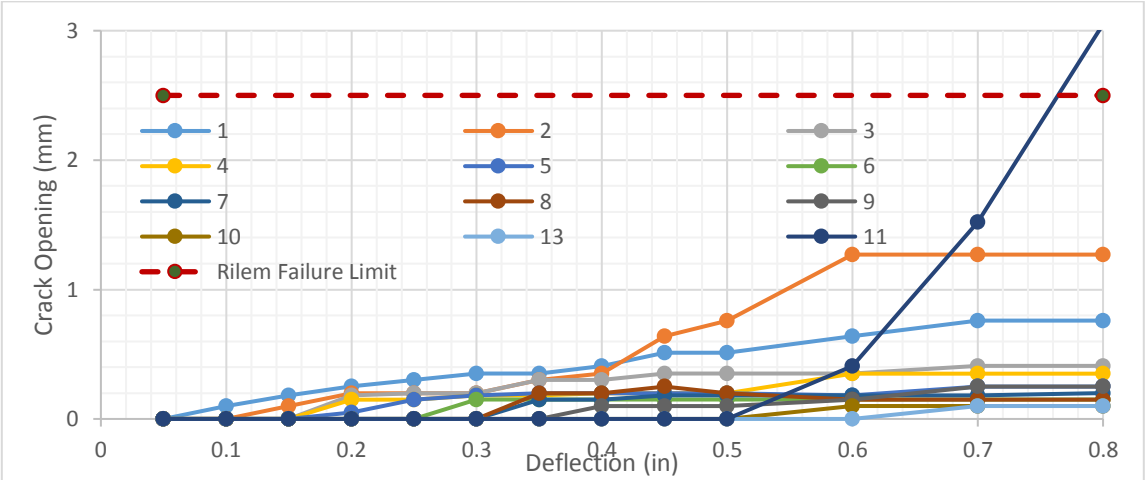

(b)

Figure 27. Crack Opening vs Strip Deflection for (a) East Face and (b) West Face

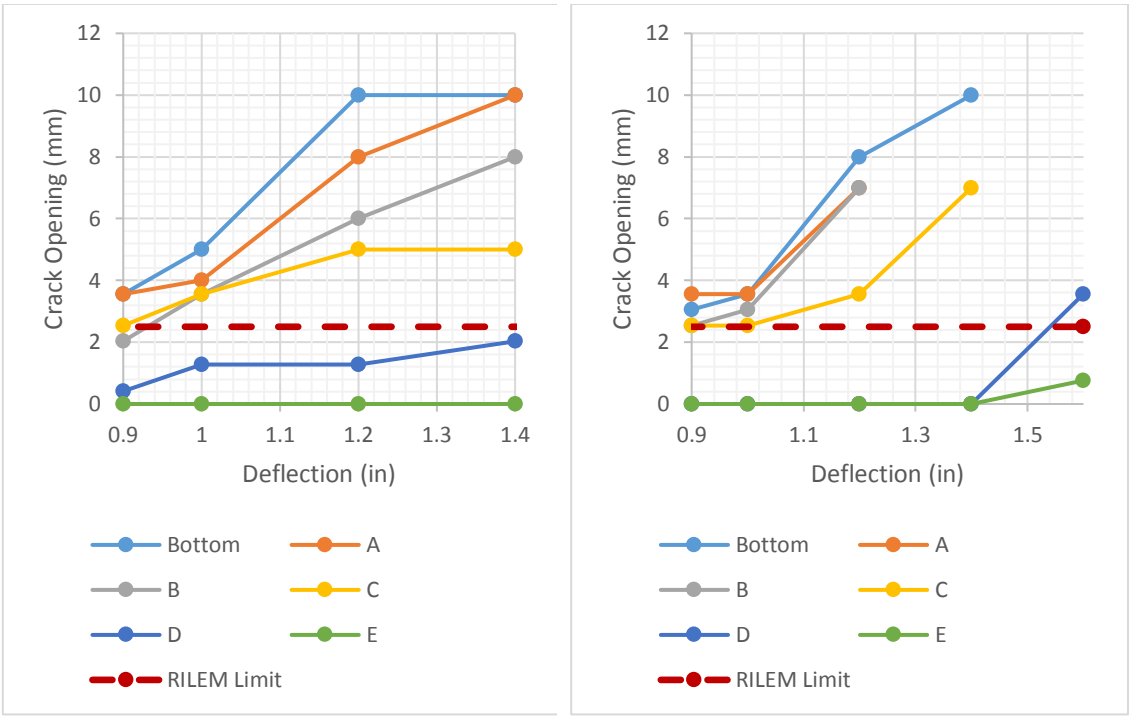

Figure 28. Crack Opening vs Strip Deflection for Primary Crack at Each Reference Elevation (a) E10 and (b) W11

Figure 29 and Figure 30 demonstrate the progression of critical cracks on the east and west faces. The crack on the west face, W11, first formed at deflection step 0.6 inches. In comparison, the critical crack, E10, on the east face formed at deflection step 0.45 inches. Each critical crack became the widest crack on their respective face by deflection step 0.7 inches. Critical crack W11 extended vertically for the final time at the next deflection step, 0.8 inches. Significant spalling at reference elevation B and C was observed where the hooked end of several fibers were near the surface of the concrete. However; steel fibers were clearly seen bridging W11 until the anchorage of the hooked ends failed.

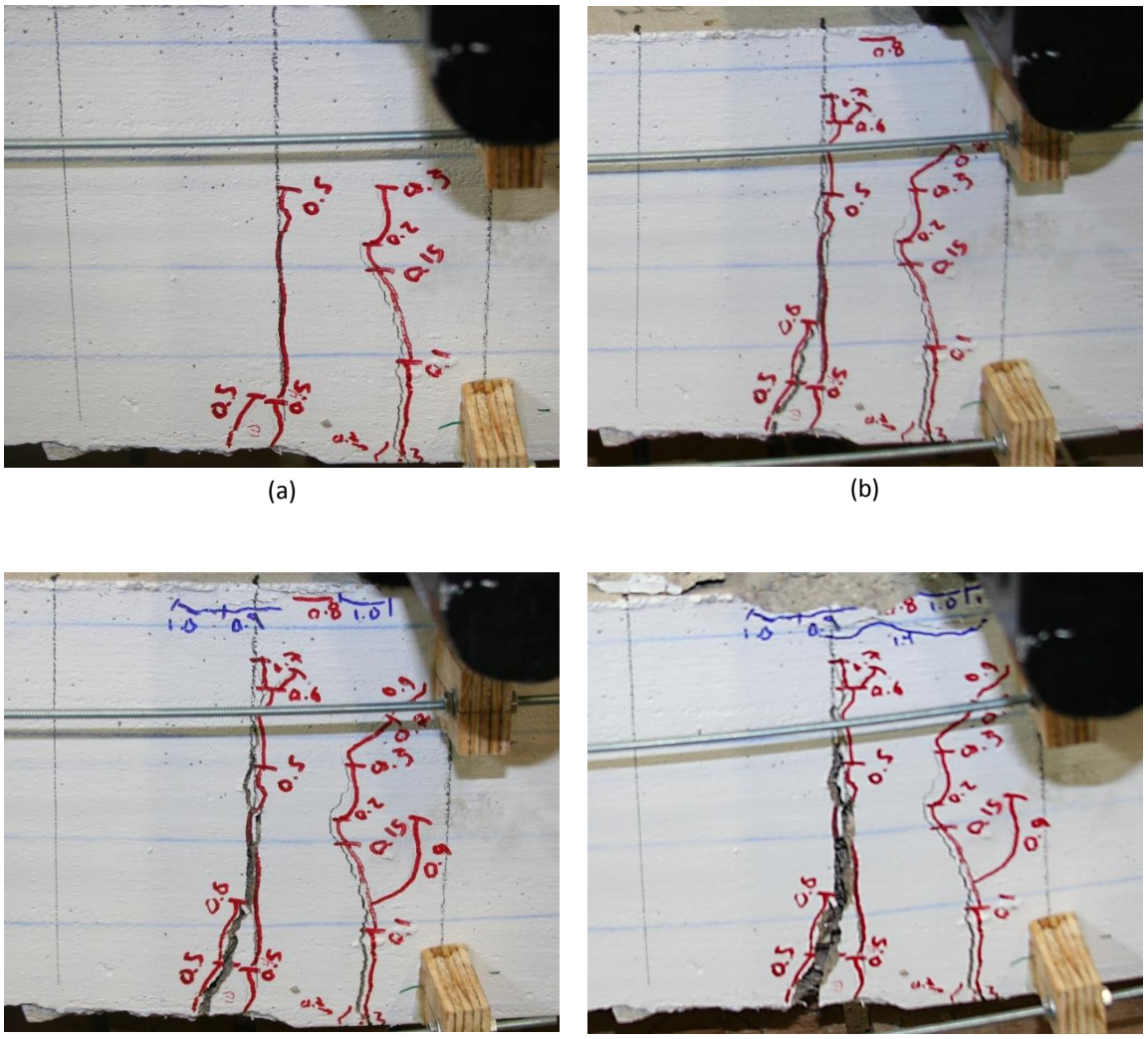

(a) (b)

(c) (d)

Figure 29. Crack Progression of E10 at deflection step:
(a) 0.5 inches, (b) 0.8 inches, (c) 1.0 inches, and 1.6 inches.

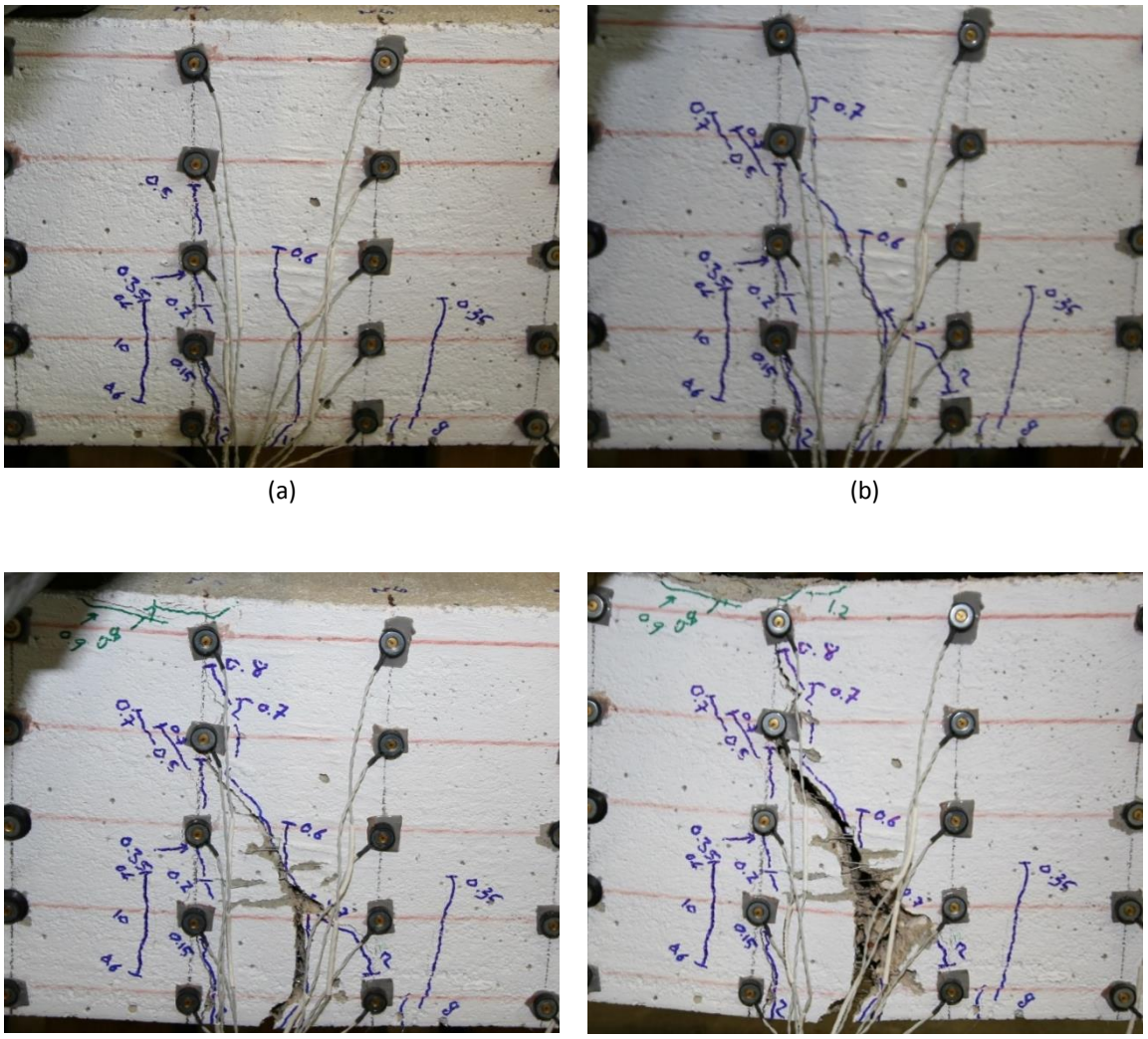

(a) (b)

(c) (d)

Figure 30. Crack Progression of W11 at deflection step:
(a) 0.6 inches, (b) 0.7 inches, (c) 1.0 inches, and 1.4 inches.

Crushing was first observed on both sides at the deflection step 0.8 inches (L/105) or a capacity of 9.82 kips. The crushing occurred between references N9 and N12. The crushed region of concrete did not extend significantly north or south. At the conclusion of the test, the steel reinforcement fractured preventing an extended crushing region. The progression of the crushed region is exhibited by Figure 31.

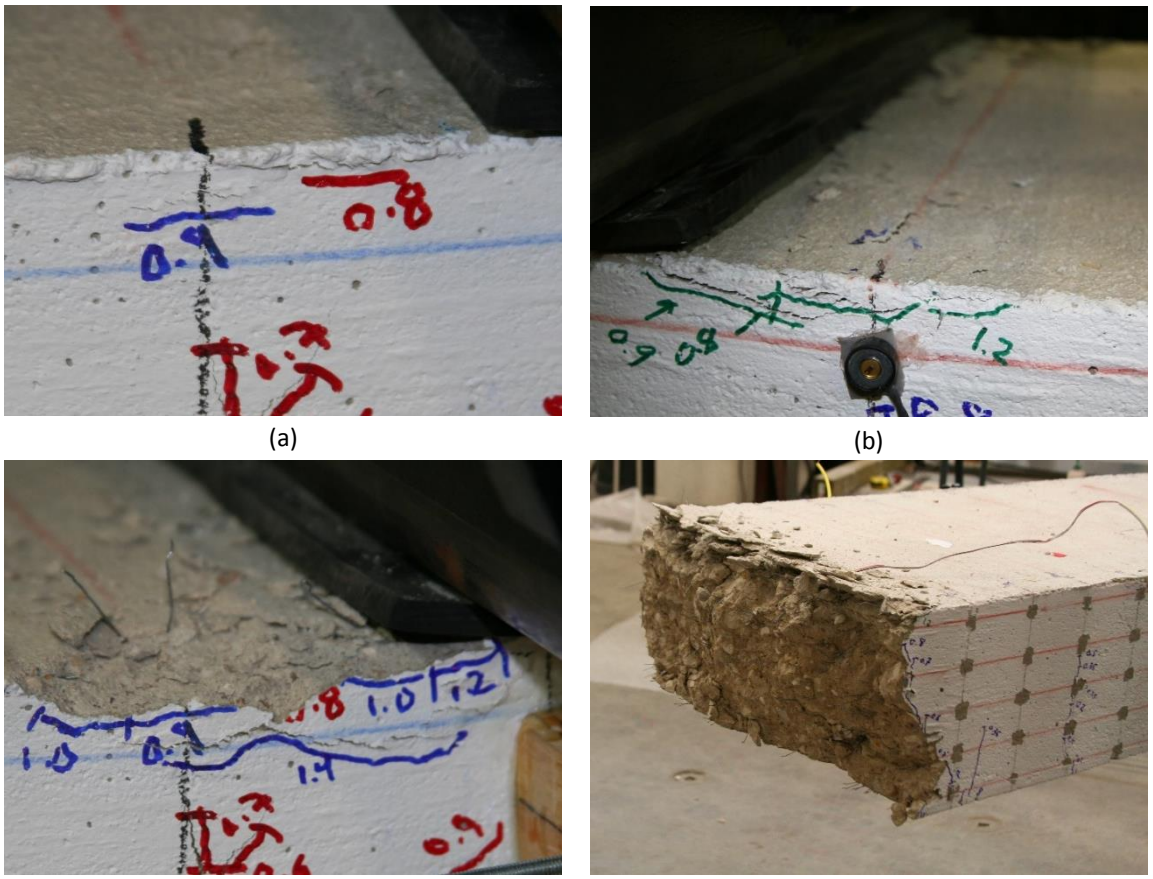

(a) (b)

(c) (d)

Figure 31. Crushing Progression of S7505BTM23 deflection of (a) 1.0 inch and (b) 1.2 inch, (c) 1.6 inches, and (d) Conclusion of Test

A.5 S7505CTR35

Slab strip specimen S7505CTR35 has 3-#5 steel bars located at the mid-depth of the specimen. The specimen has an overall depth of 7.5 inches and a fiber volume of 0.5%. The specimen achieved a maximum capacity of 16.52 kips at a deflection of 0.8 inches (L/105). At that time, all observed cracks had already formed.

The bottom edge on the west face was damaged in the demolding of the specimen between the centerline and N3. Cracks W2 and W12 formed at the base of this damaged region as shown in Figure 32.

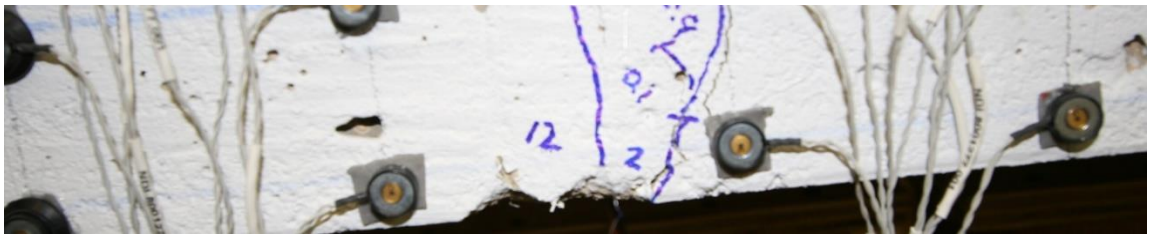

Figure 32. Damaged Corner of S7505CTR35 Where W2 and W2 Have Formed

A total of 10 cracks formed on the east face of the specimen, five inside the constant moment region, and 12 cracks on the west face of the specimen, 6 inside the constant moment region. The first crack for both the east and west face occurred during the 0.1 inch deflection step, (L/840). At the 0.30 inch deflection step, (L/280), the majority of the formed cracks had extended to the mid-depth of the specimen. Cracks outside of the constant moment region had little to no vertical extensions beyond the 0.40 inch deflection step. However, new cracks continued to form outside of the constant moment region up to the deflection step 0.7 inches (L/120). Cracks inside the constant moment region continued to extend vertically until the deflection step 0.9 inches, (L/93). At this deflection, further deflecting the specimen resulted in minor vertical extensions and significant widening of the critical cracks. The critical cracks exceeded reference elevation D by approximately one inch while non-critical cracks extended slightly below reference elevation D. Figure 33 through Figure 36 demonstrate the progression of each crack throughout the test.

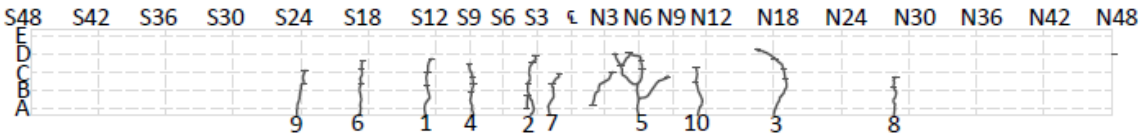

Figure 33. Crack Profile of the East Face (LVDT)

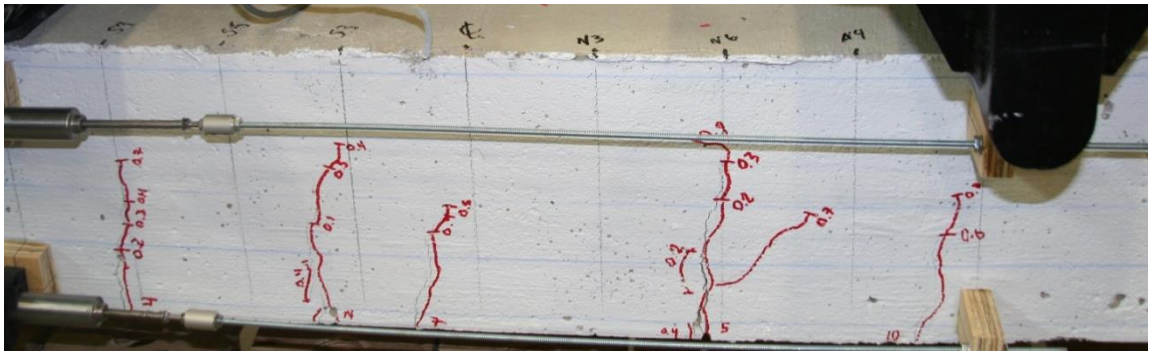

Figure 34. Crack Profile of East Face in Constant Moment Region

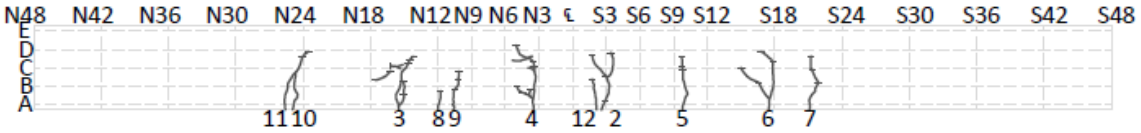

Figure 35. Crack Profile of the West Face (Optotrak)

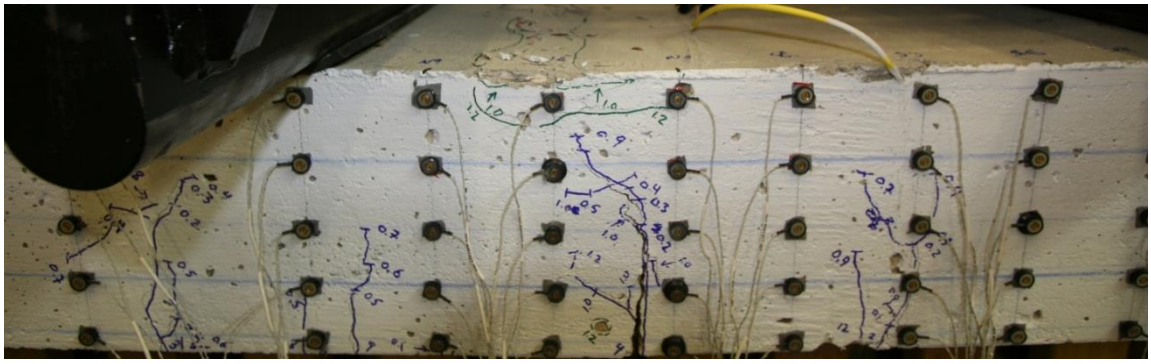

Figure 36. Crack Profile of West Face in Constant Moment Region

The average non-critical crack width on the east and west face was 0.43 mm 0.66 mm respectively. Ultimately, cracks E3 and W4 created the critical failure plane of the specimen. From deflection step 0.9 inches to 1.0 inches (L/84), the crack width of E3 doubled to 2.54. In comparison, all other cracks on the east face did not change in width. The second largest crack, E3 with a width of 1.27mm. The same behavior was observed on the west face; W4 width increased by 150% to 3.05. Figure 38 displays the critical crack on each side of the specimen. Both E5 and W4 surpassed the maximum allowed crack width at the 1.0 inch deflection step, capacity of 15.51 kips. (RILEM 2002, fib 2010) The crack width at the location of the steel, mid-

depth, did not exceed the allowable limit on the east face; however, by deflection step 1.2 inches, W4 had the maximum allowed crack width at reference elevation C. Figure 37 and Figure 38 demonstrate the relationship between the crack opening and strip deflection for each face.

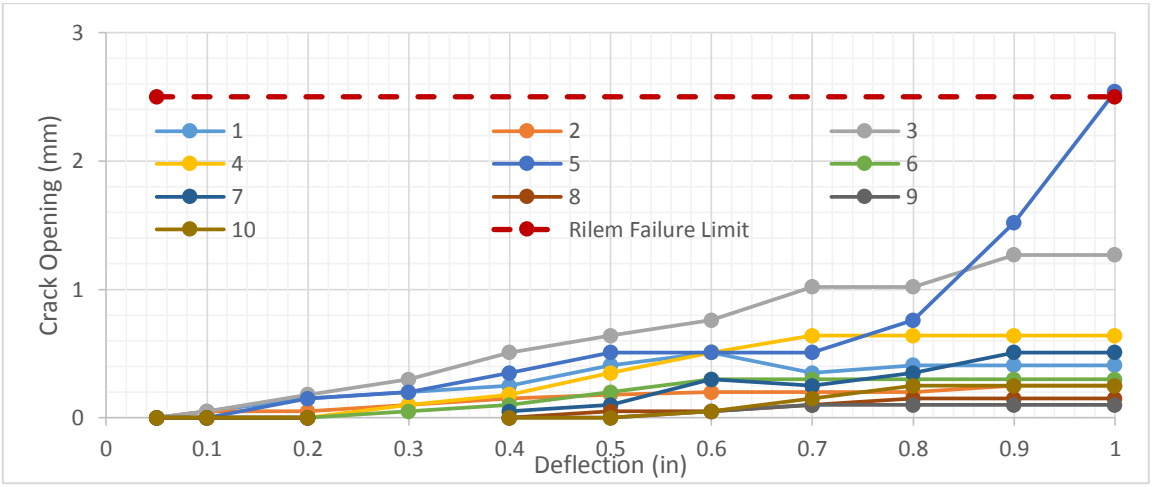

(a)

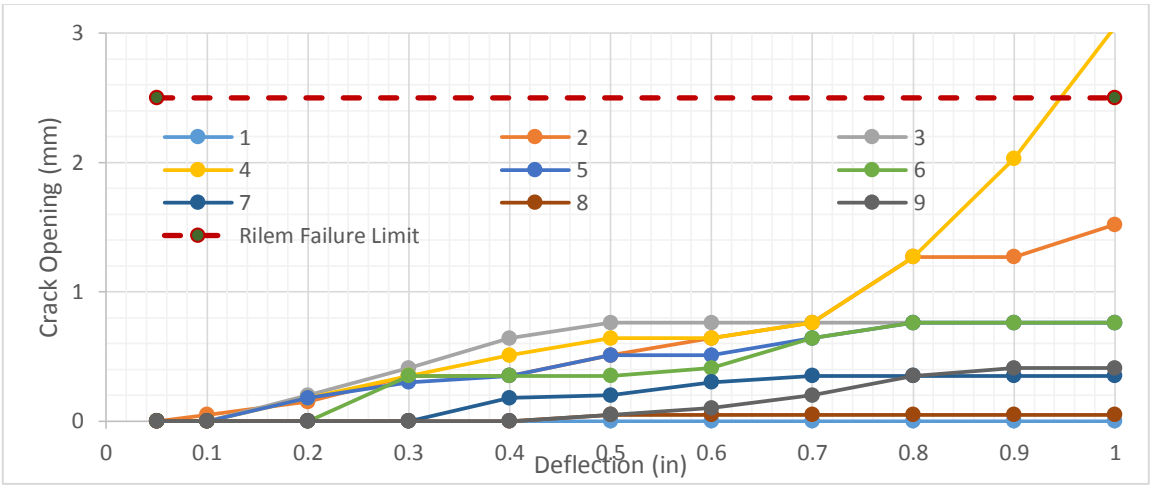

(b)

Figure 37. Crack Opening vs Strip Deflection for (a) East Face and (b) West Face

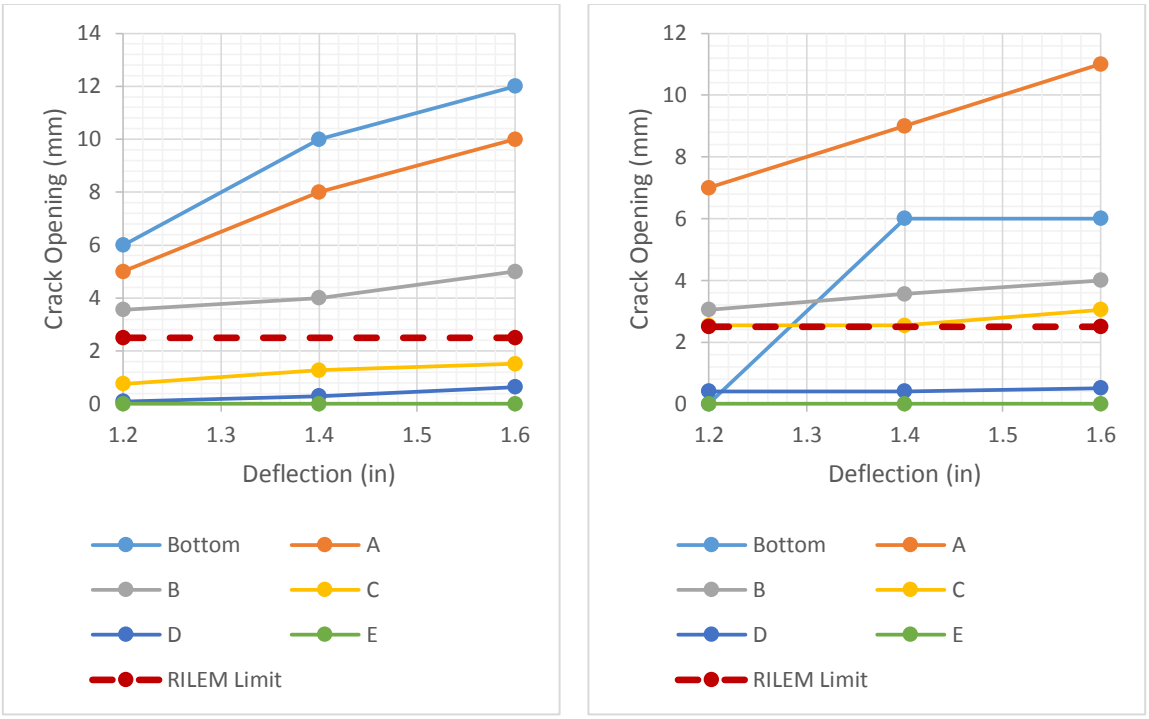

Figure 38. Crack Opening vs Strip Deflection for Primary Crack at Each Reference Elevation (a) E5 and (b) W4

Figure 38 and Figure 39 demonstrates the progression of cracks E5 and W4. Both critical cracks formed at deflection step 0.2 inches. Each critical crack became the widest crack on their respective face by deflection step 0.8 inches. With the exception of associated crack branching, each critical crack extended vertically for the final time at the next deflection step, 0.9 inches. Both E5 and W4 resulted in multiple “branch” cracks and steel fiber anchorage failure.

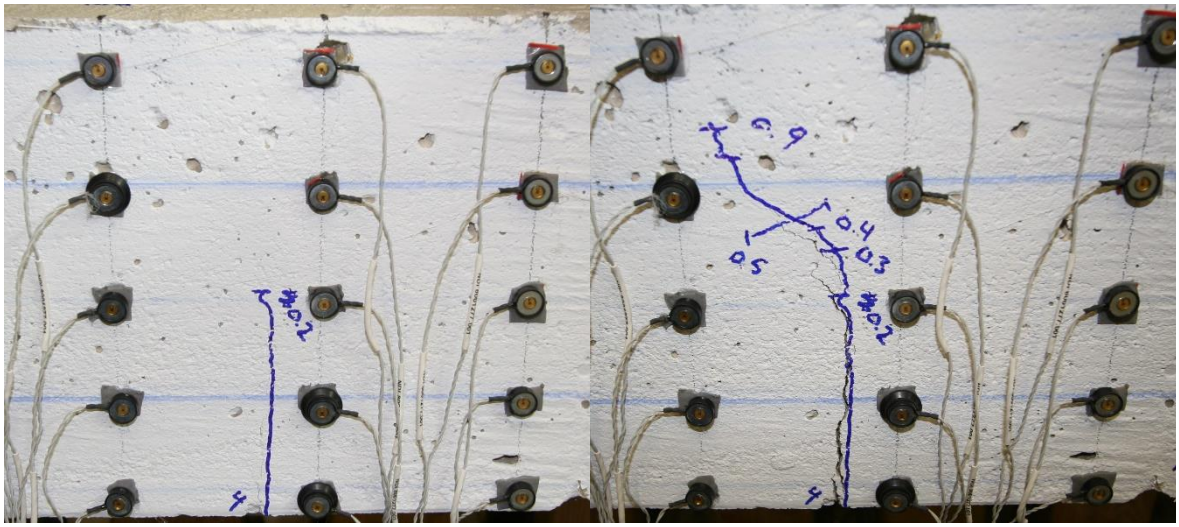

(a) (b)

(c) (d)

Figure 39. Crack Progression of W4 at deflection step:
(a) 0.2 inches, (b) 0.9 inches, (c) 1.2 inches, and 1.6 inches.

Crushing was first observed on both sides at the deflection step 1.0 inches (L/84) or a capacity of 15.51 kips. The crushing occurred between references N3 and N9. During the next deflection step, the crushing region expanded north 3 inches to include N3 through N12. As the test continued, the crushing region continue to descend vertically until diagonal cracks began to form originating at the crushed region orientated downward away from the critical cracks. The progression of the crushed region is exhibited by Figure 40.

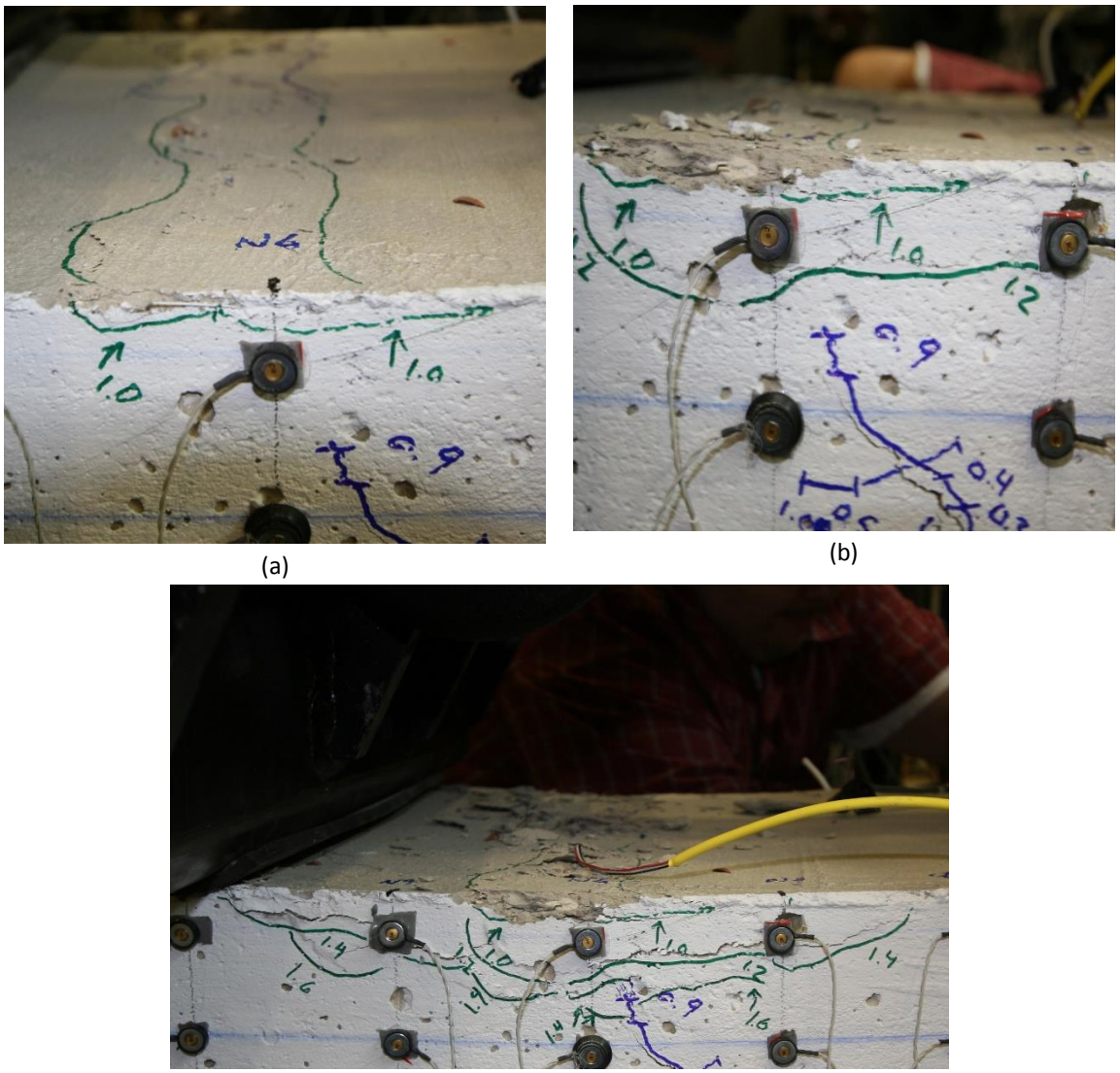

(a) (b)

(c)

Figure 40. Crushing Progression of S7505CTR35 deflection of

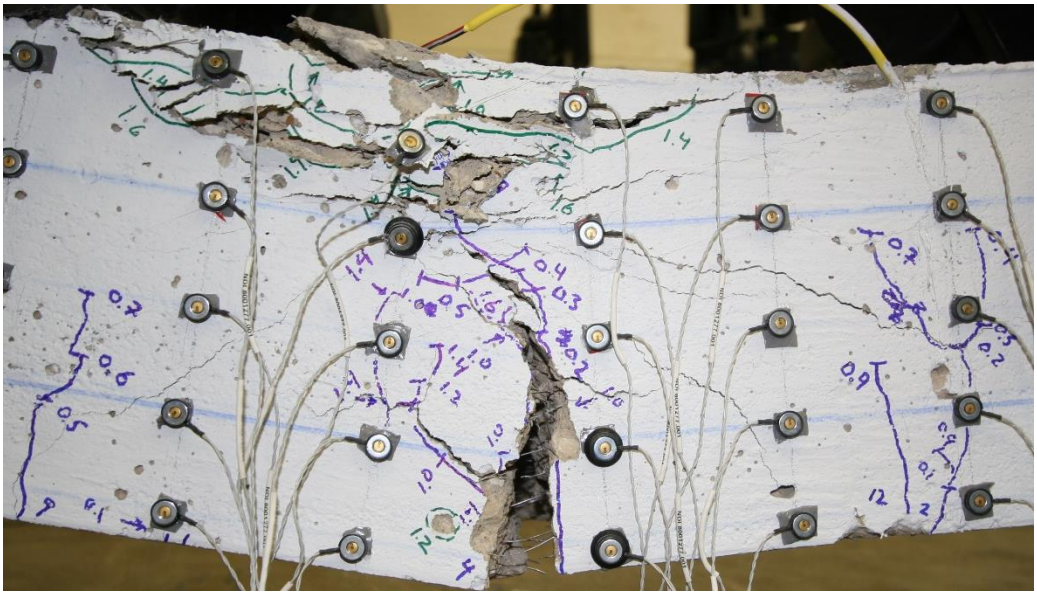

Figure 41. W4 and Crushed Region at Conclusion of Test.
Diagonal Cracking Emanating for Crushed Region

A.6 S7505CTR25

Slab strip specimen S7505CTR25 has 2-#5 steel bars located at mid-depth of the cross section. The specimen has an overall depth of 7.5 inches and a fiber volume of 0.5%. The specimen achieved a maximum capacity of 11.46 kips at a deflection of 0.7 inches (L/120). At that time, all observed cracks had already formed.

The bottom edge of the west face had imperfections near the center line of the beam. The damaged edge extended for approximately 6 inches between N3 and S3, Figure 42. One crack, E5, formed in this damaged region of the specimen; however, the crack is not the primary failure plane of the test.

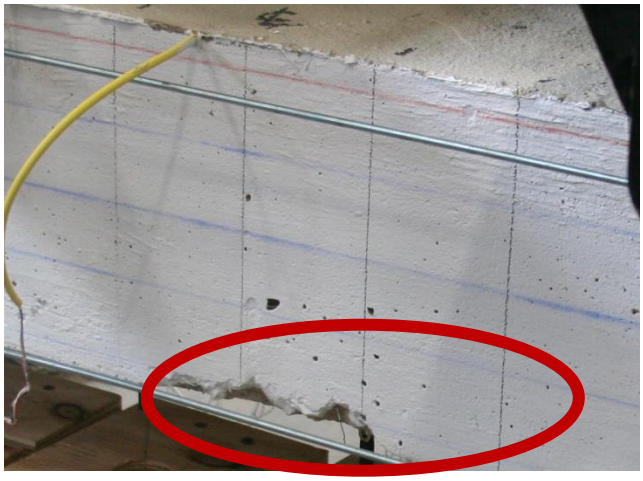

Figure 42. Damaged Corner of S7505CTR25 Where E5 Formed

A total of seven cracks formed on the east face of the specimen, four inside the constant moment region, and seven cracks on the west face of the specimen, four inside the constant moment region. The first crack on the east face formed at deflection step 0.05 inches (L/1680). The first crack on the west face occurred during the next deflection step, 0.1 inches (L/840). At the 0.30 inch deflection step, (L/280), the majority of the formed cracks had extended to the mid-depth of the specimen. Cracks outside of the constant moment region extended vertical to reference by deflection step 0.7 inches. At this point, the extension of all noncritical cracks ceased. Cracks inside the constant moment region continued to extend vertically until the deflection step 1.0 inches, (L/84). Further deflecting the specimen resulted in significant widening of the critical cracks. Figure 43 through Figure 46 demonstrate the progression of each crack throughout the test.

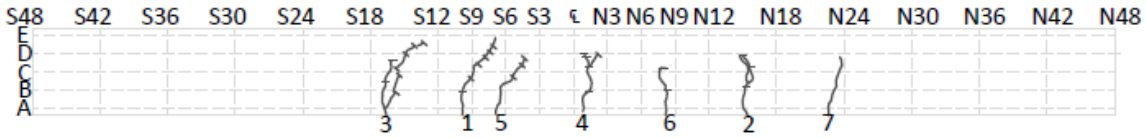

Figure 43. Crack Profile of the East Face (LVDT)

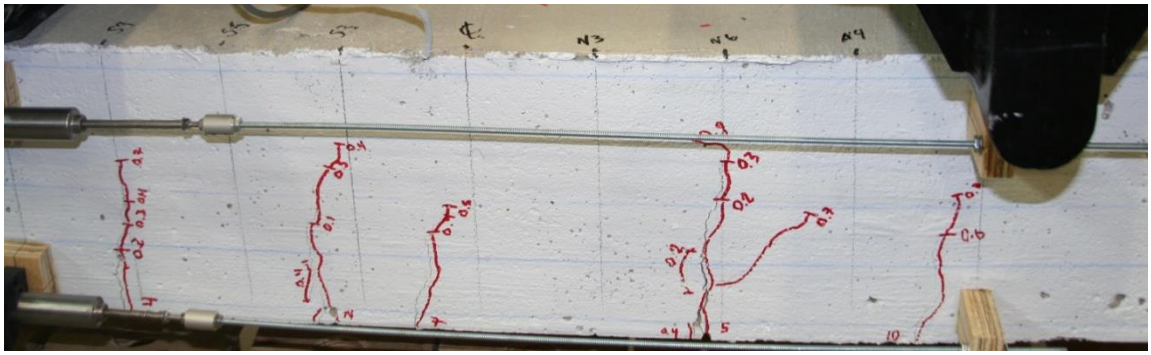

Figure 44. Crack Profile of East Face in Constant Moment Region

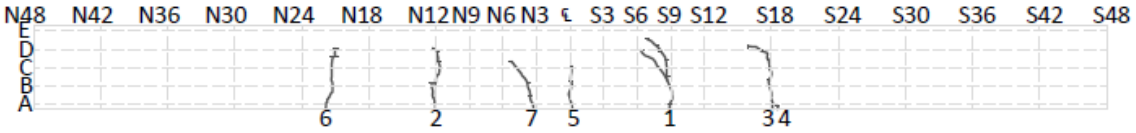

Figure 45. Crack Profile of the West Face (Optotrak)

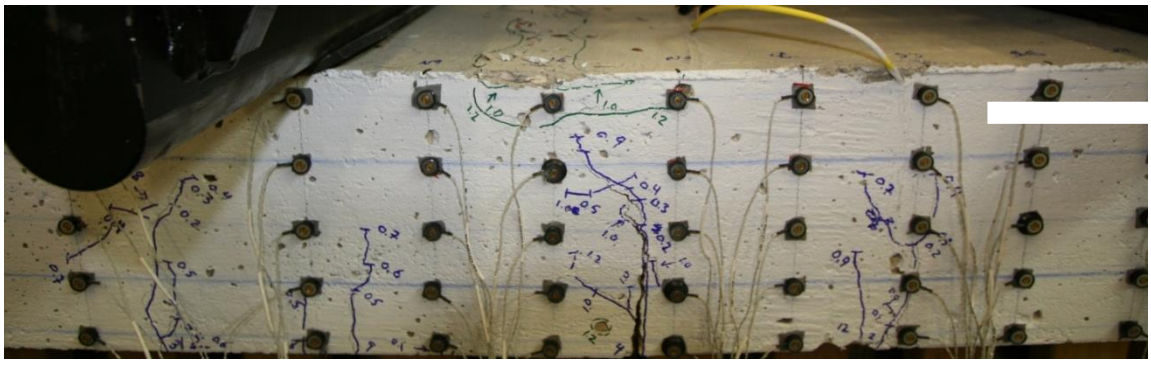

Figure 46. Crack Profile of West Face in Constant Moment Region

The average non-critical crack width on the east and west face was 0.89 mm 0.76 mm respectively. Ultimately, cracks E1 and W1 created the critical failure plane of the specimen. From deflection step 0.4 inches to 0.5 inches, the crack width of E1 doubled to 1.02 mm. The second largest crack at this step was E3 with a width of 0.64 mm. The same behavior was observed on the west face; the width of W1 increased by 300% to 1.02 mm. Critical crack E1 surpassed the maximum allowed crack width at the 0.9 inch deflection step. (RILEM 2002, fib 2010). W1 exceeded the maximum allowed width during the next deflection step of 1.0 inches. Figure 47 demonstrates the relationship between the crack opening and strip deflection for each face. Figure 48 and Figure 49 displays the critical crack progression on each side of the specimen.

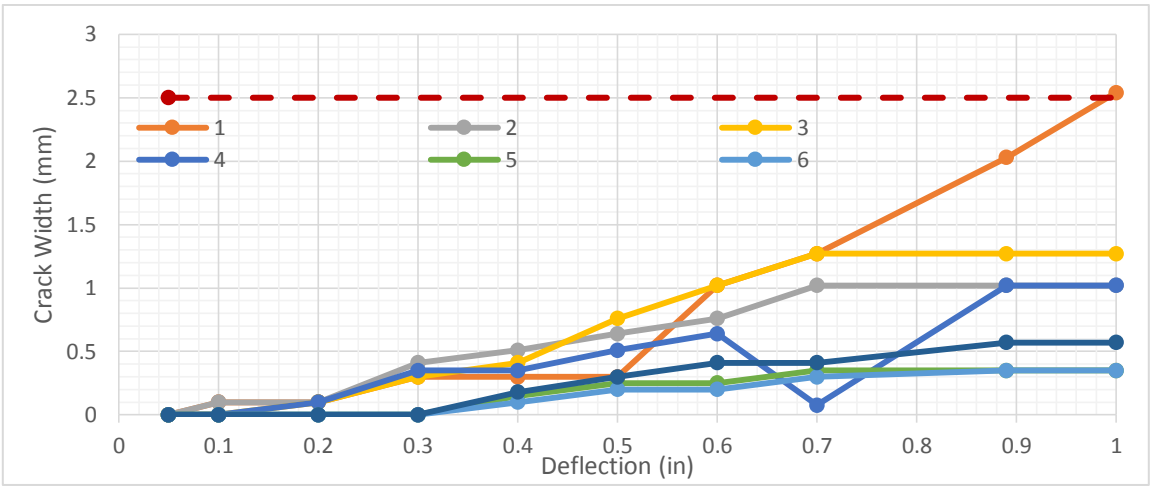

(a)

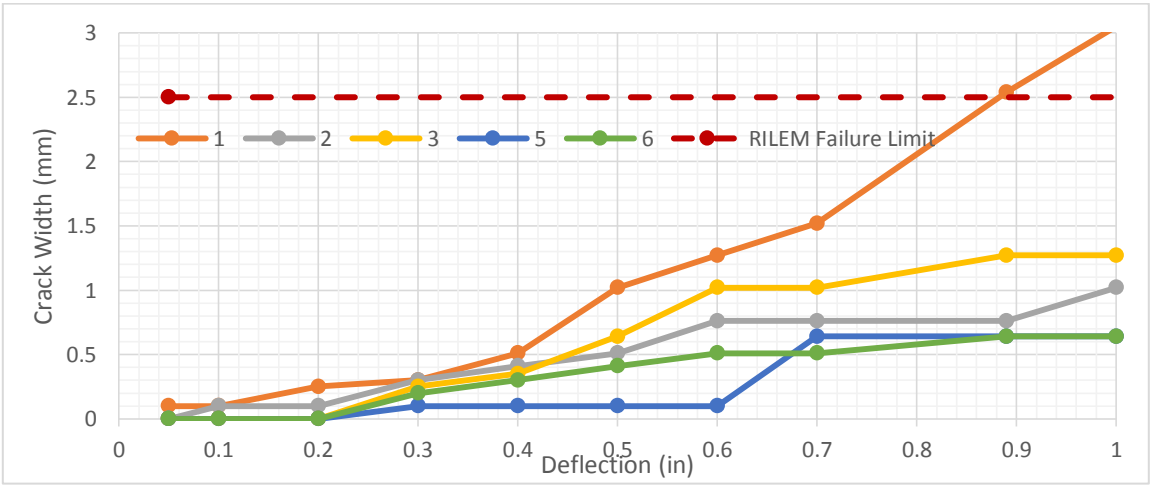

(b)

Figure 47. Crack Width vs Deflection for (a) East Face and (b) West Face

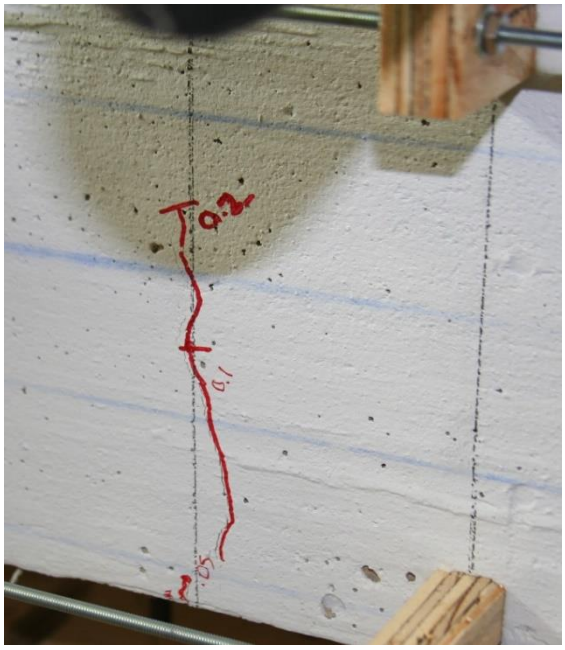

(a)

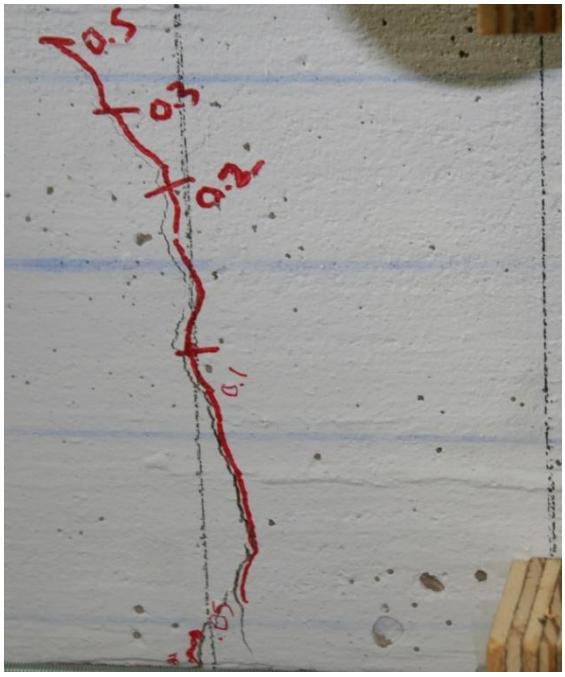

(b)

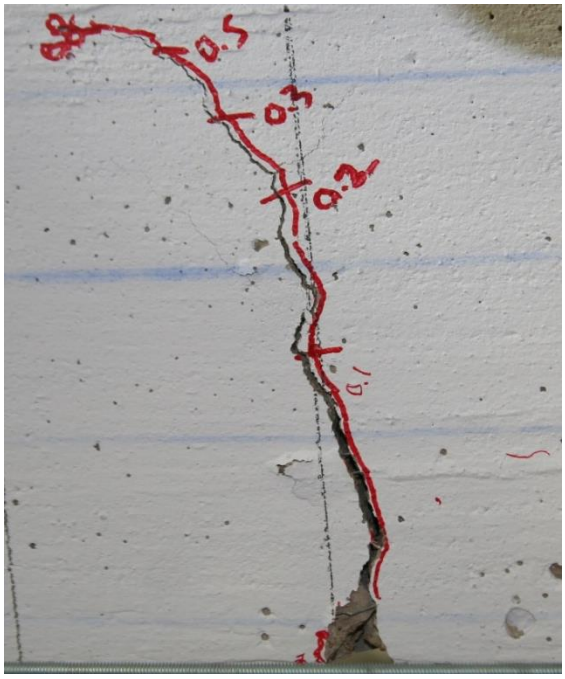

(c) (d)

Figure 48. Crack Progression of E1 at Deflection Step:
(a) 0.2 in deflection, (b) 0.5 in deflection, (c) 0.8 in deflection, and (d) 1.2 in deflection

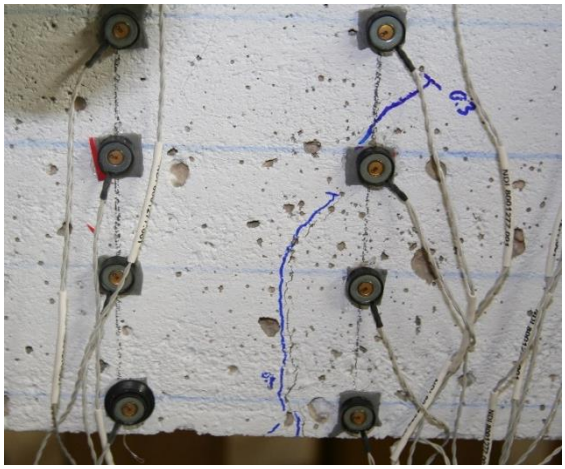

(a)

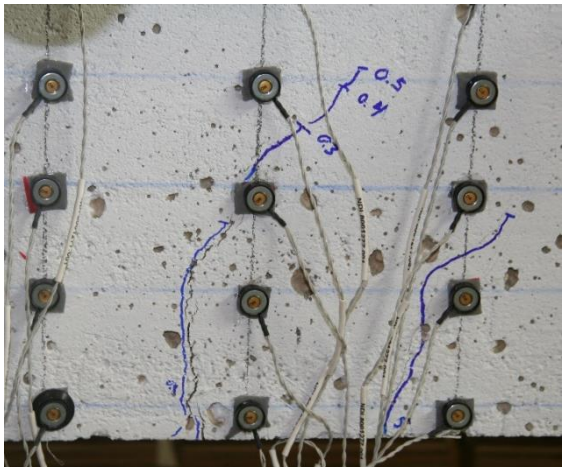

(b)

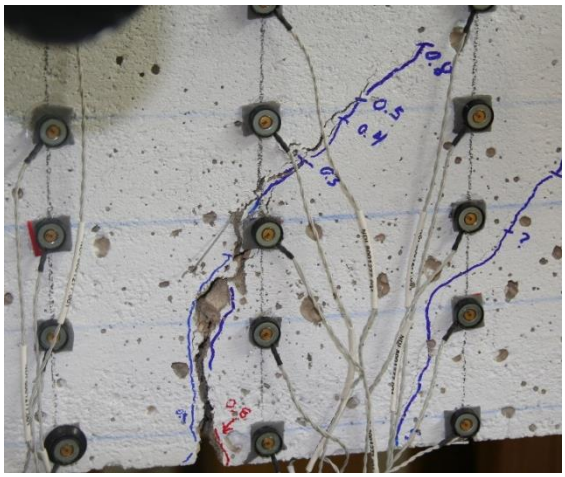

(c)

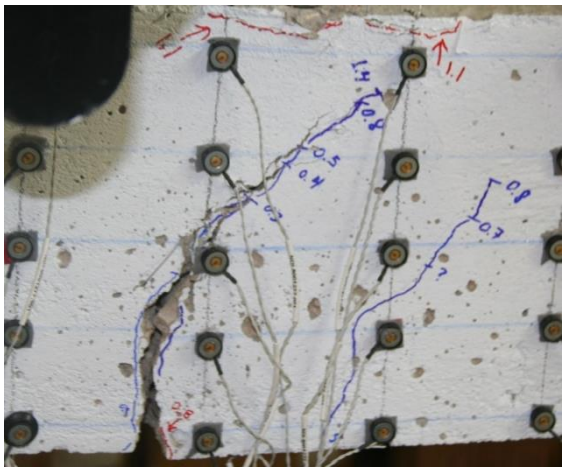

(d)

Figure 49. Crack Progression of W1 at Deflection Step:
(a) 0.3 in deflection, (b) 0.6 in deflection, (c) 1.0 in deflection, and (d) 1.4 in deflection

Crushing failure began to occur at a deflection of 0.7 inches. The crushing occurred adjacent to the north loading point and directly above the critical crack on both faces of the specimen. At the onset of crushing failure, the maximum crack width had grown to 1.52 mm. A continuous

crushing failure plane along the top face of the beam formed by a deflection of 1.2 inches. At the conclusion of the test, significant spalling and damage was noted on the top surface. At this time, the beam maintained a capacity of 76% of the peak load. Figure 50 demonstrates the progression of the crushing failure of the specimen.

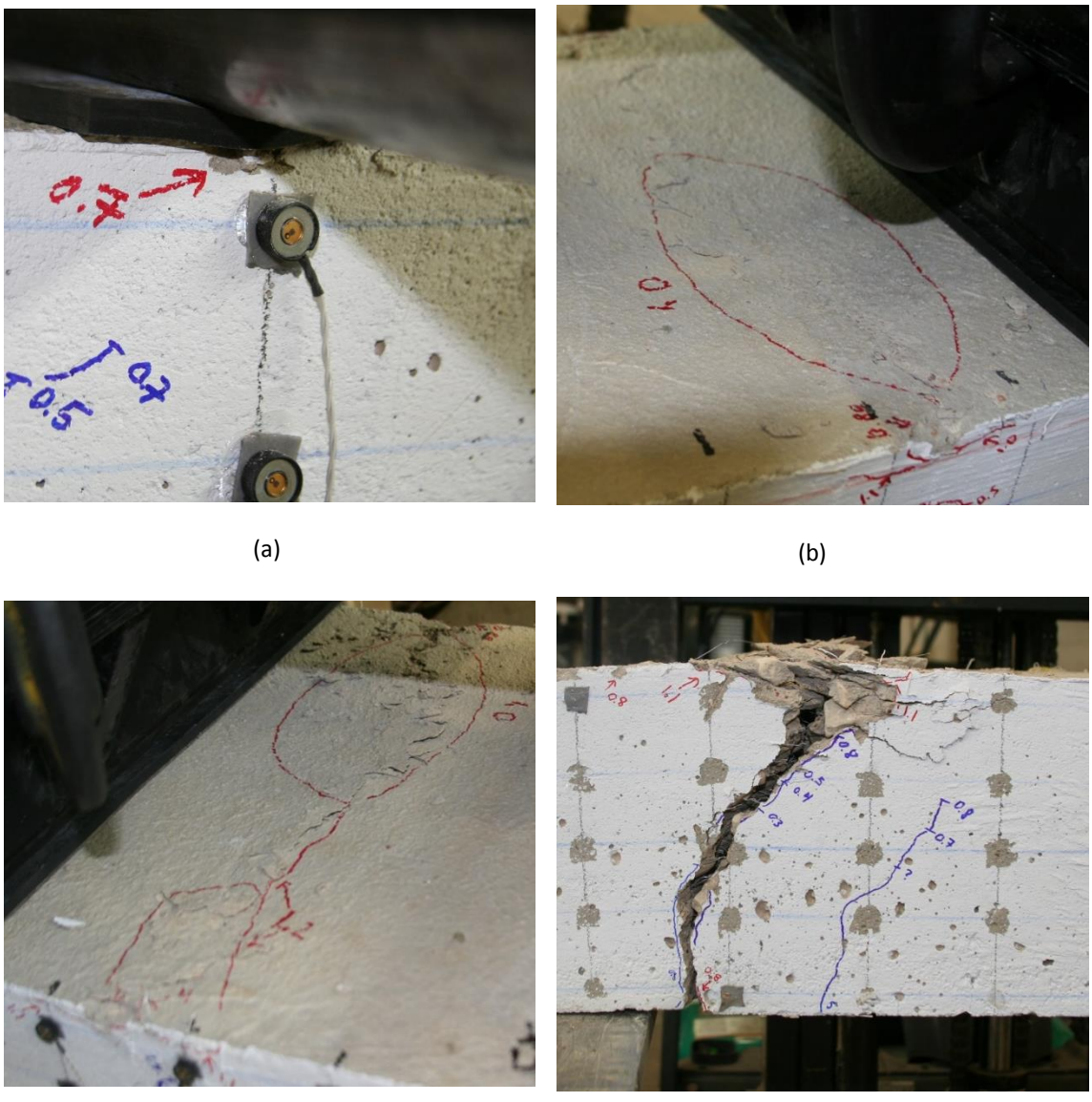

(a) (b)

(c) (d)

Figure 50. Crushing Progression of S7505CTR25 at Deflection Steps:
(a) 0.7 in Deflection, (b), 1.1 in Deflection, (c) 1.2 in Deflection, (d) Conclusion of Test

A.7 S7505NOS00

Slab strip specimen S7505NOS00 is a plain SFRC strip and does not have any steel reinforcing bars. The specimen has an overall depth of 7.5 inches and a fiber volume of 0.5%. The specimen achieved a maximum capacity of 2.54 kips at a deflection of 0.05 inches (L/1680). Without steel reinforcement, the specimen's peak capacity corresponded to its cracking strength.

A single crack developed on both the east and west face during the first deflection step, 0.05 inches. As the deflection of the specimen increased, accessory cracks formed on either side of the main cracks. The accessory cracks often formed within a steel fiber's length of the main crack. As the test continued and spalling began to occur, fibers were observed connecting the accessory cracks to the primary crack.

The critical crack on the east face, E1, extended to vertical reference E by the third deflection step, 0.15 inches. In contrast, W1 did not extend to reference E until the ninth deflection step, 0.70 inches. During the fourth deflection step, 0.20 inches, W1 developed a branching crack that ultimately formed a large wedge at the top of the specimen. Figure 51 and Figure 52 demonstrate the vertical progression of the cracks on the east and west faces respectively.

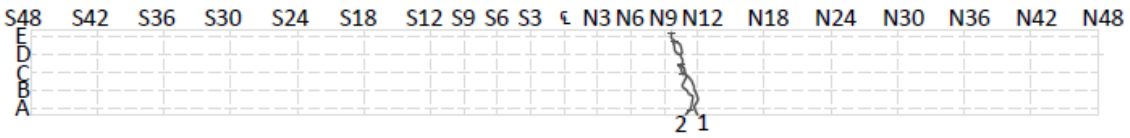

Figure 51. Crack Profile of the East Face (LVDT)

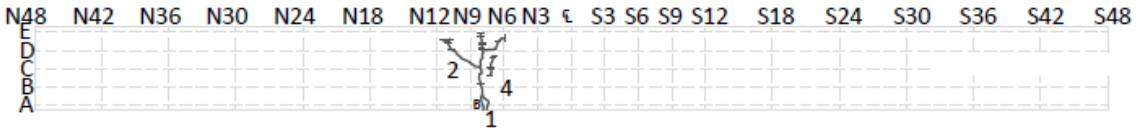

Figure 52. Crack Profile of the West Face (Optotrak)

The crack width was measured at each reference elevation throughout the entirety of the test except where excessive spalling prohibited it. The critical crack on each side achieved the maximum allowable crack width at the bottom of the specimen by the sixth deflection step. 0.3 inches. The maximum allowable crack width was achieved at a new reference elevation with each successive deflection step for E1. The width of the critical crack on the west face, W1, did not progress upwards as quickly as E1. This is consistent with the behavior of the vertical

progression of the two critical cracks. The maximum allowable crack width was not observed at mid-depth, reference elevation C, for W1 until the eighth load step, 0.5 inches. Fibers were visibly bridging the widening cracks at later deflection steps. Figure 53 through Figure 55. demonstrate the crack width progression of both critical cracks.

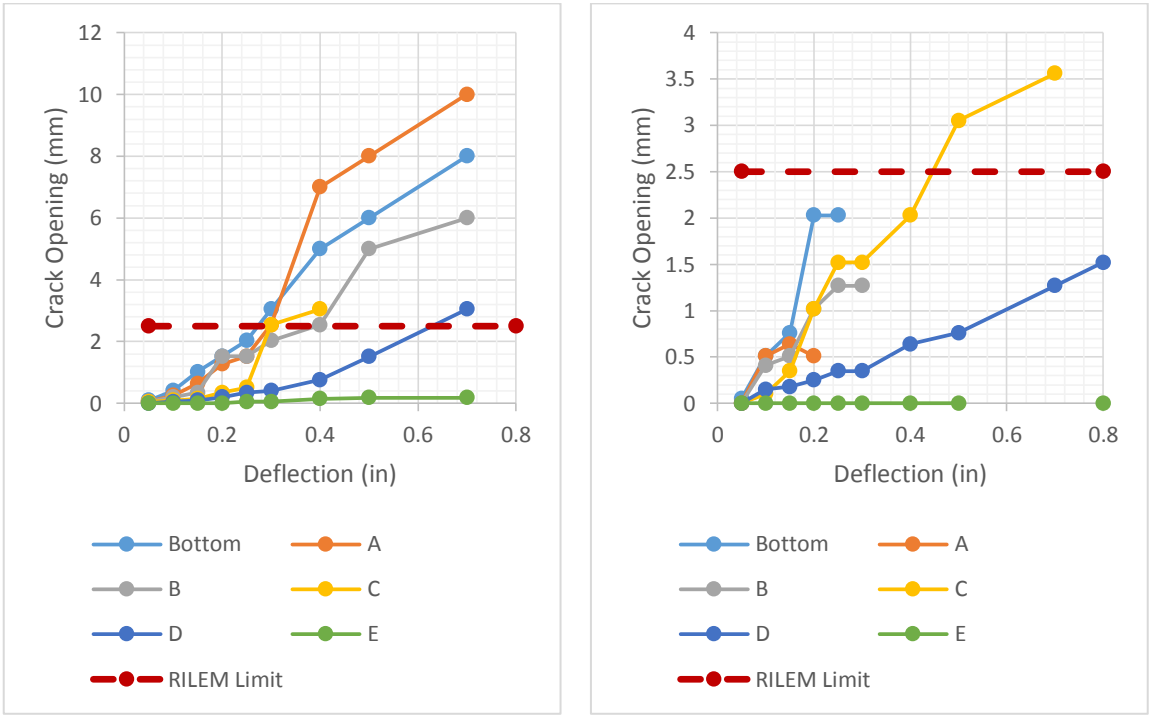

(a) (b)

Figure 53. Crack Width Progression of Critical Cracks (a) E1 and (b) W1

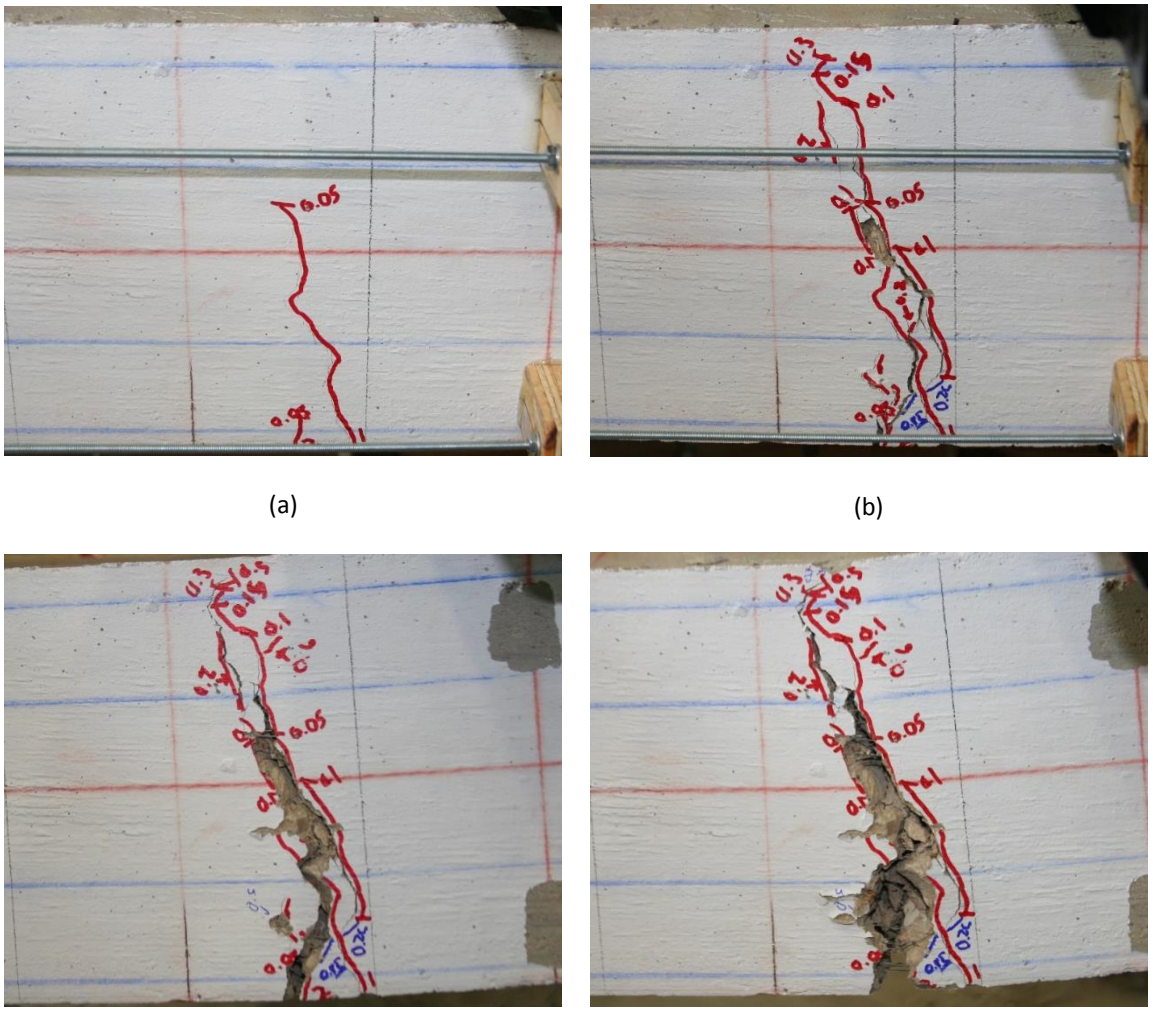

(a) (b)

(c) (d)

Figure 54. Damage Progression of the Critical Crack on the East Face, E1, at Deflection Step: (a) 0.05 inches, (b) 0.30 inches, (c) 0.80 inches, and (d) Conclusion of Test

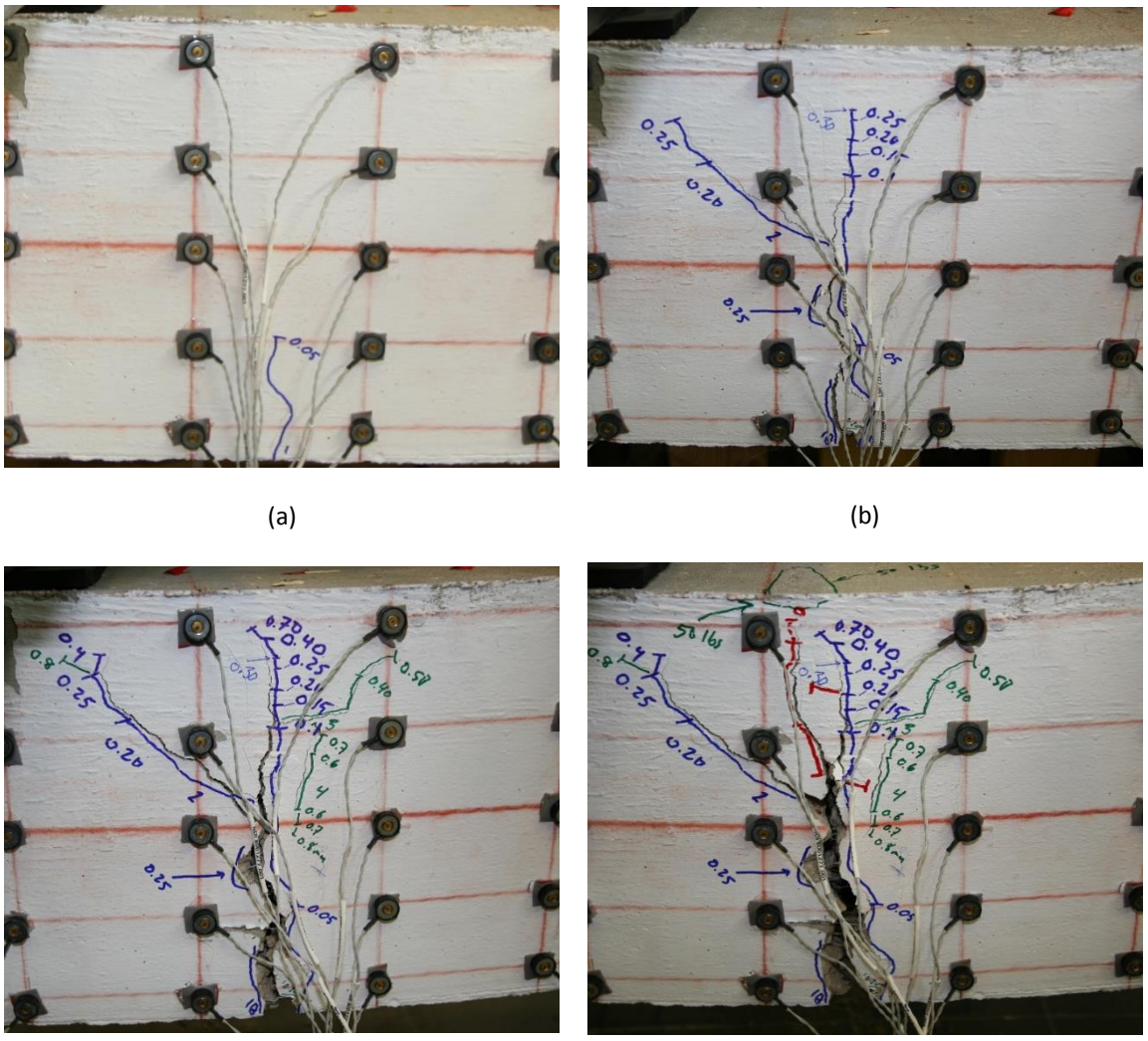

(a) (b)

(c) (d)

Figure 55. Damage Progression of the Critical Crack on the West Face, W1, at Deflection Step: (a) 0.05 inches, (b) 0.30 inches, (c) 0.80 inches, and (d) Conclusion of Test

All instrumentation was removed from the specimen at deflection step 0.70 inches to prevent damage to the equipment. Concrete crushing was observed at this deflection step on the east face. Concrete crushing was not observed on the top or west face at that time. Prior to the collapse of the specimen at a remaining capacity of 0.050 kips, crushing damage was observed on the west face. Extension of the crushed region of concrete was not observed on either face before collapse of the specimen. Figure 56 shows the first observance of crushing on each face. Figure 57 displays the failure of the specimen.

(a) (b)

Figure 56. Observation of Concrete Crushing on (a) East Face at 0.70 inches and (b) West Face at Remaining Capacity of 0.050 kips

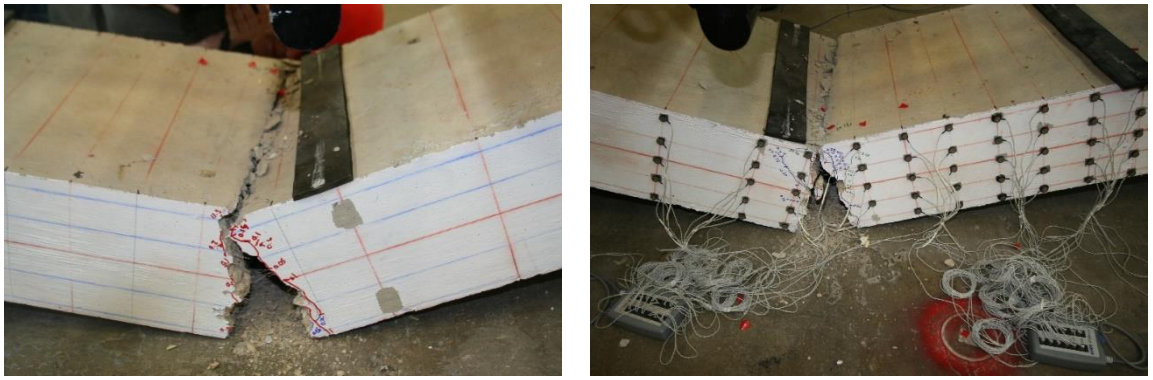

(a) (b)

Figure 57. Collapse of the Specimen Viewed from (a) East Face and (b) West Face

A.8 S7520NOS00

Slab strip specimen S7520NOS00 is a plain SFRC strip and does not have any steel reinforcing bars. The specimen has an overall depth of 7.5 inches and a fiber volume of 2.0%. The specimen achieved a maximum capacity of 7.3 kips at a deflection of 0.1 inches (L/840). At that time, all the cracks on the east face had already formed, but none of the cracks on the west face had formed.

The bottom edge on the east face was damaged in the demolding of the specimen between S3 and S6. Crack E1 formed at the base of this damaged region as shown in Figure 58.

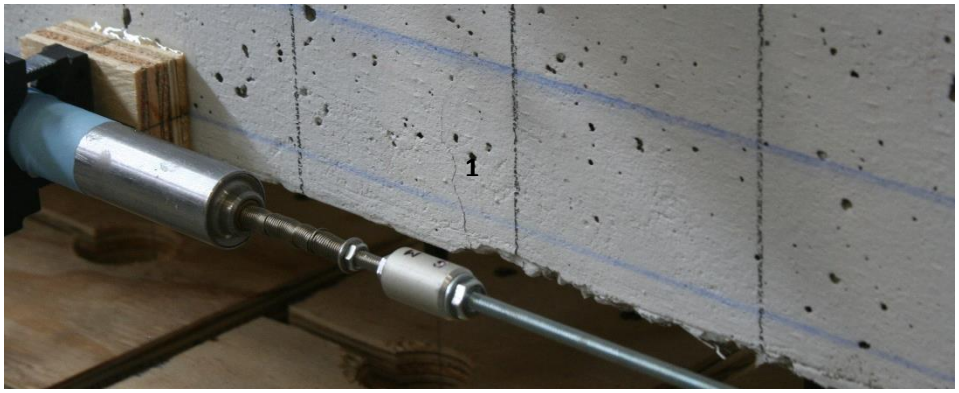

Figure 58. Damaged Corner of S7520NOS00 Where E1 Crack Formed

On the east face of the specimen a total of 2 cracks formed both of which were located in the constant moment region. On the west face a total of 3 cracks formed all of which were located in the constant moment region. The first crack for the east occurred at deflection step 0.1 inches (L/840) while the first crack on the west face did not form until deflection step 0.2 inches (L/24). All cracks formed by the 0.20 inch deflection step (L/240). Cracks inside the constant moment region progressed vertically passed reference elevation E, to approximately 0.25 inches from the top surface. Vertical progression of cracks ceased at deflection step 1.0 inches (L/84). Further increasing the deflection of the specimen resulted in widening of the primary crack and crack branching.

The critical cracks on the east face and west face are E1 and W2. Crack E1 formed during the 0.1 inch deflection step (L/840) while crack W3 formed during the 0.2 inch deflection step (L/420). The critical on the east face formed between horizontal reference S6 and S9 while the critical crack on the west face formed between horizontal references S9 and S12. The maximum allowable crack width, 2.5 mm, for each crack was observed at deflection step 0.4 inches (L/210). Critical crack W2 formed a large wedge with adjacent crack W3. The wedge remained intact and did not fall away. At the bottom of W2 and W3, fibers visibly joined the two cracks.

Crack E1 branched at vertical reference D. Spalling of the concrete occurred at the apex of the branch revealing fibers joining the two branches. Figure 59 and Figure 60 demonstrate the progression of each crack throughout the test.

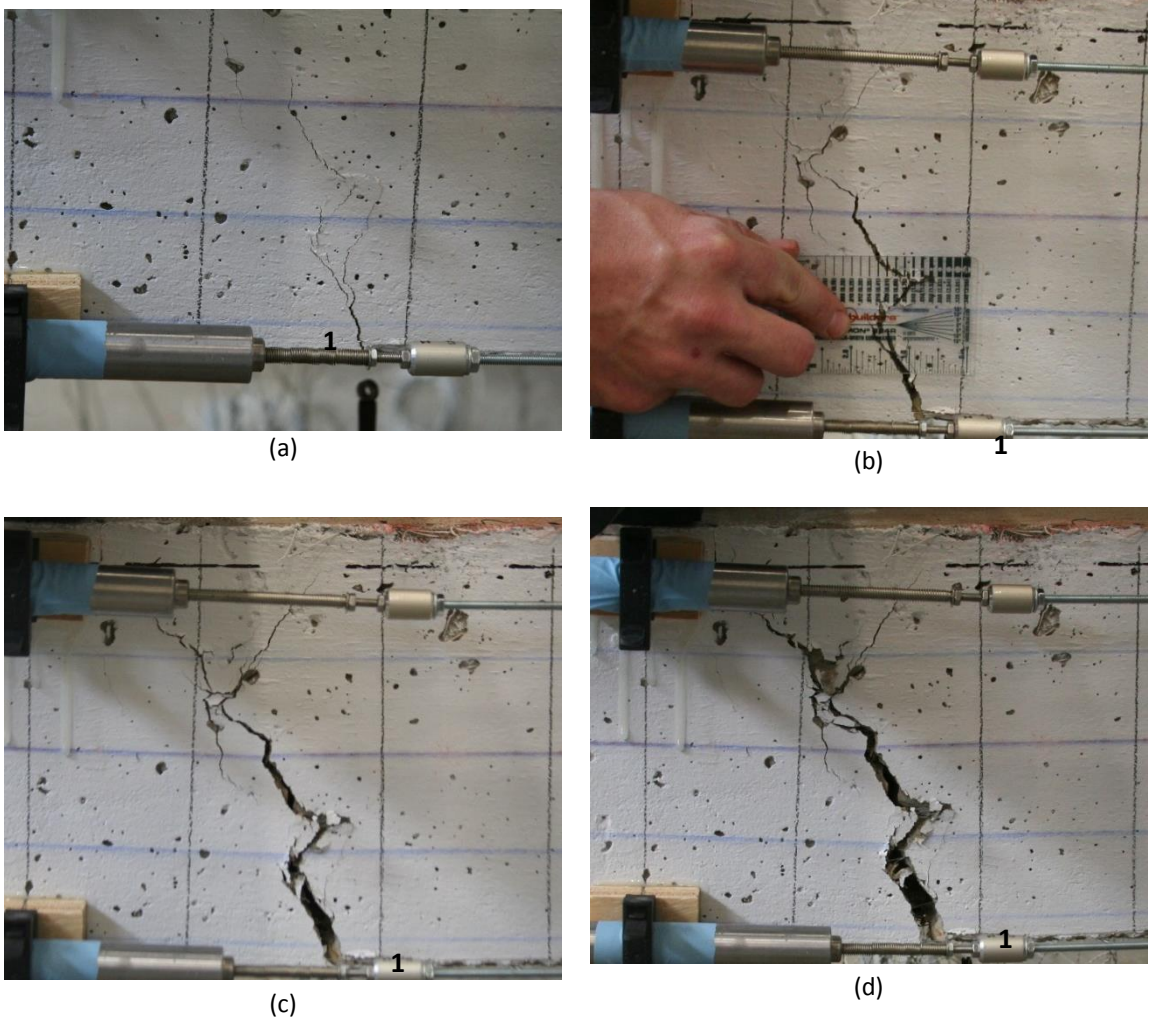

(a) (b) (c) (d)

Figure 59. Crack Progression of E1 and E12 at Deflection Step: (a) 0.1 inches, (b) 0.6 inches, (c) 0.8 inches, and 1.1 inches

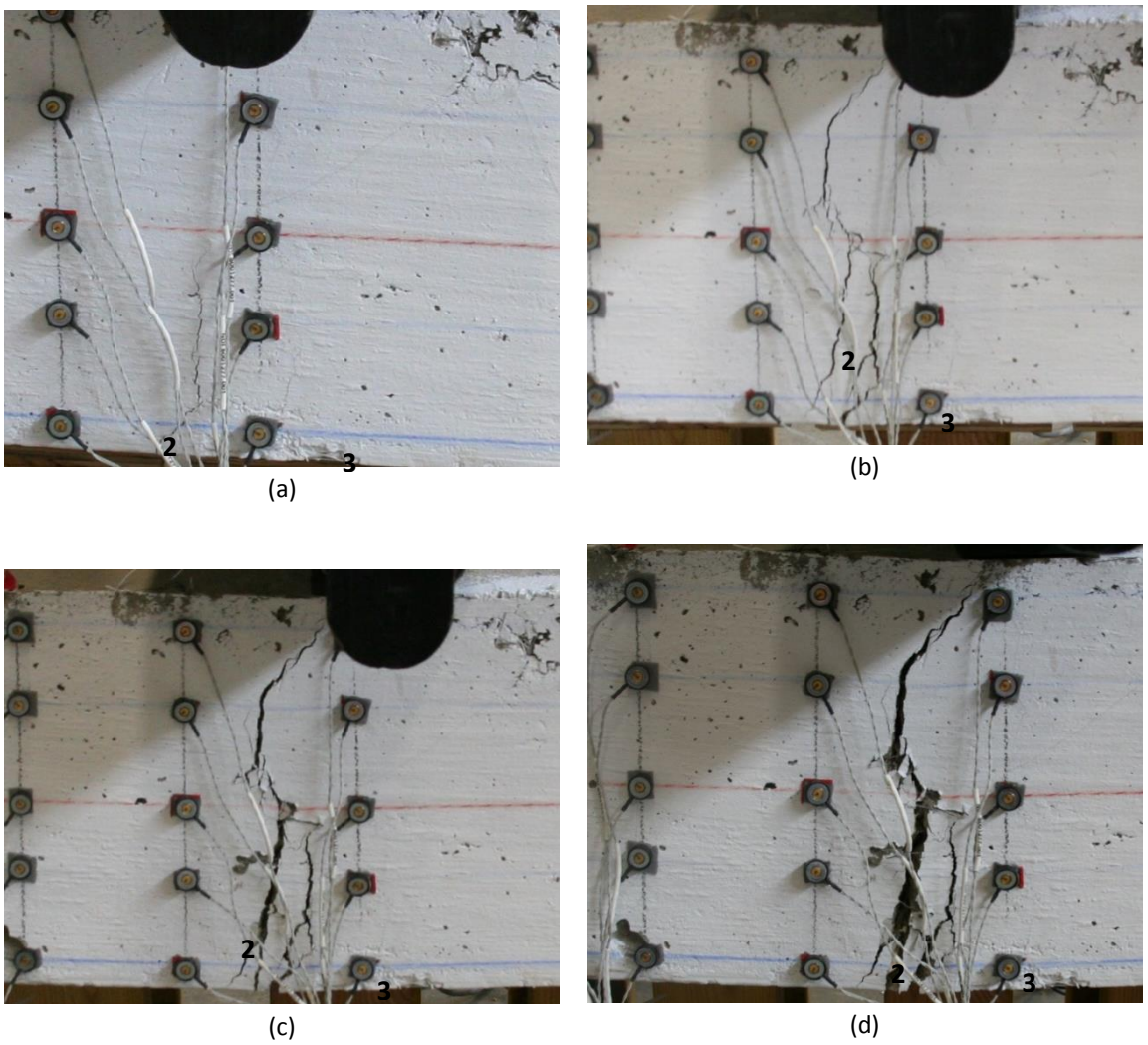

Figure 60. Crack Progression of W2 and W3 at Deflection Step: (a) 0.2 inches, (b) 0.5 inches, (c) 0.8 inches, and 1.1 inches

Crushing was first observed on the west face at deflection step 1.0 inches (L/84). The crushing began directly below the south load point at horizontal reference S12 above each critical crack. Crushing was not observed on the east face or top surface before the completion of the test. Extension of the crushing region was not observed. The test was concluded after the residual strength fell to 20 percent of the maximum applied load. Figure 61 exhibits the progression of concrete crushing and the specimen at the completion of the test.

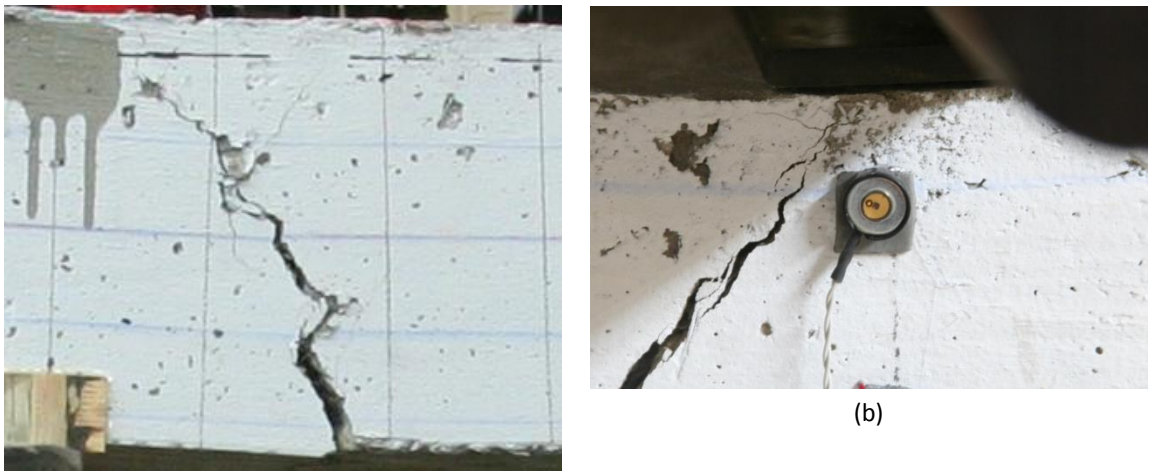

(a) (b)

Figure 61. Crushing Progression of S9005BTM23 deflection of (a) 1.0 and (b) Completion of Test

A.9 S9005BTM35

Slab strip specimen S9005CTR35 has 3-#5 steel bars located with a clear cover of 1 inch from the bottom of the specimen. The specimen has an overall depth of 9.0 inches and a fiber volume of 0.5%. The specimen achieved a maximum capacity of 31.97 kips at a deflection of 0.7 inches (L/120). Additional tension cracks formed beyond this deflection step.

A total of 18 cracks formed on the east face of the specimen, 10 inside the constant moment region, and 12 cracks on the west face of the specimen, 6 inside the constant moment region. The first crack for both the east and west face occurred during the 0.1 inch deflection step, (L/840). At the 0.40 inch deflection step, (L/210), all but three crack on the west face and one on the east face had already formed. The majority of the formed cracks in the constant moment region extended to or beyond the mid-depth of the specimen by deflection step 0.6 inches (L/140). The majority of the cracks outside of the constant moment region did not reach mid-depth. The maximum vertical elevation was achieved by deflection step 0.8 inches (L/105) to approximately 0.5 inches above reference D. Further increasing the deflection of the specimen resulted in widening and formation of "branch" and accessory cracks, such as E8 and W5. Figure 62 through Figure 65 demonstrate the vertical progression of cracks on each face.

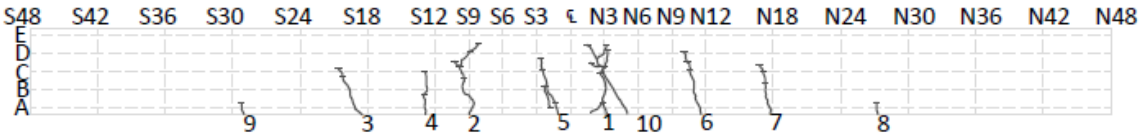

Figure 62. Crack Profile of the East Face (LVDT)

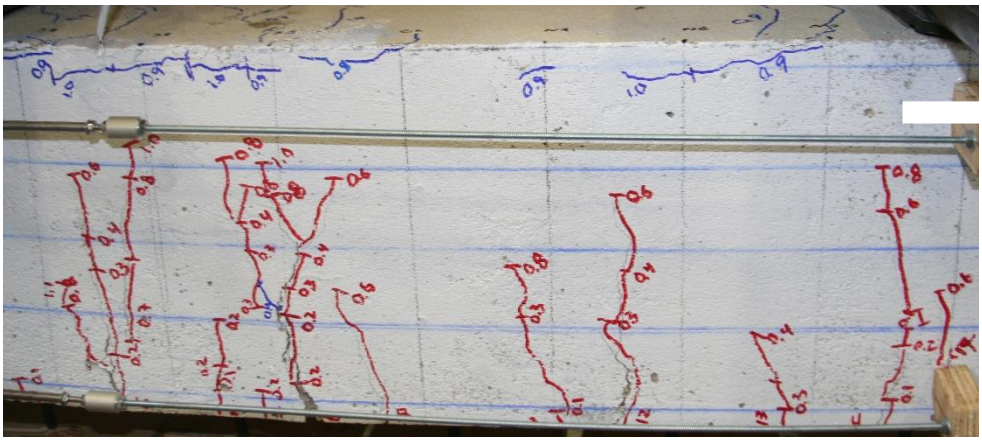

Figure 63. Crack Profile of East Face in Constant Moment Region

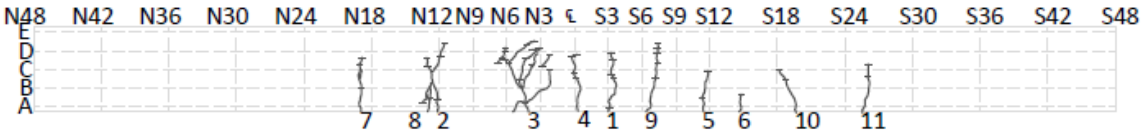

Figure 64. Crack Profile of the West Face (Optotrak)

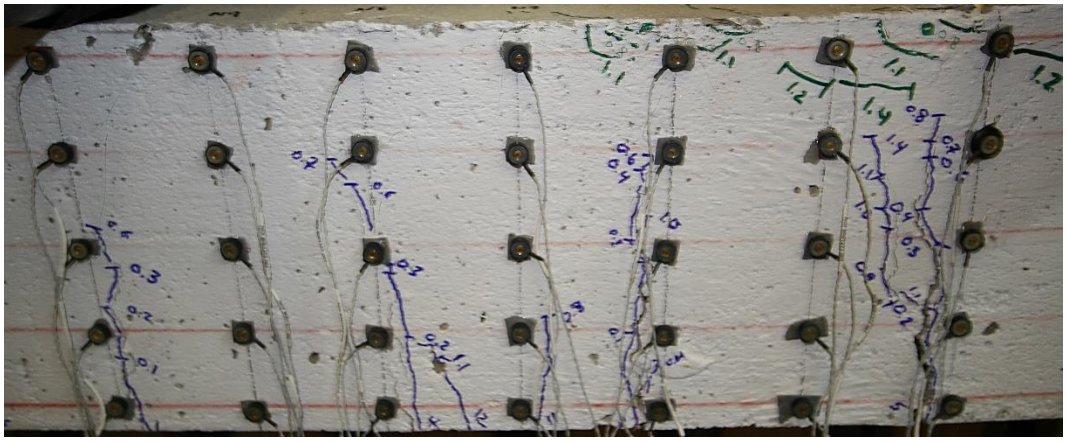

Figure 65. Crack Profile of West Face in Constant Moment Region

The average non-critical crack width on the east and west face was 0.19 mm 0.48 mm respectively. The east face developed two critical cracks, E6 and E8 that continued to widen with each deflection step. Crack E6 was approximately 4.5 inches south of E8. The two cracks joined on the bottom face of the specimen to meet the critical crack on the west face, W5. Figure 67 demonstrates the critical cracks on each face.

The critical cracks on the east face were double the size of the next largest crack by deflection step 0.9 inches (L/93). At that time, each crack was approximately 1.52 mm in width. In comparison, the critical crack on the west face was 2.54 mm wide. The growth of the individual cracks on the east face was slower than the growth of the critical crack on the west face. However, the combined growth of the cracks on the east face was comparable to the growth of the crack on the west face.

The maximum allowable crack width was observed on the east face after the deflection step 1.2 inches (L/70). In contrast, crack W5 had achieved the maximum crack width two steps earlier at 0.90 inches (L/93). The crack width limit was observed at reference elevation B on both faces, but was not observed any higher prior to the removal of all instrumentation. Figure 66 and Figure 67 demonstrate the crack width growth observed throughout the test.

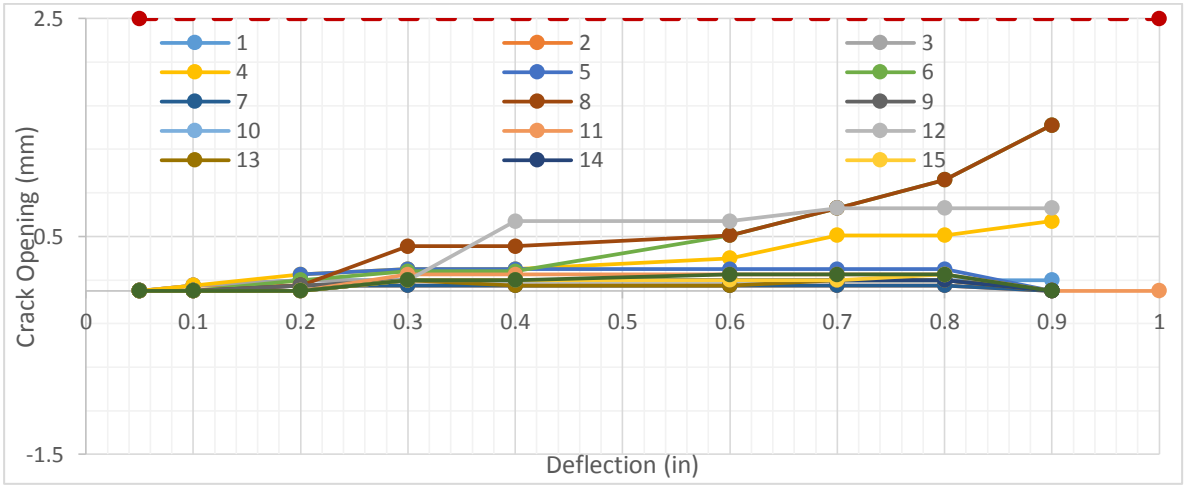

(a)

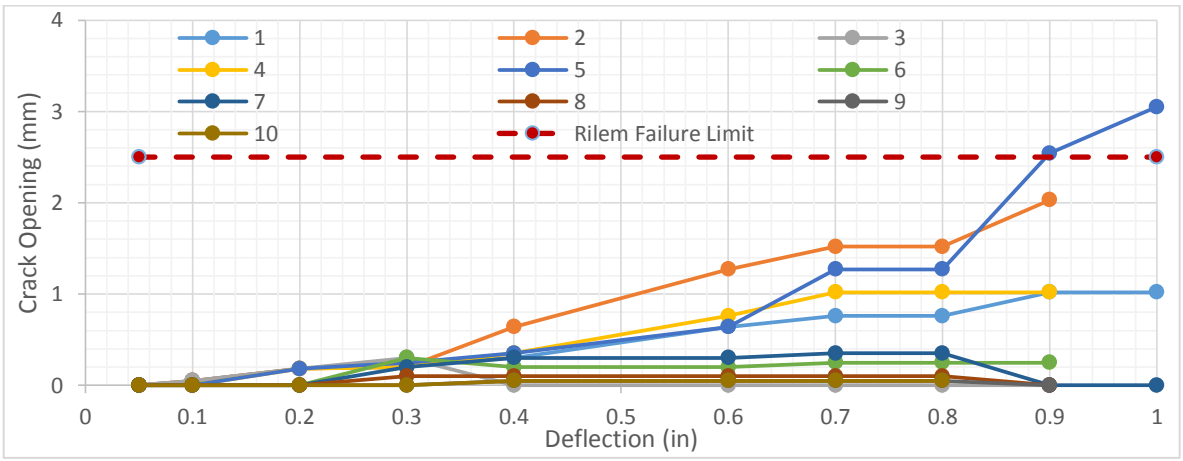

(b)

Figure 66. Crack Opening vs Strip Deflection for (a) East Face and (b) West Face

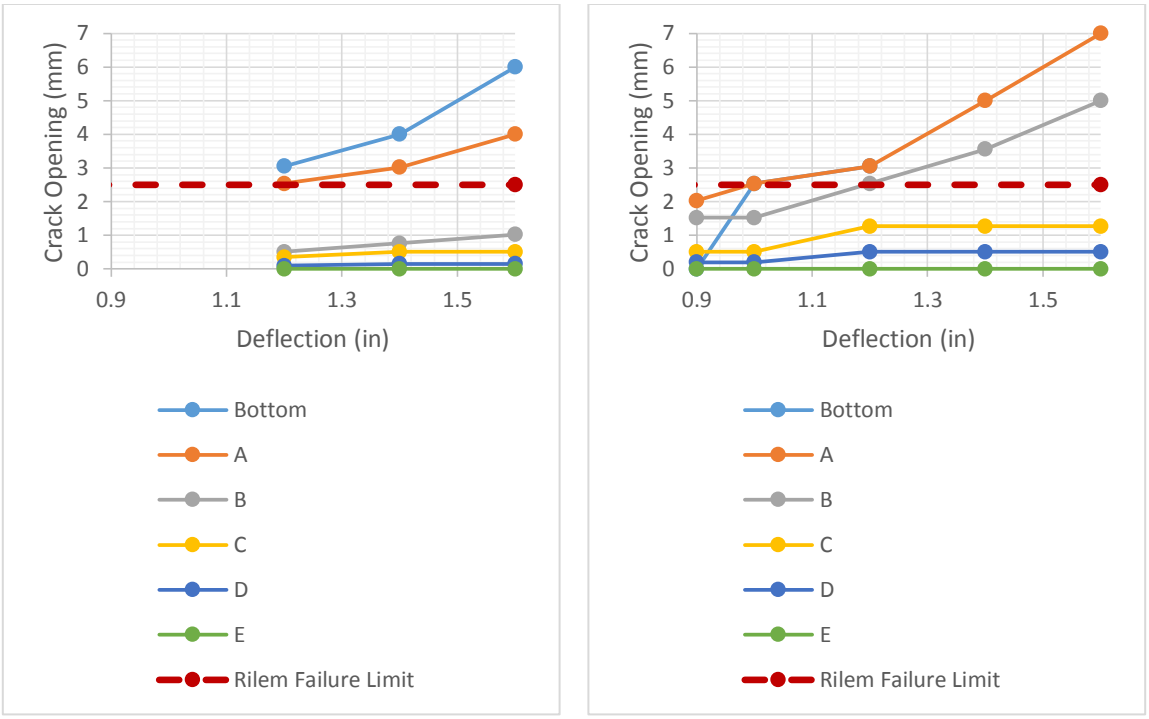

Figure 67. Crack Opening vs Strip Deflection for Primary Crack at Each Reference Elevation (a) E6 and (b) W5

Figure 68 and Figure 69 demonstrate the progression of cracks E6 and W5 respectively. Both cracks first formed at deflection step 0.2 inches. Crack E6 was the widest crack on the east face by deflection step 0.6 inches. Crack W5 did not gain that distinction until deflection step 0.9 inches. Each critical crack became the widest crack on their respective face by deflection step 0.8 inches. With the exception of associated crack branching, each critical crack extended vertically for the final time at deflection step, 0.8 inches. Both E6 and W5 resulted in multiple "branch" cracks and steel fiber anchorage failure.

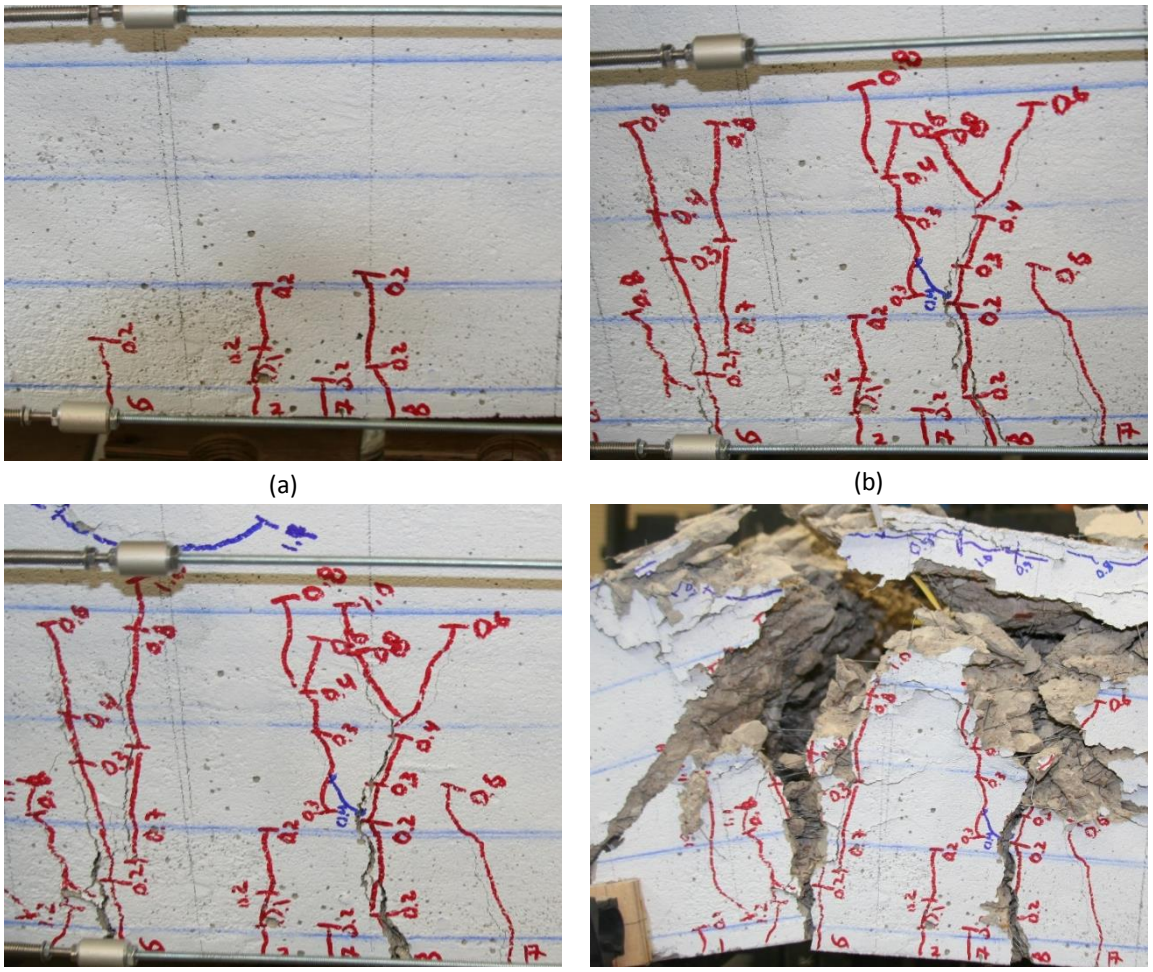

(a) (b)

(c) (d)

Figure 68. Crack Progression of E6 and E8 at Deflection Step:
(a) 0.2 inches, (b) 0.8 inches, (c) 1.4 inches, and Removal of Beam

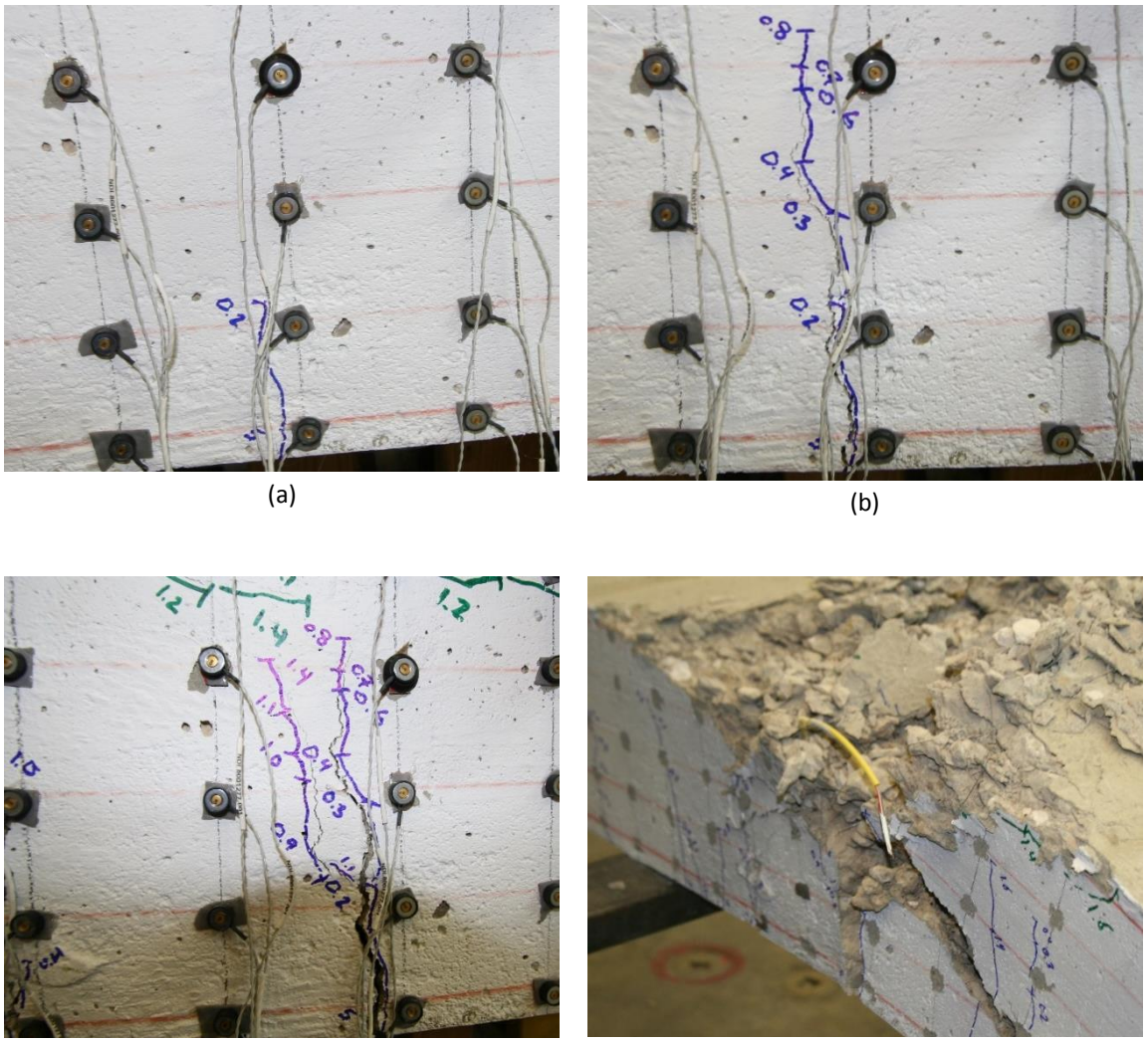

(a) (b)

(c) (d)

Figure 69. Crack Progression of W5 at Deflection Step:
(a) 0.2 inches, (b) 0.8 inches, (c) 1.4 inches, and Removal of Beam

Crushing was first observed between horizontal reference S3 and S6 on the top surface at deflection step both sides at the deflection step 0.70 inches (L/120). The crushing was observed above the critical cracks on either face. After the next step, crushing was also visible on both faces between N3 and S6. As the test continued, the crushing extended horizontally to include the entire constant moment region; however, the significant damage was focused above the critical cracks on each face. The crushed concrete region extended downward to meet the tension cracks by deflection step 1.60 inches (L/52.5). The slab strip specimen did not collapse during the test, yet the concrete experienced severe crushing damage. Figure 70 and Figure 71

exhibit the progression of concrete crushing and the extent of the damage after the specimen was removed from the test.

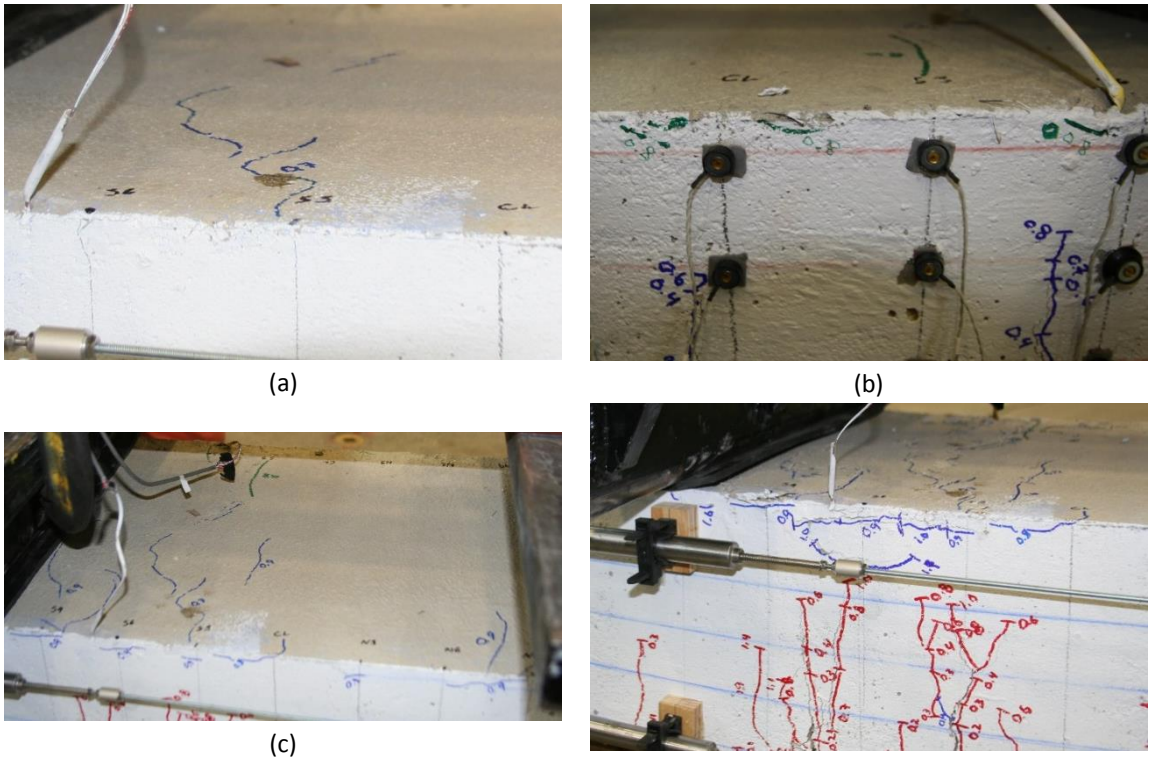

(a) (b)

(c) (d)

Figure 70. Crushing Progression of S9005BTM35 deflection of (a) 0.7 inch, (b) 0.8 inch, (c) 1.0 inches and (d) 1.6 inches

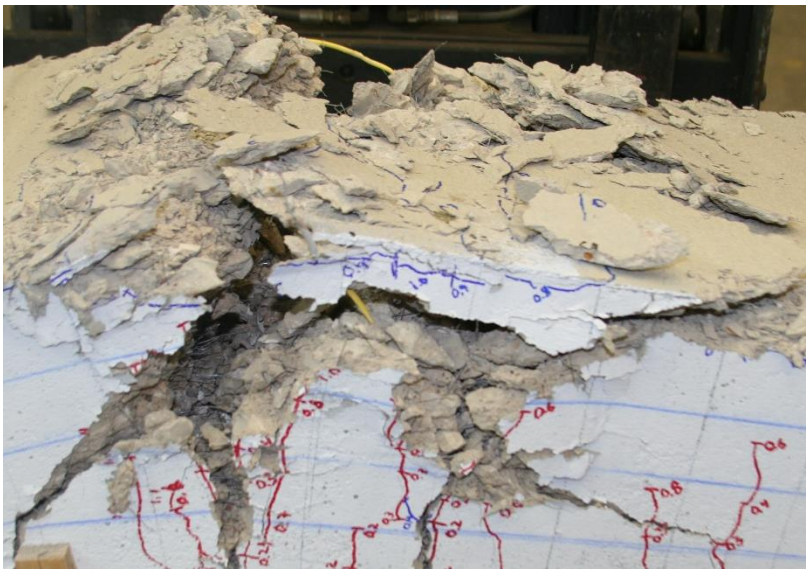

Figure 71. Severe Crushing Damage above Critical Cracks E6 and E8

A.10 S9005BTM25

Slab strip specimen S9005BTM25 has 2-#5 steel bars located with a clear cover of 1 inch from the bottom of the specimen. The specimen has an overall depth of 9.0 inches and a fiber volume of 0.5%. The specimen achieved a maximum capacity of 22.87 kips at a deflection of 0.9 inches (L/93). No new cracks formed after that deflection step.

A total of 10 cracks formed on the east face of the specimen, five inside the constant moment region, and 11 cracks on the west face of the specimen, 6 inside the constant moment region. The first crack for both the east and west face occurred during the 0.05 inch deflection step, (L/1680). All cracks formed by the 0.40 inch deflection step (L/210). The majority of the formed cracks extended to or beyond the mid-depth of the specimen by deflection step 0.3 inches (L/280). The cracks in the constant moment region did not extend vertically beyond the 0.6 inch deflection step on the east face and 0.8 inch deflection step on the west face. The maximum vertical elevation achieved was half way between reference elevation D and E, or approximately 1.75 inches from the top of the specimen. Further increasing the deflection of the specimen resulted in widening and formation of "branch" and accessory cracks, such as E1 and W3. Figure 72 and Figure 73 demonstrate the vertical progression of cracks on each face.

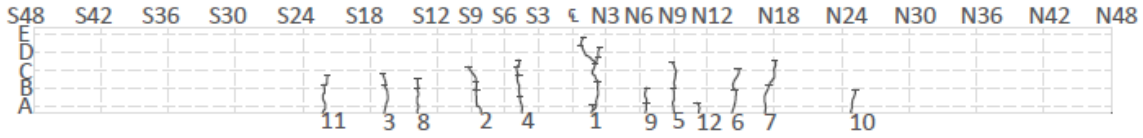

Figure 72. Crack Profile of the East Face (LVDT)

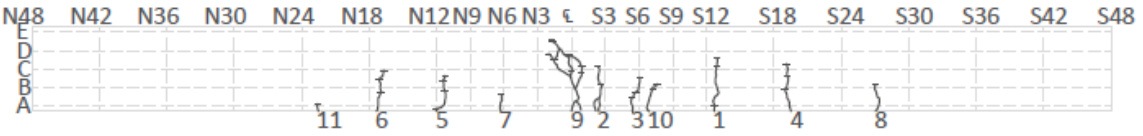

Figure 73. Crack Profile of the West Face (Optotrak)

The average non-critical crack width on the east and west face was 0.41 mm and 0.34 mm respectively. The critical crack on the east face, E1, became the largest crack on its face by deflection step 0.7 inches (L/120). The critical crack on the west face, W3, achieved this distinction at deflection step 0.4 inches (L/210). The maximum allowable crack width was observed on the east face after the deflection step 0.9 inches (L/93). In contrast, crack W3 had achieved the maximum crack width two steps earlier at 0.7 inches (L/120). The crack width limit

was observed at reference elevation C on both faces, but was not observed any higher prior to the removal of all instrumentation. Figure 74 and Figure 75 demonstrate the crack width growth observed throughout the test.

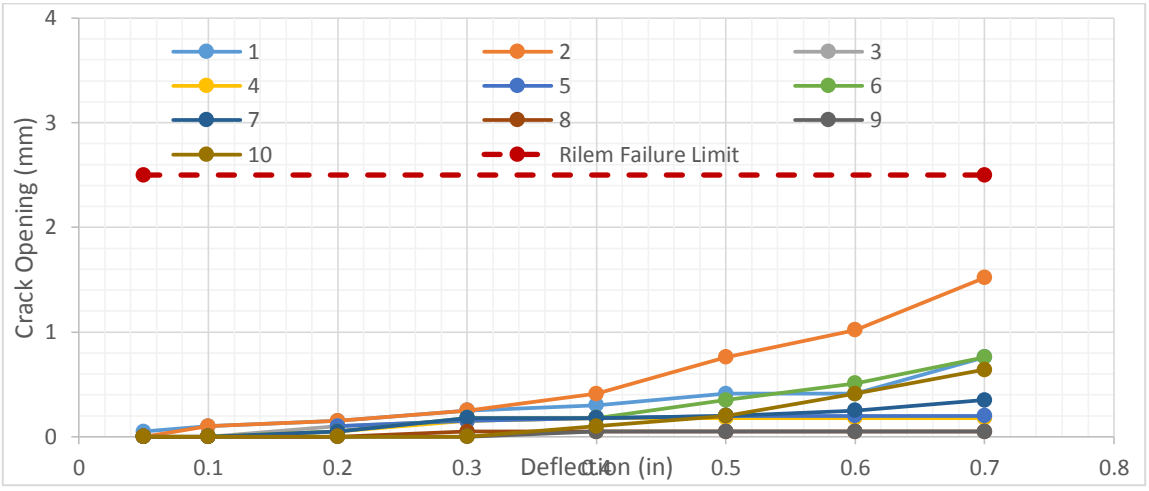

(a)

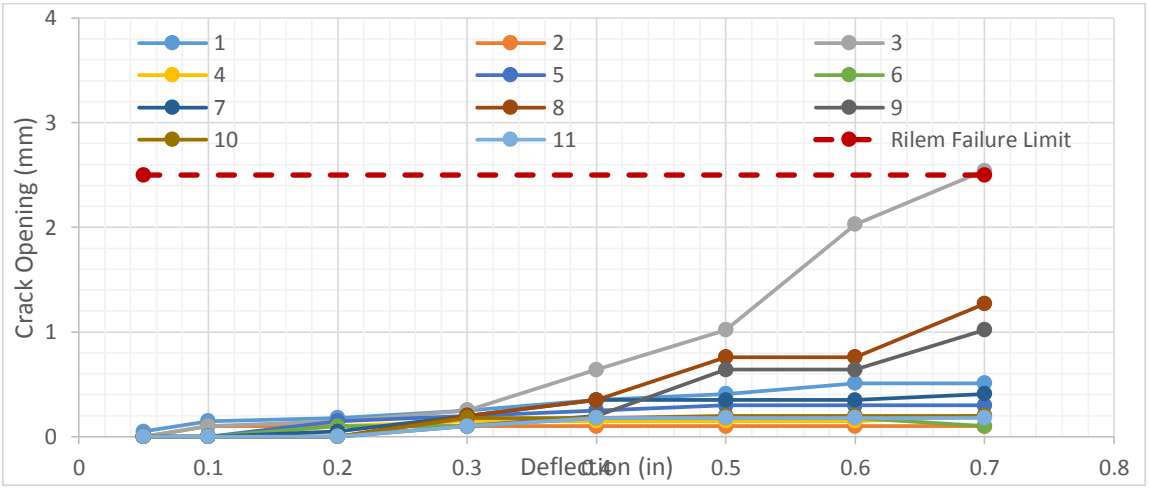

(b)

Figure 74. Crack Opening vs Strip Deflection for (a) East Face and (b) West Face

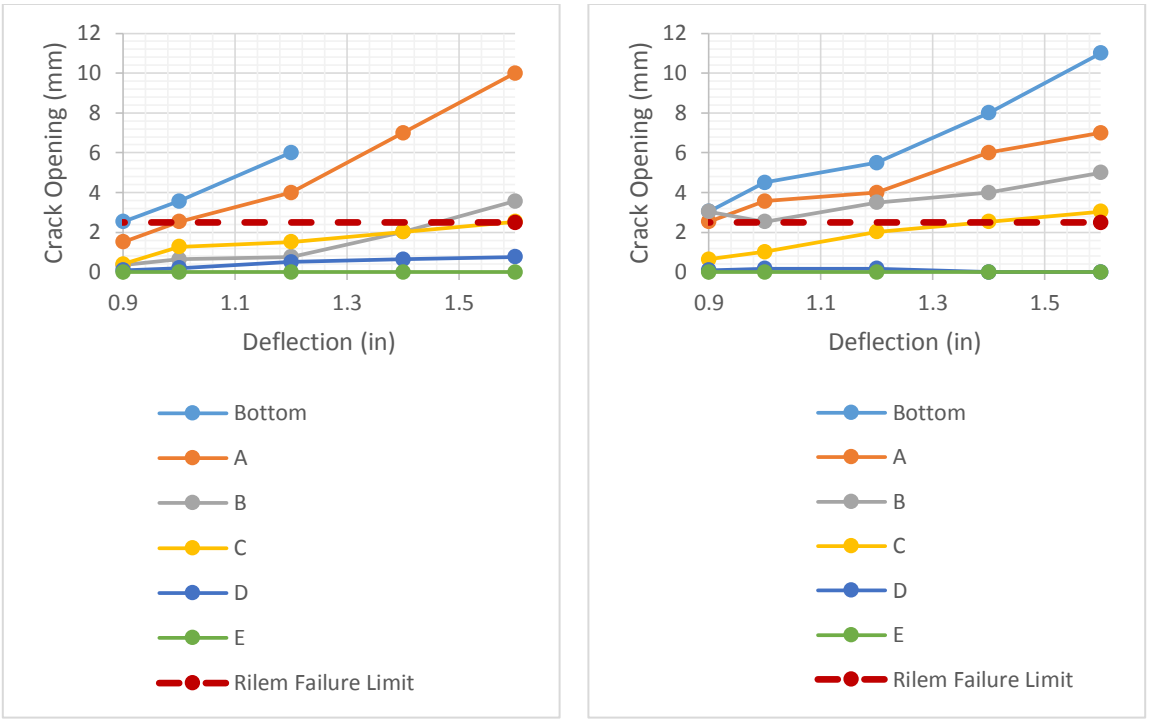

Figure 75. Crack Opening vs Strip Deflection for Primary Crack at Each Reference Elevation (a) E1 and (b) W3

Figure 76 and Figure 77 demonstrate the progression of cracks E1 and W3 respectively. Crack E1 formed during the first deflection step, 0.05 inches, while W3 did not form until the subsequent deflection step. With the exception of associated crack branching, critical crack E1 extended vertically for the final time at deflection step, 0.6 inches, and W3 at 0.8 inches. Both E6 and W5 resulted in multiple "branch" cracks and steel fiber anchorage failure.

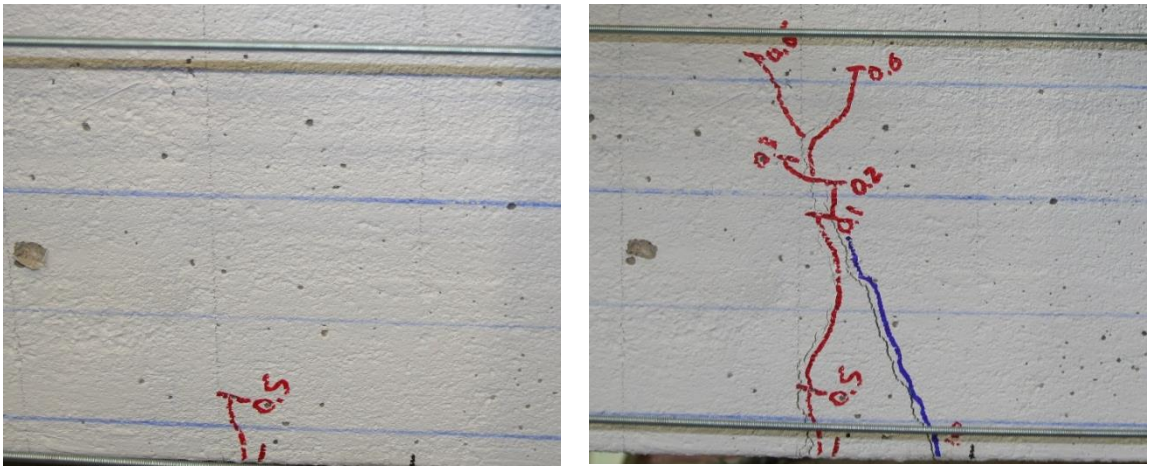

(a) (b)

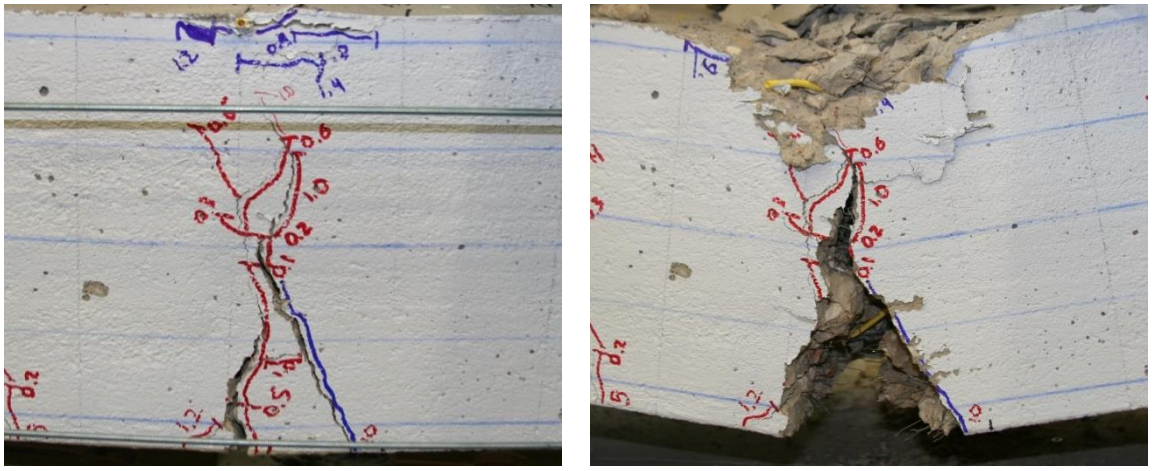

(c) (d)

Figure 76. Crack Progression of E1 at Deflection Step:
(a) 0.05 inches, (b) 0.6 inches, (c) 1.4 inches, and Removal of Beam

(a) (b)

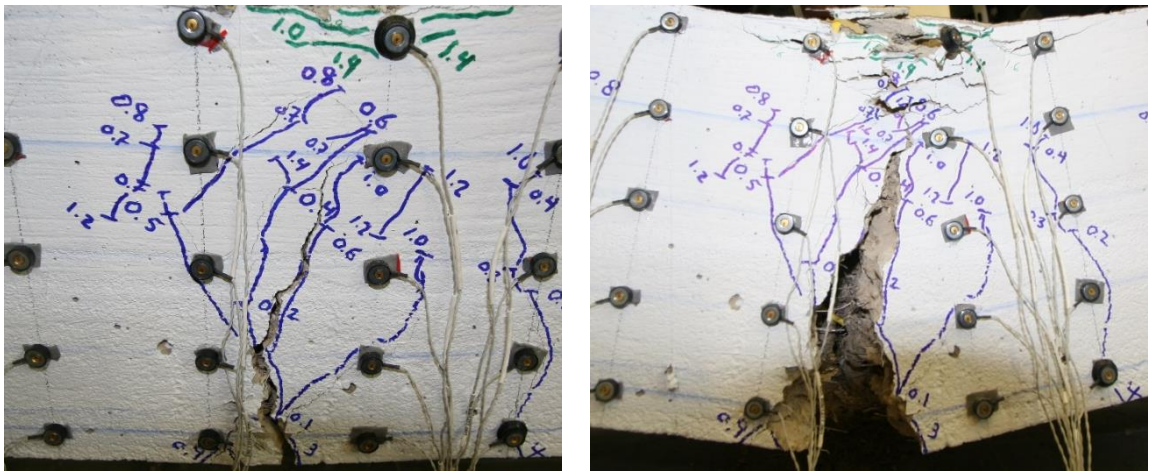

(c) (d)

Figure 77. Crack Progression of W3 at Deflection Step:
(a) 0.1 inches, (b) 0.6 inches, (c) 1.4 inches, and Removal of Beam

Crushing was first observed between horizontal reference N3 on both faces at deflection step 0.90 inches (L/93). The crushing was observed above the critical cracks on either face. As the test continued, the crushing extended horizontally to include the portion of the constant moment region between the centerline and N3. The crushed concrete region extended downward but did not meet the tension cracks prior to removal of testing instrumentation. The slab strip specimen did not collapse during the test, yet the concrete experienced severe crushing damage. Figure 78 exhibits the progression of concrete crushing and the extent of the damage prior to removal of the specimen.

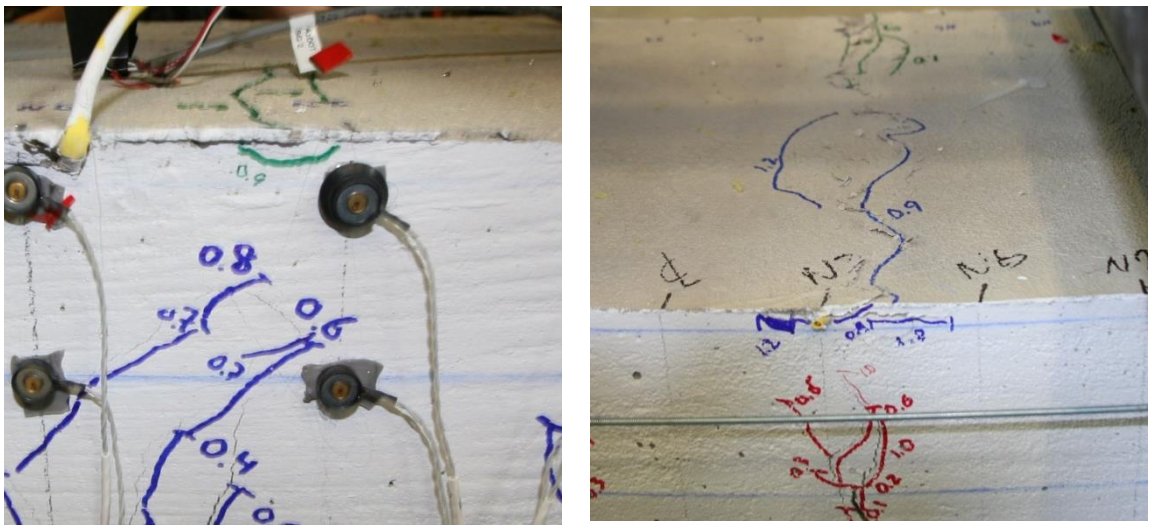

(a) (b)

(c) (d)

Figure 78. Crushing Progression of S9005BTM24 deflection of (a) 0.9 inch, (b) 1.2 inch, (c) 1.6 inches and (d) Completion of Test

A.11 S9005BTM24

Slab strip specimen S9005BTM24 has 2-#4 steel bars located with a clear cover of 1 inch from the bottom of the specimen. The specimen has an overall depth of 9.0 inches and a fiber volume of 0.5%. The specimen achieved a maximum capacity of 17.93 kips at a deflection of 0.6 inches (L/140). No new cracks formed after that deflection step.

A total of 12 cracks formed on the east face of the specimen, six inside the constant moment region, and 11 cracks on the west face of the specimen, six inside the constant moment region. The first crack formed on the east face at the first deflection step, 0.05 inches. The first crack on the west face formed at the next deflection step, 0.1 inches. All cracks formed by the 0.50 inch deflection step (L/168). Cracks outside the constant moment region progressed vertically to reference elevation D, or approximately 2.25 inches from the top surface. Vertical progression of cracks outside the moment region ceased at deflection step 0.7 inches. Cracks inside the constant moment region progressed vertically to reference elevation E, or approximately 0.5 inches from the top surface. Vertical progression of cracks inside the moment region ceased at deflection step 0.6 inches on the east face and 1.4 inches on the west face. Further increasing the deflection of the specimen resulted in widening of the primary crack. Figure 79 and Figure 80 demonstrate the final crack map for each face.

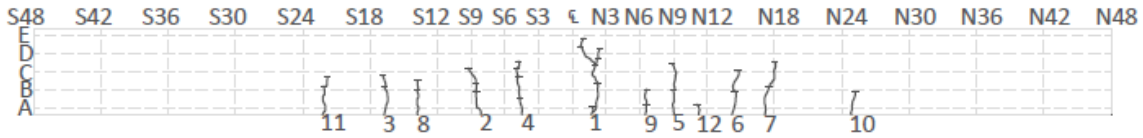

Figure 79. Crack Profile of the East Face (LVDT)

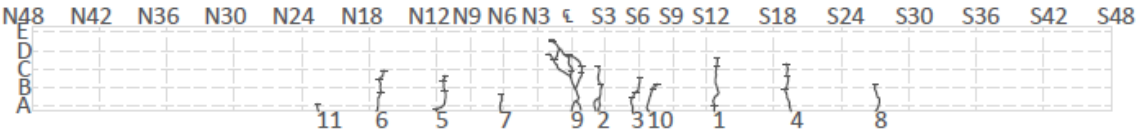

Figure 80. Crack Profile of the West Face (Optotrak)

The average non-critical crack width on the east and west face was 0.17 mm and 0.22 mm respectively. The critical crack on the east face, E1, became the largest crack on its face by deflection step 0.5 inches (L/168). The critical crack on the west face, W9, achieved this distinction at deflection step 0.4 inches (L/140). The maximum allowable crack width was observed on both the east and west face after the deflection step 0.6 inches (L/93). The crack width limit was observed at reference elevation C on both faces, but was not observed any

higher prior to the removal of all instrumentation. Figure 81 and Figure 82 demonstrate the crack width growth observed throughout the test.

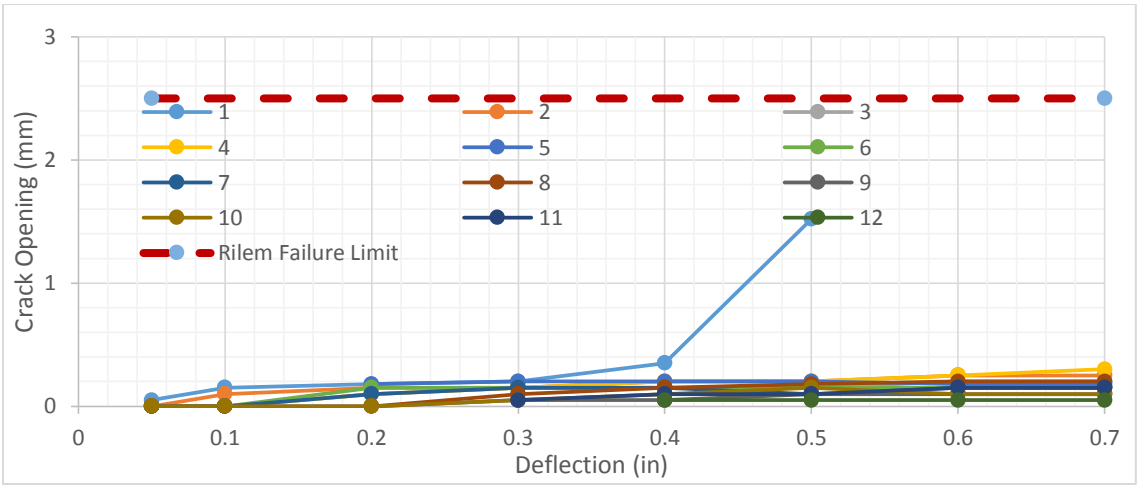

(a)

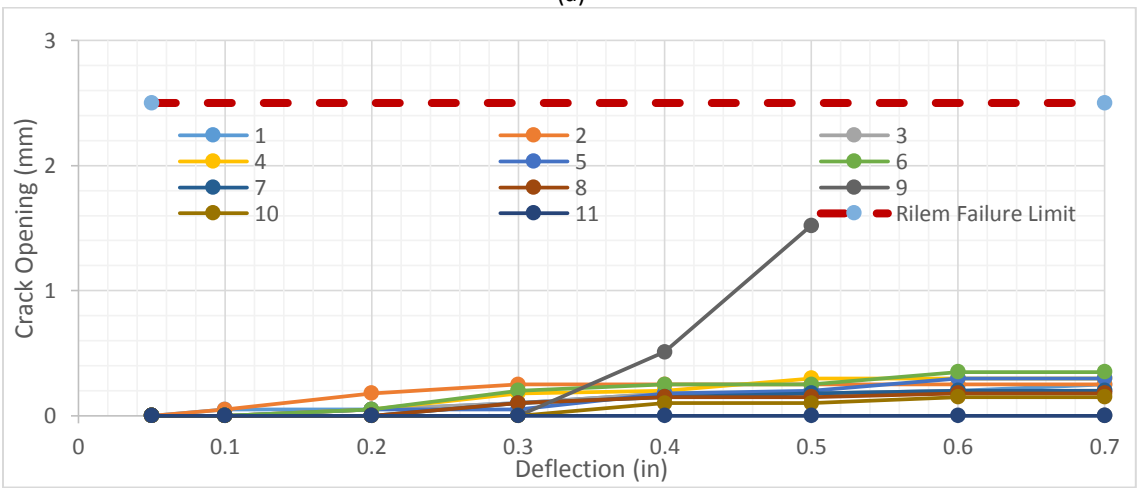

(b)

Figure 81. Crack Opening vs Strip Deflection for (a) East Face and (b) West Face

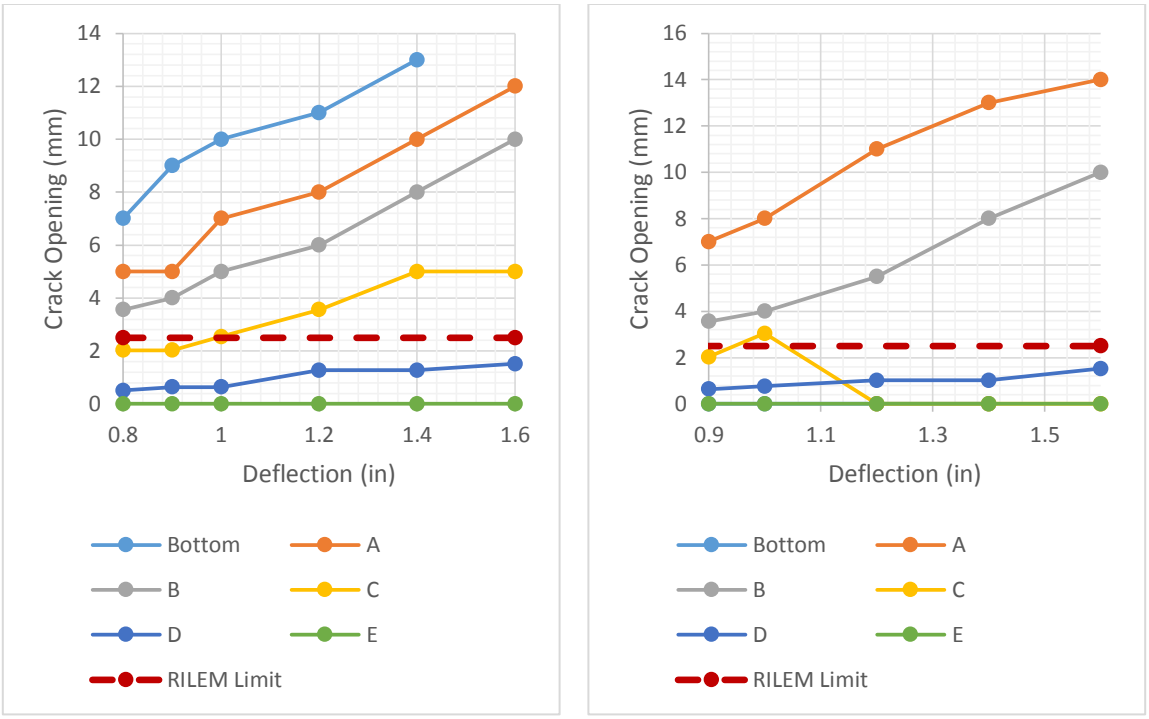

Figure 82. Crack Opening vs Strip Deflection for Primary Crack at Each Reference Elevation (a) E1 and (b) W9

Figure 83 and Figure 84 demonstrate the progression of cracks E1 and W9 respectively. Crack E1 formed during the first deflection step, 0.05 inches, while W9 did not form until deflection step 0.4 inches (L/210). With the exception of associated crack branching, critical crack E1 extended vertically for the final time at deflection step, 0.6 inches, and W9 at 1.4 inches.

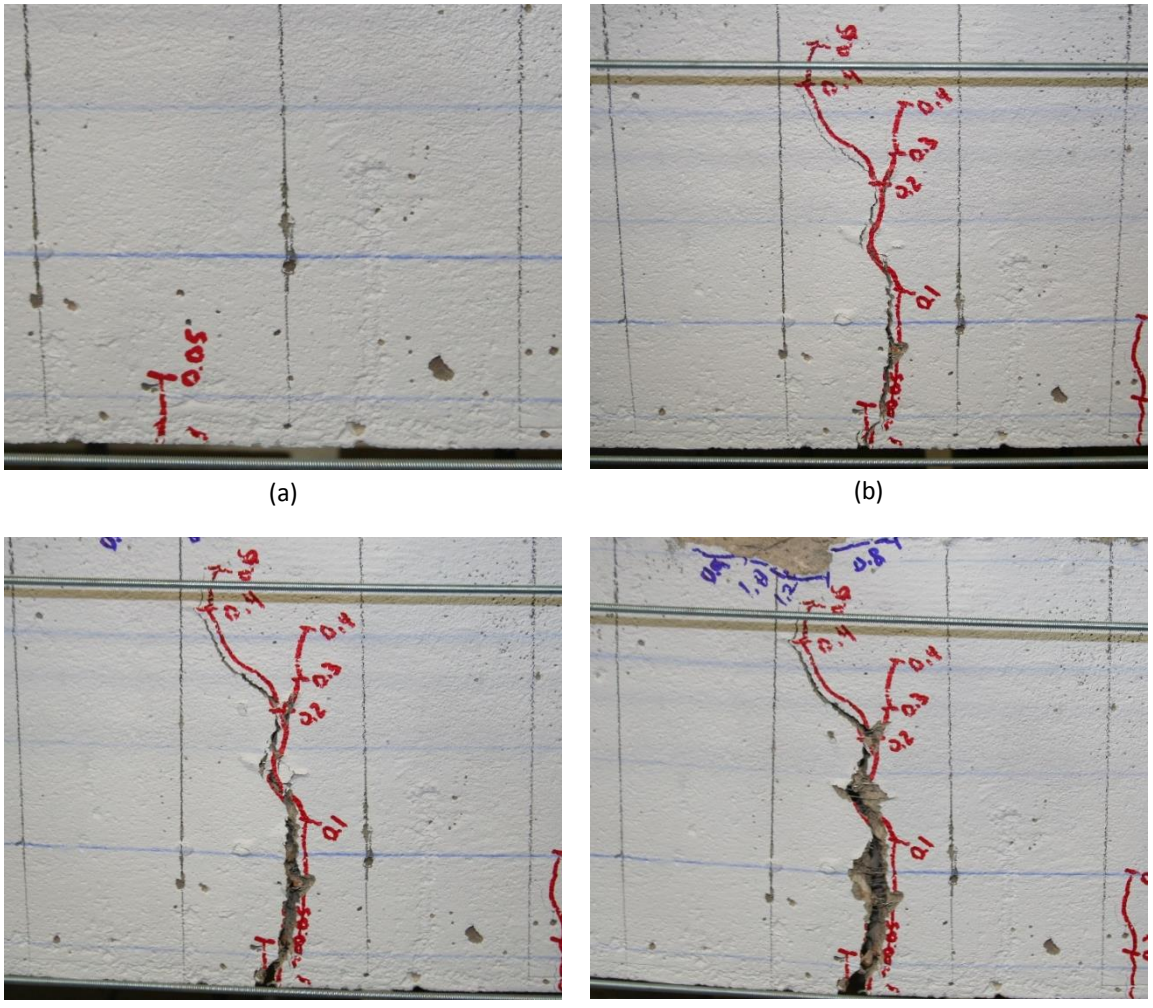

(a) (b)

(c) (d)

Figure 83. Crack Progression of E1 at Deflection Step:
(a) 0.05 inches, (b) 0.6 inches, (c) 1.0 inches, and 1.4 inches

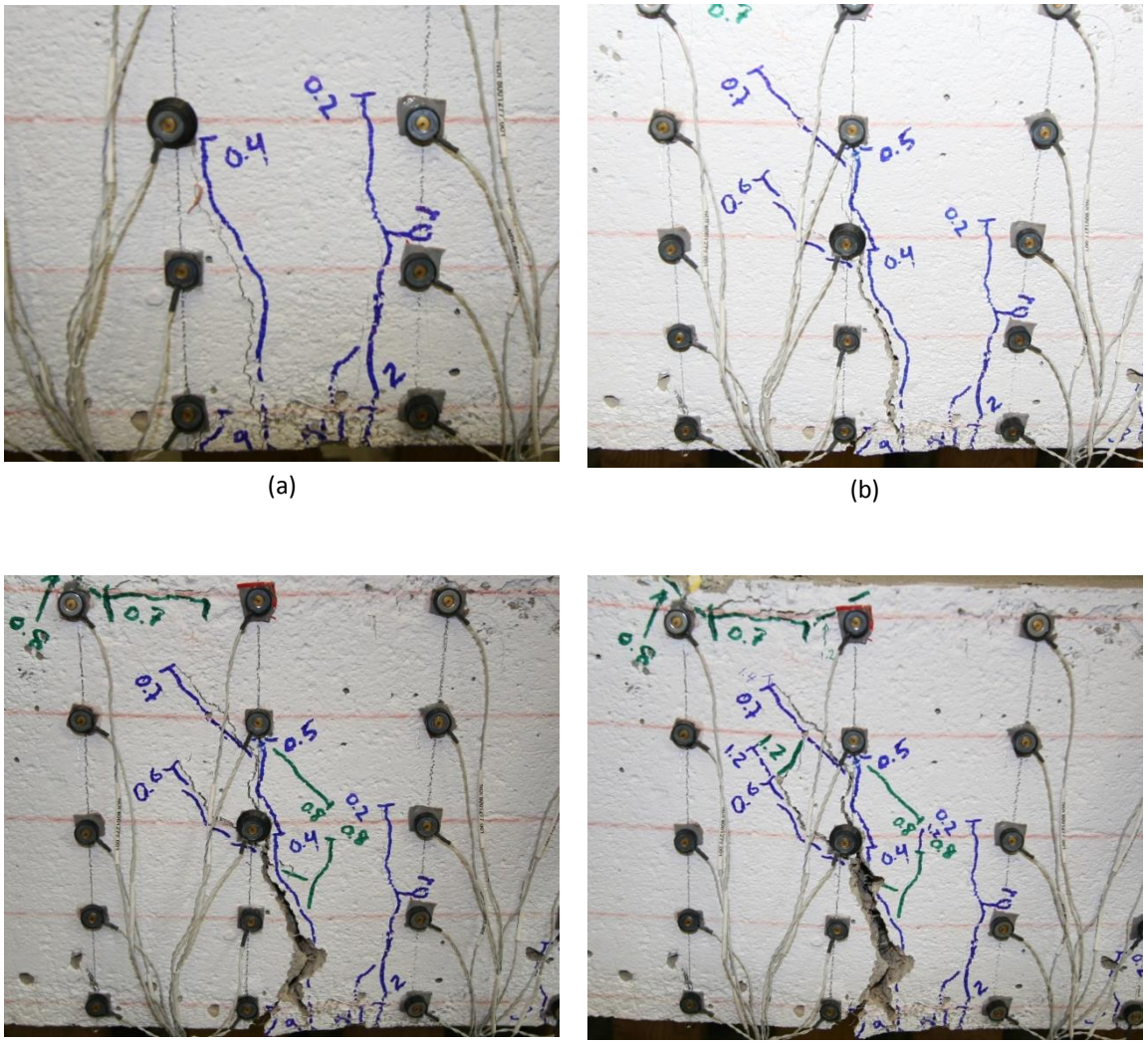

(a) (b)

(c) (d)

Figure 84. Crack Progression of W3 at Deflection Step:
(a) 0.4 inches, (b) 0.7 inches, (c) 1.0 inches, and (d) 1.4 inches

Crushing was first observed on the top surface at deflection step 0.6 inches (L/140). At step 0.70 inches (L/120), crushing was also observed on the east and west faces between the centerline and reference N3. The crushing was observed above the critical cracks on either face. As the test continued, the crushing extended horizontally to include the portion of the constant moment region between S3 and N3. The crushed concrete region extended downward to connect to the tension cracks by the completion of the test. The slab strip specimen did not collapse during the test, yet the concrete experienced severe crushing

damage. Figure 85 exhibits the progression of concrete crushing and the extent of the damage prior to removal of the specimen.

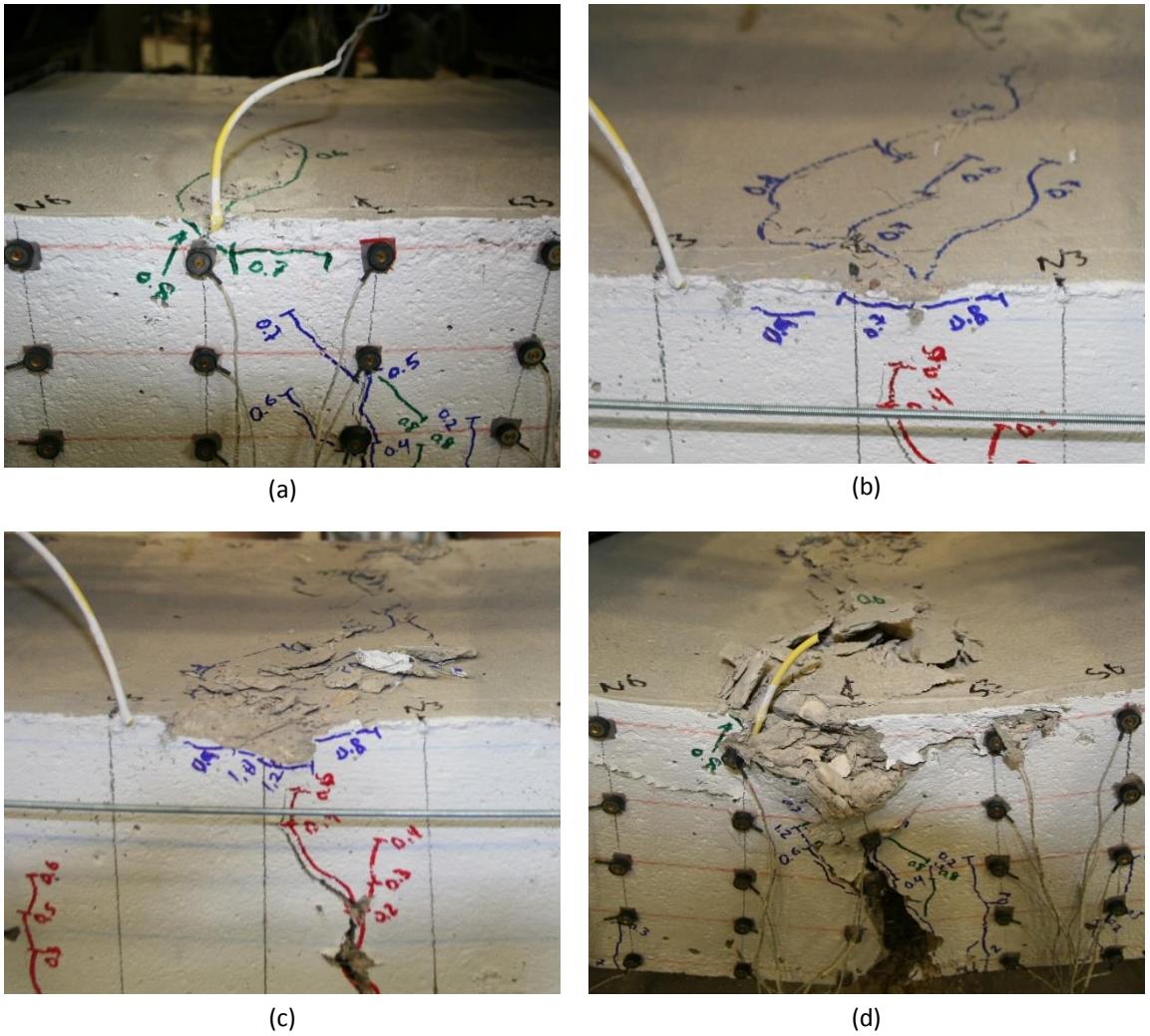

(a) (b)

(c) (d)

Figure 85. Crushing Progression of S9005BTM24 deflection of (a) 0.8 inch, (b) 1.0 inch, (c) 1.4 inches and (d) Completion of Test

A.12 S9005BTM23

Slab strip specimen S9005BTM23 has 2-#3 steel bars located with a clear cover of 1 inch from the bottom of the specimen. The specimen has an overall depth of 9.0 inches and a fiber volume of 0.5%. The specimen achieved a maximum capacity of 12.58 kips at a deflection of 0.5 inches (L/168). No new cracks formed after that deflection step.

A total of seven cracks formed on the east face of the specimen, four inside the constant moment region, and 10 cracks on the west face of the specimen, five inside the constant moment region. The first crack formed on both faces at the deflection step 0.1 inches. All cracks formed by the 0.50 inch deflection step (L/168). Cracks outside the constant moment region progressed vertically to between reference elevations D and E, or approximately 1.5 inches from the top surface. Vertical progression of cracks outside the moment region ceased at deflection step 0.6 inches. Cracks inside the constant moment region progressed vertically to reference elevation E, or approximately 0.5 inches from the top surface. Vertical progression of cracks inside the moment region ceased at deflection step 0.7 inches. Further increasing the deflection of the specimen resulted in widening of the primary crack and crack branching. Figure 86 and Figure 87 demonstrate the final crack map for each face.

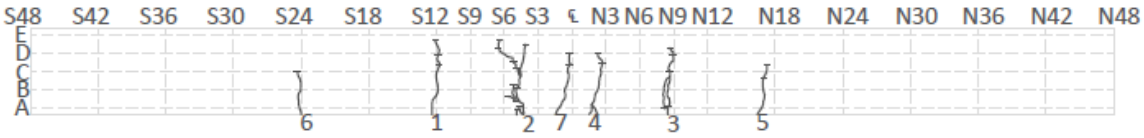

Figure 86. Crack Profile of the East Face (LVDT)

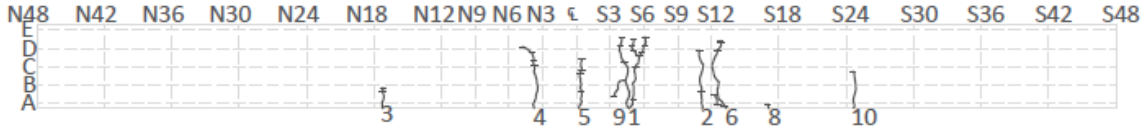

Figure 87. Crack Profile of the West Face (Optotrak)

The average non-critical crack width on the east and west face was 0.53 mm and 0.57 mm respectively. The critical cracks on the east face and west face, E2 and W1 respectively, became the largest cracks on each face by deflection step 0.7 inches (L/120). The maximum allowable crack width for each crack was also observed at this deflection step. The crack width limit was observed at reference elevation D on the east face and reference C on the west face, but was not observed any higher prior to the removal of all instrumentation. Figure 88 and Figure 89 demonstrate the crack width growth observed throughout the test.

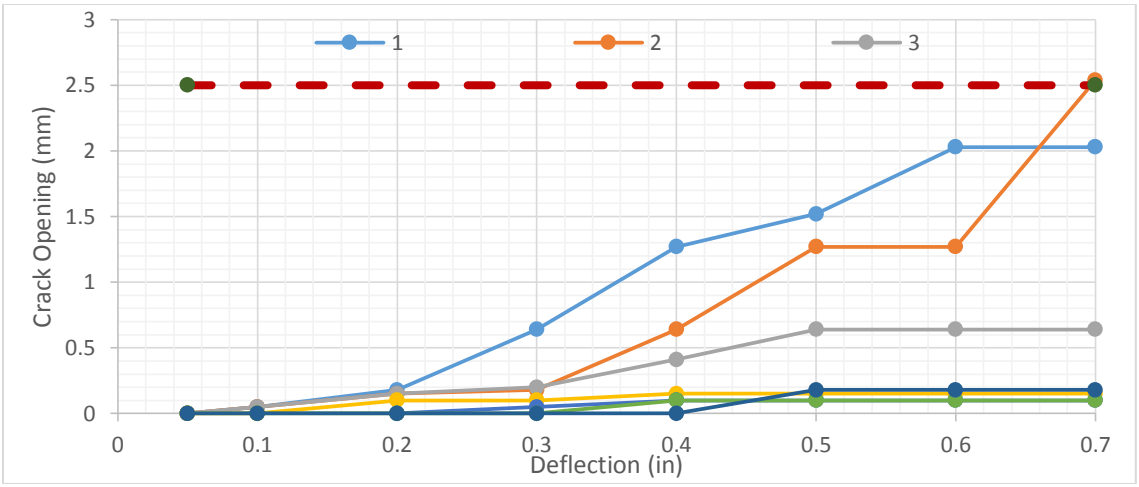

(a)

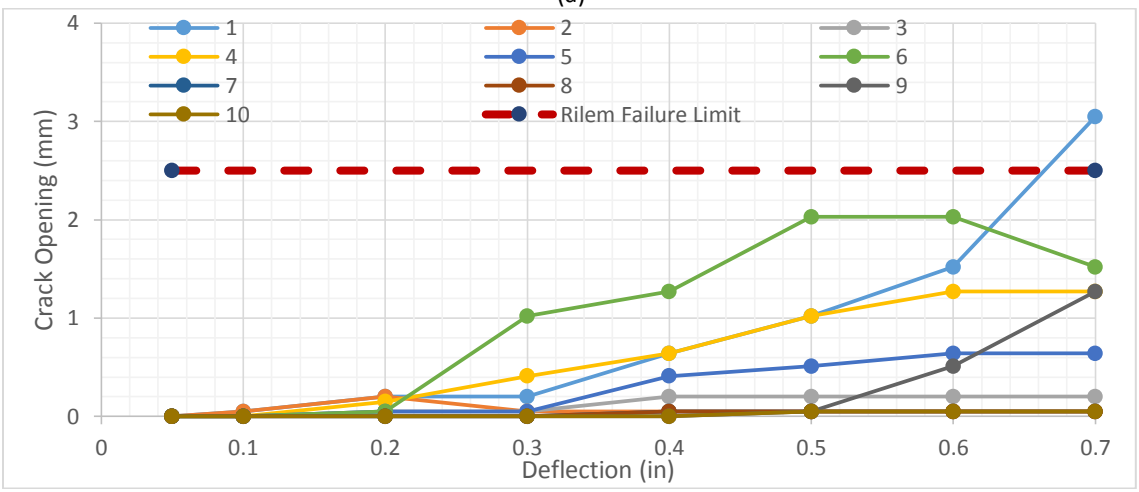

(b)

Figure 88. Crack Opening vs Strip Deflection for (a) East Face and (b) West Face

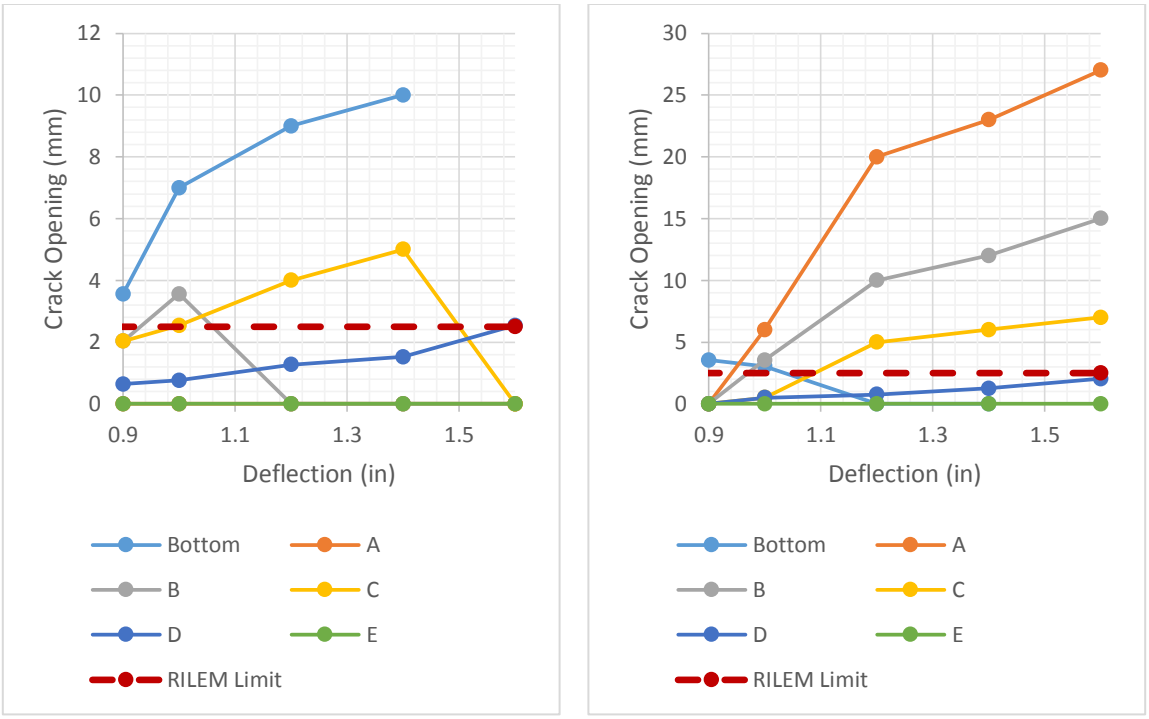

Figure 89. Crack Opening vs Strip Deflection for Primary Crack at Each Reference Elevation (a) E2 and (b) W1

Figure 90 and Figure 91 demonstrates the progression of cracks E1 and W9 respectively. Both E2 and W1 second deflection step, 0.1 inches (L/840). With the exception of associated crack branching, both critical cracks extended vertically for the final time at deflection step, 0.7 inches.

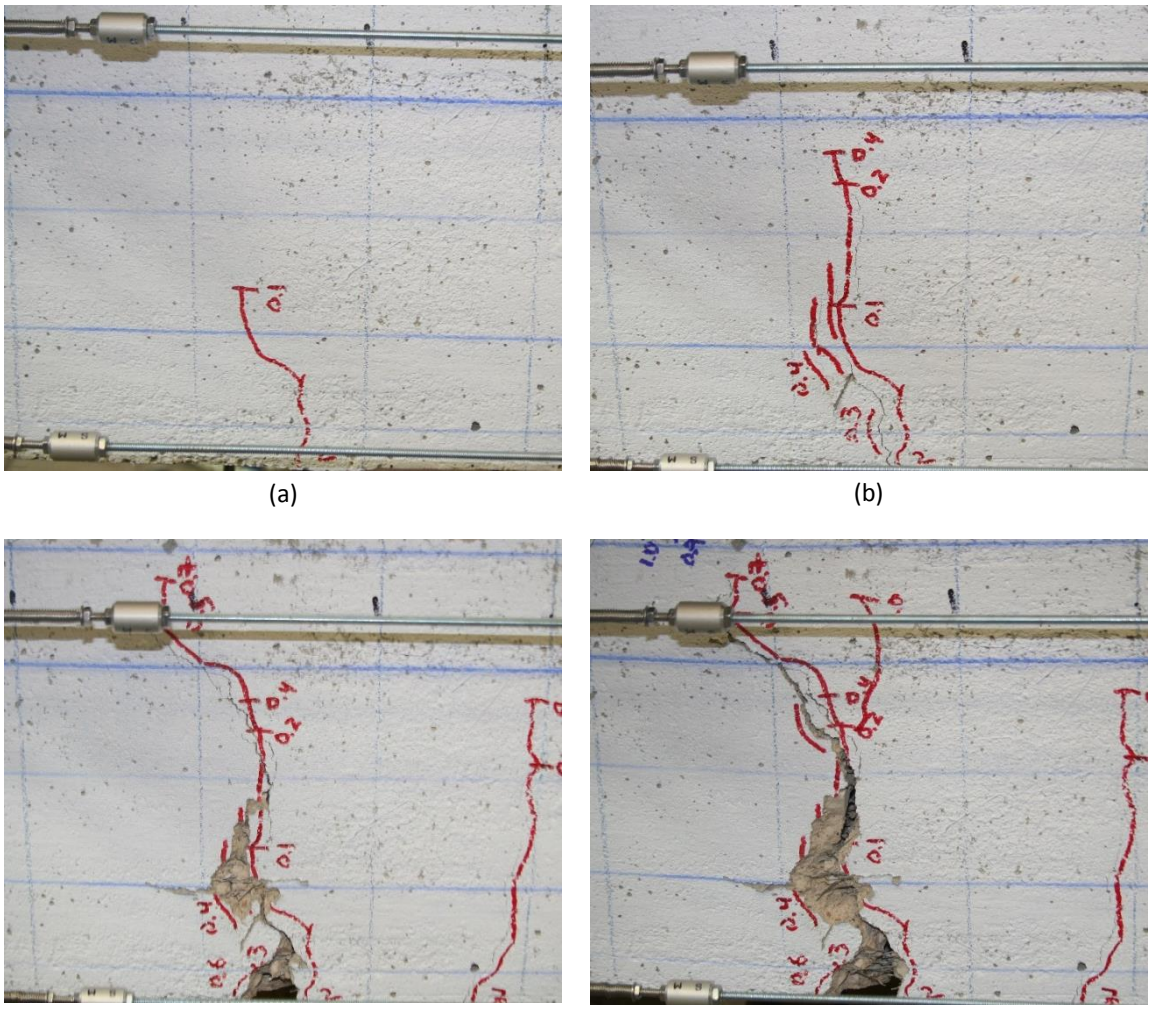

(a) (b)

(c) (d)

Figure 90. Crack Progression of E2 at Deflection Step:
(a) 0.1 inches, (b) 0.4 inches, (c) 0.7 inches, and 1.4 inches

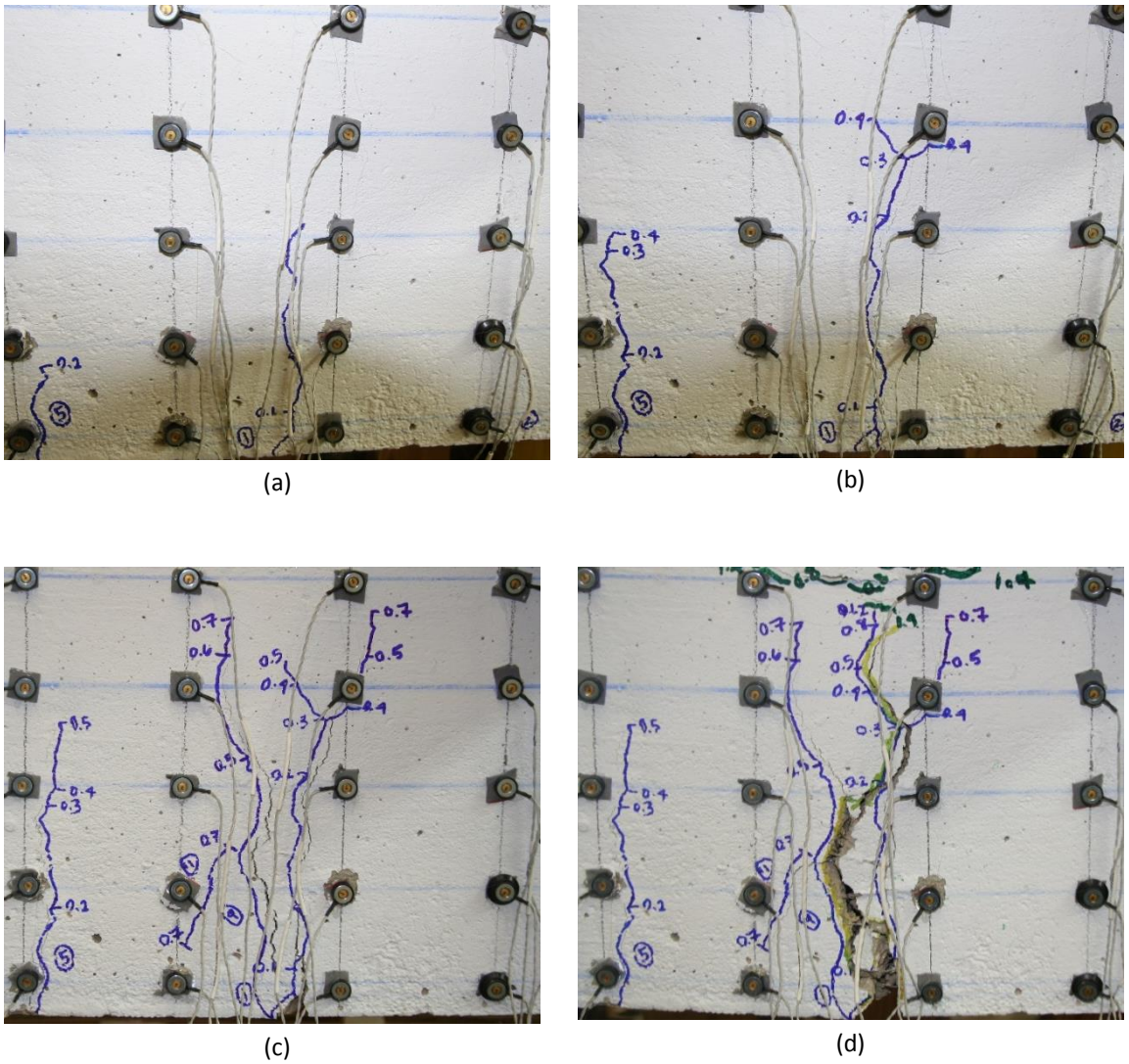

(a) (b)

(c) (d)

Figure 91. Crack Progression of W1 at Deflection Step:
(a) 0.2 inches, (b) 0.4 inches, (c) 0.7 inches, and 1.4 inches

Crushing was first observed on the east, west, and top surface at deflection step 0.8 inches (L/105). The crushing began between horizontal references S6 and S9 above each critical crack. As the test continued, the crushing extended horizontally, but did not extend beyond S6 and S9. The crushed concrete region extended downward and joined the tension cracks prior to collapse of the specimen. Figure 92 exhibits the progression of concrete crushing and the extent of the damage prior to removal of the specimen.

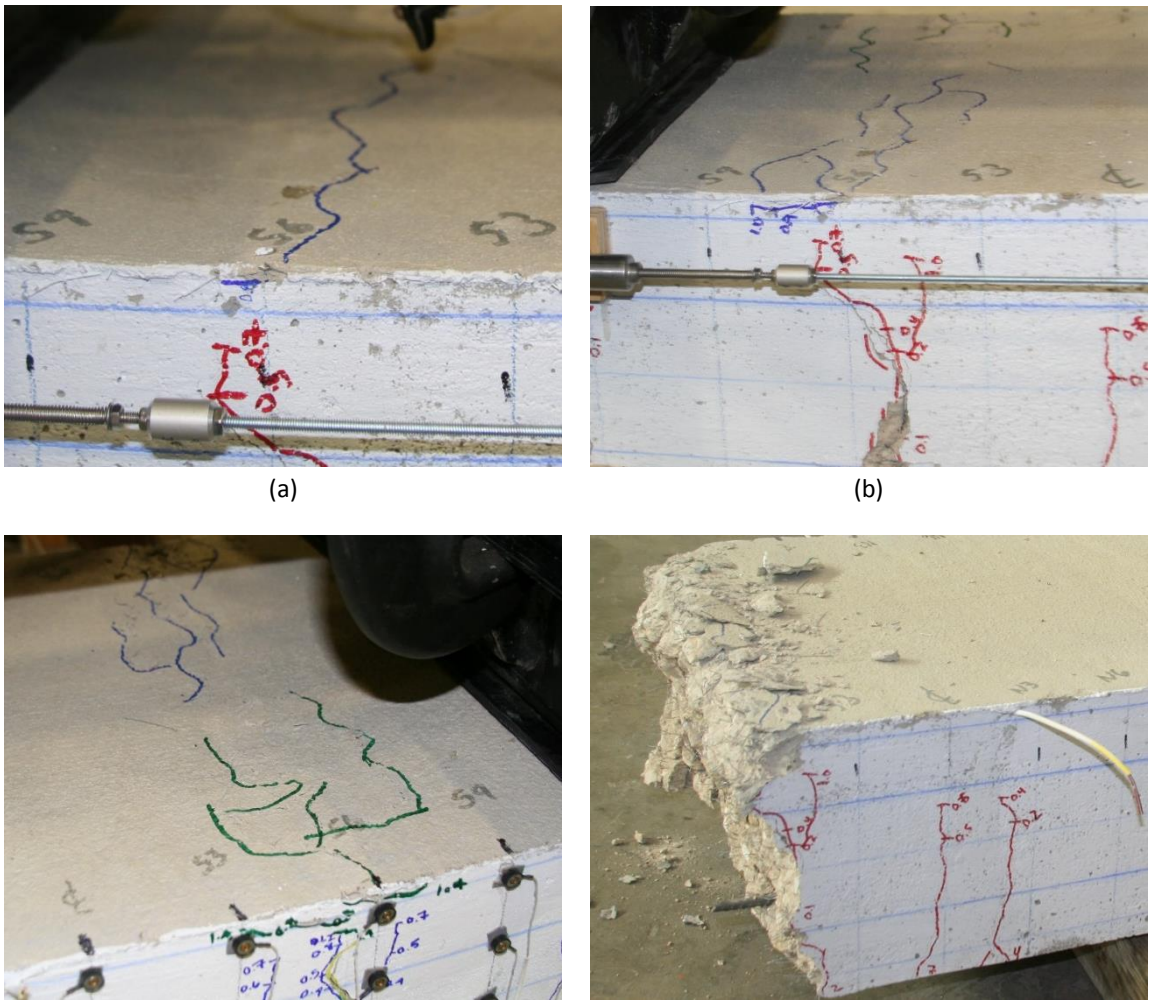

(a) (b)

(c) (d)

Figure 92. Crushing Progression of S9005BTM23 deflection of (a) 0.8 inch, (b) 1.0 inch, (c) 1.4 inches and (d) Completion of Test

A.13 S9005NOS00

Slab strip specimen S9005NOS00 is a plain SFRC strip and does not have any steel reinforcing bars. The specimen has an overall depth of 9.0 inches and a fiber volume of 0.5%. The specimen achieved a maximum capacity of 4.56 kips at a deflection of 0.05 inches (L/1680). Without steel reinforcement, the specimen's peak capacity corresponded to its cracking strength.

A single crack formed on both faces of the specimen at the first deflection step 0.05 inches. The east face formed a second crack approximately 1 inch to the south of the first crack during the next deflection step, but neither face developed additional cracks. The failure plane developed beneath the south load point at horizontal reference S12.

The critical crack on both faces extended beyond the vertical reference E at deflection step 0.35 inches (L/240). Crack W1 extended vertically slightly during deflection step 0.5 inches (L/168), otherwise, neither critical crack extended further. Both cracks rose to approximately 0.25 inches from the top surface of the slab strip specimen. Both cracks "branched" at vertical reference D. Figure 93 and Figure 94 demonstrate the vertical progression of the cracks on the east and west faces respectively.

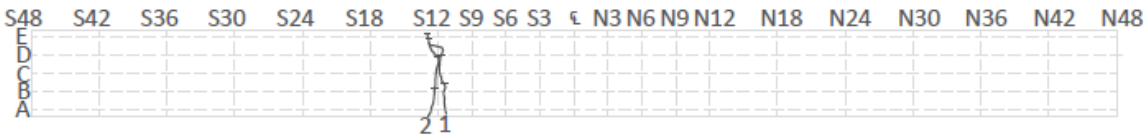

Figure 93. Crack Profile of the East Face (LVDT)

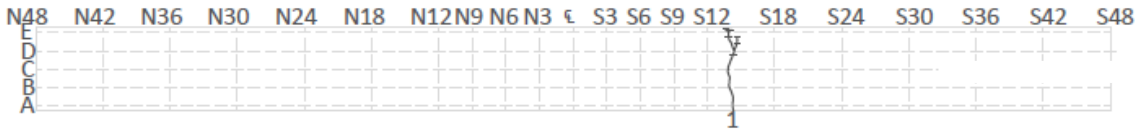

Figure 94. Crack Profile of the West Face (Optotrak)

The crack width was measured at each reference elevation throughout the entirety of the test except where excessive spalling prohibited it. The critical crack on each side achieved the maximum allowable crack width at the bottom of the specimen by the sixth deflection step. 0.3 inches (L/280). The maximum allowable crack width was achieved at a new reference elevation with each successive deflection step until reference C. Reference D did not achieve the maximum allowable crack width until the final deflection step 0.8 inches (L/105). Fibers were

visibly bridging the widening cracks at later deflection steps. Figure 95 through Figure 97 demonstrates the crack width progression of both critical cracks.

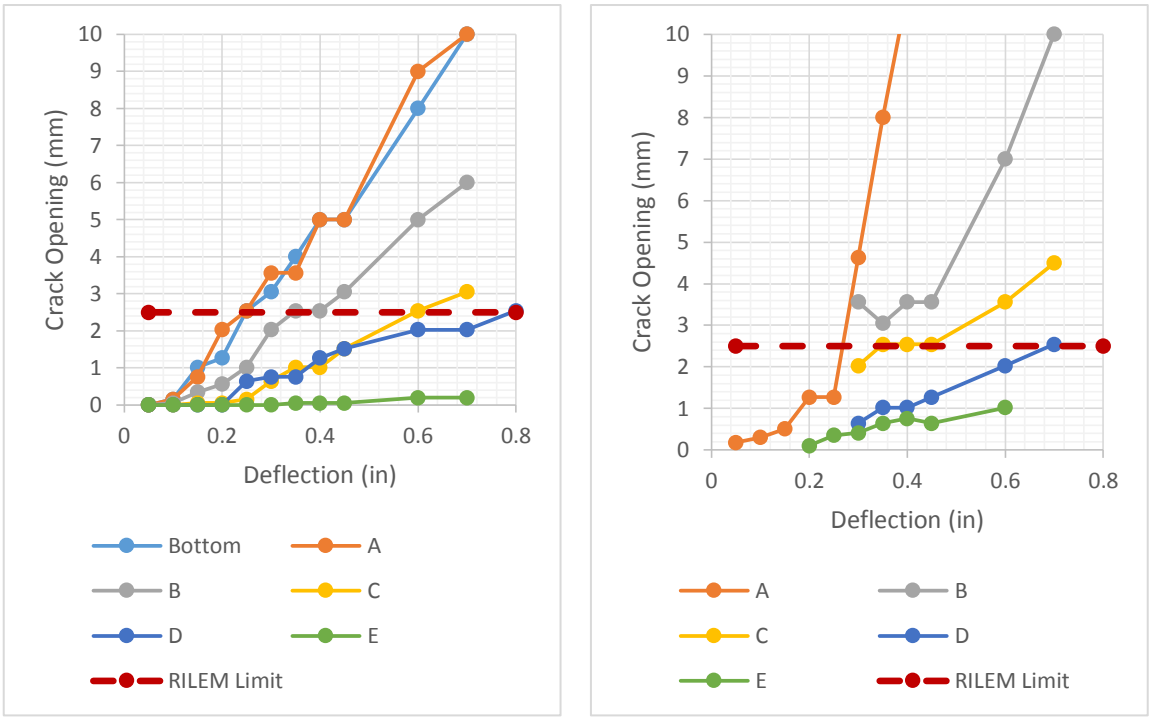

(a) (b)

Figure 95. Crack Width Progression of Critical Cracks (a) E2 and (b) W1

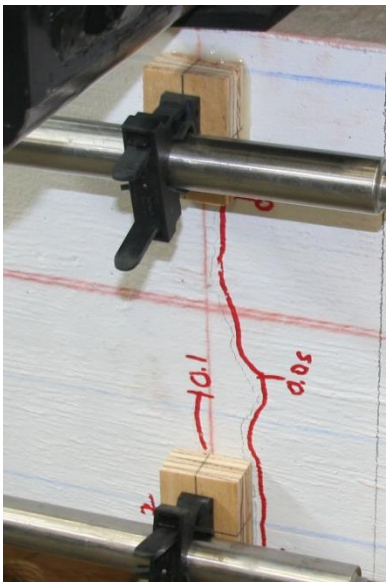

(a)

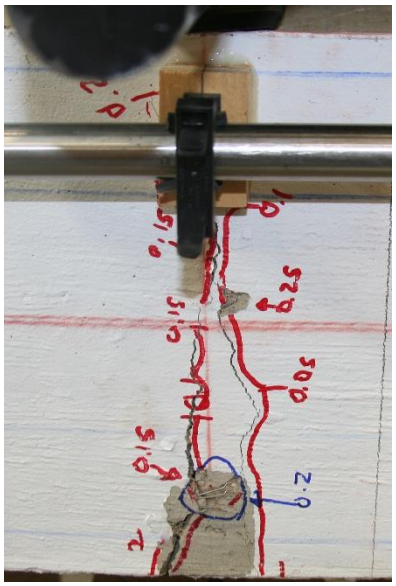

(b)

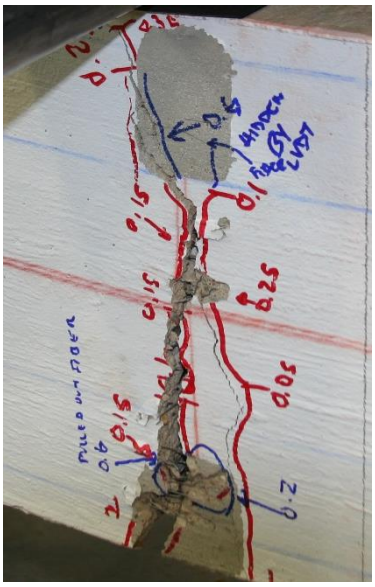

(c)

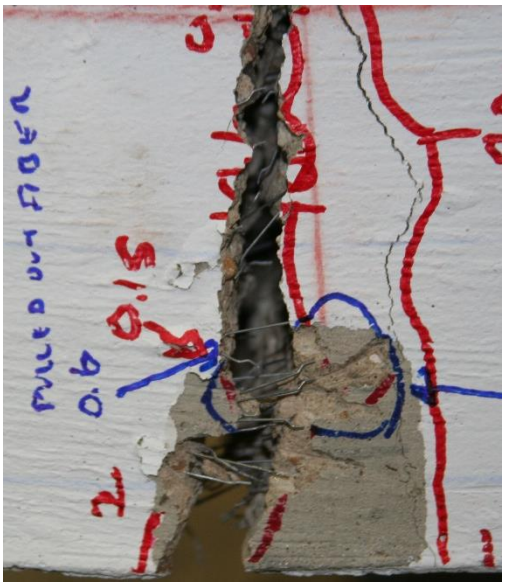

(d)

Figure 96. Damage Progression of the Critical Crack on the East Face, E2, at Deflection Step: (a) 0.1 inches, (b) 0.30 inches, and (c) 0.80 inches. (d) Fiber Bridging

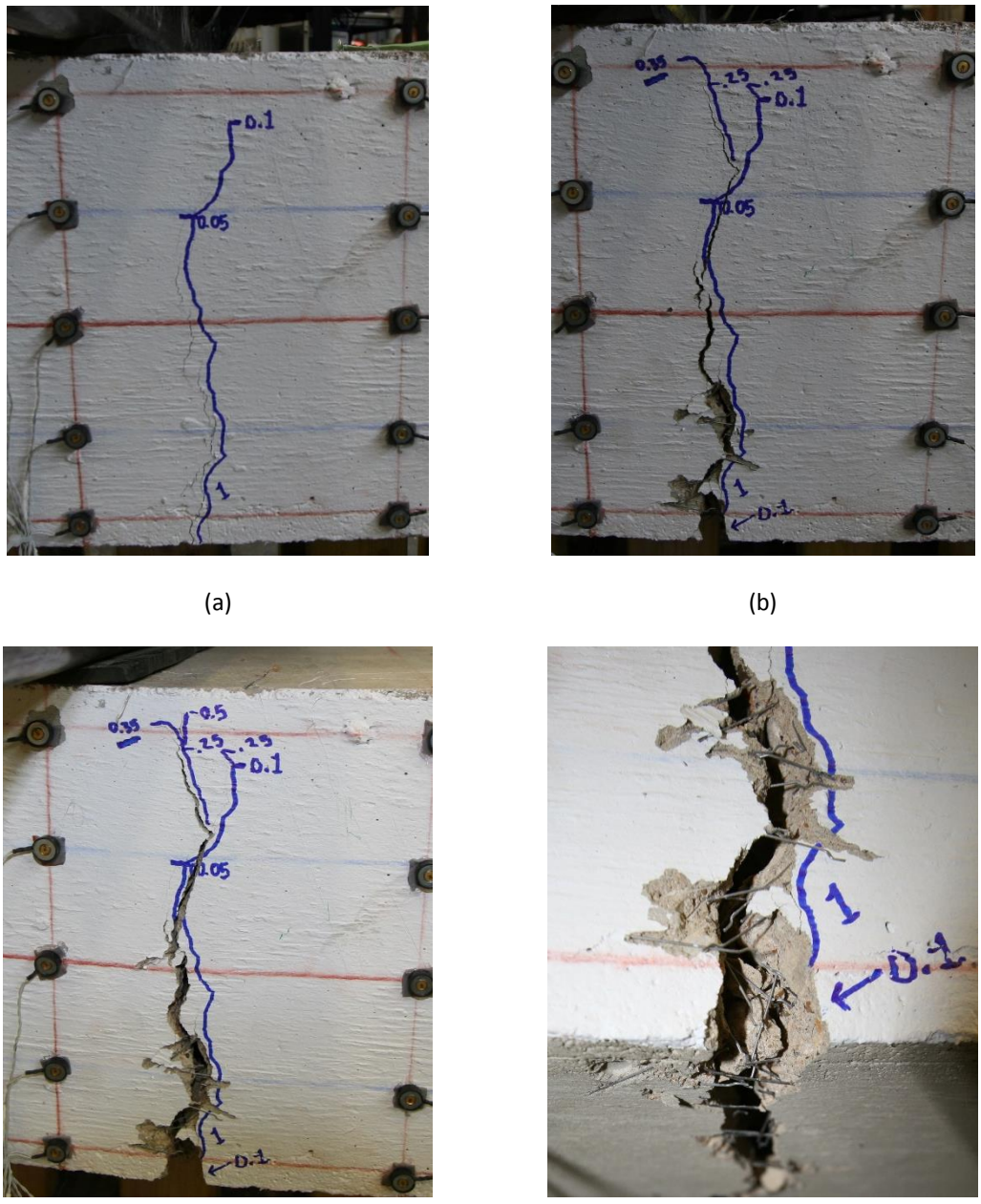

(a) (b)

(c) (d)

Figure 97. Damage Progression of the Critical Crack on the West Face, W1, at Deflection Step: (a) 0.1 inches, (b) 0.35 inches, and (c) 0.80 inches. (d) Fiber Bridging

All instrumentation was removed from the specimen at deflection step 0.80 inches (L/105) to prevent damage to the equipment. Concrete crushing was observed at this deflection step on the east face. Concrete crushing was not observed on the top or west face at that time.

Crushing was not observed on the west face prior to the collapse of the specimen. Figure 98 shows the first observance of crushing on east face.

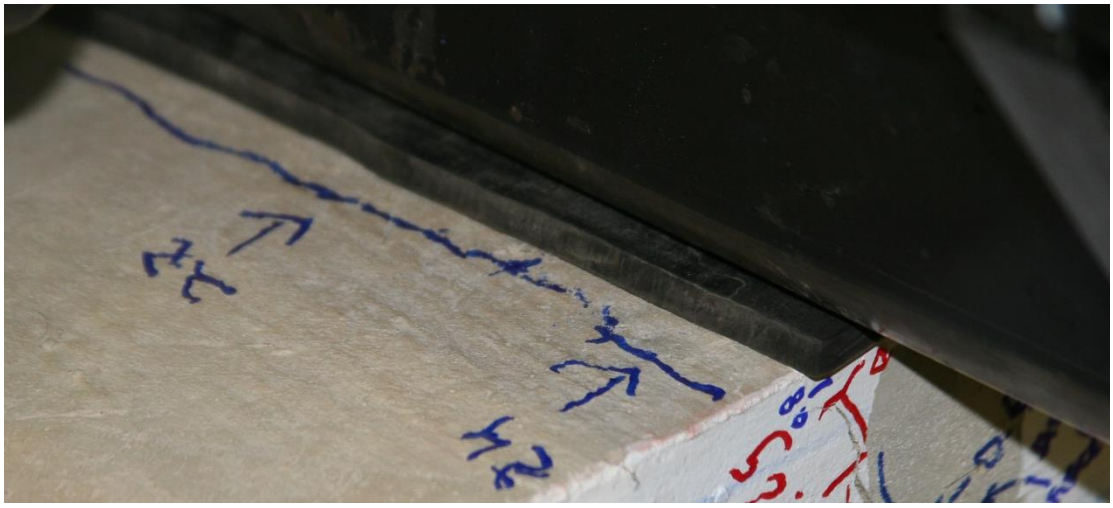

Figure 98. Observation of Concrete Crushing on East Face

A.14 S9020NOS00

Slab strip specimen S9020NOS00 is a plain SFRC strip and does not have any steel reinforcing bars. The specimen has an overall depth of 9.0 inches and a fiber volume of 2.0%. The specimen achieved a maximum capacity of 11.5 kips at a deflection of 0.1 inches (L/840). At that time all observed cracks had already formed.

A single crack formed on both the east and west face. The critical cracks formed prior to the first pause at deflection step 0.2 inches (L/420). The crack on the east face formed between horizontal references N6 and N9 while the crack on the west faced formed between N3 and N6. The cracks progressed vertically passed reference elevation E, to approximately 0.25 inches from the top surface. The maximum allowable crack width, 2.5 mm, for each crack was observed at deflection step 0.3 inches (L/280). Figure 99 and Figure 100 demonstrate the progression of each crack throughout the test.

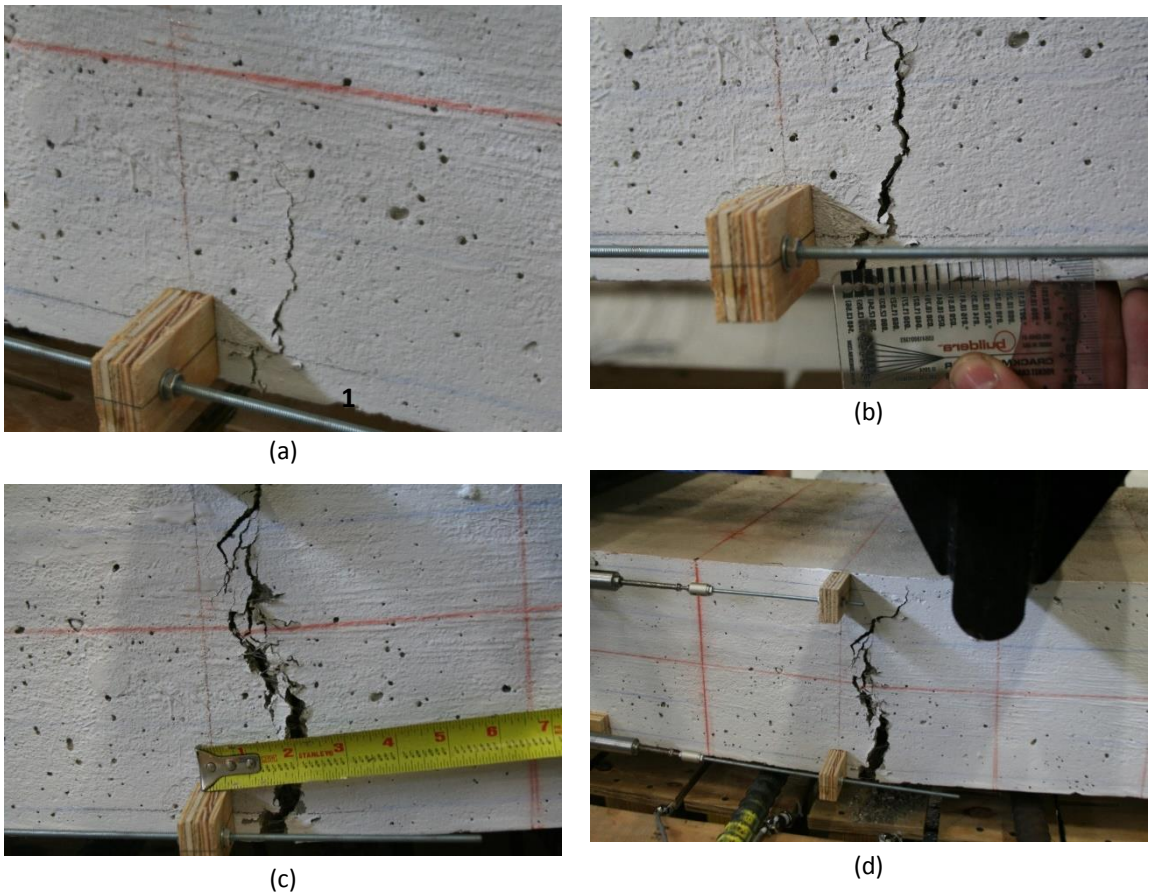

(a) (b) (c) (d)

Figure 99. Crack Progression of E1 and E12 at Deflection Step: (a) 0.2 inches, (b) 0.3 inches, (c) 1.2 inches, and 1.6 inches

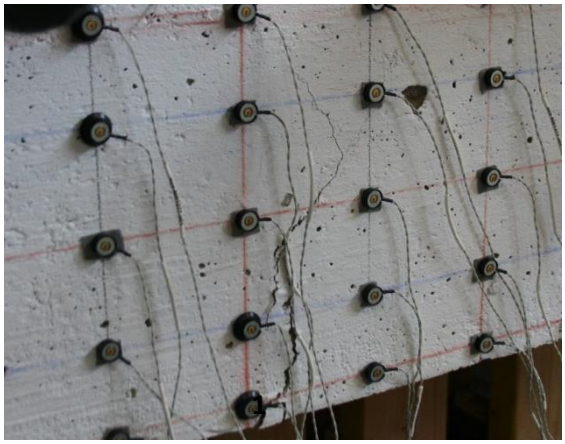

(a)

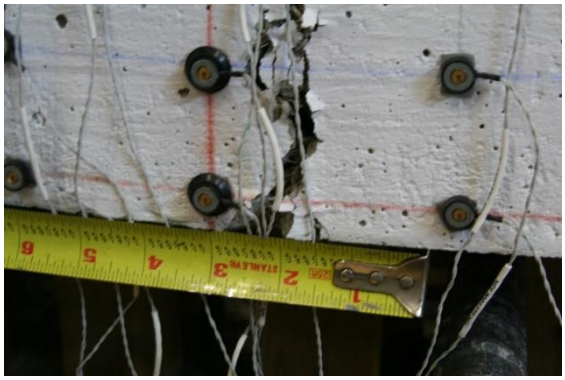

(b)

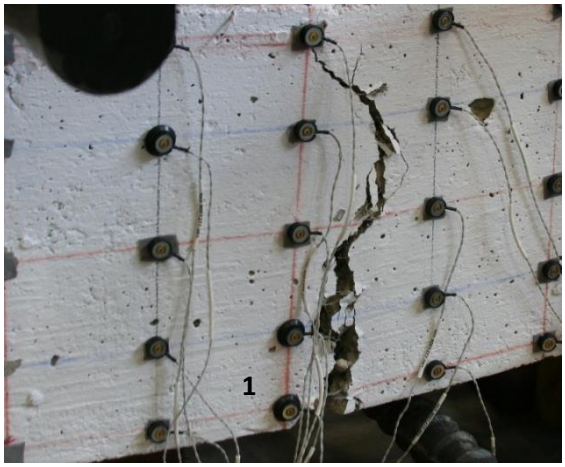

(c)

(d)

Figure 100. Crack Progression of W2 and W3 at Deflection Step:
(a) 0.35 inches, (b) 0.9 inches, (c) 1.6 inches, and Removal of Instruments

Crushing was not documented during the test. The test was continued until collapse of the specimen. Figure 101 demonstrates the failed specimen and its fiber distribution in the cross-section.

(a) (b)

Figure 101. Fiber Distribution of S9020NOS00
(a) South Face of Failure Plane and (b) North Face of Failure Plane